Flavor and evolution effects in TMD phenomenology

Flavor and evolution effects in TMD phenomenology

Manifestation of hadron structure in high-energy scattering processes

Andrea Signori

Leescommissie: prof.dr. A. Bacchetta (Università degli Studi di Pavia)
prof.dr. D. Boer (Rijksuniversiteit Groningen)
prof.dr. E.L.M.P. Laenen (Universiteit van Amsterdam, Universiteit Utrecht)
prof.dr. H.G. Raven (Vrije Universiteit Amsterdam)
prof.dr. R.J.M. Snellings (Universiteit Utrecht)

ISBN: 978-94-6233-401-4
Printed by: Gildeprint - Enschede
Front cover: Layout by A. Signori, K. Huyser. Color field designed by Freepik.com.

Dit werk maakt deel uit van het onderzoeksprogramma van de Stichting voor Fundamenteel onderzoek der Materie (FOM), die deel uitmaakt van de Nederlandse Organisatie voor Wetenschappelijk Onderzoek (NWO).

VRIJE UNIVERSITEIT

Flavor and evolution effects in TMD phenomenology

Manifestation of hadron structure in high-energy scattering processes

ACADEMISCH PROEFSCHRIFT

ter verkrijging van de graad Doctor aan
de Vrije Universiteit Amsterdam,
op gezag van de rector magnificus
prof.dr. V. Subramaniam,
in het openbaar te verdedigen
ten overstaan van de promotiecommissie
van de Faculteit der Exacte Wetenschappen
op maandag 17 oktober 2016 om 13.45 uur
in de aula van de universiteit,
De Boelelaan 1105

door

Andrea Signori

geboren te Cremona, Italië

promotor:	prof.dr. P.J.G. Mulders
copromotor:	dr. M. Radici

to Carlotta

CONTENTS

SCIENTIFIC PUBLICATIONS

This thesis is in part based on the following publications:

1. A. Signori, A. Bacchetta, M. Radici, G. Schnell
   Investigations into the flavor dependence of partonic transverse momentum
   JHEP **1311** (2013) 194 - arXiv:1309.3507 [hep-ph].

2. F. Hautmann, H. Jung, M. Krämer, P.J. Mulders, E.R. Nocera, T.C. Rogers, A. Signori
   TMDlib and TMDplotter: library and plotting tools for transverse-momentum-dependent parton distributions
   Eur.Phys.J. **C74** (2014) 3220 - arXiv:1408.3015 [hep-ph].

3. A. Bacchetta, M. Garcia Echevarria, P.J. Mulders, M. Radici, A. Signori
   Effects of TMD evolution and partonic flavor on e^+e^- annihilation into hadrons
   JHEP **1511** (2015) 076 - arXiv:1508.00402 [hep-ph].

4. D. Boer, S. Cotogno, T. van Daal, P.J. Mulders, A. Signori, Y. Zhou
   Gluon and Wilson loop TMDs for hadrons of spin ≤ 1
   arXiv:1607.01654 [hep-ph].

5. A. Bacchetta, P.J. Mulders, M. Radici, M. Ritzmann, A. Signori
   Nonperturbative effects in q_T spectra of electroweak bosons at the LHC
   In preparation.

6. M. Garcia Echevarria, T. Kasemets, J.P. Lansberg, C. Pisano, A. Signori
   Gluon TMDs and quarkonia production in hadronic collisions
   In preparation.

Reviews and collaboration documents

1. R. Angeles-Martinez et al.
   Transverse Momentum Dependent (TMD) parton distribution functions: status and prospects
   Acta Phys.Polon. **B46** (2015) 12, 2501-2534 - arXiv:1507.05267 [hep-ph].

2. A. Signori
   Transverse double spin asymmetry in inclusive hadron production
   Summer program 2012 - HERMES Internal Report 12-016 (2012).

Conference proceedings

A list of publications including conference proceedings is provided at the inSpire database.

Talks

For a list of talks given at national and international conferences and workshops see https://users.hepforge.org/~signori/talks. Slides are available for download.

CHAPTER 1

INTRODUCTION

As far as I see,
all a priori statements in physics
have their origin in symmetry.
H. Weyl

The beauty of the world we live in lies also in the description that we can give of it. Throughout this thesis, we will investigate the proton structure and present some of its representations. The proton lies at the core of matter, at the boundary between the microscopic and the macroscopic world: its properties are shaped by elementary particle physics and, in turn, they forge chemistry and molecular physics. Physics is a phenomenological science: it combines theoretical and experimental investigations, and hadronic physics is a clear example of it.

1.1 Particle physics

The Standard Model of particle physics is a Yang-Mills theory [1] with internal local symmetry (called gauge) group $SU(3)_c \otimes SU(2)_I \otimes U(1)_Y$, where the subscripts refer to the involved quantum numbers: color c, isospin I and hypercharge Y.

The two main categories into which elementary particles are divided are bosons and fermions (see Fig. 1.1). In the Standard Model, the vector bosons mediate the interactions. The scalar Higgs boson mediates the field required for the particles to gain mass in a gauge-invariant way. Fermions are divided into two categories: leptons and quarks. The latter, coming in six different flavors, are, together with gluons, the elementary degrees of freedom of the strong force, namely Quantum Chromodynamics (QCD). Due to the confining nature of the strong force, quarks

and gluons live inescapably bound inside hadrons, particles such as the proton and the neutron. In this thesis we will focus only on QCD.

QCD is a non-abelian gauge theory with gauge group $SU(N_c)$, $N_c = 3$ [2, 3]. Quarks live in the fundamental representation of this group, $\mathbb{C}^3$, and have three independent color states. Gluons, physically the mediators of the strong force and mathematically represented by the gauge connection, live in the adjoint representation of the group. They span the related Lie algebra, whose dimension is $N_c^2 - 1 = 8$. For this reason, gluons carry 8 independent combinations of a color and an anticolor charge, equivalent to the octet (8) representation in $3 \otimes 3^* = 1 \oplus 8$. The Lagrangian density for QCD is:

$$\mathcal{L}_{\text{QCD}} = -\frac{1}{4} F^{a\mu\nu} F^a_{\mu\nu} + \sum_{q=1}^{N_f} \bar{\psi}^r_q (i\gamma^\mu D^{rs}_\mu - m_q \delta^{rs}) \psi^s_q \ , \tag{1.1.1}$$

where a is the color octet index, r, s are the color triplet indexes and the sum runs over the N_f flavor species. The covariant derivative in the Lagrangian is defined as:

$$D_\mu = \partial_\mu - i g_s T^a A^a_\mu \ , \tag{1.1.2}$$

where g_s is the coupling constant, A^a_μ is the gluon field (gauge connection) and T^a are the generators of the Lie algebra. The field-strength (curvature) tensor is then introduced as:

$$F^a_{\mu\nu} \doteq \partial_\mu A^a_\nu - \partial_\nu A^a_\mu - g_s f_{abc} A^b_\mu A^c_\nu \ , \tag{1.1.3}$$

$$\text{with} \quad [T^a, T^b] = i f_{abc} T^c \ , \quad a, b, c = 1, \cdots, 8 \ , \tag{1.1.4}$$

where f_{abc} are the structure constants of the gauge group. A $SU(3)$ gauge transformation is a local phase transformation of the form:

$$\mathcal{U}(x) = e^{-i\alpha^a(x) T^a} \ , \tag{1.1.5}$$

where $\alpha^a(x)$ is a function of space and time. Thanks to the covariant derivative (1.1.2), the QCD Lagrangian density is invariant under gauge transformations [4,5]. The connection $A^a_\mu(x)$ is a geometric tool to introduce the mediators of forces in particle physics. From the mathematical point of view, it is defined in the context of fiber bundles [2, 3] and parallel transport (Sec. 2.7).

1.2 From quarks to TMDs

The non-abelian character of QCD leads both toward confinement of quarks and gluons inside hadrons at low energy and to asymptotic freedom at high energies (see Fig. 2.3). For this reason, quarks and gluons can be observed as free particles when

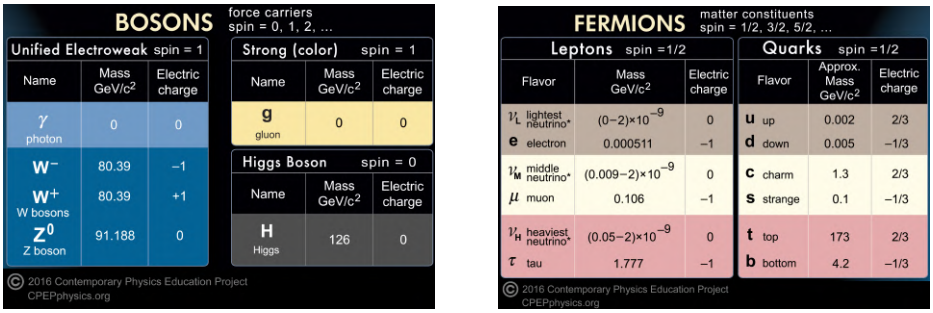

(a) (b)

Figure 1.1. An overview of the properties of the force carriers, the Higgs boson (a) and the matter constituents (b) within the Standard Model, the theory which gives a mathematical context to particle physics. For more details and extensive summaries see The Particle Data Group website and [6]. Credit: CPEP 2016.

probing a proton in a high-energy scattering process (Chap. 2). Looking at the debris of the proton undergoing a scattering experiment we can reconstruct maps of the proton structure in position and momentum space. What we actually observe is the *manifestation* of hadron structure in a chosen experiment. This manifestation changes, in some cases, according to the process considered and evolves with the energy at which the proton is probed.

Through high-energy scatterings we can access only certain *projections* of the full information available in coordinate and momentum space. For example, the simplest maps in one-dimensional momentum space that we can reconstruct are the *parton distribution functions* (PDFs), which describe the probability of finding a quark or a gluon inside the proton, with a fraction x of the momentum carried by the proton (see Fig. 1.2). We know these one-dimensional maps in good detail (see Sec. 4.3). These pictures are only sensitive to the *collinear* motion of quarks and gluons inside the proton and the other momentum components are integrated over (see Chap. 2). It is possible to enrich the description and access the dynamics of quarks and gluons in momentum space in three dimensions. In this case, the maps are named Transverse-Momentum-Dependent Parton Distribution Functions (TMD PDFs or TMDs). The TMD PDFs enlarge the amount of nonperturbative information carried by ordinary PDFs, opening the window onto explorations of the multidimensional structure of hadrons in momentum space.

1.2.1 Why investigating hadron structure

Hadron structure is related to fundamental questions in particle physics and multidimensional maps can help in answering them. For example, we know that the proton is a fermion with spin 1/2, but presently we do not know how to precisely

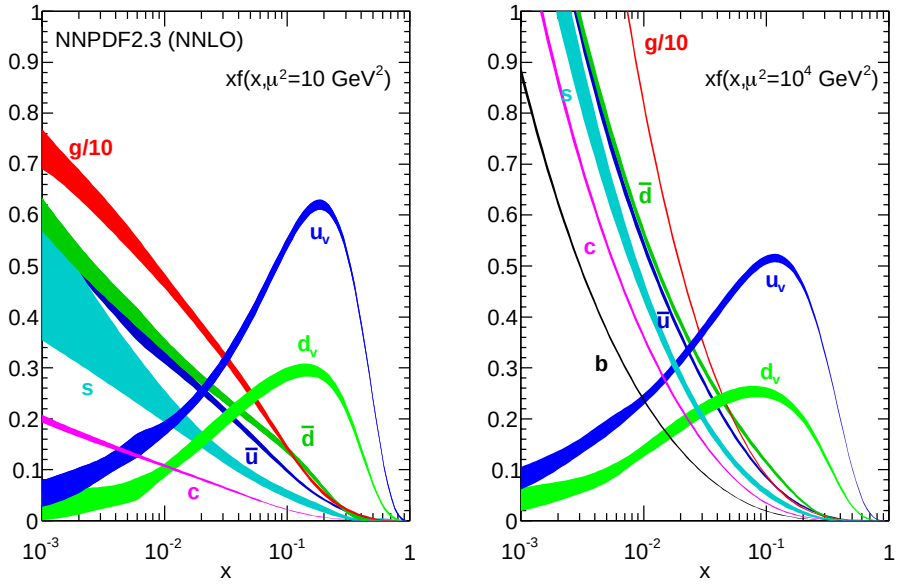

Figure 1.2. Collinear parton distribution functions studied by the NNPDF collaboration, probing the proton structure at two different energy scales (10^2 GeV^2 and 10^4 GeV^2). Different colors label different flavors for quarks and the gluons. The differences between the curve for different flavors are also of nonperturbative origin.

attribute this value to its elementary constituents. We know how to partition the proton spin among the orbital angular momentum and the spin of quarks and gluons [7–12], but we do not have very precise numerical determinations of the individual contributions, in particular for the orbital angular momentum [13]. To this extent, three-dimensional distributions of quarks and gluons in momentum space are fundamental tools: they encode all the possible spin-orbit and spin-spin correlations between the proton and its constituents and a detailed understanding of their structure can provide information on the contributions of quarks and gluons to the proton spin (see e.g. [14]). For example, the Sivers TMD PDF describes the correlation between the spin of a transversely polarized proton with the orbital angular momentum of the parton considered.

The spin structure of the proton is just one among the open problems in QCD, together with, e.g., a quantitative description of confinement and of the hadronic mass spectrum and the impact of hadron structure in (very) high-energy physics. The latter is discussed throughout the thesis, with a particular focus in Chapters 4, 5, 6, 7 and 8. Concerning hadron masses, the Higgs mechanism describes

the origin of mass for elementary particles and the three valence quarks together account only for a tiny fraction of the mass of the proton (938 MeV [6]). The rest is due to the QCD dynamics, as lattice calculations accurately predict. A detailed knowledge of multidimensional hadron structure will definitely help in shedding light on these fundamental issues. Despite many efforts, though, our level of knowledge is still limited compared to the collinear level, but thanks to improvements on both the theoretical and the experimental sides (Sec. 4.4) we are moving from an exploratory phase to a precision and consolidation phase.

1.2.2 3D maps in momentum space

Transverse-momentum-dependent parton distribution functions and their fragmentation counterpart (fragmentation functions, FFs) depend on the longitudinal and transverse components of the momentum of partons with respect to the parent hadron momentum, as well as on their flavor and polarization state. In the last years several data for single- and double-spin asymmetries in semi-inclusive deep-inelastic scattering (SIDIS) have been accumulated and can be interpreted as originating from the effect of specific combinations of (polarized) TMD PDFs and TMD FFs (for a review, see, e.g., [15–18]).

In the context of factorization theorems, TMD PDFs and TMD FFs can be defined via physical observables that are sensitive to processes with two separate scales. For example, the appropriate factorization theorem for the SIDIS cross section holds true if the virtuality Q of the hard photon is much larger than the transverse momentum $P_{h\perp}$ of the observed hadron [19, 20], which is accounted for by partonic transverse momenta.

In order to work with gauge invariant hadronic matrix elements, it is necessary to include the so-called gauge links, related to gluon radiation (Sec. 2.7), in the operator definition of TMDs. Gauge links provide also the necessary phase to generate the above mentioned spin asymmetries [21–23]. Because initial-state and final-state gluon interactions are summed into different gauge links, the TMD functions may be process-dependent, although parity and time reversal invariance simplify this non-universality to calculable proportionality factors [24].

To account for scale dependence, the TMD functions obey evolution equations that generalize the standard Renormalization Group Evolution (RGE) to a multi-scale regime in hard processes. Despite recent developments, the phenomenological implementation of these effects is still under active debate [25–28].

From the experimental point of view, only few data sets are available with enough statistics allowing for a multidimensional analysis and a direct access to transverse momentum distributions [29, 30]; in other cases, the studies were limited in the multidimensional coverage and by the restricted variety of targets and final-state hadrons [31–35].

1.3 This thesis

In this thesis we will present strategies and studies to deepen into the phenomenology of TMDs.

In Chap. 1 we introduce the Standard Model of particle physics as a gauge theory. The need for multidimensional distributions to investigate the nonperturbative structure of hadrons is addressed and an overview of the properties of TMDs, 3D maps in momentum space, is presented.

Chap. 2 will briefly overview the genesis of the parton model for hadron structure and introduce the Operator Product Expansion technique and the Diagrammatic Approach. Relying on the latter, we will present the formalism leading to the definition of TMD PDFs and TMD FFs for quarks and gluons. We will address the role of discrete symmetries, gauge symmetry and their interplay. The latter gives rise to time reversal odd (T-odd) effects, a peculiarity of the TMD formalism for distribution functions. A detailed analysis of some T-odd structures will be given in App. C.

Chap. 3 will review the role of TMD factorization and evolution in high-energy scattering processes. We will also look at the definition of TMD structures from the point of view of perturbation theory, complementing the analysis given in Chap. 2. We will focus on perturbative accuracy of evolution and address the role of nonperturbative contributions in different kinematic regions. Other factorization and evolution schemes will be briefly reviewed.

In Chap. 4 we will compare different experimental observables useful to provide an insight into the three-dimensional structure of the proton in momentum space. Moreover, we will briefly overview the status of TMD phenomenology, focusing on unpolarized distributions and we will present possible strategies to improve the current level of knowledge.

Chap. 5 will present an extraction of unpolarized TMD PDFs and TMD FFs from data of Semi-Inclusive Deep-Inelastic Scattering (SIDIS), taking into account the flavor and kinematic dependence of the average square intrinsic transverse momentum of quarks. The analysis is based on the "replica method", where $\mathcal{N}$ replica of the original experimental data are generated and fitted, producing statistical distributions for best-fit parameters. The power of the replica method in fitting data and in predicting observables will be presented in Chap. 5, 6, 7.

Given the results presented in Chap. 5, what is their impact on medium/high-energy physics? We will address this question first considering e^+e^- annihilation

and then electroweak boson production. Chap. 6 will analyze the combined impact of TMD evolution effects and the flavor and kinematic dependence of intrinsic transverse momentum on electron-positron annihilation into two almost back-to-back hadrons. We will test the impact of different phenomenological choices on hadron multiplicities. In particular, we will compute predictions for two different experimental setups, BELLE and BES-III, investigating the impact of the hard energy scale on the possibility of studying nonperturbative parameters.

Chap. 7 will investigate the impact of the flavor dependence of intrinsic transverse momentum on the transverse momentum spectrum of electroweak boson produced at the LHC. We will estimate the uncertainties introduced by this yet unexplored degree of freedom and compare them to the other sources of error already presented in literature.

Chap. 8 will consider the role of gluons in hadronic collisions. First of all, we will investigate TMD factorization for quarkonium production in proton-proton collisions from an effective field theory point of view, focusing on perturbative and nonperturbative contributions to gluon TMD PDFs. In particular, the role of linearly polarized gluons in unpolarized collisions will be studied. For reference, we will also overview past investigations (Sec. 8.1). We will present predictions for unpolarized proton-proton collisions, looking at the complete spectrum in the transverse momentum of the produced quarkonium. In particular, we will address the problem of the matching between TMD and collinear factorization. We will also present a strategy to extract time reversal odd gluon TMD PDFs from polarized collisions at A Fixed Target experiment at the LHC (AFTER@LHC [36, 37]).

Chap. 9 will summarize the results presented in the previous chapters and outline strategies for the future.

The goal of this thesis is two-fold: first of all, the results achieved during the PhD program will be presented; secondly, I would like to leave an introduction to TMD phenomenology, which might be useful for researchers interested in the field. In the following, I will use a first-person plural perspective. This is because the results presented in this thesis have not been achieved by the author only, but through a collective effort based on fruitful collaborations. This is a literary form to acknowledge the people that took part in it.

CHAPTER 2

UNRAVELING HADRON STRUCTURE

Stat rosa pristina nomine,
nomina nuda tenemus.
U. Eco

2.1 The parton model of hadron structure

The quest to understand what lies in the deep heart of matter reached a milestone around 1910, when Geiger and Marsden, under Rutherford's supervision, performed scattering of α particles off a thin gold foil [38], observing many particles scattered with an angle bigger than 90 degrees (Fig. 2.1). To explain this phenomenon, they made the hypothesis that a positive electrically charged nucleus lies at the core of atoms. This fundamental experiment opened the way to nuclear physics. Almost 50 years later, between 1967 and 1973, scientists at MIT and SLAC repeated the same experiment but on a smaller scale [39]. Performing scattering of electrons off a proton target, they investigated the inner structure of protons, relying on the theory of Quantum Electrodynamics (QED) to control the behavior of the probe (the photon). This process, called Deep-Inelastic Scattering (DIS) (see Fig. 2.2), is an "evolution" of Rutherford's scattering to higher energies of the probe, which enables a finer resolution of the components of the nuclei and allows to unravel the inner structure of the proton. In those years, Gell-Mann and Ne'eman proposed [40, 41] an explanation of the spectrum of the observed baryons and mesons through group theory. This led also to the concept of *quarks*, hypothetical elementary constituents of strongly interacting particles [42, 43].

DIS experiments supported this idea, because their outcome was compatible with elastic scattering off free, pointlike, spin one-half, electrically charged particles:

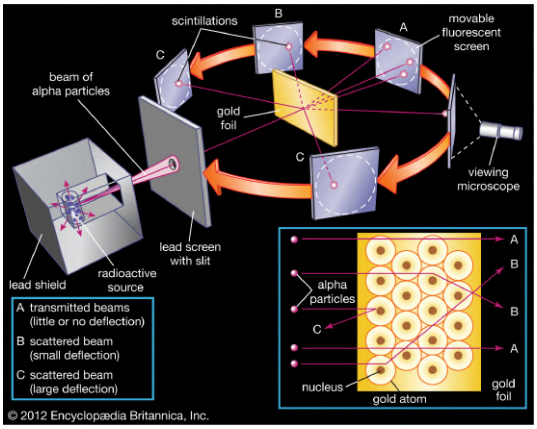

Figure 2.1. In Rutherford's experiment α particles scatter off a gold foil, bouncing in different directions. The amount of particles scattered at high angles led to the hypothesis of an atomic *nucleus* with positive charge. Credit: Encyclopedia Britannica).

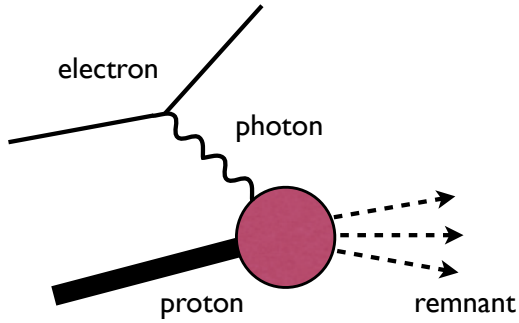

Figure 2.2. The process of Deep-Inelastic Scattering (DIS), where an electron scatters off a proton, probing its structure through the exchange of a virtual photon. Another electron is observed in the final state. DIS has been the first fundamental tool to investigate the structure of the proton.

at high energy, the proton looked like an ensemble of free charged fermions. This simple model was named *parton model* after Feynman and Bjorken [44].

The cross section for a scattering process between a lepton and a hadron is proportional to the contraction between a leptonic tensor L and a hadronic tensor W:

$$d\sigma \sim L_{\mu\nu} W^{\mu\nu} \ , \tag{2.1.1}$$

where, in general, the form of the two tensors depend on the process. The hadronic tensor cannot be completely calculated, due to the nonperturbative nature of the target. Nonetheless, its structure can be parametrized following hermiticity, the

discrete symmetries of the theory and Ward identities as guiding principles [4]. In the case of a QED-mediated process, it can be represented as:

$$W^{\mu\rho} = W_1(\nu, q^2)\big(-g^{\mu\rho} + \frac{q^\mu q^\rho}{q^2}\big) + \frac{W_2(\nu, q^2)}{M^2}\big(p^\mu - \frac{p\cdot q}{q^2}q^\mu\big)\big(p^\rho - \frac{p\cdot q}{q^2}q^\rho\big) \ , \quad (2.1.2)$$

where p is the four-momentum of the parton, M is the mass of the proton, q is the four-momentum of the exchanged photon, ν is its energy, $q^2 = -Q^2$, $Q^2 > 0$, is its invariant mass squared[1] and $W_{1,2}(\nu, q^2)$ are two nonperturbative functions describing the structure of the proton as seen by the probe. Experimentally it was observed that these two functions do not depend on the invariant mass of the photon, but only on a Lorentz invariant variable measuring the degree of inelasticity of the reaction, named Bjorken-x (x_B):

$$\nu W_2(\nu, Q^2) \longrightarrow F_2(x_B) \ , \quad (2.1.3)$$

$$M W_1(\nu, Q^2) \longrightarrow F_1(x_B) \ , \quad (2.1.4)$$

$$x_B \doteq \frac{Q^2}{2P\cdot q} \ , \quad (2.1.5)$$

where P is the four momentum of the proton. This property of the structure functions in deep-inelastic regime (ν, $Q^2 \to \infty$, x_B fixed) is called *Bjorken scaling* [45]. Such a behavior of the structure functions coincides with the one obtained by the elastic scattering of a lepton off a free pointlike spin 1/2 particle and leads to the parton model interpretation of the proton structure. In particular, assuming that the elementary scattering is elastic and mediated by one photon only, we obtain the Callan-Gross relation [46]:

$$2x_B F_1(x_B) = F_2(x_B) = x_B \sum_f e_f^2 \phi_f(x_B) \ , \quad (2.1.6)$$

where $\phi_f(x_B)$ is a density function describing the probability of finding a parton of flavor f inside the proton, as a function of x_B. The concept of density function (and its generalizations) is at the core of the phenomenology of the proton structure, as we will see in the next chapters. (2.1.6) implies that partons carry a well defined fraction x_B of the proton momentum and the probability density ϕ_f does not depend on the energy scale at which the snapshot of the proton by the virtual photon has been recorded.

Notably, the Callan-Gross relation has been experimentally verified by measuring a vanishing ratio between the structure functions W_L, W_T (related to $W_{1,2}$ and accounting for the two polarization states in which the photon probes the proton)

[1] In SIDIS the photon is space-like, in hadronic collisions instead it is time-like, $q^2 = Q^2$, $Q^2 > 0$.

as a function of x_B [47, 48].

After the introduction of Quantum Chromodynamics between 1972 and 1973 as a non-abelian gauge theory (thus asymptotically-free) [49–53][2], the partons were identified with the quarks, which, together with the gluons, constitute the elementary degrees of freedom of the theory at high energy. The fact that quarks appear as free partons when the energy of the probe is high enough is due to the asymptotic freedom of QCD, namely the fact that the coupling constant $\alpha_s(\mu)$ is governed by a negative derivative with respect to the renormalization scale μ [4] (see Fig. 2.3).

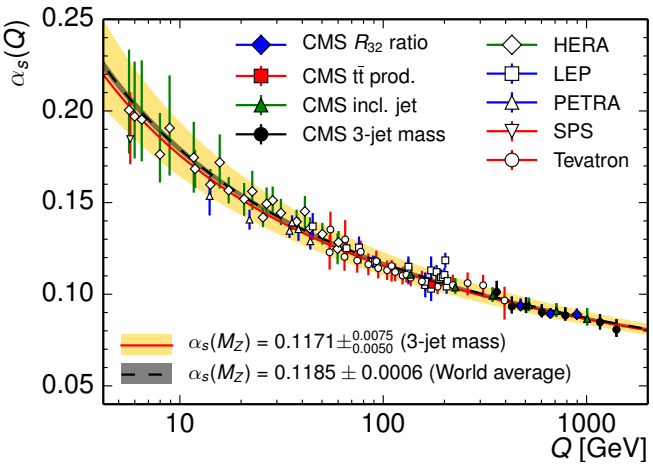

Figure 2.3. The coupling constant of QCD is governed by a negative derivative with respect to the renormalization scale μ. This leads to asymptotic freedom [54] of quarks and gluons and suggests that the theory is confined at low energy scales (e.g. at the scale of the proton mass). The picture collects part of the available experimental determinations at different energies and the world average at the Z pole [6, 55].

Despite being successful in describing the DIS experimental results, it was soon realized that the parton model is a poor approximation of QCD. In particular, gluons and all the effects induced by them are neglected. Among the others, two striking violations of the parton model are the violations of Bjorken scaling [4] and the momentum sum rule. Violations of the Bjorken scaling are induced by perturbative corrections (see Fig. 2.4) proportional to $\alpha_s(Q^2)\ln Q^2$ (see Chap. 3), suppressed when the value of the coupling constant is small. These corrections are accounted by the DGLAP evolution equations [4]. Increasing the energy scale, these equations allow to resolve finer structures. Investigations of the (longitudinal) momentum sum rule reveals that, neglecting gluons, quarks can reproduce only about half of the momentum of the parent proton.

[2] In [49–51] the asymptotic freedom on non-abelian gauge theories was discussed. In [52, 53] the concept of color symmetry as non-abelian gauge symmetry was proposed.

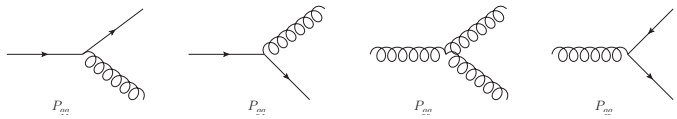

Figure 2.4. The diagrams related to the lowest order QCD splitting functions. Each splitting is described by the probability that a parton p becomes p' carrying a fraction of the momentum carried by p. DGLAP equations govern their behavior with the hard scale Q^2 [4].

2.2 The hadronic tensor

The hadron tensor W describes the interaction between the probe and the hadron target. At the level of operators, the hadronic tensor introduced in (2.1.2) is proportional to a product of matrix elements of currents (whose nature depends on the interaction):

$$W^{\mu\nu} \sim \langle \text{in}|j^{\mu}(0)|\text{out}\rangle_c \, \langle \text{out}|j^{\nu}(0)|\text{in}\rangle_c \, . \tag{2.2.1}$$

If the probe is a photon, this feels the electromagnetic current in the target, acting on the "in" state and generating the "out" state. The subscript c indicates that only the connected diagrams are considered[3]. More precisely, the current j acts on the on-shell $|\text{in}\rangle$ state producing an on-shell $|\text{out}\rangle$ state, respecting conservation of four-momentum. In the final state there is the remnant X of the target and, depending on the process, also other on-shell particles. Integrating over all possible on-shell momenta P_X of the remnant, the hadronic tensor can be in general written as:

$$2MW^{\mu\nu}_{[\text{proc}]} = \frac{1}{(2\pi)^4} \sum_X \int \frac{d^3\boldsymbol{P}_X}{(2\pi)^3 2E_X} (2\pi)^4 \delta^{(4)}(P_{\text{in}} - P_{\text{out}}) H^{\mu\nu}_{[\text{proc}]} \, , \tag{2.2.2}$$

where the argument of the delta function and the form of the H tensor (containing the products of currents) depend on the process [proc] under consideration. In this thesis we will deal mainly with three processes involving hadrons in the initial and/or final state(s): one-particle inclusive (or semi-inclusive) deep inelastic scattering (1P DIS or SIDIS), Drell-Yan (DY) and semi-inclusive electron positron annihilation into two almost back to back hadrons ($e^+e^- \to 2h$). The H tensors involving the currents are:

$$H^{\mu\nu}_{[\ell h]} = \langle PS|j^{\mu}(0)|P_h S_h; P_X\rangle \, \langle P_h S_h; P_X|j^{\nu}(0)|PS\rangle \tag{2.2.3}$$

$$H^{\mu\nu}_{[DY]} = \langle P_A S_A; P_B S_B|j^{\mu}(0)|P_X\rangle \, \langle P_X|j^{\nu}(0)|P_A S_A; P_B S_B\rangle \tag{2.2.4}$$

$$H^{\mu\nu}_{[e^+e^-]} = \langle 0|j^{\mu}(0)|P_{h_1} S_{h_1}; P_{h_2} S_{h_2}; P_X\rangle \, \langle P_{h_1} S_{h_1}; P_{h_2} S_{h_2}; P_X|j^{\nu}(0)|0\rangle \, . \tag{2.2.5}$$

[3]From now on, it will be omitted, but it is understood that we always work with connected diagrams.

In the case of SIDIS (2.2.3), $|PS\rangle$ is the in-state representing a proton with four-momentum P and spin S and the out state $|P_h S_h; P_X\rangle$ represents the remnant of the proton with momentum P_X and one hadron h detected in the final state with momentum P_h and spin S_h. For DY (2.2.4), A and B refer to the two colliding hadrons (protons) in the initial state. In e^+e^- annihilation (2.2.5), $|0\rangle$ is the vacuum state of QCD (the reaction is initiated by two leptons) and in the final state we have two hadrons h_1 and h_2.

Relying on the previous equations, the cross sections differential with respect to the three-momentum of the particle(s) in the final state are:

$$\textbf{SIDIS} \;:\; E_h E_{\ell'} \frac{d^6\sigma}{d^3\ell' d^3\boldsymbol{P}_h} = \frac{M}{s}\frac{\alpha_s^2}{Q^4} L^{[\ell h]}_{\mu\nu} W^{\mu\nu}_{[\ell h]} \; (1 + \mathcal{O}(\alpha_s)) \tag{2.2.6}$$

$$\textbf{DY} \;:\; E_\ell E_{\ell'} \frac{d^6\sigma}{d^3\ell d^3\ell'} = \frac{\alpha_s^2}{sQ^4} L^{[DY]}_{\mu\nu} W^{\mu\nu}_{[DY]} \; (1 + \mathcal{O}(\alpha_s)) \tag{2.2.7}$$

$$\mathbf{e^+e^-} \to \mathbf{2h} \;:\; E_{h_1} E_{h_2} \frac{d^6\sigma}{d^3\boldsymbol{P}_{h_1} d^3\boldsymbol{P}_{h_2}} = \frac{\alpha_s^2}{4Q^6} L^{[e^+e^-]}_{\mu\nu} W^{\mu\nu}_{[e^+e^-]} \; (1 + \mathcal{O}(\alpha_s)) \; . \tag{2.2.8}$$

For SIDIS (2.2.6), ℓ' is the four-momentum of the lepton in the final state, M is the mass of the proton target, s the Mandelstram invariant [4]. In DY (2.2.7), ℓ and ℓ' represent the detected leptons in the final state. In all processes, Q is the relevant hard scale and the tensors $L_{\mu\nu}$ represent the leptonic currents [56,57]. Perturbative corrections to the tree level processes are summarized in the $\mathcal{O}(\alpha_s)$ terms.

There are two main methods to further resolve (2.2.1), accessing the information encoded in the structure of the $H^{\mu\nu}_{[\text{proc}]}$ tensor. The first one is the *operator product expansion* (OPE), proposed by Wilson [58] in 1968. The second one is the *diagrammatic approach*, proposed by Politzer [59] in 1980. Both establish a hierarchy of corrections as powers of the inverse hard scale (the *twist*[4] expansion), complementary to the corrections proportional to α_s introduced by the perturbation theory. The OPE is mathematically proven only for fully inclusive DIS and e^+e^- annihilation. The diagrammatic approach is a generalized form of the parton model, which *assumes* an extension of the OPE to less inclusive cases.

2.3 The Operator Product Expansion

For a detailed treatment of the OPE see [4, 5, 57, 60–62]. Within the hadronic tensor, it would be ideal to separate in distinct pieces the hadronic (nonperturbative) part from the part describing the interaction with the probe (perturbative and calculable). The goal is to *factorize* the perturbative contributions from the

[4]Different definitions of twist exist, which are not equivalent. Nonetheless, they all introduce an expansion in powers of the inverse hard scale. For more details see Sec. 2.3.

nonperturbative ones, for which universality properties hold between different processes [24].

Wilson proposed [58] that a product of local operators $A(x)B(y)$ has an expansion, when $|x-y|$ is small, of the form:

$$A(x)B(y) = \sum_n C_n(x-y)O_n(x) \ . \tag{2.3.1}$$

This expression is called the Operator Product Expansion (OPE) of the non-local product $A(x)B(y)$ on the basis of local operators $O_n(x)$. The OPE has been demonstrated by Zimmerman in perturbation theory [63] for a time-ordered product of operators (which, in turn, can be normal-ordered products of field operators, as for a current). It turns out that the only two processes for which an OPE on W is allowed are inclusive DIS and e^+e^- annihilation [5]. This is because in both cases the hadronic tensor contains a *commutator* of currents, which is related to time-ordered products of currents. For DIS, e.g.:

$$2MW^{\mu\nu}_{[DIS]} = \frac{1}{2\pi}\int d^4x \ e^{iq\cdot x}\langle PS|\ [j^\mu(x), j^\nu(0)]\ |PS\rangle \ , \tag{2.3.2}$$

$$\text{sign}(x^0)\ [j^\mu(x), j^\nu(0)] = T[j^\mu(x)j^\nu(0)] - T[j^\mu(x)j^\nu(0)]^\dagger \ . \tag{2.3.3}$$

From (2.3.3), it is possible to show [5] that W in the case of inclusive e^+e^- is dominated by short distances $x \sim 0$ (short distance expansion). In inclusive DIS, instead, there is a dominance from the light-cone region $x^2 \sim 0$ (light cone expansion).

Performing an OPE of the hadronic tensor in DIS, we can show that the parton model is not just an effective way of interpreting experimental results, but it can be formally derived calculating (2.3.2) and (2.3.3) relying on the expression for currents of *free fermion fields* (as the partons are in DIS regime):

$$j^\mu(x) = :\bar{\psi}(x)\gamma^\mu\psi(x): \quad . \tag{2.3.4}$$

In this way, it is possible to isolate four different contributions to the hadronic tensor (2.3.2), with a diagrammatic interpretation given in Fig. 2.5 [5]. The first one (a) involves the identity $\mathbb{I}$ and, being disconnected, does not contribute to it. Part (b) represents the extraction of an (anti)quark from the proton and its reinsertion in the remnant at distance $|x|$ after the interaction with a photon, via a vector or an axial coupling. We name these contributions $O_{V,A}(x,0)$, respectively. Only O_V is probed in unpolarized DIS. The last one, named $O_{\mu\nu}$, (c) is the least singular and involves the extraction of two partons.

Accordingly, the hadronic tensor of fully unpolarized inclusive DIS is dominated

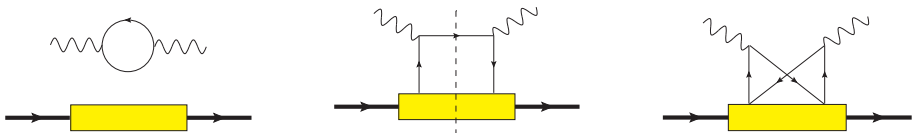

(a) (b) (c)

Figure 2.5. Diagrammatic interpretations of the operators contributing to (2.3.2). (a) represents the identity operator $\mathbb{I}$, namely there is no interaction between the probe and the proton. (b) represents the action of $O_{V,A}(x,0)$, which extract an (anti)quark from the proton and reinsert it at a distance x. (c) represents $O_{\mu\nu}(x,0)$, which performs multiple extractions and insertions of (anti)quarks.

by the bi-local operator $O_V(x,0)$. Inserting its expression [5] in (2.3.2) we get:

$$2MW^{\mu\nu}_{[DIS]} \sim \int d^4x e^{iq\cdot x} x^\lambda \sigma_{\mu\lambda\nu\rho} \langle PS|O^\rho_V(x,0)|PS\rangle \tag{2.3.5}$$
$$\sim \langle PS| : \bar\psi(x)\gamma^\rho\psi(0) : |PS\rangle_{|_{\xi^+=0}} - \langle PS| : \bar\psi(0)\gamma^\rho\psi(x) : |PS\rangle_{|_{\xi^+=0}} \ .$$

Consistently with the diagrammatic interpretation given in Fig. 2.5, we can interpret the first term as the extraction of a quark from the proton at point x and its reinsertion into the remnant at point 0, restoring a proton in the final state. The second term has the same interpretation, but in terms of an antiquark. Notably, the matrix elements are evaluated at fixed light cone time $\xi^+ = 0$, so the time ordering on the currents eventually does not have a practical effect. Mathematically the last two terms can be seen as the trace of two Dirac structures, γ^ρ and a quark-quark *correlator*, proportional to the expectation value on the proton state of the fermion bilinear $\bar\psi(x)\psi(0)$. This object describes part of the nonperturbative quark content of the proton (see Sec. 2.6).

The concept of twist

In general, the light-cone expansion for the product of two currents is of the form:

$$j^\mu(x)j^\nu(0) = \sum_{i,n} C^{(i)}_n(x^2) x^{\mu_1}\cdots x^{\mu_n} O^{(i)}_{\mu_1\cdots\mu_n}(0) \ , \tag{2.3.6}$$

where $O^{(i)}_{\mu_1\cdots\mu_n}$ is an irreducible symmetric traceless tensor of rank n, referred to as the spin of the local operator. The singularity structure of the coefficients functions $C^{(i)}_n$ is crucial to determine which operators contribute most, but their form depends on the structure of the currents (it is not a general property of the OPE). In a free field theory we can perform a power counting of the mass dimensions in (2.3.6) and

see that the singularity structure of the coefficients is of the form:

$$C_n^{(i)}(x^2) \sim (x^2)^{-d_j - n/2 + d_O^{(i)}(n)/2} \,, \tag{2.3.7}$$

where d_j is the dimension of the current j and $d_O^{(i)}(n)$ is the dimension of the local operator $O^{(i)}_{\mu_1 \cdots \mu_n}$. The strength of the singularity for each term in the OPE is governed by $d_O^{(i)}(n) - n$, the *twist* of the local operator $O^{(i)}_{\mu_1 \cdots \mu_n}$ [64]. The smaller the twist of the operator, the higher is the singularity of its coefficient and, accordingly, the more important the local operator will be in physical applications. Performing the Fourier transform in the definition of the DIS W tensor (2.3.2) in the free field case, the coefficient functions are proportional to [62, 65]:

$$\left(\frac{M}{Q}\right)^{d_O^{(i)}(n) - n - 2} \tag{2.3.8}$$

This suggests that we can evaluate the relevance of local operators in the OPE looking at the power of M/Q to which they contribute to the coefficient functions[5]. To correctly evaluate twist t effects in a OPE, we need to identify *all the contribution of twist* t from different local operators i (with increasing spin) and re-sum them in a "tower" of fixed twist t. This procedure (first expanding the bilocal operators, Fourier transforming and then summing all the contributions with the same twist), though, is rather lengthy. It should be possible to introduce a concept of twist directly on the non-local operators.

A *working* definition of twist *for a matrix element* of a bi-local operator is given in [62], as the order in M/Q at which the element contributes to the cross section of deep inelastic processes. Twist-t matrix elements contributes as $(M/Q)^{t-2}$. From a phenomenological point of view, the working definition is more practical than looking at the OPE-based twist and allows to label immediately a distribution or fragmentation function as a leading or sub-leading contribution in powers of M/Q (for this reason in the following we will adopt this definition). Matrix elements of definite twist in the *working* sense should coincide with the tower of resummed local operators of the same twist and increasing spin, but this is not always the case [62, 65]. The twist as given by the working definition, though, coincides with the canonical dimension of the operator in the matrix element [57]. As an example, given the light-cone vector n_- as defined in App. A, the operator[6]

$$\overline{\psi}(0) \not{n}_- \psi(x) \tag{2.3.9}$$

[5] This argument, based on power counting, holds true when no other mass scales appear in the theory. In an interacting theory, extra care is needed [4, 5, 60, 61].

[6] See Sec. 2.6 for definitions and details.

has canonical dimension 2 (in a frame where $\dim[n_-] = -1$) and its matrix elements on the proton states contribute to cross sections as $(M/Q)^0$. We will see in Sec. 2.6.3 that the operator in (2.3.9) is related to the unpolarized and Sivers quark distributions. The same counting holds for the operator

$$F^{n-i}(0)F^{n-j}(x) \ , \tag{2.3.10}$$

which represents the gluon content of the proton at twist-2 (see Sec. 2.6.4).

Thanks to the twist decomposition and considering the possibility of introducing perturbative corrections, it is possible to give a description of QCD-observables based on a double expansion in α_s and M/Q, as illustrated in Fig. 2.6. In Chap. 3

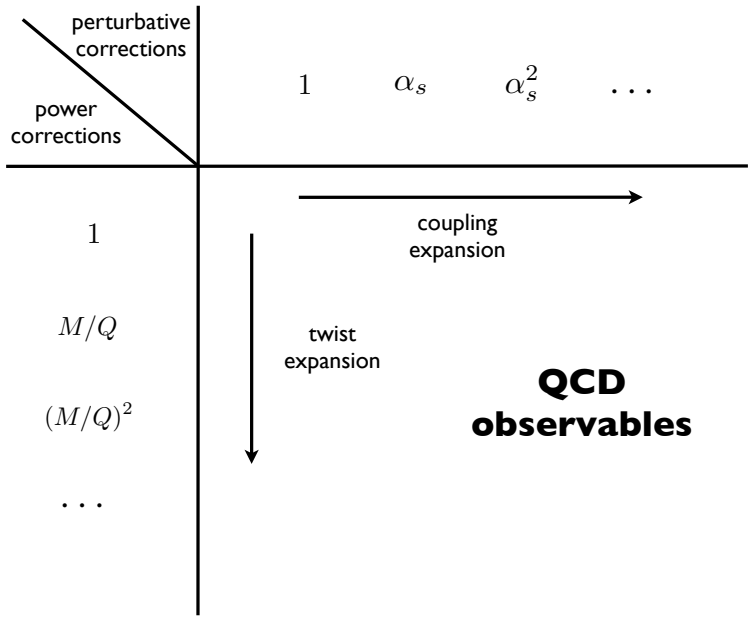

Figure 2.6. A physical observable can be expanded in terms of two parameters: the coupling constant α_s, quantifying the zoom in the perturbative structure of the theory, and the ratio M/Q, quantifying the level of accuracy in the nonperturbative structure of QCD. For a specific correlator, the twist expansion is limited to a certain order, whereas the perturbative one is not.

a further expansion will be added, in terms of logarithmic corrections arising from the renormalization/factorization scale.

Since the hadronic tensor in DIS is dominated by the light-cone region $x^2 \sim 0$, we will work with the *light-cone* expansion for four-vectors, relying on a light-cone basis (see Sec. 2.6 and A). Accordingly, the theory will be quantized at fixed light-cone time $\xi.n = \xi^+ = 0$ and not at "standard time" $\xi^0 = 0$. In standard

Minkowski components, a light-cone expansion corresponds to working in a frame where the target has very high (infinite in the DIS limit) momentum, called Infinite Momentum Frame (IMF). Definitions that will be given in the next chapters with light-cone kinematics shall be transposed to the IMF only. Working with the light cone kinematics corresponds also to introducing *good* and *bad* components for the fields [57, 62]. The good components of Dirac spinors are independent propagating degrees of freedom; the bad components are fields depending (through the Dirac equation) on the good quarks components and gluons. Because of their quark-gluon composite nature, they play a role only beyond twist two. Since the short-distance condition ($x \sim 0$) implies the light-cone condition ($x^2 \sim 0$), the view point of light cone coordinates can be extended to the inclusive e^+e^- too.

The Fourier transform in the definition of the hadronic tensor for semi-inclusive processes guarantees that for all the processes the light-cone region $x^2 \sim 0$ is a dominant one [5] (despite potentially not being the only one because of the absence of the commutator [62, 65]). This legitimizes us in using light-cone variables to describe the kinematic of the processes. From (2.2.5) we see that the hadronic tensor for $e^+e^- \to h_1h_2$ cannot be represented by a product of currents, because the final states do not allow the usage of a completeness relation on the remnant states in (2.2.2). The same holds for SIDIS, (2.2.3). In the case of Drell-Yan (2.2.4), the hadronic tensor is in a form of a product of currents, but it is not dominated by the light-cone region only, so an OPE is not applicable (for the role of time ordering see the comments after (2.3.5)). Accordingly, we need to find a way of generalizing this approach to less inclusive processes.

2.4 The diagrammatic approach

One could try to identify the dominant diagrams counting their degree of divergence in powers of the free fermion propagator [62,65]. This approach introduces the same ordering of operators rigorously achieved by the OPE where it is applicable [66,67] and serves as a guideline to perform an expansion in powers of M/Q (working twist) for bi-local operators in semi-inclusive processes, classifying the contributions according to the OPE philosophy. This approach, introduced by Politzer in [59], is called "diagrammatic expansion". In essence, a *factorization* of the cross section in terms of hard partonic parts and soft hadronic parts is *assumed* in this approach: it is the starting point of the calculation, which classifies soft hadronic parts according to the concept of twist. Moreover, at a fixed twist order, it is possible to check if the factorization holds true introducing α_s correction. This topic will be addressed in Chap. 3.

The diagrammatic approach can be seen as a generalization of the parton model, which allows to unravel power corrections not accessible from the simple parton

picture, nor from its improvements via pQCD [68–70].

Outline of the approach

There are a number of assumptions underlying this approach: incoming and outgoing hadron must be well separated in momentum space ($P_i \cdot P_j \sim \mathcal{O}(Q^2)$, where i, j run among in and out states and Q^2 is the hard scale of the process), interactions between outgoing jets can be neglected, interactions can be adiabatically introduced [56]. The procedure to calculate a cross section can be outlined in the following steps [56]:

1 choose a perturbative accuracy and write all the possible Feynman diagrams relevant to a process

2 replace external spinors and polarization vectors with appropriate *correlators* (see Sec. 2.5); each correlator can contribute to different twist orders

3 impose total momentum conservation via $(2\pi)^4\delta^{(4)}(P_{\rm in} - P_{\rm out})$

4 use standard Feynman rules to calculate any QED, EW or perturbative QCD (pQCD) part

5 compute the cross section dividing by the flux and multiplying by the phase space of the produced particles.

The diagrammatic approach allows to express any cross section in a set of correlators, each of which contributes to different twist orders. Then, according to the accuracy in M/Q, only certain contributions from each correlator are retained. In Sec. 2.5 we will investigate the *correlators* mentioned in point 2.

2.5 Correlations in spacetime

In order to grasp the meaning of correlators, let us start from QED. The wave function of an electron shows up as the spacetime dependent coefficient in the expansion of the fermionic quantum field[7] $\psi(x)$:

$$\psi(x) = \sum_s \int \frac{d^3\boldsymbol{k}}{(2\pi)^3 2E_k} \left(\hat{b}_{k,s}\ u(k,s)e^{-ik\cdot x} + \hat{d}^\dagger_{k,s} v(k,s)e^{ik\cdot x}\right) , \tag{2.5.1}$$

where k is the four-momentum of the particle, s =1,2 is the polarization index, $\hat{b}_{k,s}$ and $\hat{d}^\dagger_{k,s}$ are creation/annihilation operators satisfying equal-time anticommutation relations. The wavefunction of a free electron is a plane wave multiplied by a Dirac spinor:

$$\psi_{k,s}(x) = u(k,s)e^{-ik\cdot x} = \langle 0|\psi(x)|k,s\rangle \ . \tag{2.5.2}$$

[7] Eq. (2.5.1) is consistent with (2.5.3) and different from the convention used in [4].

The wavefunction can be thought as the probability amplitude of "presence" for the fermion at spacetime point x and the field operator ψ connects the one-particle (1P) state $|k,s\rangle$ to the vacuum state $|0\rangle$. In a scattering process between two electrons, we need such wavefunctions to account for electrons in the initial and/or final states [4]. The completeness relation for Dirac spinors is used to compute cross sections. For a massless fermion it reads:

$$\sum_s u_i(k,s)\bar{u}_j(k,s) = \not{k}_{ij} \ , \tag{2.5.3}$$

where i,j are Dirac indexes. Inserting (2.5.2) in (2.5.3), we see that the Dirac matrix $\not{k}_{ij}$ is related to the expectation value on 1P states of a local operator:

$$\not{k}_{ij} = \sum_s \langle ks|\bar{\psi}_j(x)|0\rangle\langle 0|\psi_i(x)|ks\rangle \to \sum_s \langle ks|\bar{\psi}_j(x)\psi_i(x)|ks\rangle \ , \tag{2.5.4}$$

where we recognized in $|0\rangle\langle 0|$ the identity in the Fock space with zero particles. Note that the in (2.5.4) the middle term refers to electrons, whereas the last one contains both electrons and positrons. In QCD quarks and gluons are not free, but bound inside hadrons. For this reason, at the operator level the wavefunction of a quark inside a proton needs to be modified into:

$$\langle 0|\psi(x)|ks\rangle \longleftrightarrow \langle \mathcal{X}|\psi(x)|P\rangle \ , \tag{2.5.5}$$

where $|P\rangle$ is the proton state labeled by the momentum four-vector P and $\langle\mathcal{X}|$ is the final on-shell state for the remnant X (with momentum P_X) of the proton, after the extraction of one quark performed by the operator ψ. We would like to generalize the completeness relation for an electron to the case of a quark bound inside a proton. Plugging (2.5.5) in the first part of (2.5.4), integrating over all the possible values for the on-shell P_X four-momentum, summing over all the other quantum numbers $\mathcal{X}$ of X, imposing momentum conservation on the extraction of the quark, we get:

$$\sum_{\mathcal{X}} \int \frac{d^3\boldsymbol{P}_X}{(2\pi)^3 2E_X} \langle P|\bar{\psi}_j(x)|\mathcal{X}\rangle\langle\mathcal{X}|\psi_i(x)|P\rangle\delta^{(4)}(p+P_X-P) \doteq \Phi_{ij} \ . \tag{2.5.6}$$

This is the analogue of (2.5.3) for a quark with four-momentum p bound inside a proton with momentum P (the sum over the quark polarization has been intended). Expanding the delta distribution and using the eigenvalue equation for momentum operators, we can further express this Dirac matrix as:

$$\Phi_{ij}(p;P) = \frac{1}{(2\pi)^4}\int d^4\xi e^{ip\cdot\xi}\langle P|\bar{\psi}_j(x)\mathbb{P}_{3^*}\psi_i(x+\xi)|P\rangle \ , \tag{2.5.7}$$

where ξ is the *non-locality* in spacetime introduced by the delta function. The extraction of a color triplet (quark) from the proton forces the remnant in anti-triplet color configuration. For this reason, the completeness relation over the remnant state produces an identity operator in the Hilbert space of the anti-triplet configuration, $\mathbb{P}_{3^*}$. For sake of brevity this projector will be omitted in the following. (2.5.7) is the analogue for a quark of (2.5.4).

The wavefunction of a quark inside a hadron is determined by QCD in a range of energies where the coupling constant α_s is too high to apply perturbation theory. As a consequence, we can propose a relation (which will be formally explained in Sec. 2.6) between the completeness relation for a free fermion with momentum p in QED (2.5.4) and a fermion with flavor q bound inside a proton by QCD (2.5.7) as:

$$\Phi_{ij}(p,P) = f^q(p)\ \not{p}_{ij} + \cdots\ , \tag{2.5.8}$$

where f^q is a *nonperturbative* quantity shaped by the QCD dynamics, describing the behavior of the quark bound inside the proton[8]. This is an intuitive example of the concept of *quark distribution function*. The dots represent additional terms which will be introduced and justified in Sec. 2.6.

$\Phi(p,P)$ is called a *quark-quark correlator*. Diagrammatically, we can interpret it as in Fig. 2.5 (b), where a quark of momentum p and Dirac index i is extracted from the proton with state $|P\rangle$ at the spacetime point $x+\xi$, the remnant crosses the cut (on-shellness condition) and another quark with momentum p and Dirac index j is "reinserted" in the remnant to restore the proton state $\langle P|$ at spacetime point x. Φ_{ij} collects the effects related to the quark content of the proton entering a scattering process and coincides with the hadronic object (traced with a γ matrix) appearing in the leading term of the OPE expansion for the hadronic tensor in inclusive DIS (2.3.5) (parton model).

In a scattering process involving hadrons, more contractions between field operators and the hadron state are possible. For example:

$$\langle \mathcal{X}|A^\mu(\xi)|P\rangle\ ,\ \langle \mathcal{X}|A^\mu(\eta)\psi(\xi)|P\rangle\ ,\ \cdots \tag{2.5.9}$$

Based on (2.5.9) and using arguments similar to the previous one for the quark completeness relation, we can introduce the following correlators:

$$\Gamma^{\mu\nu;\rho\sigma}(p;P) \doteq \frac{1}{(2\pi)^4}\int d^4\xi e^{ip\cdot\xi}\langle P|F^{\mu\nu}(0)F^{\rho\sigma}(\xi)|P\rangle \tag{2.5.10}$$

$$\Phi^\mu_{A\ ij}(p,p_1;P) \doteq \frac{1}{(2\pi)^4}\int d^4\xi e^{i(p-p_1)\cdot\xi}e^{ip_1\cdot\eta}\langle P|\bar{\psi}_j(0)A^\mu(\eta)\psi_i(\xi)|P\rangle\ . \tag{2.5.11}$$

Eq. (2.5.10) is the *gluon-gluon correlator*, in analogy to the quark case, and repre-

[8]Similarly, Φ_{ij} is calculated in the free-quark case in [57, 71].

sents the extraction of a gluon with momentum p from the proton and its reinsertion in the remnant in the complex conjugated amplitude. The usage of F fields rather than A fields is motivated by gauge invariance and is explained in Sec. 4.4 in [56]. (2.5.11) is an example of a *quark-gluon-quark correlator*, representing the "interference" between the extraction from the proton state of a quark with momentum $p - p_1$ and of a gluon with momenetum p_1 and the reinsertion of the quark only in the remnant in the complex conjugate amplitude. In principle, gauge symmetry requires to resum all the correlators with emission of multiple gluons in one single gauge-invariant correlator. This will be explained in Sec. 2.7. The leading twist contribution to the cross section from $\Phi^{\mu}_{A\ ij}$ is three, so it can be neglected in a twist-two analyses. The projectors on the Hilbert spaces of the remnants are omitted in (2.5.10) and (2.5.11). As explanied for (2.5.7), after extraction of a gluon, the remnant is forced in a specific color configuration by $\mathbb{P}_{8^*}$. After the extraction of a quark and a gluon, the color configuration of the remnant is specified by $\mathbb{P}_{3^*\otimes 8^*}$ [57].

Matrix elements of the form

$$\langle K_h, S_h; \mathcal{X}|\bar{\psi}(0)|0\rangle \ , \tag{2.5.12}$$

are responsible for creating a quark out of the vacuum, which *fragments* into a hadron h in the final state. It is possible to introduce a quark fragmentation correlator as:

$$\begin{aligned}\Delta_{ij}(k; K_h) &\doteq \sum_{\mathcal{X}} \frac{1}{(2\pi)^4} \int d^4\xi e^{ik\cdot\xi} \langle 0|\psi_i(\xi)|K_h, S_h; \mathcal{X}\rangle\langle K_h, S_h; \mathcal{X}|\bar{\psi}_j(0)|0\rangle \\ &= \frac{1}{(2\pi)^4} \int d^4\xi e^{ik\cdot\xi} \langle 0|\psi_i(\xi) a_h^{\dagger} a_h \bar{\psi}_j(0)|0\rangle \ ,\end{aligned} \tag{2.5.13}$$

where the sum is intended over all the quantum numbers of the remnant X. A completeness relation over the remnant and the produced hadron states does not generate an identity but a number operator in Hilbert space, which counts the number of hadrons produced in the final state. Quark fragmentation correlators with an additional gluon $\Delta^{\mu}_{A\ ij}$ can be defined, as in (2.5.11). A fragmentation correlator exists also for gluons, see [72]. In distribution correlators a summation over the color indexes of quarks and gluons is assumed. For fragmentation correlators we average over color [57].

Correlators "mediates" between the partons when bound inside hadrons and partons as free on-shell particles outside a bound state. To illustrate how these correlator enter a cross section, we apply the diagrammatic approach outlined in Sec. 2.4 to the case of SIDIS. The hadronic tensor in SIDIS (2.2.6) at complete

order[9] $(M/Q)^0$ reads:

$$2MW^{\mu\nu} = 2z \sum_a e_a^2 \int d^2\boldsymbol{p}_T d^2\boldsymbol{k}_T \delta^{(2)}(\boldsymbol{p}_T + \boldsymbol{q}_T - \boldsymbol{k}_T) \mathrm{Tr}^{\mathrm{D}} \left\{ \Phi^a(x, \boldsymbol{p}_T) \gamma^\mu \Delta^a(z, \boldsymbol{k}_T) \gamma^\nu \right\}, \tag{2.5.14}$$

where the sum runs over the quark and antiquark flavors a, and e_a denotes the fractional charge of the struck quark or antiquark. $\boldsymbol{p}_T$ is the transverse momentum (in light-cone components) of the (anti)quark extracted from the target and $\boldsymbol{k}_T$ is the transverse momentum of the (anti)quark fragmenting into the detected hadron. The complete expression up to M/Q order is available in [15, 73, 74] and involves $\Phi_{A\ ij}$ and $\Delta_{A\ ij}$ correlators. Notably, the two correlators in (2.5.14) involve only the light-cone plus and transverse components of partonic momenta (due to the four dimensional delta distribution to conserve momentum in (2.2.2)). Projections and parametrizations of correlators will be discussed in Sec. 2.6.

2.6 Transverse momentum distributions

In the following we use two different reference frames to describe the structure of the proton and introduce distributions. The first one is specified by a generic light-like basis (see Sec. A). The second one relies on a "Sudakov" basis, which becomes a light-like basis in the high-energy limit, namely where the mass of the hadron is negligible with respect to the hard scale of the process. In the quark case, correlators are Lorentz scalars, so they are not affected by basis transformations. For gluons, instead, different frame choices lead to different prefactors in the parametrizations of the correlators.

Frame A

In the first frame we choose a light-like basis $\{n_+, n_-\}$ (A) and define:

$$P = P^+ n_+ + \frac{M^2}{2P^+} n_- \tag{2.6.1}$$

$$p = xP^+ n_+ + p_T + p^- n_- \tag{2.6.2}$$

$$S = S_L \frac{P^+}{M} n_+ + S_T - S_L \frac{M}{2P^+} n_- \ , \tag{2.6.3}$$

[9] As already mentioned, Φ_{ij} and Δ_{ij} contain all the twist-2 terms and some terms beyond twist-2.

where P is the proton momentum, p is the parton momentum, S is a spin vector for the proton (which will be introduced in Sec. 2.6.2). The previous equations satisfy:

$$n_+ \cdot n_- = 1, \quad n_+^2 = n_-^2 = 0 \tag{2.6.4}$$

$$P^2 = M^2, \quad P \cdot S = 0 \ . \tag{2.6.5}$$

In essence, in this frame the basis is light-like (see conventions in App. A) and the proton momentum is time-like. In the high energy limit, the component of P along n_- becomes irrelevant and the momentum goes on the light-cone ($P^\mu = P^+ n_+^\mu$). We choose this frame to describe proton-proton collisions at the LHC, producing a pseudoscalar quarkonium bound state (see Chap. 8). Examples of parametrizations and calculations performed in this frame are available, among the others, in [57, 71, 72, 75].

Frame B

An alternative is to choose two vectors provided by the process and build a light-cone basis out of them. As a first vector, we consider the momentum P of the proton. Then the second vector n depends on the type of experiment. We can then define:

$$n_+ = P - \frac{M^2}{2} n, \quad n_- = n \ . \tag{2.6.6}$$

Accordingly, we have:

$$p = xP + p_T + \underbrace{(p \cdot P - xM^2)}_{\sigma} n \tag{2.6.7}$$

$$S = \frac{S_L}{M} P + S_T - M S_L n \ , \tag{2.6.8}$$

which again satisfy $P^2 = M^2$ and $P \cdot S = 0$. The n vector can, for convenience, involve the momentum of the exchanged photon in SIDIS and e^+e^- annihilation or the momentum of the second hadron in DY [57]. In the high-energy limit $n_+ \equiv P$, so the proton momentum fixes the light-cone plus direction (note the different P^+ factor with respect to (2.6.1) in the high-energy limit).

If n has dimension mass, then $P \cdot n \equiv P^+$ has dimension mass^2. If, instead, n has dimension mass^{-1}, then $P \cdot n \equiv P^+$ can be set to be 1. For example, considering q the momentum of a photon, $n \doteq q'/(P \cdot q')$, where $q' \doteq q + x_B P$, implies $P \cdot n = 1$. It is also possible [57] to introduce a covariant Cartesian time-like vector $\hat{t}$ (mimicking a time direction) and space-like vector $\hat{z}$ (mimicking a z direction) reproducing the Sudakov basis (2.6.6) in the high-energy limit, up to negligible corrections.

In the lab frame or in the center of mass frame, the energy scales for the momentum components in (2.6.7) are $P \sim \mathcal{O}(Q)$, $p_T \sim \mathcal{O}(M)$, $\sigma n \sim \mathcal{O}(1/Q)$ [71],

where Q is the hard scale and M is the proton mass. xP describes the hadron momentum fraction that the parton carries in the $n_+ = P$ direction, namely collinear to the proton. σn is less relevant, being suppressed by a Q^2 factor with respect to xP. Moreover, it is integrated over to automatically ensure time ordering of the operators. p_T is the momentum component *transverse* with respect to P and n.

In the following, when presenting parametrizations of light front correlators, we always specify the choice of the frame.

2.6.1 Projections

There are no processes probing the full momentum structure of the correlators. Depending on what is measured in the final state, there is sensitivity only to certain projections of the correlators. Considering $\Phi_{ij}(p)$, where p is the full four momentum of the quark, dropping the P-dependence for convenience and assuming a light-cone decomposition for p (frame A), we have:

$$\Phi_{ij}(p) \xrightarrow{\int dp^-} \Phi_{ij}(x, p_T) \xrightarrow{\int d^2p_T} \Phi_{ij}(x) \xrightarrow{\int dp^+} \Phi_{ij} \ . \tag{2.6.9}$$

$\Phi_{ij}(p)$ is referred to as the unintegrated correlator. Correlators sensitive to $p^+ = xP^+$ and p_T enter cross sections where a particle is detected in the final state, together with its momentum transverse with respect to a defined direction (e.g. the $\hat{z}$ axis). For example[10] (see the case of SIDIS (2.5.14)):

$$\begin{aligned}\Phi_{ij}(x, \boldsymbol{p}_T) &\doteq \int dp^- \Phi_{ij}(p; P)_{|_{p^+ = xP^+}} \\ &= \int \frac{d\xi^- d^2\boldsymbol{\xi}_T}{(2\pi)^3} e^{ip\cdot\xi} \langle P|\bar{\psi}_j(0)\psi_i(\xi)|P\rangle_{|_{\xi^+=0}}.\end{aligned} \tag{2.6.10}$$

The minus component is integrated over due to the four dimensional delta distribution imposing momentum conservation in a scattering process. This is the Transverse Momentum Dependent (TMD) correlator, evaluated on the light-front $\xi^+ = 0$ (condition that renders time ordering trivial). Correlators sensitive to $p^+ = xP^+$ only play a role in more inclusive processes, where no hadrons in the final state are present, or when one or more hadrons are detected with no sensitivity to their transverse momenta:

$$\begin{aligned}\Phi_{ij}(x) &\doteq \int d^2\boldsymbol{p}_T \Phi_{ij}(x, \boldsymbol{p}_T) \\ &= \int \frac{d\xi^-}{2\pi} e^{ip\cdot\xi} \langle P|\bar{\psi}_j(0)\psi_i(\xi)|P\rangle_{|_{\xi^+=0, \xi_T=0}}.\end{aligned} \tag{2.6.11}$$

[10] Prefactors in definition of integrations, as in (2.6.10), depend on the definition of the trace with other Dirac structures. Here we choose the one given in (C.0.1), following the convention of [57].

The latter is the collinear correlator, evaluated on the light-cone ($\xi^2 = 0$). Integrating it over p^+ we obtain [57] a local matrix element:

$$\Phi_{ij} \doteq \int dp^+ \Phi_{ij}(x) = \langle P|\bar{\psi}_j(0)\psi_i(\xi)|P\rangle_{|_{\xi=0}} \ , \tag{2.6.12}$$

which can be parametrized in terms of "charges" describing the quark content of the proton [57] and has a relation with form factors and Generalized Parton Distributions [76, 77].

In SIDIS, for a fragmentation correlator the light-cone basis vectors are interchanged. From the physics point of view, this corresponds to a target incoming from the light-cone plus direction and a produced hadron outgoing along the light-cone minus direction. In defining a TMD fragmentation correlator this translates into:

$$\begin{aligned}\Delta_{ij}(z, \boldsymbol{k}_T) \doteq & \frac{1}{2z} \int dk^+ \Delta_{ij}(k; K)_{|_{k^- = \frac{1}{z} K_h^-}} \\ = & \sum_{\mathcal{X}} \int \frac{d\xi^+ d^2\boldsymbol{\xi}_T}{(2\pi)^3} e^{ik\cdot\xi} \langle 0|\psi_i(\xi)|K_h; \mathcal{X}\rangle \langle K_h; \mathcal{X}|\bar{\psi}_j(0)|0\rangle_{|_{\xi^- = 0}}. \end{aligned} \tag{2.6.13}$$

Its integrated version is given by:

$$\begin{aligned}\Delta_{ij}(z) \doteq & \frac{z}{2} \int d^2\boldsymbol{k}_T dk^+ \Delta_{ij}(k; K)_{|_{\xi^- = 0}} \\ = & z^2 \int d^2\boldsymbol{k}_T \Delta_{ij}(z, \boldsymbol{k}_T) = \int d^2\boldsymbol{K}_T \Delta_{ij}(z, -z\boldsymbol{k}_T) \ , \end{aligned} \tag{2.6.14}$$

where $\boldsymbol{K}_T = -z\boldsymbol{k}_T$ is the transverse momentum of the hadron acquired during the fragmentation process. This variable is more convenient from a phenomenological point of view with respect to the transverse momentum of the parton $\boldsymbol{k}_T$ (see Chap. 5). The same scheme of integrations holds for a gluon-gluon correlator [57, 72, 78].

2.6.2 Inclusion of hadron spin

In (2.5.7) we did not consider the fact that the target hadron can have a spin. Considering a proton, we could insert a dependence on two Pauli indexes α, β describing its spin state being up or down. Accordingly, the definition in (2.5.7) modifies as:

$$\Phi_{ij,\alpha\beta}(p; P) = \frac{1}{(2\pi)^4} \int d^4\xi e^{ip\cdot\xi} \langle P, \beta|\bar{\psi}_j(0)\psi_i(\xi)|P, \alpha\rangle \ . \tag{2.6.15}$$

This correlator, though, is of no practical use because experimentally we can control only the polarization degree of an ensemble of protons (inside a target or a beam)

and not the spin state of a single one. Quantum mechanics helps us, defining a density matrix for the proton spin as:

$$\rho \doteq \sum_{\alpha} p_\alpha |\alpha\rangle\langle\alpha| \equiv \frac{1}{2}(\mathbb{I}_2 + \boldsymbol{\sigma}\cdot\boldsymbol{S}) \ , \tag{2.6.16}$$

where $|\alpha\rangle$ is a spin state and p_α is the associated probability. $\boldsymbol{\sigma}$ is a vector of the three Pauli matrices and $\boldsymbol{S}$ is a three dimensional spin vector (Bloch vector), such that $0 \leq |\boldsymbol{S}|^2 \leq 1$. If $|\boldsymbol{S}|^2 = 1$, the proton is represented by a pure spin state. Moreover, in the rest frame of the proton we can introduce a covariant form S^μ [57] of $\boldsymbol{S}$, which will be considered in the following.

Following the definition of the expectation value of an operator on the mixed state represented by ρ, we define the spin-averaged quark-quark correlator as:

$$\Phi_{ij}(p;P,S) = \mathrm{Tr}\Big\{\Phi_{ij,\alpha\beta}(p;P)\rho_{\alpha\beta}(\boldsymbol{S})\Big\} \ . \tag{2.6.17}$$

This definition holds also in the case of gluon and fragmentation correlators.

2.6.3 Quark distributions

Definitions in this section are presented using the decomposition in (2.6.2) for the parton momentum (frame A). The corresponding definitions given in frame B are available, e.g., in [24] and are equivalent to ours. E.g. $\not{n}_+ \equiv \gamma^-$ in frame A and $\not{P} \equiv \gamma^-$ in frame B.

$\Phi_{ij}(p;P,S)$ is a Dirac matrix collecting the quark content of the proton in a nonperturbative energy regime. A strategy to tackle it is to provide a parametrization on a basis of 16 Dirac matrices [79][11]

$$\Big\{\mathbb{I}\ ,\gamma^\mu\ ,\sigma_{\mu\nu}\ ,i\gamma_5\ ,\gamma_5\gamma^\mu\Big\} \ , \tag{2.6.18}$$

contracting the open Lorentz indexes in the basis elements with Lorentz coefficients built out of the available structures provided by the kinematics: p^μ, $n_+^\mu \sim P^\mu$, S^μ if the target is polarized ($T^{\mu\nu}$ for a spin-1 hadron), n_-. In [80] it is shown that n_- contributes only to higher twist terms and it can be neglected in a leading twist analysis. The quark-quark correlator must be hermitean and comply with the parity (P) and time reversal (T) symmetries of QCD. Hermiticity and P-invariance of the QCD Lagrangian translate into:

$$\text{Hermiticity:} \qquad \Phi^\dagger(p;P,S) = \gamma^0\Phi(p;P,S)\gamma^0 \tag{2.6.19}$$

$$\text{Parity:} \qquad \Phi(p;P,S) = \gamma^0\Phi(\bar{p};\bar{P},-\bar{S})\gamma^0 \ , \tag{2.6.20}$$

[11] Other equivalent choices are available, see e.g. [75].

where $\bar{p} = (p^0, -\vec{p})$ (or $\bar{p}^\mu \equiv \delta^{\mu\nu} p_\nu$). For the moment, we do not consider T because, as Φ_{ij} is defined in (2.6.17), it would constrain physical terms in the correlator to zero. A physically correct treatment of T must be connected to implementation of the gauge symmetry. This will be discussed in Sec. 2.8.

Relying on the basis in (2.6.18), the available kinematic and basis vectors, the constraints from hermiticity and parity, it is possible to give a parametrization of the fully unintegrated correlator $\Phi(p; P, S)$. The case of spin 1/2 hadrons is treated in [71,73,81,82], spin 1 hadrons are discussed in [75,83], antiquarks are treated in [73, 84–86]. A revised notation is presented in this thesis and in [78]. After integration over the minus component of the parton momentum, the TMD correlator for an unpolarized (spin-less or spin-averaged) hadron up to twist-2 contributions is:

$$\Phi_U(x, \boldsymbol{p}_T; P) = \frac{1}{2}\left\{ f_1(x, p_T^2)\not{n}_+ + h_1^\perp(x, p_T^2)\frac{\sigma_{\mu\nu} p_T^\mu n_+^\nu}{M} \right\}, \tag{2.6.21}$$

where M is the mass of the hadron. For a spin 1/2 hadron like the proton, we can further introduce other two correlators associated to the longitudinal and transverse polarization states (S_L and S_T, respectively). Considering the definition

$$\Delta\Phi(p; P, S) \doteq \frac{1}{2}\Big[\Phi(p; P, S) - \Phi(p; P, -S)\Big], \tag{2.6.22}$$

the parametrizations are:

$$\Delta\Phi_L(x, \boldsymbol{p}_T; P, S_L) = \frac{S_L}{2}\left\{ g_1(x, p_T^2)\gamma_5\not{n}_+ + h_{1L}^\perp(x, p_T^2)\frac{i\sigma_{\mu\nu}\gamma_5 n_+^\mu p_T^\nu}{M} \right\} \tag{2.6.23}$$

$$\begin{aligned}\Delta\Phi_T(x, \boldsymbol{p}_T; P, S_T) =& \frac{1}{2}\left\{ f_{1T}^\perp(x, p_T^2)\frac{\epsilon_T^{S_T p_T}}{M}\not{n}_+ + g_{1T}(x, p_T^2)\frac{\boldsymbol{p}_T \cdot \boldsymbol{S}_T}{M}\gamma_5\not{n}_+ \right. \\ &\left. + h_1(x, p_T^2)\; i\sigma_{\mu\nu}\gamma_5 n_+^\mu S_T^\nu - h_{1T}^\perp(x, p_T^2)\frac{i\sigma_{\mu\nu}\gamma_5 n_+^\mu p_T^{\nu\rho} S_{T\rho}}{M^2} \right\}.\end{aligned} \tag{2.6.24}$$

The eight[12] functions presented in (2.6.21), (2.6.23), (2.6.24) are the transverse-momentum-dependent parton distribution functions (TMD PDFs) for quarks. They depend on the collinear fraction of momentum x and on the modulus of the transverse momentum p_T^2. A summary of names, properties and level of knowledge of the twist-2 TMD PDFs will be discussed in Sec. 4.3. Here we summarize them in Tab. 2.1.

In (2.6.21), (2.6.23), (2.6.24) partonic transverse momentum enters through

[12] A complementary operator analysis shows that the independent TMD PDFs are 10, because there are three $h_{1T}^\perp$ functions [24].

nucleon pol. \ quark pol.	U	L	T
U	f_1		$h_1^\perp$
L		g_{1L}	$h_{1L}^\perp$
T	$f_{1T}^\perp$	g_{1T}	h_1, $h_{1T}^\perp$

Table 2.1. Twist-2 quark transverse-momentum-dependent distribution functions. U,L,T correspond to unpolarized, longitudinally polarized and transversely polarized nucleons (rows) and quarks (columns). Blue and black functions are T-even. Functions in black survive transverse momentum integration (rank-0 in p_T). Functions in red are T-odd (see Sec. 2.8).

symmetric traceless tensors (STTs) in p_T (see App. B). Namely, only combinations of

$$p_T^\mu,\ p_T^{\mu\nu},\ p_T^{\mu\nu\rho},\cdots \tag{2.6.25}$$

tensors of definite rank (up to rank-2 for quarks), are used in defining the coefficients of the correlators. Expansions of the correlators in structures with definite rank are essential to study the generalized universality properties of the distributions [24, 87]. Moreover, TMDs in a STT form can be easily translated to position space and thus QCD-evolved, their rank in p_T being equal to the order of the Bessel function involved in the Fourier transformation. This is essential to have a unique correspondence between the functions parametrizing the correlators in p_T and b_T space (see App. D).

Upon integration over transverse momentum, only the rank-0 terms in p_T survive (see Tab. 2.1). Accordingly, the parametrization of the collinear correlator is:

$$\Phi(x;P,S) = \frac{1}{2}\left\{ f_1(x)\ \not{n}_+ + g_1(x)\ S_L\gamma_5\not{n}_+ + h_1(x)\ i\sigma_{\mu\nu}\gamma_5 n_+^\mu S_T^\nu \right\}, \tag{2.6.26}$$

where we have defined $h_1(x)$ the integrated version of $h_1(x,p_T^2)$. These are the three collinear parton distribution functions (PDFs) for unpolarized quarks in unpolarized hadrons ($f_1(x)$, the unpolarized PDF), longitudinally polarized quarks in longitudinally polarized hadrons ($g_1(x)$, the helicity PDF) and transversely polarized quarks in transversely polarized hadrons ($h_1(x)$, transversity PDF).

Following the same philosophy, it is possible to introduce parametrizations for TMD (2.6.13) and collinear (2.6.14) quark fragmentation correlators, complying with hermiticity and discrete symmetries of QCD. Again, for the moment we impose constraints from hermiticity and parity. Time reversal symmetries manifests itself

hadron pol. \ quark pol.	U	L	T
U	D_1		$H_1^\perp$
L		G_{1L}	$H_{1L}^\perp$
T	$D_{1T}^\perp$	G_{1T}	H_1, $H_{1T}^\perp$

Table 2.2. Twist-2 transverse-momentum-dependent fragmentation functions. U,L,T correspond to unpolarized, longitudinally polarized and transversely polarized nucleons (rows) and quarks (columns). Blue and black functions are T-even. Functions in black survive transverse momentum integration (rank-0 in k_T). Functions in red are T-odd. Note that the T-oddness has a different physical origin between distribution and fragmentation correlators (see Sec. 2.8).

in a different way with respect to the distribution correlator (see Sec. 2.8). In this thesis we will deal only with TMD unpolarized fragmentation functions, so we present a parametrization of the TMD correlator in the unpolarized case only [57, 75]:

$$\Delta_U(z, -z\boldsymbol{k}_T; P_h) = \frac{1}{2}\left\{ D_1(z, |-z\boldsymbol{k}_T|^2)\, \not{n}_- + H_1^\perp(z, |-z\boldsymbol{k}_T|^2)\, \sigma_{\mu\nu} \frac{k_T^\mu n_-^\nu}{M_h} \right\}, \quad (2.6.27)$$

where we used the hadronic transverse momentum $\boldsymbol{K}_T = -z\boldsymbol{k}_T$. $D_1(z, |-z\boldsymbol{k}_T|^2)$ is the fragmentation of an unpolarized quark into an unpolarized hadron, whereas $H_1^\perp(z, |-z\boldsymbol{k}_T|^2)$ is the fragmentation of a transversely polarized quark into an unpolarized hadron (the Collins function). For a complete list of the eight TMD FFs at twist-2 see Tab. 2.2. For the polarized correlators in spin 1/2 and 1 and beyond the leading twist see, e.g., [57, 75].

2.6.4 Gluon distributions

As for the quarks in the previous section, definitions here are presented using the decomposition in (2.6.2) for the parton momentum (frame A). The corresponding definitions given in frame B (where $\dim[n] = -1$ and $P \cdot n \equiv P^+ = 1$) are available in [78]. Parametrizations in such a frame can be obtained setting $P^+ = 1$ in the following equations.

It is possible to introduce parametrizations for unintegrated, TMD and collinear gluon distribution and fragmentation correlators, following the same path outlined in Sec. 2.6.3. Gluon correlators are Lorentz matrices and we need to replace (2.6.18) with a suitable set of Lorentz structures provided by the kinematics of the process [57, 78]. As for the case of quarks, the correlator must comply with hermticity

and discrete symmetries of QCD and, for the moment, we only consider constraints from hermiticity and parity:

$$\text{Hermiticity:} \qquad \Gamma^{\rho\sigma;\mu\nu *}(p,P,S) = \Gamma^{\mu\nu;\rho\sigma}(p,P,S) \tag{2.6.28}$$

$$\text{Parity:} \qquad \Gamma^{\mu\nu;\rho\sigma}(p,P,S) = \Gamma_{\mu\nu;\rho\sigma}(\bar{p},\bar{P},-\bar{S}) \ , \tag{2.6.29}$$

where, as in (2.6.19) and (2.6.20), $\bar{p}^\mu \equiv \delta^{\mu\nu} p_\nu$. The interplay between discrete and gauge symmetries will be addressed in Sec. 2.8. Since we have not introduced Wilson lines yet, the dependence on the n_- vector is not considered when building parametrizations. Gluon-gluon correlators are antisymmetric in both pairs of indices μ, ν and ρ, σ.

Parametrizations for TMD and collinear gluon correlators, for scalar and vector polarized targets have been investigated in [72, 76]. Ref. [78] introduces the tensor polarized case. As for the quarks, this thesis and [78] present a revised notation. We define the leading twist TMD correlator (see also (2.5.10)) as:

$$\begin{aligned} \Gamma^{+i;+j}(x,\boldsymbol{p}_T;P,S) &\doteq \int dp^- \ n_{-\mu} n_{-\rho} \ \Gamma^{\mu i;\rho j}(p;P,S) \\ &= \int \frac{d\xi^- d^2\xi_T}{(2\pi)^3} \ e^{ip\xi} \ \langle PS|F^{+i}(0)F^{+j}(\xi)|PS\rangle_{|_{\xi^+=0}} \ . \end{aligned} \tag{2.6.30}$$

Comparing with (2.5.10), μ and ρ have been contracted with n_- to select the leading twist contributions. ν and σ are then indicated as transverse indexes i, j. From now on, the two + indexes will be omitted. The parametrization for the twist-2 TMD distribution correlator for gluons in the case of a scalar target is [72, 78]:

$$\Gamma^{ij}(x,\boldsymbol{p}_T;P) = \frac{xP^+}{2}\left[-f_1(x,p_T^2)\ g_T^{ij} + h_1^\perp(x,p_T^2)\ \frac{p_T^{ij}}{M^2}\right], \tag{2.6.31}$$

The prefactors are fixed in order to satisfy the momentum sum rule for gluons [78]. We employed the STT form for the p_T structures (see App. B).

For a vector polarized target (spin 1/2 hadron), the polarized correlators are [72, 78]:

$$\Delta\Gamma_L^{ij}(x,\boldsymbol{p}_T;P,S_L) = \frac{xP^+}{2} S_L \left[g_1(x,p_T^2)\ i\epsilon_T^{ij} + h_{1L}^\perp(x,p_T^2)\ \frac{\epsilon_T^{\{i}{}_\alpha p_T^{j\}\alpha}}{2M^2}\right], \tag{2.6.32}$$

$$\Delta\Gamma_T^{ij}(x,\boldsymbol{p}_T;P,S_T) = \frac{xP^+}{2}\left[-f_{1T}^\perp(x,p_T^2)\ \frac{g_T^{ij}\epsilon_T^{S_T p_T}}{M} + g_{1T}(x,p_T^2)\ \frac{i\epsilon_T^{ij}\boldsymbol{p}_T\cdot\boldsymbol{S}_T}{M} +\right.$$

nucleon pol. \ gluon pol.	U	circ.	lin.
U	f_1^g		$h_1^{\perp g}$
L		g_1^g	$h_{1L}^{\perp g}$
T	$f_{1T}^{\perp g}$	g_{1T}^g	h_1^g, $h_{1T}^{\perp g}$

Table 2.3. Twist-2 gluon transverse-momentum-dependent distribution functions. U,L,T correspond to unpolarized, longitudinally polarized and transversely polarized nucleons. U, circ., lin. correspond to unpolarized, circularly polarized and linearly polarized gluons. Functions in blue are T-even. Functions in black are T-even and survive integration over $\boldsymbol{p}_T$. Functions in red are T-odd (see Sec. 2.8).

$$
\begin{aligned}
&-h_1(x,p_T^2)\,\frac{\epsilon_T^{p_T\{i}S_T^{j\}}+\epsilon_T^{S_T\{i}p_T^{j\}}}{4M}\\
&-h_{1T}^{\perp}(x,p_T^2)\,\frac{\epsilon_T^{\{i}{}_{\alpha}p_T^{j\}\alpha S_T}}{2M^3}\Bigg].
\end{aligned}
\tag{2.6.33}
$$

The relation between the TMDs and the coefficient functions in the parametrization of the unintegrated correlator can be found in [78]. The functions $h_{1L}^{\perp}$, $f_{1T}^{\perp}$, h_1, and $h_{1T}^{\perp}$ are T-odd (see Sec. 2.8). A more traditional form of the parametrization [76, 88] can be recovered expanding the STT forms for the p_T tensors (see App. B), considering the following relation among three h-type functions:

$$
h_1(x,p_T^2) \doteq h_{1T}(x,p_T^2)+\frac{\boldsymbol{p}_T^2}{2M^2}\,h_{1T}^{\perp}(x,p_T^2). \tag{2.6.34}
$$

For a comparison between the current and previous notations see [78]. Looking at (2.6.33), we see that h_1 is a rank-1 function and $h_{1T}^{\perp}$ is a rank-3 function. Considering the more traditional forms in [76, 88], h_{1T} contains both rank-1 and rank-3 pieces, so it is not a function with definite rank. For this reason, its usage within a rank expansion or cross sections with TMDs in b_T-space would be problematic[13].

Eventually note that, despite the similarity in name, the function h_1 for gluons is different from the quark transversity function h_1 (e.g., it does not survive integration over transverse momentum). The properties of the gluon TMD PDFs are summarized in Tab. 2.3. It is possible to introduce gluon TMD fragmentation functions too. See, e.g, [57, 72]. In App. D we give the parametrization of the Fourier-transformed gluon distribution correlator, $\Gamma^{ij}(x,\boldsymbol{b}_T)$, and the relations between the TMD PDFs in momentum ($\boldsymbol{p}_T$) space and position ($\boldsymbol{b}_T$) space.

[13] E.g., eqs. (2.17, 2.18, 2.20) in [89] are inconsistent from a rank point of view.

2.7 Gauge links

In order to deal with gauge invariant correlators, we need to introduce the concept of *gauge link*. It arises from the geometrical notion of parallel transport, which defines a way of comparing elements from different linear spaces via the connection.

The transportation of a vector is defined "parallel" if the scalar products are conserved while the vector is transported along a path in spacetime. This provides a specific way of moving fields along a path, defining an isomorphism between the spaces where the fields live. The parallel transport equation for a fermion field ψ along the curve c in spacetime parametrized by $t \in \mathbb{R}$ is:

$$D_{\dot{c}}\ \psi(x(t)) = 0\ , \quad t \in I \subset \mathbb{R}\ . \tag{2.7.1}$$

The solution of (2.7.1) is given in terms of a path-ordered exponential factor involving the gauge connection:

$$\begin{aligned}\psi'_\beta(x(t)) &= \mathbb{P}\exp\left\{ -ig\int_0^t ds \frac{dx^\mu}{ds} A^a_\mu(x(s)) T^a_{\beta\alpha}\right\}\ \psi_\alpha(x(0)) \\ &\doteq U_{\beta\alpha}(x(t), x(0))\ \psi_\alpha(x(0))\ .\end{aligned} \tag{2.7.2}$$

$U_{\beta\alpha}(x(t), x(0))$ is a *gauge link*, or *Wilson line*. In the case of QCD, it is a matrix in color space and T^a are the Gell-Mann matrices. A gauge link $U(x_2, x_1)$ connecting x_1 to x_2, under local gauge transformations $\mathcal{U}(x)$ behaves as [4, 5]:

$$U'(x_2, x_1; A') = \mathcal{U}(x_2)\ U(x_2, x_1; A)\ \mathcal{U}^\dagger(x_1)\ . \tag{2.7.3}$$

As a result, the operator

$$\bar{\psi}_j(0)\ U(0, \xi)\ \psi_i(\xi) \tag{2.7.4}$$

is invariant under $SU(3)$ gauge transformations. This shows the interplay between the geometrical interpretation of the concepts underlying particle physics and the gauge invariance of the theory. A similar argument holds for matrix elements involved in gluon-gluon correlators (2.5.10), with the difference that we need two links to ensure gauge invariance:

$$F^{\mu\nu}(0)\ U(0, \xi)\ F^{\rho\sigma}(\xi)\ U'(\xi, 0)\ . \tag{2.7.5}$$

This is because gluons live in the octet representation of $3 \otimes 3^*$ and, accordingly, we need two color matrices to connect each of the factor representation 3 and 3^* [24]. One of the two links might be omitted for sake of brevity from (2.7.5) when both are chosen along the same path in spacetime. Introducing a Sudakov decomposition for the gauge field A^μ, we see that the component $A^+ \sim P^+$ is dominant, $A_T \sim M$ is sub-leading, whereas $A^- \sim 1/P^+$ is suppressed. Given two light-cone directions

n_+, n_- (see App. A), we denote $U^{[n_-]}$ a link running along the light-cone minus component in spacetime and for which the integrand A is projected along the n_- direction. A notation with similar meaning is introduced for $U^{[T]}$. The integral over the minus component in spacetime can be further decomposed in two consecutive integrations, one from a^- to $\pm\infty$ and another from $\pm\infty$ to b^-. In this way, it is possible to introduce the so-called *staple-like* links:

$$U^{[\pm]}(b,a) \doteq U^{[n_-]}(\pm\infty, a^-)\; U^{[T]}(b_T, a_T)\; U^{[n_-]}(b^-, \pm\infty)\;. \tag{2.7.6}$$

The path chosen in the gauge link depends on the process considered. In particular, $U^{[-]}$ contributes to DY, whereas $U^{[+]}$ enters the SIDIS cross section. In all the correlators introduced in Chap. 2, gauge links need to be introduced to bridge the non-locality in spacetime and guarantee their gauge invariance. The links have important physical consequences on the study of the proton structure and leave footprints in scattering experiments (see Sec. 2.8 and 4.2).

2.8 Discrete symmetries

We turn now our attention to discrete symmetries, in particular time reversal (T) symmetry, in order to understand their impact on the correlators. Despite being interesting a priori, this is also motivated by some observables that display an odd behavior under time reversal transformations. Single spin azimuthal asymmetries (SSAs), linked to T-odd TMDs, are an example discussed in Sec. 4.2. In the following we prove that T-odd effects , in hadronic physics, can be a consequence of the interplay between the gauge symmetry and the behavior under time reversal transformation. A time reversal transformation interchanges the staple links $U^{[+]}$ and $U^{[-]}$, whereas parity and hermiticity do not[14]. These properties are based on $U^{\dagger}_{[0,\xi]} = U_{[\xi,0]}$, $U^{P}_{[0,\xi]} = U_{[\bar{0},\bar{\xi}]}$ and $U^{T}_{[0,\xi]} = U_{[-\bar{0},-\bar{\xi}]}$. Accordingly, taking into account also gauge links and time reversal properties, the conditions imposed on the quark distribution correlator, (cf. (2.6.19), (2.6.20)), are:

$$\text{Hermiticity:} \qquad \Phi^{[\pm]\dagger}(p;P,S) = \gamma^0\Phi^{[\pm]}(p;P,S)\gamma^0 \tag{2.8.1}$$

$$\text{Parity:} \qquad \Phi^{[\pm]}(p;P,S) = \gamma^0\Phi^{[\pm]}(\bar{p};\bar{P},-\bar{S})\gamma^0 \tag{2.8.2}$$

$$\text{Time reversal:} \qquad \Phi^{[\pm]\dagger}(p;P,S) = i\gamma^1\gamma^3\Phi^{[\mp]}(\bar{p};\bar{P},\bar{S})i\gamma^1\gamma^3\;, \tag{2.8.3}$$

where the subscript $[\pm]$ refers to the staple gauge links (2.7.6) and the bar refers to quantities transformed according to parity (2.6.20).

We summarize also the behavior of the twist-2 gluon-gluon correlator under hermiticity, parity and time reversal, considering their interplay with the gauge

[14] This is essentially due to the fact that the staple links $[\pm]$ run through light-cone infinity.

link structure:

$$\text{Hermiticity:} \quad \Gamma^{[U,U']\,\rho\sigma;\mu\nu *}(k,P,S,n) = \Gamma^{[U,U']\,\mu\nu;\rho\sigma}(k,P,S,n), \quad (2.8.4)$$

$$\text{Parity:} \quad \Gamma^{[U,U']\,\mu\nu;\rho\sigma}(k,P,S,n) = \Gamma^{[U,U']}_{\mu\nu;\rho\sigma}(\bar{k},\bar{P},-\bar{S},\bar{n}), \quad (2.8.5)$$

$$\text{Time reversal:} \quad \Gamma^{[U,U']\,\mu\nu;\rho\sigma *}(k,P,S,n) = \Gamma^{[U^T,U'^T]}_{\mu\nu;\rho\sigma}(\bar{k},\bar{P},\bar{S},\bar{n}). \quad (2.8.6)$$

By omitting the gauge links from the gluon-gluon correlator, the dependence on n is no longer present.

As shown by (2.8.2), (2.8.5) (and their counterparts for fragmentations), parity does not mix with the gauge link structure and does not exchange final and initial states. For this reason, it always poses *constraints* on correlators, preventing the possibility of defining P-odd structures. For time reversal, instead, the interplay with the gauge link structure generates T-odd effects. A detailed overview of some cases for distribution and fragmentation functions, both TMD and collinear, is given in App. C. The role of charge-conjugation for quarks and gluons is discussed in [78, 86] respectively.

2.9 Outlook and future developments

In Chap. 2 we discussed the structure and the symmetry properties of quark-quark and gluon-gluon correlators with staple-like gauge links. Parametrizations in terms of transverse momentum dependent distributions which respect parity invariance and the hermiticity properties have been introduced in Sec. 2.6.3 and Sec. 2.6.4. In Sec. 2.8 the interplay between the gauge symmetry and the time reversal symmetry is presented, which accounts for T-odd distributions.

The same arguments based on gauge and discrete symmetries can be applied to correlators of a single Wilson loop [78, 90]:

$$\Gamma_0^{[U,U']}(\boldsymbol{p}_T;P,S,n) \doteq \int \frac{d^2\xi_T}{(2\pi)^2}\, e^{ip\cdot\xi}\, \langle PS|\, U(0,\xi)\, U'(\xi,0)\, |PS\rangle_{|\xi\cdot n=0} \ . \quad (2.9.1)$$

Parametrizations of the correlator in (2.9.1) for the unpolarized, vector polarized and tensor polarized case have been presented in [78]. For a $[+,-]$ link configuration, they provide insight into the behavior of gluons at $x = 0$. Investigations on their physical content and on a possible role in the description of diffractive processes is still required.

CHAPTER 3

QCD EVOLUTION

In this chapter we investigate how perturbative QCD (pQCD) enters the study of hadron structure and its footprints in scattering experiments. Through pQCD it is possible to give a complementary definition of TMDs, which consolidates the picture introduced in the previous chapters. We also see how to enrich the structure of the QCD corrections outlined in Fig. 2.6.

The way hadron structure is affected by perturbative corrections and *evolves* changing the relevant scales in the process is referred to as QCD evolution. The equations which govern QCD evolution are a byproduct of factorization theorems. Understanding how to separate hard and soft scales in a cross section, automatically teaches how to evolve and match the different contributions. Factorization is a vast topic by itself and here we only want to provide an overview of some results relevant for phenomenology. For an overview of factorization, evolution and phenomenology in the collinear limit we refer to [91, 92] and references therein. Factorization in terms of TMD distributions is a lively topic. As a comprehensive treatment we indicate [20], despite not being the only one available. Effective theories are widely employed to address factorization and evolution issues (see also Chap. 8). Introductory material is available in [93], via the MIT online lecture series and notes and the TASI lecture notes 2013, 2014.

3.1 Factorization

A high-energy collision involving hadrons is a multi-scale problem. E.g., when two protons collide producing a $W^{\pm}$ boson at the LHC, the initial states of the reaction need to be described in terms of the proton structure, which is shaped by QCD at

low energy (~ 1 GeV), whereas the interaction among the elementary constituents takes place at higher energy ($\sim m_W \sim 80$ GeV). Intuitively, one could expect that the soft (i.e. referred to a low energy scale) process of extracting partons out of the two protons and the hard (i.e. referred to a high energy scale) partonic interaction are decoupled, being related to different energy and time scales. As a consequence, a generic differential cross section for such a process could look like:

$$d^{(n)}\sigma \sim \sum_{a,b} H \; f_a(x_a;\mu) \; f_b(x_b;\mu) \; + \mathcal{O}(\Lambda_{\rm QCD}/Q) \; , \tag{3.1.1}$$

where the functions f are generic parton distribution functions (describing the probability of extracting a parton from the proton), H represents the hard interaction, the sum runs over the active partons a, b, $x_{a,b}$ are the partonic momentum fractions, $Q \sim m_W$ is the hard scale of the process, $\Lambda_{\rm QCD}$ is a low-energy scale representing the Landau pole of QCD and μ is the energy scale at which the factorization between hard and soft contributions takes place. The last factor accounts for corrections to the factorized expression, relevant for low values of the hard scale. In general, the structure of (3.1.1) depends on the number of separate energy scales present in the reaction, on the process and on the observable.

Let us assume that the produced W boson has a transverse momentum q_T. When q_T is well separated from the hard scale Q, namely

$$q_T \ll Q \; , \tag{3.1.2}$$

the cross section can be factorized in terms of nonperturbative hadronic matrix elements sensitive to partonic transverse momenta (TMD factorization). Schematically[1]

$$d^{(n)}\sigma \sim \sum_{a,b} \mathcal{H}(Q,\mu) \; f_a(x_a, p_{Ta};\mu,\zeta_a) \otimes f_b(x_b, p_{Tb};\mu,\zeta_b) \; \delta^{(2)}(p_{Ta}+p_{Tb}-q_T) + \mathcal{O}\left(\frac{q_T}{Q}\right) , \tag{3.1.3}$$

where TMD PDFs $f_{a,b}$ have been used and the meaning of the additional ζ scales will be clarified later. The delta function accounts for momentum conservation. The last term accounts for correction to the factorized formula relevant when $q_T \sim Q$. In the limit of very large $q_T \geq Q$, the transverse momentum of the produced boson is generated almost entirely by emission of perturbative radiation calculable at a fixed order in perturbation theory. Soft partonic transverse momenta are not relevant in the hadronic matrix element any more and collinear factorization applies. In the intermediate region $q_T \lesssim Q$, a matching prescription is needed to bridge the two factorization schemes (see Sec. 3.3 and Chap. 8). Fig. 3.1 summarizes the regions

[1] The hard function H for collinear factorization differs from the hard function $\mathcal{H}$ in the context of TMD factorization.

of applicability for TMD and collinear factorization.

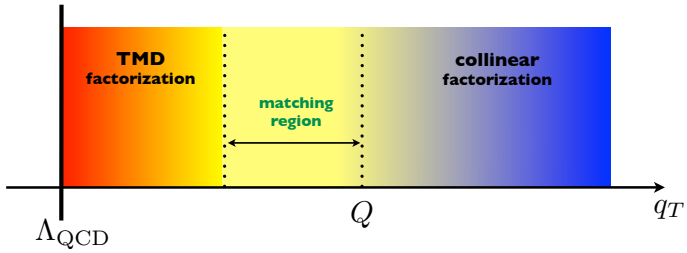

Figure 3.1. There are three kinematical regions relevant in a process where a particle with momentum q_T is produced out of a proton-proton collision. When q_T is much smaller than the mass of the particle (the relevant hard scale), TMD factorization applies and the cross section is described in terms of TMDs. When $q_T \geq M$, collinear factorization applies and the cross section is described by collinear distributions dressed by emission of perturbative radiation (responsible for the generation of q_T). In the middle, where $q_T \lesssim Q$, a matching prescription is required.

Moreover, within the TMD factorization region $q_T \ll Q$, each TMD distribution contributes both at low and high partonic transverse momentum (see Fig. 3.2). The region of high partonic transverse momentum p_T (low b_T, where b_T is the Fourier-conjugated variable to p_T) is described by means of an OPE in b_T space onto the collinear distributions (see Sec. 3.6). The involved Wilson coefficients account for the perturbative splitting of the parton with high transverse momentum. The low transverse momentum region needs to be described by models. The latter is the nonperturbative core of the TMD distribution, shaping the structure of the proton in the transverse plane. Since $p_{Ta} + p_{Tb} = q_T$, the values of Q and q_T control the relevance of the low and high transverse momentum region.

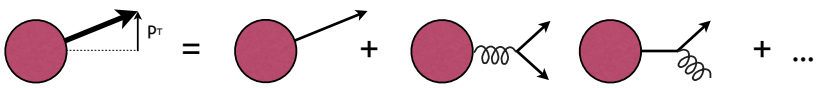

Figure 3.2. The extraction of a quark with transverse momentum p_T from the proton, up to order $\mathcal{O}(\alpha_s)$ effects. In zeroth order approximation, all the transverse momentum p_T can be accounted for by the intrinsic transverse momentum of the quark, namely the one coming from the nonperturbative wavefunction of the quark inside the proton. As p_T gets larger, also perturbative contributions play a role, entering the calculation as a power series in α_s. Here we represent only the first order contributions, namely the extraction of a collinear gluon splitting into a quark with high transverse momentum and the extraction of a collinear quark splitting into another quark with high transverse momentum. The dots represent the higher order terms. This illustrates the possibility of perturbatively expanding a TMD PDF on a set of collinear distributions with coefficients proportional to the DGLAP splitting kernels [92].

In Chap. 2 we outlined how the OPE and the diagrammatic approach introduced a decomposition of the hadronic tensor W in powers of M/Q (the twist expansion, see Fig. 2.6), where each term in the sum is factorized in a singular coefficient and a finite local matrix element representing the interaction of the probe with the hadron. Then, for each contribution of definite twist, one could check that the separation between "hard" and "soft" physics[2] holds adding α_s corrections: in this chapter we refer to this kind of factorization. Proofs of TMD factorization at leading twist and at all orders in α_s exist for DY, SIDIS and e^+e^- annihilation into two hadrons [19, 20, 94–96][3]. A proof for the case of double parton scattering for DY in collinear and TMD regime has been recently presented [97]. The SCET methodology allows to establish factorization theorems looking at the IR structure of cross sections. Several examples are available in literature for the q_T-spectra in specific processes, e.g. [96] for DY and [89] for Higgs production. In Chap. 8 and [98] the case of pseudoscalar quarkonium production is discussed.

3.1.1 Factorization and phenomenology

Factorization plays a special role for phenomenology, because it assures that the (non)perturbative effects that physicists measure and fit have indeed a solid theoretical foundation. Factorization theorems and generalized universality of the TMDs are at the basis of the predictive power of QCD. TMD factorization is expected not to hold in reactions with color flow between initial and final states, e.g. $pp \to \pi X$ (with π in a color octet representation). Nonetheless, TMD factorization is often *assumed* for these processes, neglecting any kind of factorization breaking effect. Fitting nonperturbative TMD effects to data sets for processes where factorization is not proved is possible, but on the interpretations of these results legitimate doubts are pending [99]. Quantifying phenomenologically factorization breaking effects is non trivial: in [100] it was shown that they can generate specific spin asymmetries. Moreover, fits to data where TMD factorization is valid are important in quantitatively assessing factorization breaking elsewhere.

From a practical point of view, factorization is essential also because it generates perturbative corrections for, e.g. the hard part, which are fundamental for phenomenology.

3.2 SCET

Here we outline some basic concepts about Soft-Collinear-Effective-Theory (SCET) and its role in establishing factorization theorems.

SCET is an effective theory of QCD based on a systematic expansion of the QCD Lagrangian in powers of a small parameter characterizing the momentum

[2] See Sec. 3.2 and Chap. 8 for more details.
[3] The list of references is not exhaustive.

modes of the theory. For a definition of these modes relevant to TMD factorization see, e.g., [96]. For q_T spectra, the SCET Lagrangian attempts to reproduce QCD describing the physics of low and high energy modes through *separate* Lagrangians for soft and (anti)collinear modes:

$$\mathcal{L}_{\rm QCD} \longleftrightarrow \mathcal{L}_n + \mathcal{L}_{\bar{n}} + \mathcal{L}_{\rm soft} \ . \tag{3.2.1}$$

This feature automatically ensures a separation between the momentum modes of the theory. Upon description of a certain observable, it is always *assumed* that SCET reproduces the IR structure predicted by QCD (namely the structure in $1/\epsilon$ poles) for that observable. Finite matching coefficients are then calculated in order to reproduce the result of full QCD. In particular, for a q_T-spectrum we have:

$$\text{QCD} \underset{C_H}{\longrightarrow} \text{SCET}_{q_T} \underset{C_{i/j}}{\longrightarrow} \text{SCET}_{\Lambda_{\rm QCD}} \ . \tag{3.2.2}$$

In the first step the hard scale of the process is integrated out and the cross section is factorized in terms of TMDs, defined through operators sensitive to partonic transverse momenta (SCET_{q_T} [96]). The coefficient matching the two descriptions, C_H, is spin-independent and its modulus squared is the hard part $\mathcal{H}$ of the process. The second step re-factorizes the description in terms of TMDs into a basis of collinear functions, defined via operators sensitive only to the collinear dynamics of partons ($\text{SCET}_{\Lambda_{\rm QCD}}$). The Wilson coefficients of this OPE are spin-dependent and match TMDs onto collinear distributions, describing the physics of high partonic transverse momentum.

SCET is particularly useful for phenomenology because it allows conceptually simple checks of the factorization properties for QCD observables. For a q_T spectrum, to *establish* factorization it is sufficient to check that the IR structure generated by all the diagrams calculable in the TMD factorized form (SCET_{q_T}) reproduces the one available from the calculation in full QCD. If this is the case, the matching coefficient C_H can be calculated by subtraction of the two descriptions. In this case, C_H is finite, since the IR poles are exactly the same in the two approaches. If the two descriptions produce a different structure in the IR singularities, SCET does not reproduce the physical QCD result, namely the observable cannot be described in a factorized form. We will give an example of this procedure in Chap. 8 for the q_T spectrum of a pseudoscalar quarkonium produced in a proton-proton collision.

Last but not least, the resummation techniques which are byproducts of factorization theorems allow for fast developments in the perturbative description of TMDs [101–103].

3.3 Transverse-momentum resummation

There are different approaches to TMD factorization. The quark parton model is the simplest one, where factorization is always assumed. The same happens in model calculations, like the spectator di-quark model (e.g. [21, 104]), in which perturbative corrections can also be accommodated via model-dependent Feynman rules. The most widespread approach within pQCD is transverse-momentum (TM) resummation, e.g. [105–109].

3.3.1 Fixed-order calculation

At Born level, the cross section for a hadronic process producing a particle with mass M and with high transverse momentum q_T is zero, because at least one emission of a hard particle is needed. Adding a correction of order α_s, such a cross section can be written as:

$$\frac{d\sigma}{dq_T^2} \sim \frac{1}{q_T^2}\ f_a(x_a) f_b(x_b)\ \alpha_s\ \ln\frac{M^2}{q_T^2}\ , \tag{3.3.1}$$

where the f functions are generic PDFs for the two partons involved in the process. (3.3.1) describes correctly the physics at high transverse momentum, but diverges in the limit $q_T \to 0$, where the cross section should instead vanish.

3.3.2 Resummation of large logarithms

A solution was proposed in 1978 in [110], where the double-leading-log approximation[4] (DLLA) was proposed to have a vanishing cross section in the limit $q_T \to 0$:

$$\frac{d\sigma}{dq_T^2} \sim \frac{1}{q_T^2}\ f_a(x_a) f_b(x_b)\ \alpha_s\ \ln\frac{M^2}{q_T^2} \exp\left\{ -\alpha_s \ln^2\frac{M^2}{q_T^2} \right\} \xrightarrow[q_T \to 0]{} 0\ . \tag{3.3.2}$$

In Sec. 3.6 we will show that the exponential factor in (3.3.2) is a resummation to all orders of logarithms of the type $\alpha_s L$ (where L can be a generic large logarithm).

3.3.3 Matching

The DLLA in [110] has been the starting point for extensive studies of the resummation of large logarithms depending on the transverse momentum q_T (referred to as resummation in momentum space) or its Fourier conjugated variable b_T (resummation in position space), going well beyond the leading log terms. The resummed cross section in (3.3.2) has the correct behavior at small q_T, but not at high q_T (it vanishes too soon): a prescription to *match* the two regions of small and high transverse momentum is thus required. At this purpose, we can use the function $Y(q_T, M)$ [105, 111]:

$$Y(q_T, M) \doteq \frac{d\sigma}{dq_T^2}_{|\text{f.o.}} - \frac{d\sigma}{dq_T^2}_{|\text{ASY}}\ , \tag{3.3.3}$$

[4] The adjective double refers to the logarithm, being squared.

where the first piece is the calculation at a fixed order (f.o.) n for high q_T and the subtracted piece represents the asymptotic (ASY) limit ($q_T \to 0$) of the fixed order n, which is equal to the expansion at order n of the resummed (Sudakov) cross section. The Y term should vanish in the low transverse momentum region, grow in the intermediate q_T regime and match to the fixed order calculation at high q_T. Through this matching a cross section can be decomposed in a sum of two pieces,

$$\frac{d\sigma}{dq_T^2} \sim \text{resummed part (TMDs)} + \text{finite part (Y-term)} , \tag{3.3.4}$$

which realizes the separations outlined in Fig. 3.1. This prescription has been successfully tested at high invariant mass M [107–109]. There are indications that it fails at low M, see [112]. Recently, a revised version of the method based on a nonperturbative transition function has been proposed[5] in [113]. We discuss the calculation of the matching term for a pseudoscalar quarkonium produced in pp collision in Chap. 8.

3.3.4 From transverse momentum resummation to TMDs

The common point between TM resummation and TMD factorization is that the resummed part in (3.3.4) is a convolution in momentum space of two TMD distributions. This recognition is not commonly widespread in the literature of TM resummation, which focuses mostly on the perturbative effects. Defining the resummed cross section at low q_T in terms of TMDs has specific advantages, namely the possibility of studying the full spectrum of polarization effects and the relevance of nonperturbative effects at low transverse momentum.

In the literature of TM resummation there is the tendency to include as less nonperturbative (NP) effects as possible. This is correct from a high-energy physics point of view (e.g. W/Z/Higgs production) because there NP effects are suppressed. This might lead, though, to underestimate their importance. At the LHC, e.g., Fig. 11b in [114] shows that NP contributions improve the description of experimental data. Moreover, in Chap. 7 we will show that flavor dependent NP effects have a non-trivial impact on the description of q_T spectra for $Z/W^{\pm}$ and potentially also on the determination of the W mass. To which extent NP effects are important in high-energy physics is a lively debate within the TMD phenomenology community. Neglecting them is an underestimation, but quantitative statements of their impact depend on the process, the energy scale and the accuracy of the perturbative description. At lower energies, they turn out to be fundamental in order to describe experimental data. A global description of TMD effects from low to high energy should be a mix of both. This problem is relevant also for MC gen-

[5] See also the results presented by T.C. Rogers at the workshop "Parton TMDs at large x" (ECT*, 2016).

erators used in high-energy physics simulations (e.g. Pythia, Herwig++, $\cdots$) and for automatic tools to compute TM resummation (e.g. ResBos). Their description of transverse momentum resummation is based on unpolarized collinear distributions dressed by parton shower algorithms to describe the emission of radiation. Inclusions of polarization and nonperturbative effects are still in their infancy, even though it is well recognized within the community that their inclusion in automatic generators would be important [28]. TMD factorization offers a natural framework to incorporate both perturbative and NP contributions, setting the ground to apply transverse-momentum resummation also to other structures, different from the unpolarized ones and exploring in both perturbative and NP ways all the possible effects arising from the spin-spin and spin-orbit correlations in the proton.

3.4 TMDs from the pQCD viewpoint

Following the structure of TMD factorization, the hadronic tensor $W^{\mu\nu}$ in the case of, e.g., DY, can be expressed as [20]:

$$W^{\mu\nu} = \sum_f \mathcal{H}_f^{\mu\nu}(Q,\mu) \int d^2\boldsymbol{p}_{T1} d^2\boldsymbol{p}_{T2}\; F_{f/P_1}(x_1, p_{T1}; \mu, \zeta_1)\; F_{\bar{f}/P_2}(x_2, p_{T2}; \mu, \zeta_2) \times\; \delta^{(2)}(\boldsymbol{p}_{T1} + \boldsymbol{p}_{T2} - \boldsymbol{q}_T) \;+\; Y(q_T; Q) \;+\; \mathcal{O}(\Lambda_{\rm QCD}/Q)\;. \tag{3.4.1}$$

(3.4.1) encodes also the decomposition in q_T regions outlined in the previous section. The two F functions are the TMD PDFs: their convolution over the partonic transverse momenta represents the resummed part of the cross section. The TMDs themselves contain the resummed exponential factors (see Sec. 3.6). $\mathcal{H}$ is the hard function of the process, calculated from on-shell hard scattering amplitudes. Y introduces corrections at medium and high transverse momentum, whereas the last piece accounts for corrections to the factorized formula suppressed with the hard scale (e.g. higher twist contributions).

With respect to the TMDs introduced in Chap. 2, there are two additional variables μ and ζ, whose presence is related to the perturbative structure of the function. Ultraviolet (UV) divergences are cured by means of renormalization group (RG) transformations [4]. μ is the renormalization scale through which the RG equation for F is introduced (Sec. 3.5). Infrared (IR) divergences, instead, cannot be renormalized and indicate that the cross section is sensitive to large-distance effects, that in QCD are ultimately nonperturbative. In QCD, the Kinoshita-Lee-Nauenberg theorem [5] guarantees that the S-matrix is free from soft and collinear IR divergences upon summation of all the possible degenerate initial and final states[6]. Instead, if one looks at some specific initial and/or final states with partons, collinear

[6]There is an analogue theorem for QED, the Bloch-Norton theorem [5], which guarantees that

divergences are still present and need to be reabsorbed by the parton distribution (or fragmentation) functions. This is why we refer to PDFs and FFs as nonperturbative objects, encoding the long-distance physics of hadron structure. In the case of TMD distributions, there is an additional rapidity divergence[7] (RD) associated with the light-like gauge links [20, 96]. A detailed discussion on the cancellation of RDs goes beyond the scope of this thesis. The cancellation mechanism depends on the regulator used to parametrize the divergences. In general, however, the cancellation is performed by means of a soft factor S (defined as the expectation value on the vacuum states of products of Wilson lines) acting on the "unsubtracted" (with RDs) hadronic matrix elements, which are the ones introduced in Chap. 2:

$$\tilde{F}(x, b_T; \mu, \zeta) \;\sim\; \tilde{F}^{\text{unsub.}}(x, b_T; \mu, \text{reg.})\; \tilde{S}^{\alpha}(b_T; \mu, \text{reg.}, \zeta)\;. \tag{3.4.2}$$

The specific form of (3.4.2) (including the value of α) depends on the chosen regulator (reg.). The TMD function in b_T space is related to the one in p_T space through a Fourier transform (see App. D). (3.4.2) shows that the ζ dependence enters in the RD-free (physical) TMDs only through the soft factor S.

There are different types of regulators and definitions of RD-free TMDs in literature. All respect (3.4.2). For example, [20] and, based on the SCET methodology, [96, 115]. Among the differences between the approaches in [20] and [96], there is the fact that in the first Wilson lines are tilted off the light-cone to regularize the RDs, whereas in the second (SCET based) the cancellation happens with Wilson lines on the light-cone. Because of this reason, in the latter a number of diagrams vanish with respect to the first case. In the following we will refer to the approach in [96].

To summarize, μ enters via RG equations to cure UV divergences, whereas ζ enters through the cancellation of RDs via the soft factor. The evolution via ζ is sometimes referred to as "rapidity" evolution, because the value of ζ is related to a rapidity cutoff y_c [20], whose value determines a criterion to "organize" the gluons from the soft factor. Gluons with $y < y_c$ will be reabsorbed in the first hadron (canceling the RDs in the related unsubtracted matrix element), gluons with $y > y_c$ will cure the second hadron.

observables are free from IR soft divergences, which cancels between real and virtual contributions. In (massive) QED no IR collinear divergences arises.

[7] Which cancels in the collinear case.

3.5 Evolution equations

Three equations govern the QCD evolution of TMD distributions, two from RG and one rapidity evolution. The latter, named Collins-Soper (CS) equation, reads:

$$\frac{\partial \ln \tilde{F}(x, b_T; \mu, \zeta)}{\partial \ln \zeta} = -K(b_T; \mu) \ , \tag{3.5.1}$$

where K is the Collins-Soper kernel. As a consequence of the different definition of the RD cancellation, the definitions of the kernel between [20] and [96] differ for a $-1/2$ factor and for a square root in the ζ variable. In both approaches, the kernel is related to the logarithm of the soft factor, so rapidity evolution is physically governed by the soft factor. It is important to stress that the same kernel drives the ζ evolution for all quark or gluon TMDs, since the soft factor entering their definition does not depend on the spin (it is universal but different from quarks to gluons). The solution for the CS equation is:

$$\begin{aligned} \tilde{F}(x, b_T; \mu, \zeta_f) &= \tilde{F}(x, b_T; \mu, \zeta_i) \exp\left\{ - K(b_T; \mu) \ \ln \frac{\zeta_f}{\zeta_i} \right\} \\ &= \tilde{F}(x, b_T; \mu, \zeta_i) \ \left(\frac{\zeta_f}{\zeta_i} \right)^{-K(b_T;\mu)} \ , \end{aligned} \tag{3.5.2}$$

where the subscripts i, f indicate initial and final values in the evolution.

The second equation we deal with is the RG evolution of the CS kernel [20]:

$$\frac{dK(b_T; \mu)}{d\ln\mu} = \Gamma_{\rm cusp}[\alpha_s(\mu)] \ . \tag{3.5.3}$$

Since UV renormalization is multiplicative, the anomalous dimension $\Gamma_{\rm cusp}$ [20] is additive in α_s. UV divergences arise from virtual diagrams only: therefore, $\Gamma_{\rm cusp}$ does not depend on b_T (conjugated to q_T). The solution is:

$$K(b_T; \mu_f) = K(b_T; \mu_i) + \int_{\mu_i}^{\mu_f} \frac{d\mu}{\mu} \ \Gamma_{\rm cusp}[\alpha_s(\mu)] \ . \tag{3.5.4}$$

The third equation is the RG evolution of the TMD function (μ-evolution of the TMD distribution):

$$\frac{d\ln \tilde{F}(x, b_T; \mu, \zeta)}{d\ln\mu} = \gamma_F[\alpha_s(\mu), \zeta/\mu^2] \ , \tag{3.5.5}$$

where γ_F is the anomalous dimension of the TMD function. The same comments

about α_s and b_T for (3.5.3) apply here. The solution reads:

$$\tilde{F}(x, b_T; \mu_f, \zeta) = \tilde{F}(x, b_T; \mu_i, \zeta) \exp\left\{ \int_{\mu_i}^{\mu_f} \frac{d\mu}{\mu} \, \gamma_F[\alpha_s(\mu), \zeta/\mu^2] \right\} . \tag{3.5.6}$$

Solving the CS equation and the RG equations, we can write the expression of a TMD evolved from the scales μ_i, ζ_i to μ_f, ζ_f:

$$\tilde{F}(x, b_T; \mu_f, \zeta_f) = \tilde{F}(x, b_T; \mu_i, \zeta_i) \exp\left\{ \int_{\mu_i}^{\mu_f} \frac{d\mu}{\mu} \, \gamma_F[\alpha_s(\mu), \zeta_f/\mu^2] \right\} \left(\frac{\zeta_f}{\zeta_i} \right)^{-K(b_T;\mu_i)} . \tag{3.5.7}$$

The factor multiplying the TMD at the initial scales is the *evolution kernel* of the distribution or the *Sudakov form factor* for the parton considered and it is *independent* from the spin content of the TMD distribution.

3.5.1 Natural scales

In essence, factorization tackles the logarithmic divergence in (3.3.1) splitting the logarithm via a factorization/renormalization scale:

$$\alpha_s \, \ln \frac{Q}{q_T} \longrightarrow \alpha_s(\mu) \, \ln \frac{Q}{\mu} \, + \, \alpha_s(\mu) \, \ln \frac{\mu}{q_T} \quad \left(\text{or} \quad \ln \frac{\mu}{\mu_b} \right) , \tag{3.5.8}$$

$$\mu_b \doteq \frac{2e^{-\gamma_E}}{b_T} \sim q_T \ , \tag{3.5.9}$$

where the first logarithm will be absorbed by the hard part of the process and the second one will enter the resummed piece, namely the TMDs. In order to maximize the convergence of a perturbative expression, all the logarithms should be minimized. Therefore, the *natural* value for the renormalization scale in the hard part is $\mu = Q$ and for the TMDs is $\mu = \mu_b$ (or q_T). The logarithmic content of the Wilson coefficients in (3.6.1) implies also $\zeta_i = \mu_i^2 \equiv \mu_b^2$. Then, RG and CS equations for the TMDs are used to match two different values for each scale:

$$\begin{aligned} \sigma \sim \mathcal{H}(Q, \mu = Q) \; & \tilde{F}(x_1, b_T; \mu_b, \mu_b^2) \tilde{F}(x_2, b_T; \mu_b, \mu_b^2) \\ & \times \; \exp\left\{ 2 \int_{\mu_b}^{Q} \frac{d\mu}{\mu} \gamma_F[\alpha_s(\mu), Q^2/\mu^2] \right\} \left(\frac{Q^2}{\mu_b^2} \right)^{-2K(b_T;\mu_b)} , \end{aligned} \tag{3.5.10}$$

where in the CS evolution $\zeta_f = Q^2$ has been chosen. Evolution equations are essential in order to match the energy scales of different terms, each one evaluated at its natural scale.

3.6 TMD and collinear distributions

As mentioned in Sec. 3.1 and Fig. 3.2, for each TMD distribution it is possible to give a perturbative treatment of the extraction of a parton with high transverse momentum from the proton. A generic TMD function F_i can be matched onto a basis of collinear distributions f_j via Wilson coefficients $C_{i/j}$ (see the OPE in Chap. 2), calculable in perturbation theory. These coefficients, together with the collinear distributions, provide the description of the high-transverse momentum parton:

$$\tilde{F}_i(x, b_T; \mu, \zeta) \;=\; \sum_{j=q,\bar{q},g} C_{i/j}(x, b_T; \mu, \zeta) \otimes f_j(x; \mu)\; \tilde{F}_{i,NP}(x, b_T; Q, \{\boldsymbol{\lambda}\}) \;, \quad (3.6.1)$$

where i, j are partonic indexes, $\otimes$ represents a convolution over the collinear momentum fractions (see Chap. 6). The $C_{i/j}$ coefficients contain the terms $\alpha_s(\mu)\times$ log introduced in (3.5.8). Due to the natural choice of the renormalization scale $\mu = \mu_b \sim 1/b_T$ for the TMD distribution, this expansion is valid from the perturbative point of view only at low b_T (high p_T). For this reason, a model $\tilde{F}_{NP}$ is introduced to account for the nonperturbative behavior at large b_T values. It might depend on the collinear momentum fraction x and the flavor of the parton i (see Chap. 5), on the hard scale of the process Q and on a set of parameters $\{\boldsymbol{\lambda}\}$ to be determined experimentally. (3.6.1) can be used to write the TMD at the initial scales μ_i, ζ_i in (3.5.7).

Contrary to the Sudakov form factor, the Wilson coefficients depend on the spin content and are different for each TMD distribution. These coefficients are important tools from the phenomenological point of view, since they allow to maximize the perturbative content of the analysis. For T-odd TMD PDFs (see Sec. 2.8 and App. C), though, the matching is performed onto higher twist collinear PDFs, which are poorly known from the phenomenological point of view. For this reason, e.g., the Boer-Mulders effect is still neglected in pQCD descriptions of DY events at the LHC.

In Chap. 8 we will use the Wilson coefficients at $\mathcal{O}(\alpha_s)$ for the unpolarized and linearly polarized gluon TMD PDFs, $f_1^g(x, p_T^2)$ and $h_1^{\perp g}(x, p_T^2)$, available from [89].

From TMDs to PDFs and viceversa

Considering a generic TMD function $f(x, p_T^2; \mu, \zeta)$ and its collinear counterpart $f(x; \mu)$, how legitimate is to write

$$f(x; \mu) \equiv \int d^2\boldsymbol{p}_T \; f(x, p_T^2; \mu, \zeta) \;, \quad (3.6.2)$$

assuming that the function survives transverse momentum integration? From the operator point of view it is fine and it is precisely what lies behind the definition of collinear functions in Chap. 2. Functions appearing at the operator level are *bare* quantities from the point of view of perturbation theory. Renormalization is then required to cure the UV divergences. Since integration over transverse momentum and renormalization transformations do not commute, (3.6.2) is valid only for the bare quantities (the operator level) and not for the physical (renormalized) functions [20, 96]. Moreover, also the rapidity scale ζ contributes to the mismatch between the two sides of (3.6.2) [116, 117]. Rather than determining the collinear distribution from the TMD one as in (3.6.2), from the perturbative point of view it is more appropriate to determine the TMD distribution from the collinear ones, as in (3.6.1).

3.7 Implementing TMD evolution

QCD evolution plays an important role in studying the proton structure for at least two reasons. First of all, it introduces corrections to the normalization and the shape of the observed distributions. Moreover, it provides a way of estimating theoretical uncertainties associated to renormalization and rapidity scales (see Chap. 6, 7 and 8).

3.7.1 Logarithmic expansion

The structure of the anomalous dimension of the TMD reads [20, 96]:

$$\gamma_F[\alpha_s(\mu), \zeta/\mu^2] = -\Gamma_{\rm cusp}[\alpha_s(\mu)]\ \ln\frac{\zeta}{\mu^2} - \gamma_{nc}[\alpha_s(\mu)]\ , \tag{3.7.1}$$

where γ_{nc} is the non-cusp term, which contains also the RG evolution of the coupling. Since the anomalous dimensions are additive in powers of α, we decompose the cusp and non-cusp terms as:

$$\Gamma_{\rm cusp}[\alpha_s(\mu)] \doteq \sum_{k=1}^{\infty}\left(\frac{\alpha_s}{4\pi}\right)^k \Gamma_k^{\rm cusp} \tag{3.7.2}$$

$$\gamma_{\rm nc}[\alpha_s(\mu)] \doteq \sum_{k=1}^{\infty}\left(\frac{\alpha_s}{4\pi}\right)^k \gamma_k^{\rm nc}\ , \tag{3.7.3}$$

where the coefficients $\Gamma_k^{\rm cusp}$ and $\gamma_k^{\rm nc}$ are calculable and known up to 3 loops ($k = 3$) in perturbation theory. In perturbative regime α_s is small and $L \doteq \ln\zeta/\mu^2$ is large,

so that $\alpha_s L \sim 1$. Accordingly, we can organize (3.7.1) as:

$$\begin{aligned}\gamma_F[\alpha_s(\mu), \zeta/\mu^2] &\sim \alpha_s L + \alpha_s^2 L + \alpha_s^3 L + \cdots \quad \text{[cusp terms]} \\ &\quad + \alpha_s + \alpha_s^2 + \alpha_s^3 + \cdots \quad \text{[non-cusp terms]} \\ &\sim \underbrace{\alpha_s L}_{\text{LL}} + \underbrace{(\alpha_s + \alpha_s^2 L)}_{\text{NLL}} + \underbrace{(\alpha_s^2 + \alpha_s^3 L)}_{\text{NNLL}} + \cdots \\ &\sim 1 + \alpha_s + \alpha_s^2 + \cdots \ .\end{aligned} \tag{3.7.4}$$

γ_F is thus expanded in a series of logarithmic accuracy, equivalent to a power series in α_s. The first terms is the leading log (LL), the second is the next-to-leading log (NLL), the third the next-to-next-to-leading log (NNLL), and so on. (3.7.4) shows that the Γ_{cusp} is required at one higher-order in α_s with respect to the γ_{nc}. Choosing the LL approximation, the RG equation for a TMD distribution can be solved as:

$$\tilde{F}(x, b_T; \mu_f, \zeta) = \tilde{F}(x, b_T; \mu_i, \zeta) \ \exp\left\{ -\frac{\alpha_s}{4\pi} \ln^2 \frac{\mu_f^2}{\mu_i^2} \right\} . \tag{3.7.5}$$

Selecting $\mu_i = q_T$ and $\mu_f = Q$, this result reproduces the DLLA outlined in (3.3.2).

3.7.2 Perturbative accuracy

Inserting (3.6.1) in the RG equation for the TMD (3.5.5), we can derive the RG evolution for the Wilson coefficients (see, e.g., eq. (2.17) in [114]). A consistency condition for such an equation is that the order in α_s for γ_F should not be lower than the one for $C(\mu, \zeta)$. This sets a relation between the accuracy in the Wilson coefficients and in γ_F (see Tab. 3.1).

Overall, the perturbative accuracy is driven by the anomalous dimension of the TMD, γ_F. Choosing the α_s order of the CS kernel K to be the same of γ_F, the order of Γ_{cusp} will be one order higher than the one for K (see Tab. 3.1). The α_s accuracy for the hard part $\mathcal{H}$ of the process is usually chosen equal to the accuracy for the Wilson coefficients (but other choices are possible, see Chap. 8). Tab. 3.1 summarizes (some of) the available choices to set the α_s and logarithmic accuracy in the Sudakov form factor in (3.5.7). From (3.7.4) and Tab. 3.1, we see that besides the (nonperturbative) twist and the (perturbative) α_s expansion, it is possible to introduce a set of corrections driven by large logarithms of the form $\ln(\mu/q_T)$. Fig. 3.3 summarizes them (cf. with Fig. 2.6). Note that not all combinations in α_s and logarithmic accuracy are available (Tab. 3.1).

$C_{i/j}$	$\gamma_{\rm nc}$	$\Gamma_{\rm cusp}$	K	*accuracy*	*process*	*chapter*
0	0	0	0	QPM	$\ell P \to \ell h X$	[5]
0	0	1	0	LO-LL		
0	1	2	1	LO-NLL	$e^+e^- \to h_1 h_2 X$	[6]
0	2	3	2	LO-NNLL	$pp^\uparrow \to \eta X$	[8]
1	1	2	1	NLO-NLL		
1	2	3	2	NLO-NNLL	$pp \to \eta X$, $pp \to Z/W^\pm$	[8,7]
2	2	3	2	NNLO-NNLL	$pp \to Z/W^\pm (\to \text{lept.})$	[7]

Table 3.1. In this table we summarize the order of accuracy in powers of α_s (LO, NLO, NNLO) and logarithmic accuracy (LL,NLL,NNLL) for some of the ingredients entering a TMD-evolved cross section. The numbers refer to powers of α_s. The driving accuracy is the one for the anomalous dimension of the TMD, γ_F, equal to the accuracy of $\gamma_{\rm nc}$ and K. $\Gamma_{\rm cusp}$ is one order higher. The accuracy for the Wilson coefficients $C_{i/j}$ cannot be higher than the one for γ_F. The first line refers to the quark parton model (QPM) with intrinsic transverse momentum, where no pQCD corrections at all are present. For some of the combinations, we indicate a process for which such an accuracy level has been (or currently is) under consideration. Note that in literature different naming schemes exist (see also Sec. 7.3). Here we refer to powers of α_s in the small q_T region, namely the accuracy in α_s is the one of $C_{i/j}$ (see [107] for a comparison between conventions referred to small and large q_T regions).

3.7.3 Evolution and the Landau pole

The b_T and μ dependence in the CS kernel can be expressed as [96]:

$$K(b_T;\mu) = \sum_{n=1}^{\infty} d_n \left[\ln\left(\frac{\mu^2}{\mu_b^2}\right)\right] \left(\frac{\alpha_s(\mu)}{4\pi}\right)^n , \tag{3.7.6}$$

where d_n are perturbatively calculable coefficients. For this reason, the natural choice for the renormalization scale in the CS kernel is $\mu = \mu_b \sim 1/b_T$. This implies that at small b_T the kernel can be computed as a perturbative expansion and the coefficients d_n can be obtained from the calculation of the soft function S at the desired accuracy. At large b_T, instead, it has to be modeled and extracted from experimental data. Because of the universality of the soft function, this nonperturbative contribution is *universal* among all the measurable TMD structures (but different between quarks and gluons).

Due to a Fourier transformation with respect to b_T (see, e.g., Sec. 6.2), in calculating cross sections we integrate over b_T from 0 to $+\infty$. Since perturbative expansion can be trusted up to a maximum value of b_T, say $b_{\rm max}$, in practical

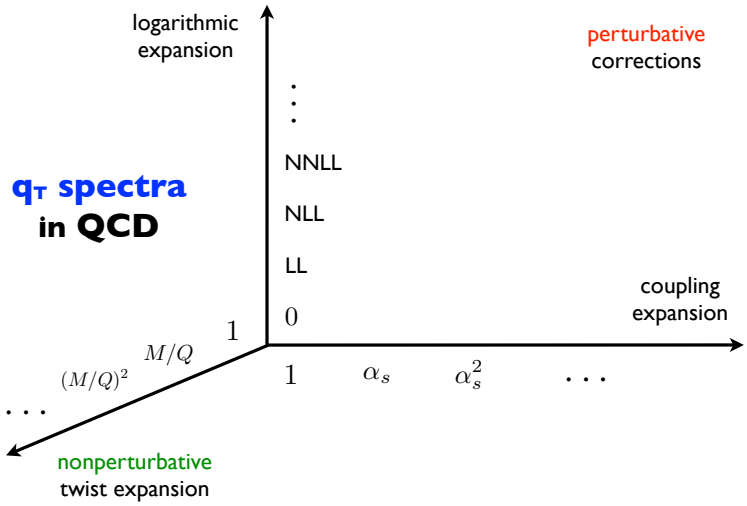

Figure 3.3. Transverse momentum spectra of reactions with hadrons in the initial and/or in the final state in QCD can be approximated by means of three complementary expansions. The twist expansion represents the nonperturbative direction, accounting for the effects emerging from the structure of hadrons. Then, a perturbative plane is generated by expansions in α_s and $\ln(\mu/q_T)$ (see Sec. 3.7). Note that not all the combinations in the perturbative plane are possible (see Tab. 3.1). The origin, the point $(1, 1, 0)$, represents the quark parton model.

implementations of TMD evolution it is convenient to correct all the perturbative quantities integrated over b_T by introducing a new variable $\hat{b}_T(b_T)$ that freezes at $b_{\max}$ in the limit of large b_T:

$$\lim_{b_T \to +\infty} \hat{b}_T(b_T) = b_{\max} \ . \tag{3.7.7}$$

Different functional forms are available in the literature. In Chap. 6 and 8 we will test two of them involving a square root and an exponential function. Another possible choice to avoid the region at high b_T is to extend the integral over b_T to the complex plane, avoiding the Landau pole which lies on the real axis. This method, named complex-b prescription, has been introduced in [118,119], applied to the DY cross section in [120] and to the SIDIS one in [121]. In the literature it is also referred to as the *minimal* prescription, because it does not require the introduction of a nonperturbative paramter like $b_{\max}$ and introduces the least amount of corrections to the perturbative expression.

When using a prescription as defined in (3.7.7), the model needed to parametrize

the behavior of the kernel for $b_T > b_{\max}$ is defined as:

$$g_{\rm np}(b_T;\{\boldsymbol{\lambda}\}) \doteq -K(\hat{b}_T;\mu_{\hat{b}}) + K(b_T;\mu_b) \ , \tag{3.7.8}$$

where $\{\boldsymbol{\lambda}\}$ is a set of nonperturbative parameters. In (3.7.8) we have explicitly chosen the natural scale μ_b and $\mu_{\hat{b}}$ is as in (3.5.9) with $\hat{b}_T$ replacing b_T. Phenomenological implementations of the $g_{\rm np}$ factor will be presented in Chap. 6 and 8. (3.7.8) implies that the evolution driven by emission of soft gluons is partly perturbative and partly nonperturbative.

There is a lively debate in the literature about the role and the relevance of the nonperturbative factor in the CS kernel. First of all, as it is defined in (3.7.8), it affects the kernel not only at high b_T but also at low b_T, where the perturbative calculation should dominate. In particular, the parameters in the model will be determined so that the model itself induces the perturbative expression (function of $\hat{b}_T$) to match the pure perturbative result (3.7.6) at low b_T, correcting the convergence of $K(\hat{b}_T;\mu)$ to a constant value k due to the freezing of b_T towards $b_{\max}$. This "spurious" behavior in the low b_T region could be avoided through a different definition [122]:

$$K(b_T;\mu) = K^{\rm res}(b_T;\mu)\theta(b-b_c) + g'_{\rm np}(b_T;\{\boldsymbol{\lambda'}\})\theta(b_c-b) \ , \tag{3.7.9}$$

where "res" indicates the pure perturbative expression from (3.7.6) and b_c is a cut-off value which separates sharply - via a theta function - the regions of low (perturbative) and high (nonperturbative) transverse momentum. In this case the model does not interact with the perturbative part. It is important to stress that it does not make sense from the phenomenological point of view to compare the parameters $\{\boldsymbol{\lambda}\}$ and $\{\boldsymbol{\lambda'}\}$, because the nonperturbative contributions defined in (3.7.8) and (3.7.9) play very *different roles*. Besides the definition, also the impact of different implementations of $g_{\rm np}$ is a phenomenological hot topic. In [122] it is shown that, without introducing a freezing prescription $\hat{b}_T$ and if the scales $\zeta_{i,f}$ in (3.5.7) are separated enough, the K-dependent part of the evolution kernel converges to zero already before the nonperturbative high b_T region. Being already zero in the perturbative region, the evolution kernel should vanish also in the nonperturbative regime, so there is no need for a model. This statement applies to production of particles with high mass, e.g. $Z/W^{\pm}$ and the Higgs boson. Its verification and discussion is anyway obfuscated by the introduction of a $\hat{b}_T$ prescription, which modifies the behavior of the CS kernel also at low b_T. For those cases and in presence of a Gaussian model $g_{\rm np}$, it is found [122] that a value of $b_{\max} \sim 1.5$ GeV^{-1} is the best to reproduce the correct perturbative result of the CS kernel at low b_T (3.7.6), without any freezing prescription.

3.7.4 The limit $b_T \to 0$

As explained in Sec. 3.1, the q_T spectrum in the region of high transverse momentum should be described by a fixed-order calculation in pQCD. Choosing the natural scale $\mu_b \sim 1/b_T$ for the Wilson coefficients and choosing $\zeta = Q^2$, leads to a logarithmic behavior $\ln(Qb_T)$ in (3.7.1) and in the Sudakov form factor. This means that in the limit of small b_T (high transverse momentum q_T) the resummed part contaminates the fixed order calculation, because the logarithm does not vanish. In order to cure this undesired effect, a possibility is to modify the logarithm in (3.7.1) as [123, 124]

$$\ln\left(\frac{Q}{\mu_b}\right) \to \ln\left(\frac{Q}{\mu_b} + 1\right) . \tag{3.7.10}$$

In the region of large b_T, where resummation is needed, $Qb_T \gg 1$ and the result for the anomalous dimension in (3.7.1) is unchanged. In the opposite limit $b_T \to 0$, instead, $Qb_T \ll 1$ and the logarithm in (3.7.10) vanishes. As a consequence, the Sudakov form factor at high transverse momentum reduces to 1, leaving the fixed-order calculation unchanged. In [124] the impact on the total cross section is also discussed.

A different way of regulating the small b_T region is to choose a different resummation scale, such as [113, 125, 126]:

$$\mu_b \to \mu_b' \doteq \frac{Q}{Q + \mu_b}\ \mu_b\ . \tag{3.7.11}$$

Accordingly, the scale in (3.7.11) can be chosen as the natural scale both in the Sudakov factor and in the TMDs, not only in the argument of the anomalous dimension as in (3.7.10). In particular, this substitution guarantees that, when integrating over b_T, $\mu_b' < Q$ for all b_T values. In the language of [113], this corresponds to introducing a new cutoff $b_{\min} \sim 1/Q$, which quantifies the upper limit of the small b_T region.

It is important to keep in mind that this region mainly shapes the physics at high q_T, but also affects the other q_T regions via the Fourier transform in the cross section. This is evident especially at low Q, where the small b_T region is larger. Comparing the effects of the two methods in (3.7.10) and (3.7.11) gives an idea of the uncertainty associated to the small b_T region [125, 126]. It is proven that the μ_b' prescription leads also to a significant improvement in the description of SIDIS data at low q_T and Q [127].

3.7.5 Intrinsic transverse momentum

The last prescription we deal with is the form of $\tilde{F}_{i,NP}$ in (3.6.1), namely the parametrization of the large b_T region (small partonic transverse momentum p_T) in the expansion of a generic TMD function. $\tilde{F}_{i,NP}(b_T; Q, \{\boldsymbol{\lambda}\})$ encodes the nonper-

turbative wavefunction of the parton inside the proton and its Q-independent part is related to the *intrinsic* transverse momentum of the parton.

There are different ways of parametrizing $\tilde{F}_{i,NP}$ (or its Fourier transform in p_T space) in the literature. The most common one is a Gaussian function in p_T, because of, e.g., its mathematical simplicity. We will explore it in Chapters 5, 6, 7, 8. Despite being particularly "user-friendly", it should not be used outside its limited scope. In particular, it does not reproduce the correct behavior at high transverse momentum. Other parametrizations are available in the literature, e.g. a weighted exponential functions [114].

The distributions in the intrinsic transverse momentum are the quantities that should be fitted to experimental data. It is important to keep in mind that non-perturbative effects are always defined as a subtraction, namely what we observe experimentally minus the calculable perturbative corrections. Accordingly, the way QCD evolution is implemented (the accuracy together with the chosen models and prescriptions), has an impact on what we interpret as nonperturbative structure that should be investigated and quantified. In literature different approaches to TMD evolution are present. In [128] a method was proposed to compare different approaches to factorization and evolution schemes, checking their consistency.

The simple picture of the parton model can be recovered turning off all the perturbative corrections presented in this chapter (see Fig. 3.3). In that case, the unpolarized TMD PDF for a quark with flavor i in a proton can be written as:

$$F_i(x, p_T^2) = f_1^{i/P}(x) \frac{1}{\pi \langle p_T^2 \rangle_i(x)} e^{-\frac{p_T^2}{\langle p_T^2 \rangle_i(x)}} , \tag{3.7.12}$$

where we have chosen a Gaussian model to parametrize the whole p_T spectrum of the quark. The parameter $\langle p_T^2 \rangle_i(x)$ represents the average square transverse momentum of the parton considered (quark or gluon). For an unpolarized parton in an unpolarized proton, its definition as the first moment of the unpolarized TMD PDF is divergent, due to the $1/p_T^2$ behavior of f_1^i at high p_T:

$$\langle p_T^2 \rangle_i(x) = \int d^2\boldsymbol{p}_T \; \boldsymbol{p}_T^2 \; f_1^i(x, p_T^2) \equiv 2M^2 f_1^{(1)i}(x) \; . \tag{3.7.13}$$

An alternative definition is provided by the Bessel weighting [116, 129] with the replacement $f_1^{(1)i}(x) \to \tilde{f}_1^{(1)i}(x, b_T^2)$ in the limit $b_T \to 0$ (see App. D). The average square transverse momentum can be a function of the collinear momentum fraction and, for quarks, the flavor (Chap. 5) and it needs to be determined by means of nonperturbative techniques (e.g., lattice QCD or fits). Phenomenology based on this Gaussian assumption will be presented in Chap. 5 and we will elaborate on its results in Chap. 6 and 7.

3.8 Other factorization and evolution schemes

TMD factorization and evolution are not the only frameworks to describe the QCD evolution of functions dealing with the transverse momentum of partons. A different scheme called *high-energy* or *small-x* factorization [130, 131] provides factorization of cross sections in the kinematic limit where the Mandelstram variable s [4] is very large and $Q^2 = M^2$ (where M is the mass of the produced particle) is large but finite:

$$\Lambda_{\mathrm{QCD}} \ll Q^2 \ll s \to \infty \quad [\text{ideally}] \; . \tag{3.8.1}$$

This is different from the kinematic regime for TMD factorization:

$$q_T^2 \ll Q^2 \to \infty \quad [\text{ideally}] \; , \tag{3.8.2}$$

where q_T is the transverse momentum of the produced particle. In both approaches it is possible to define partonic distributions sensitive to transverse momentum. In the context of small-x factorization they are sometimes referred to as unintegrated distributions. There are attempts to define common grounds for discussion and applications. Recently, these connections have been discussed in a series of workshops (REF meetings [28]). The following are among the key points to draw a relation between the two frameworks: an operator definition for unintegrated distributions has been provided in [132, 133]; the same structures appear in the operator connection between gluon TMDs at $x = 0$ and TMDs from gauge loop correlators discussed in [78]. Studies of resummation including small-x (BFKL) and transverse momentum effects have been performed in [134–136].

Looking ahead, the computational tool TMDlib [137] collects parametrizations of functions defined in both schemes. A review dealing with both definitions in the case of gluons is available in [138].

CHAPTER 4
PHENOMENOLOGY

La sapienza è figliuola della sperienza.
Leonardo da Vinci

TMD phenomenology combines all the concepts that we introduced so far, in order to quantify the impact of hadron structure in scattering processes. In this chapter we outline how to obtain information about the TMD structures introduced in the first part of this thesis, focusing on the available observables and the tools to analyze them. We introduce the motivation for the studies presented in the next chapters and we summarize the current level of knowledge for the unpolarized TMDs. A major goal of phenomenology is also to collect and organize the knowledge gained so far. For this reason, a repository is introduced as a reference point for future studies and applications.

4.1 Observables

In order to study the impact of TMDs in specific processes, it is possible to analyze different kinds of observables, e.g. cross sections, multiplicities and spin asymmetries. The first ones have been introduced in Sec. 2.2. Multiplicities are ratios of cross sections (see Chap. 5 and 6), whereas spin asymmetries involve cross sections with certain spin configurations (see Sec. 4.2). Each one has specific advantages.

Predictions and fits of cross sections are important because they can be a direct test of TMD factorization and the formalism generating from it, namely the matching from the TMD to the collinear region via the Y term (Sec. 3.3). Multiplicities, defined as the ratio of a TMD cross section over the corresponding one integrated

over the observed transverse momentum (see Chap. 5 and 6), keep the same advantages of cross sections, reducing systematic experimental errors (like acceptance effects) through the ratio. Moreover, as explained in Chap. 6, ratios of multiplicities are less sensitive to theoretical uncertainties arising from the renormalization and the rapidity scales. Considering ratios, though, some of the TMD effects of interest might be reduced.

Asymmetries, instead, allow to isolate contributions to cross sections coming from specific TMD structures: they are useful for investigations targeted to certain TMD PDFs or FFs. Among all the possible examples, they are a useful tool to investigate the transversity[1] quark TMD PDF $h_1(x, p_T^2)$ (see Sec. 2.6.3), and in general all the structures involving the polarization of the parton and/or the hadron (see Chap. 8). As for multiplicities, the definition as ratios of TMD cross sections allows the cancellation of systematic effects but might complicate the determination of nonperturbative effects specific of the TMD formalism (see Chap. 3).

Which observable is best depends on the phenomenological goal. Studies of certain polarized TMD functions are naturally performed via spin asymmetries. For example, in Fig. 4.1 the experimental kinematic coverage for the Sivers asymmetry [15] is presented. Experimental investigations for that asymmetry allow the determination of the quark Sivers function $f_{1T}^{\perp}(x, p_T^2)$. Tests of the formalism and determinations of the impact of nonperturbative contributions to QCD evolution are better provided by cross sections and multiplicities, where there are no undesired cancellations [113, 139]. Nonetheless, also asymmetries are useful in testing the formalism, namely to address the process dependence of the T-odd (polarized) TMD PDFs (see the case of the Sivers asymmetry).

4.2 Asymmetries

4.2.1 The case of QED

Between 1949 and 1959, Ehrenberg and Siday [140] and Aharonov and Bohm [141] showed that the wave function of an electron passing around a long solenoid experiences a phase shift as a result of the enclosed magnetic field, despite the magnetic field being negligible in the region through which the particle moves. Experimental investigations were performed using double slits experiments. Relying on a path-integral formulation, it is possible to show [142] that the amplitude of the interference pattern on the screen is proportional to a phase involving the integral of the electromagnetic potential $\exp\{-ie \oint d\boldsymbol{x} \cdot \boldsymbol{A}(\boldsymbol{x})\}$. This phase shift due to a gauge loop proves that the potential A^μ has a physical role, it is not just a mathematical artifact to introduce the electric and magnetic fields $\vec{E}$, $\vec{B}$. The direction

[1] Which, being chiral-odd, needs to be coupled to another chiral-odd distribution.

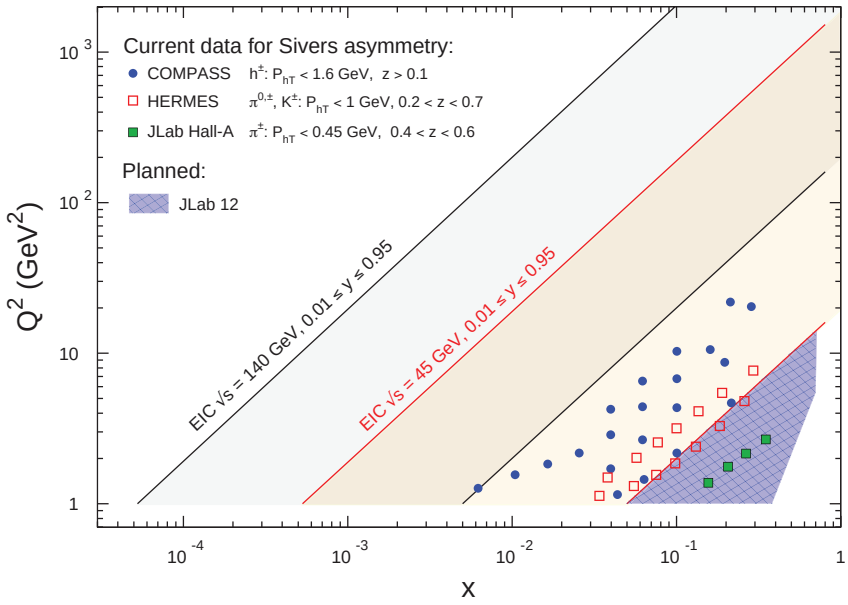

Figure 4.1. The kinematic x-Q^2 ranges for the Sivers asymmetry covered by different experimental collaborations. The Electron-Ion-Collider will probe new ranges not experimentally explored yet. Figure from [77].

of the shift for the interference pattern changes sign depending on the direction of the magnetic field: such an effect can be considered an *asymmetry*.

4.2.2 QCD and spin

The analogue of this effect in QCD are asymmetries governed by the spin of the involved hadrons (single or double, depending on the number of spins involved). Experimentally, they can manifest with specific dependencies on the azimuthal angles entering a cross section (e.g. the azimuthal angle of the spin vector). For this reason they classify as *azimuthal* spin asymmetries.

The interest in the polarization properties of hadrons arose in the late ′80s from the so-called "Spin-Crisis"[2]. Later, at Fermilab, single transverse spin asymmetries of order $\sim 10\%$ were measured in hadronic polarized hyperon production [144, 145] and pion production [146–149]. Since then, the study of spin asymmetries has rapidly evolved, both from the theoretical and experimental point of view. For a deeper insight into spin physics and azimuthal asymmetries see the textbooks [150, 151], the theses [56, 152] and the reviews [153–159].

[2]It was found by the EMC collaboration that quarks account only for a small fraction of the helicity of the proton [143].

Notably, the observations of spin asymmetries could not be accounted for by the collinear quark parton model (QPM). This triggered an investigation of hadron structure beyond the collinear QPM and different mechanism were proposed to account for spin asymmetries [56, 152].

Considering the polarization of only one hadron, the first proposal relied on a collinear factorization framework [160, 161], involving interactions of soft gluons from the target remnants with the active partons in the initial and final state. This is accounted for by collinear twist-3 matrix elements (Qiu-Sterman [QS] matrix element). Later, Sivers proposed an explanation [162, 163] based on a correlation between the transverse momentum of the quark and the polarization of the proton, introducing the Sivers quark TMD PDF $f_{1T}^{\perp}(x, p_T^2)$. The Sivers effect and its interplay with the time reversal invariance of QCD (see App. C) initiated a theoretical endeavor culminated with the introduction of gauge links in the definition of partonic distributions [21, 164, 165].

The common feature of these mechanisms is that an imaginary phase required for the non-vanishing asymmetry is generated by taking into account an additional soft gluon exchange (from the QS matrix element in the collinear case, from the gauge-link in the TMD case) between the active parton and the remnant of the transversely polarized hadron. These two explanations are linked, since the TMD (quark and gluon) Sivers function is matched onto QS matrix elements.

From the behavior of quark and gluon correlators under time reversal transformation (see Sec. 2.8), we can deduce that a Feynman amplitude involving an odd (even) number of spins[3] is odd (even) under time reversal. For this reason, single spin asymmetries (SSAs) are proportional to T-odd kinematic correlations, whereas double spin asymmetries (DSAs) are described by T-even kinematic correlations.

4.2.3 TMDs of definite rank and azimuthal asymmetries

An advantage of using distribution and fragmentation TMD correlators in a STT form with definite rank structures is the possibility of linking the rank of the functions to the angular dependence with which they contribute to structure functions and azimuthal asymmetries. As an example, let us consider SIDIS. The differential cross section involving the transverse momentum of the observed hadron, the azimuthal angle of the hadron plane ϕ_h (defined according to the Trento conventions [166]) and the azimuthal angle ϕ_S of the transverse spin vector is available in [15] in terms of structure functions and TMDs, including twist-2 and twist-3 terms. For the structure functions built with TMDs of definite rank, we conjecture that:

$$F^{\mathcal{F}(\phi_h,\phi_S)}_{[\text{pol. } \ell][\text{pol. } h]} \sim \mathcal{C}[fD] \implies \mathcal{F}(\alpha\phi_h, \beta\phi_S) \ , \tag{4.2.1}$$

[3] We refer to a covariant spin vector entering the density matrix, as in Sec. 2.6.2.

where $F_{[\text{pol. }\ell][\text{pol. }h]}$ is a structure function related to certain polarization states of the lepton ℓ and the target h. The superscript labels a specific Fourier mode of the structure function. f and D are, respectively, two generic TMD PDF and TMD FF and $\mathcal{C}$ is the convolution operator as defined in [15]. The coefficient α and β are related to the ranks of f and D in transverse momentum and spin, respectively.

The ϕ_S-dependent term enters (4.2.1) only when the transverse spin S_T plays a role. Eq. (4.2.1) is a way of connecting a specific Fourier mode of a structure function with the rank of the involved TMDs. Its specific form for SIDIS with correlators in STT form is under investigation. The dependence of α and β on the ranks in transverse momentum and spin might depend on the process considered.

As an example of azimuthal asymmetry, let us consider the twist-2 contribution to the SIDIS cross section coming from the configuration with a longitudinally polarized lepton beam and a transversely polarized target [15]:

$$\frac{d\sigma_{LT}}{dxdydzd\phi_h d\phi_S d\boldsymbol{P}_{hT}^2} \sim S_T \lambda_l \left[\sqrt{1-\epsilon^2}\, \cos(\phi_h - \phi_S)\; F_{LT}^{\cos(\phi_h-\phi_S)} \right]. \tag{4.2.2}$$

λ_l is the polarization of the lepton beam, S_T is the transverse spin of the target.[4] The Fourier moment of the spin asymmetry [166]

$$A_{LT}^{\cos(\phi_h-\phi_S)} \sim g_{1T}(x, p_T^2) \otimes D_1(z, k_T^2) \;/\; f_1 \otimes D_1 \tag{4.2.3}$$

allows to access the T-even worm gear TMD PDF g_{1T}, in combination with the unpolarized TMD FF. g_{1T} and D_1 are functions with definite rank, see Sec. 2.6.3. The denominator of spin asymmetries is built by the unpolarized TMD PDF and FF, $f_1(x, p_T^2)$ and $D_1(z, k_T^2)$. A detailed knowledge of the unpolarized TMDs is thus of utmost importance to get information on the polarized TMDs via spin asymmetries. Preliminary[5] experimental results on different moments of the DSA A_{LT} as a function of transverse momentum are summarized in the report written by the author for the Desy Summer School program 2012.

[4] For the other variables see [15].
[5] The report is HERMES internal.

4.3 What do we know?

In this thesis we mostly deal with the properties of the unpolarized TMDs. Here we outline their phenomenological knowledge. The repository

http://tmd.hepforge.org

has been introduced to collect material interesting for TMD studies. A summary of fits and parametrizations of TMDs is also available in Sec. 5 in [28].

4.3.1 Unpolarized quark TMDs

In the past years TMDs have been investigated mainly within the generalized[6] QPM. This model, as mentioned in Tab. 3.1, neglects corrections from perturbation theory. If gauge links are absent in the operator definitions, the process dependence of TMDs must be inserted ad-hoc. Its success relies on the fact that, up to now, the available experimental data sensitive to partonic transverse momentum do not extend over large Q^2 ranges (see Fig. 4.1). Within the generalized QPM, a Gaussian behavior in the partonic transverse momentum is the most common assumption, whose details are described in, e.g., [167, 168]. Nowadays TMD phenomenology is moving towards a "precision phase", where perturbative corrections play an increasingly important role. This is important in view of new experimental setups, like the Electron-Ion-Collider (EIC) [77]. Introducing perturbative corrections at low Q^2 is challenging from the point of view of TMD factorization and may even lead to correcting the formalism (see the case of the Y-term [113]).

Unpolarized distribution $f_1^a(x, p_T^2)$. We know fairly well its x-dependence, which relies on fits of global data sets. For an overview of the knowledge of the x-dependence see, e.g., [169–172] and http://hepdata.cedar.ac.uk/pdfs. Moreover, the LHAPDF project provides a computational interface to many parametrizations. The knowledge of the transverse momentum dependence, instead, is still more limited.

From SIDIS: QPM fits of unpolarized data assuming Gaussian behavior in the transverse momentum [167, 173] or a Gaussian behavior with dependence on the kinematics and the flavor [174–177]; QPM analyses of the Cahn effect (unpolarized data with dependence on the azimuthal angle) [167, 178]. A study of the nonperturbative component of the evolution via unpolarized TMDs in SIDIS is available in [179].

From DY: QPM analyses of data with and without azimuthal dependence [167, 180]; analyses with QCD evolution with $\mathcal{O}(\alpha_S)$ corrections at low transverse momentum (see Tab. 3.1) [181–183] based on the CSS formalism in its original [105]

[6] Originally the parton model was introduced to account for the collinear motion of partons. We refer to a "generalized" parton model because transverse momentum effects are considered.

and new [20] formulation; [114] within the framework of TMD factorization on the light cone (see Chap. 3); [184] based on a TMD extension of the DGLAP formalism [185–187]. The last analysis includes a theoretical and phenomenological comparison of the three mentioned evolution schemes. [188] presents a study based on the minimal (complex-b) prescription (see Chap. 3). A study of the nonperturbative effects in DY and Higgs production has been carried out, e.g., in [189, 190]. The theoretical uncertainty arising from variations of the renormalization and factorization scales is comparable with the one associated to nonperturbative effects.

Combined SIDIS and DY: [191–193] address the issue of the global description of SIDIS and DY data, obtaining qualitative results (the last two do not provide the χ^2 or the sample of analyzed data). The first also compares different approaches to TMD evolution.

At small-x: Quark TMDs at small-x have been introduced in [194,195]. In [196] the SIDIS cross section is described by TMD quark distributions in the framework of small-x TMD factorization.

Summarizing, it is important to stress that phenomenological extractions depend on the perturbative content and the chosen accuracy. For this reason, it would be interesting to check if the nonperturbative information that we can extract from experimental data converges while adding more perturbative information.

Unpolarized fragmentation $D_1^{a\to h}(z, p_T^2)$. A review about parton fragmentation functions has been recently presented in [197]. An overview of the available knowledge of collinear $D_1^{a\to h}$ is also available at http://www2.pv.infn.it/∼radici/FF-database/. An online interface to calculate collinear fragmentation functions in different kinematic regimes is provided at http://lapth.cnrs.fr/ffgenerator/. The most up-to-date global fit of collinear D_1 is the DSEHS (or new DSS) parametrization [198] (whose baseline for perturbative accuracy has become NLO in α_s). In essence, the available information concerning the transverse momentum dependence comes from the SIDIS analyses outlined in the previous paragraph for unpolarized distribution. Notably, the flavor dependence in the TMD part is more evident with respect to the case of distributions (see Chap. 5 for more details).

4.3.2 Unpolarized gluon TMDs

We only know with fair precision the x-dependence of f_1^g (see the LHAPDF project). There are no fits of the transverse momentum dependence within the TMD factorization approach. Predictions exist, linked to Higgs production (e.g. [89, 199]), Higgs plus jet production (e.g. [200]) and quarkonium production (e.g. [98, 201]) from proton-proton collisions. For unpolarized gluon TMD FFs, see the paragraph for quarks. The most recent parametrization is the one given in the DSEHS release.

Behavior at small-x. There are several studies of unintegrated gluon distribution functions at small-x. Within the high-energy approach [132] (see Chap. 3),

it is possible to introduce two operator structures associated to two gluon distributions: the Weizsäcker-Williams (WW) distribution and the dipole distribution. For a link between these structures and the gluon-gluon correlator introduced in Sec. 2.6 see [78].

Unintegrated distributions have also been introduced without an operator definition, e.g. in [202–205]. In this context, phenomenological investigations relying on the CCFM [206, 207] evolution framework are discussed, e.g., in [208–210].

4.4 How to improve

As mentioned earlier, a large portion of TMD phenomenology has been performed in the generalized QPM, namely without considering corrections from perturbation theory. In view of current and future experimental facilities exploring new kinematic frontiers, such as the LHC, AFTER@LHC, the LHeC and the EIC, it is important to improve the tools to perform phenomenological investigations of TMDs (see Fig. 4.2), combining theoretical accuracy and a detailed understanding of the nonperturbative structure.

The relevance of nonperturbative effects at different energy scales is a hot topic in TMD phenomenology. Their impact is reduced in the limit $Q/\Lambda_{\rm QCD} \to +\infty$ [123, 211]. For this reason, in order to be sensitive to nonperturbative effects, we should explore relatively low Q regions. Not too low, though: otherwise TMD factorization could break and higher-twist effects could contaminate the results. Working at medium Q (say $Q \sim 10$ GeV, as in Chap. 6 and 8) should be optimal to study NP effects safely, trusting to a good extend TMD factorization and evolution. There are several strategies to improve our phenomenological knowledge of TMDs and the analysis framework can be refined on all its sides (see Fig. 4.2): theoretical, experimental and phenomenological.

Theory

From the theory viewpoint, hot topics are, among the others, the process dependence of TMDs [212], perturbative accuracy (see Chap. 3), connections with small-x formalism [28], quantifying factorization breaking effects [100, 213] and higher twist effects.

Adding perturbative corrections has a two-fold importance: it introduces corrections to the observables and it allows for an estimate of the theoretical uncertainties associated to the renormalization scale and the rapidity scale (see Chap. 6, 7, 8). In view of experimental facilities exploring both high Q^2 and small x kinematic regions (e.g. potentially the EIC), it would be important to implement frameworks where both Sudakov and BFKL-like effects are taken into account, e.g. [134–136].

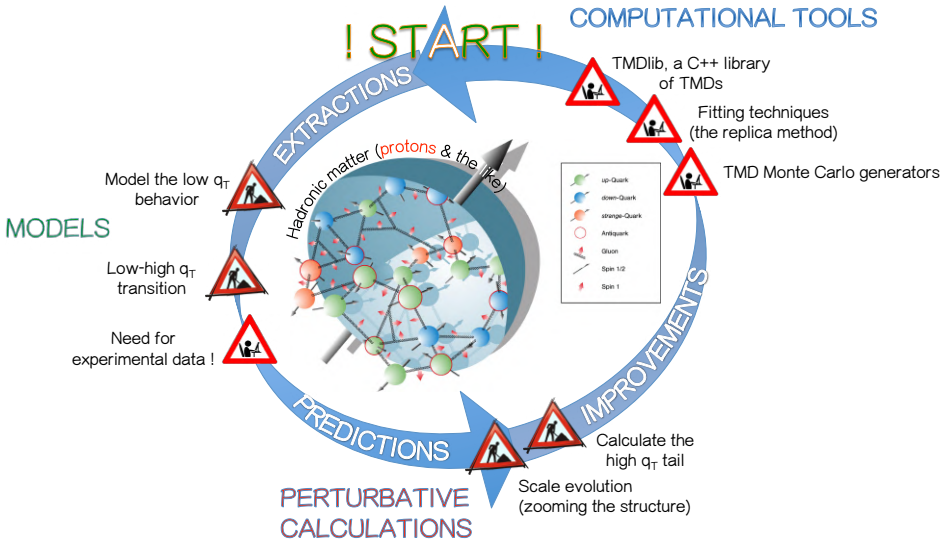

Figure 4.2. Here we illustrate the major steps required along the road to phenomenology of TMD distributions. Definitions of the functions and investigations of their universality properties need to be complemented by models for the low transverse momentum spectrum and perturbative calculations for the high transverse momentum regime. Experimental data need to be tackled by means of simulations and fitting techniques.

Experiments

An overview of the current and future experimental programs that will open new windows on TMD phenomenology is available in App. F. Among the new ones, we mention the 12 GeV program at Jefferson Lab, the LHeC, the EIC for SIDIS, the hadronic collisions at RHIC, COMPASS, LHC, AFTER@LHC, the fragmentation studies at Belle-II, BES-III, the ILC.

Besides extending the Q^2 range to appreciate TMD evolution effects, it is important to achieve multidimensional binning in the data, diminishing the correlations among the kinematic variables. This is of relevance in order to deepen the knowledge of the nonperturbative part of the TMDs at low partonic transverse momentum (see Chap. 5).

Concerning SIDIS, nowadays we still benefit of the heritage of the HERMES experiment and the most recent results of the COMPASS collaboration. In the near future, we will benefit of new multidimensional data collected by the JLab 12 GeV program. Considering DY, the Relativistic Heavy Ion Collider (RHIC) is at the moment the only machine in the world delivering polarized data. In Europe the COMPASS experiment will soon follow. The LHC is the most powerful apparatus to collide unpolarized protons. Its possible spin-offs are A Fixed Target Experiment at

the LHC (AFTER@LHC) (with the possibility of polarizing a hadron target, see [36] and Chap. 8), the Large Hadron-electron Collider (LHeC, to perform SIDIS studies). Along this line, the Electron-Ion Collider [77] in the United States will be an optimal setting for TMD studies. Considering e^+e^- annihilation, besides the knowledge delivered so far by BELLE , BABAR and BES III , the International Linear Collider (ILC) will contribute to the investigations of fragmentation functions in the future.

Phenomenology

At this stage, a global fit of different experimental data sets has not been achieved yet. An almost global study will be presented in [127]. Along this road and connecting to the previous paragraph, one of the most compelling phenomenological challenges is to improve the knowledge of the nonperturbative part of (un)polarized TMDs and of TMD evolution. Among the hot topics there are the flavor and kinematic dependence in the transverse momentum part [174–177, 214], how to implement the separation between intrinsic and perturbative transverse momenta, the prescription to treat the Landau pole problem in TMD evolution (Sec. 3.7.3).

Improving the statistical tools is also important. For example, fit procedures based on neural network techniques [215] and the method of replicas [174] help in achieving a deeper insight into the statistical uncertainties connected to experimental data and best-fit values (Chap. 5). Moreover, defining standardized frameworks for data analysis can be helpful for comparing different extractions of phenomenological parameters. An example for collinear distributions is [216].

Recently TMDlib [137], a library of TMDs, has been created as a framework to collect parametrization of TMDs via a user-friendly interface. It follows the philosophy of the successful LHAPDF project [217] for collinear parton distribution functions. A list of Monte Carlo generators with sensitivity to the transverse momentum of partons is provided in Sec. 6 in [28], ranging from semi-inclusive to exclusive generators (see also the discussion in Sec. 3.3.4).

In the next chapters of this thesis we focus on topics and techniques that can help improving the phenomenological knowledge on the TMDs. In Chap. 2 we presented notation based on symmetric traceless tensors, that facilitates the translation into b_T space to implement QCD evolution (Chap. 8) and can shed light on the azimuthal angular behavior of asymmetries. We will focus on the strategies to improve the understanding of the baseline of *all* the spin asymmetries, namely the unpolarized distributions. In particular, we will investigate their flavor and kinematic dependence in the TMD part, addressing SIDIS (Chap. 5), e^+e^- annihilation (Chap. 6) and $W^\pm/Z$ production at the LHC (Chap. 7), each at different energy ranges. Eventually, we will investigate the effect of QCD evolution and theoretical uncertainties on gluon TMDs in (un)polarized proton-proton collisions at LHC and AFTER@LHC (Chap. 8).

CHAPTER 5

SEMI-INCLUSIVE DIS

Provando e riprovando.
Accademia del Cimento

In this Chapter we present a phenomenological investigation of the flavor and kinematic dependence of partonic intrinsic transverse momentum from SIDIS data released by the HERMES collaboration, in the framework of the generalized quark parton model (QPM). The replica method (Sec. 5.3.2) plays a fundamental role, allowing to access physically equivalent configurations for the nonperturbative parameters and to compute expectation values for observables. This work is the foundation for the analyses presented in Chap. 6 and 7. An analysis based on preliminary COMPASS results is available in the M.Sc. thesis of the author.

Text and results are based on [174–177, 214]. The convention for labeling partonic and hadronic momenta is specified in Fig. 5.1.

5.1 Introduction and motivation

In spite of the recent advancements in TMD phenomenology, we have still little knowledge about the most simple and most common of all TMD PDFs: the "unpolarized" distribution, $f_1^a(x, \boldsymbol{k}_\perp^2)$, i.e., the distribution of partons with flavor a summed over their polarization and averaged over the polarization of the parent hadron. The features of the corresponding collinear standard PDF $f_1^a(x)$ strongly depend on the parton flavor a (see, e.g., Refs. [169–172, 218, 219]). It comes natural, therefore, to question whether or not partons of different flavors have different transverse-momentum distributions. Several model calculations predict different

transverse-momentum behaviors for different quarks [104, 220–225], although others do not [226–228]. Indications of flavor dependence in TMD PDFs come also from pioneering studies in lattice QCD [229]. Therefore, at this stage there are compelling motivations to study the flavor dependence of TMD PDFs.

The measurements recently published by the HERMES collaboration [29] are ideal to address this issue, since they refer to SIDIS off different targets (protons and deuterons), with different final-state hadrons (charge-separated pions and kaons), and with multidimensional binning. This is a landmark achievement in the knowledge of the internal structure of hadrons. Earlier data already gave some indications, but were limited in the variety of targets, or final-state hadrons, or multidimensional coverage (see, e.g., [31–35]).

The COMPASS collaboration has recently released similar data [30]. The amount of statistics is in this case impressive and the kinematic coverage is in general wider than the HERMES one. However, at the moment these data are available only for deuteron targets and for unidentified final charged hadrons. Therefore, we decided not to use these data, although they will certainly play an essential role in the near future.

Dealing with SIDIS, we need to consider also fragmentation functions and their transverse-momentum dependence. Also in this case, it is possible that different quark flavors fragment into different hadrons with characteristic transverse-momentum distributions [224, 230]. This is another fundamental question that has never been addressed at the phenomenological level.

Since our work represents one of the first explorations on this topic, we adopt a simplified framework, based on the generalized QPM picture. We neglect any modification that can be induced by QCD evolution, both in the collinear PDFs and FFs as well as in the TMD ones (see Chap. 3 and Tab. 3.1). This approximation is justified by the limited range in Q^2 of the experimental data: no difficulty arises in describing them with this simplified framework. Improvements based on perturbation theory, though, will be welcome for future analyses. All the assumptions, the notation, and the general theoretical framework are outlined in Sec. 5.2. In Sec. 5.3, we describe the fitting procedure. In Sec. 5.4, we present the results, and in Sec. 5.5 conclusions and outlooks are drawn.

5.2 Theoretical framework

In one-particle semi-inclusive DIS, a lepton ℓ with momentum l scatters to a final state with momentum l' off a hadron target N with mass M and momentum P, producing (at least) one hadron h in the final state with mass M_h and momentum P_h:

$$\ell(l) + N(P) \to \ell(l') + h(P_h) + X\,. \tag{5.2.1}$$

The space-like momentum transfer is $q = l - l'$, with $Q^2 = -q^2$. We introduce the usual invariants

$$x = \frac{Q^2}{2\,P\cdot q}, \qquad y = \frac{P\cdot q}{P\cdot l}, \qquad z = \frac{P\cdot P_h}{P\cdot q}, \qquad \gamma = \frac{2Mx}{Q}. \tag{5.2.2}$$

The available data refer to hadron multiplicities in SIDIS, namely to the differential number of hadrons produced per corresponding inclusive DIS event. In terms of cross sections, we define the multiplicities as

$$m_N^h(x, z, \boldsymbol{P}_{hT}^2, Q^2) = \frac{d\sigma_N^h/(dxdzd\boldsymbol{P}_{hT}^2 dQ^2)}{d\sigma_{\rm DIS}/(dxdQ^2)}\,, \tag{5.2.3}$$

where $d\sigma_N^h$ is the differential cross section for the semi-inclusive DIS process and $d\sigma_{\rm DIS}$ is the corresponding inclusive one, and where $\boldsymbol{P}_{hT}$ is the component of $\boldsymbol{P}_h$ transverse to $\boldsymbol{q}$. In the single-photon-exchange approximation, the multiplicities can be written as ratios of structure functions [15]:

$$m_N^h(x, z, \boldsymbol{P}_{hT}^2, Q^2) = \frac{\pi\, F_{UU,T}(x, z, \boldsymbol{P}_{hT}^2, Q^2) + \pi\,\varepsilon F_{UU,L}(x, z, \boldsymbol{P}_{hT}^2, Q^2)}{F_T(x, Q^2) + \varepsilon F_L(x, Q^2)}\,, \tag{5.2.4}$$

where

$$\varepsilon = \frac{1 - y - \frac{1}{4}\gamma^2 y^2}{1 - y + \frac{1}{2}y^2 + \frac{1}{4}\gamma^2 y^2}\,. \tag{5.2.5}$$

We recall that the notation $F_{XY,Z}$ indicates the response of the hadron target with polarization Y to a lepton beam with polarization X and for the virtual photon exchanged in the polarization state Z. Therefore, the numerator of Eq. (5.2.4) involves SIDIS processes with only unpolarized beam and target. We remark that the above expressions assume a complete integration over the azimuthal angle of the detected hadron. Acceptance effects may modify these formulae, due to the presence of azimuthal modulations in the cross section, though for the data used here such effects were included in the systematic uncertainties.

We consider the limits $M^2/Q^2 \ll 1$ and $\boldsymbol{P}_{hT}^2/Q^2 \ll 1$. Within them, the longitudinal structure function $F_{UU,L}$ in the numerator of (5.2.4) can be neglected [231]. In the denominator, the standard inclusive longitudinal structure function F_L is non negligible and contains contributions of order α_S. However, in our analysis we assume a parton-model picture and we neglect such contributions; hence, consistently, we neglect the contribution of F_L in the denominator of (5.2.4). It may also be noted that in the transverse-momentum analysis of the data, F_L induces a change in normalization that depends on x, but is independent of z and $\boldsymbol{P}_{hT}^2$, the kinematic variables most relevant in the fitting procedure. Hence, we do not expect

large effects on the resulting parameters.

To express the structure functions in terms of TMD PDFs and FFs, we rely on the factorized formula for SIDIS at low transverse momenta [19, 20, 22, 96, 105, 122, 183, 232, 233]:

$$\begin{aligned} F_{UU,T}(x,z,\boldsymbol{P}_{hT}^2,Q^2) &= \sum_a \mathcal{H}^a_{UU,T}(Q^2;\mu^2) \\ &\times \int d\boldsymbol{k}_\perp\, d\boldsymbol{P}_\perp\, f_1^a\big(x,\boldsymbol{k}_\perp^2;\mu^2,\zeta^2\big)\, D_1^{a\to h}\big(z,\boldsymbol{P}_\perp^2;\mu^2,\zeta^2\big) \\ &\times \delta\big(z\boldsymbol{k}_\perp - \boldsymbol{P}_{hT} + \boldsymbol{P}_\perp\big) + Y_{UU,T}\big(Q^2,\boldsymbol{P}_{hT}^2\big) + \mathcal{O}\big(M^2/Q^2\big)\,. \end{aligned} \tag{5.2.6}$$

Here, $\mathcal{H}_{UU,T}$ is the hard scattering part; $f_1^a(x,\boldsymbol{k}_\perp^2;\mu^2,\zeta^2)$ is the TMD PDF for an unpolarized parton of flavor a in an unpolarized proton, carrying longitudinal momentum fraction x and transverse momentum $\boldsymbol{k}_\perp$ at the factorization scale μ and rapidity scale ζ (see Chap. 3) which in the following we both choose to be equal to Q^2. $D_1^{a\to h}(z,\boldsymbol{P}_\perp^2;\mu^2,\zeta^2)$ is the TMD FF for an unpolarized parton of flavor a fragmenting into an unpolarized hadron h carrying longitudinal momentum fraction z and transverse momentum $\boldsymbol{P}_\perp$; the term $Y_{UU,T}$ is introduced to ensure a matching to the perturbative calculations at high transverse momentum. The expression for $F_{UU,T}$ is known up to at least $\mathcal{O}(\alpha_S^2)$, including the resummation of at least next-to-next-to-leading logarithms of the type $\log(P_{hT}^2/Q^2)$. However, we are going to use here only the lowest-order expression (QPM), which should still provide a good description at low $\boldsymbol{P}_{hT}^2$ and in a limited range of Q^2. Eventually, (5.2.6) simplifies to (see, e.g., [15, 180, 234])

$$F_{UU,T}(x,z,\boldsymbol{P}_{hT}^2,Q^2) = \sum_a e_a^2\, \big[f_1^a \otimes D_1^{a\to h}\big](x,z,\boldsymbol{P}_{hT}^2,Q^2)\,, \tag{5.2.7}$$

where the convolution upon transverse momenta is defined as

$$\big[f\otimes D\big](x,z,\boldsymbol{P}_{hT}^2,Q^2) \doteq x\int d\boldsymbol{k}_\perp\, d\boldsymbol{P}_\perp\, \delta\big(z\boldsymbol{k}_\perp+\boldsymbol{P}_\perp-\boldsymbol{P}_{hT}\big)\, f(x,\boldsymbol{k}_\perp^2;Q^2)\, D(z,\boldsymbol{P}_\perp^2;Q^2)\,. \tag{5.2.8}$$

In Fig. 5.1, we describe the notation for the transverse momenta used in this Chapter, in agreement with the one suggested in [17], which is also reproduced below for convenience:

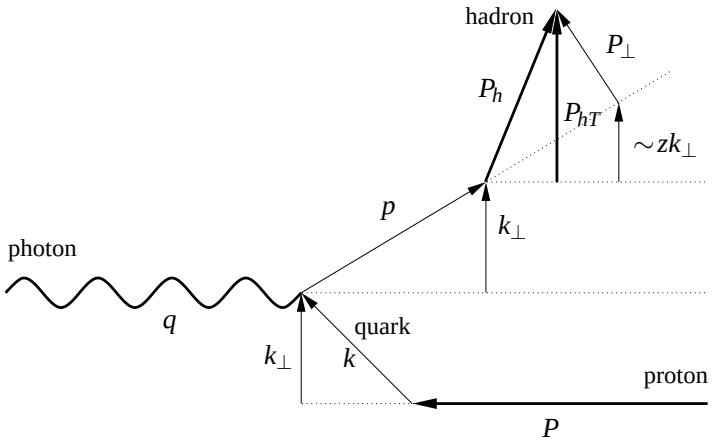

Figure 5.1. Diagram describing the relevant momenta involved in a SIDIS event (see also [224, 235]): a virtual photon (defining the reference axis) strikes a parton inside a proton. The parton has a transverse momentum $\boldsymbol{k}_\perp$ (not measured). The struck parton fragments into a hadron, which acquires a further transverse momentum $\boldsymbol{P}_\perp$ (not measured). The total measured transverse-momentum of the final hadron is $\boldsymbol{P}_{hT}$. When Q^2 is very large, the longitudinal components are all much larger than the transverse components. In this regime, $\boldsymbol{P}_{hT} \approx z\boldsymbol{k}_\perp + \boldsymbol{P}_\perp$.

Momentum	Physical description
k	4-momentum of parton in distribution function
p	4-momentum of fragmenting parton
$\boldsymbol{k}_\perp$	transverse momentum of parton in distribution function
$\boldsymbol{P}_\perp$	transverse momentum of final hadron w.r.t. fragmenting parton
$\boldsymbol{P}_{hT}$	transverse momentum of final hadron w.r.t. virtual photon

5.2.1 Flavor-dependent Gaussian ansatz

The Gaussian ansatz consists in assuming the following functional form for the transverse-momentum dependence of both the TMD PDF f_1^a and the TMD FF $D_1^{a\to h}$ in (5.2.7):

$$f_1^a(x, \boldsymbol{k}_\perp^2; Q^2) = \frac{f_1^a(x; Q^2)}{\pi\langle \boldsymbol{k}_{\perp,a}^2 \rangle}\, e^{-\boldsymbol{k}_\perp^2/\langle \boldsymbol{k}_{\perp,a}^2 \rangle}\,, \tag{5.2.9}$$

$$D_1^{a\to h}(z, \boldsymbol{P}_\perp^2; Q^2) = \frac{D_1^{a\to h}(z; Q^2)}{\pi\langle \boldsymbol{P}_{\perp,a\to h}^2 \rangle}\, e^{-\boldsymbol{P}_\perp^2/\langle \boldsymbol{P}_{\perp,a\to h}^2 \rangle}\,. \tag{5.2.10}$$

Due to its simplicity, this ansatz has been widely used in phenomenological studies but with constant widths $\langle \boldsymbol{k}_\perp^2 \rangle$ and $\langle \boldsymbol{P}_\perp^2 \rangle$. Here, for the first time, we introduce an explicit dependence on flavor a for both average transverse momenta $\langle \boldsymbol{k}_{\perp,a}^2 \rangle$ and $\langle \boldsymbol{P}_{\perp,a\to h}^2 \rangle$. In principle, there are no reasons to prefer the Gaussian ansatz over other functional forms, and indeed more flexible forms should be investigated in the future. Model calculations typically lead to a non-Gaussian behavior [104, 221, 226–228, 236]. The ansatz is also not compatible with the proper QCD evolution of TMD PDFs: it could be at most applicable at one specific starting scale, but would soon be spoiled by QCD corrections. In our analysis, we completely neglect Q^2 evolution, even in the collinear part of the functions, which we evaluate at $Q^2 = 2.4$ GeV^2. From now on, we drop the Q^2 dependence of the involved functions.

The convolution on transverse momenta in (5.2.8) can be solved analytically:

$$\begin{aligned}\left[f_1^a \otimes D_1^{a\to h}\right](x, z, \boldsymbol{P}_{hT}^2) &= f_1^a(x)\, D_1^{a\to h}(z) \left[\frac{e^{-\boldsymbol{k}_\perp^2/\langle \boldsymbol{k}_{\perp,a}^2\rangle}}{\pi\langle \boldsymbol{k}_{\perp,a}^2\rangle} \otimes \frac{e^{-\boldsymbol{P}_\perp^2/\langle \boldsymbol{P}_{\perp,a\to h}^2\rangle}}{\pi\langle \boldsymbol{P}_{\perp,a\to h}^2\rangle}\right] \\ &= x\, f_1^a(x)\, D_1^{a\to h}(z)\, \frac{1}{\pi\langle \boldsymbol{P}_{hT,a}^2\rangle}\, e^{-\boldsymbol{P}_{hT}^2/\langle \boldsymbol{P}_{hT,a}^2\rangle}\,,\end{aligned} \tag{5.2.11}$$

where the relation between the three variances is

$$\langle \boldsymbol{P}_{hT,a}^2 \rangle = z^2 \langle \boldsymbol{k}_{\perp,a}^2 \rangle + \langle \boldsymbol{P}_{\perp,a\to h}^2 \rangle\,. \tag{5.2.12}$$

In this way, for each involved flavor a, the average square value of the transverse momentum $\boldsymbol{P}_{hT}$ of the detected hadron h can be related to the average square values of the intrinsic transverse momenta $\boldsymbol{k}_\perp$ and $\boldsymbol{P}_\perp$, not directly accessible by experiments. Inserting (5.2.11) in (5.2.7), we simplify the multiplicities as

$$\begin{aligned} m_N^h(x, z, \boldsymbol{P}_{hT}^2) = &\frac{\pi}{\sum_a e_a^2\, f_1^a(x)} \\ &\times \sum_a e_a^2\, f_1^a(x)\, D_1^{a\to h}(z)\, \frac{e^{-\boldsymbol{P}_{hT}^2/\left(z^2\langle \boldsymbol{k}_{\perp,a}^2\rangle + \langle \boldsymbol{P}_{\perp,a\to h}^2\rangle\right)}}{\pi\left(z^2\langle \boldsymbol{k}_{\perp,a}^2\rangle + \langle \boldsymbol{P}_{\perp,a\to h}^2\rangle\right)}\,. \end{aligned} \tag{5.2.13}$$

If the distribution functions describe a parton a in a proton target, obviously the above expression is valid for $N = p$, i.e., for a proton target. We can deduce the corresponding result for a neutron target by assuming isospin symmetry. For a deuteron target, we can assume an incoherent sum of proton and neutron contributions. Under these assumptions the necessary label for the parent hadron on PDFs is omitted and PDFs refer to the ones of the proton. We remark also that each quark flavor is described by a single Gaussian with a specific width: the multiplicity is then a sum of Gaussians and thus no longer a simple Gaussian. The

above expression can be used with minor modifications also if we assume that the distribution and fragmentation functions for some flavor are themselves sums of Gaussians. We will in fact adopt such an assumption for the up and down quarks, where we distinguish a valence and a sea contribution, each one having a different Gaussian width. For example, the up contribution to the multiplicities is

$$\begin{aligned}\big[f_1^u \otimes D_1^{u\to h}\big](x,z,\boldsymbol{P}_{hT}^2) &= \big[(f_1^{u_v}+f_1^{\bar u})\otimes D_1^{u\to h}\big](x,z,\boldsymbol{P}_{hT}^2) = \\ &= x\, f_1^{u_v}(x)\, D_1^{u\to h}(z)\, \frac{e^{-\boldsymbol{P}_{hT}^2/\left(z^2\langle \boldsymbol{k}^2_{\perp,u_v}\rangle+\langle \boldsymbol{P}^2_{\perp,u\to h}\rangle\right)}}{\pi\left(z^2\langle \boldsymbol{k}^2_{\perp,u_v}\rangle+\langle \boldsymbol{P}^2_{\perp,u\to h}\rangle\right)} \\ &+ x\, f_1^{\bar u}(x)\, D_1^{u\to h}(z)\, \frac{e^{-\boldsymbol{P}_{hT}^2/\left(z^2\langle \boldsymbol{k}^2_{\perp,\bar u}\rangle+\langle \boldsymbol{P}^2_{\perp,u\to h}\rangle\right)}}{\pi\left(z^2\langle \boldsymbol{k}^2_{\perp,\bar u}\rangle+\langle \boldsymbol{P}^2_{\perp,u\to h}\rangle\right)}\,,\end{aligned} \tag{5.2.14}$$

where $f_1^{u_v} = f_1^u - f_1^{\bar u}$, and similarly for the down quark.

Previous data obtained in unpolarized Drell-Yan (DY) and SIDIS processes were compatible with calculations based on a Gaussian ansatz for unpolarized TMD PDFs and TMD FFs with flavor-independent constant widths. In this case, (5.2.13) would display a simple Gaussian behavior in $\boldsymbol{P}_{hT}$ with the same width in every target-hadron combination. However, the HERMES multiplicities display significant differences between proton and deuteron targets, and between pion and kaon final-state hadrons. Hence, they strongly motivate our choice in (5.2.10) for a flavor-dependent Gaussian ansatz.

5.2.2 Assumptions concerning average transverse momenta

As mentioned in the previous section, we introduce different widths for the Gaussian forms of the valence and sea components of up and down TMD PDFs. However, we assume that the Gaussian widths of all sea quarks ($\bar u$, $\bar d$, s and $\bar s$) are the same (i.e., they have the same average square transverse momenta). State-of-the-art parametrizations of collinear PDFs have a more complex structure and introduce differences between sea quarks of different flavors; we leave this flexibility to future studies.

We include the possibility that the average square transverse momentum depends on the longitudinal fractional momentum x. This connection can certainly be useful in fitting the data, but above all it is dictated by theoretical considerations, in particular by Lorentz invariance. Many models predict such a connection (see, e.g., [104, 220–228]), and similarly do parametrizations of light-front wave functions (see, e.g., [237–239]).

We choose the following functional form for the average square transverse mo-

mentum of flavor a:

$$\langle \boldsymbol{k}^2_{\perp,a} \rangle(x) = \langle \hat{\boldsymbol{k}}^2_{\perp,a} \rangle \, \frac{(1-x)^\alpha x^\sigma}{(1-\hat{x})^\alpha \hat{x}^\sigma} \,, \tag{5.2.15}$$

$$\text{where } \langle \hat{\boldsymbol{k}}^2_{\perp,a} \rangle \equiv \langle \boldsymbol{k}^2_{\perp,a} \rangle(\hat{x}), \text{ and } \hat{x} = 0.1. \tag{5.2.16}$$

$\langle \hat{\boldsymbol{k}}^2_{\perp,a} \rangle$, α, σ, are free parameters. For sake of simplicity, we keep the same exponents α and σ for all flavors. According to the above assumptions, we have three more parameters: $\langle \hat{\boldsymbol{k}}^2_{\perp,a} \rangle$ for $a = u_v$, d_v, sea. In total, we use five different parameters to describe all TMD PDFs. Since the present data have a limited coverage in x, we found no need of more sophisticated choices.

As for TMD FFs, fragmentation processes in which the fragmenting parton is in the valence content of the detected hadron are usually defined *favored*. Otherwise the process is classified as *unfavored*. The biggest difference between the two classes is the number of $q\bar{q}$ pairs excited from the vacuum in order to produce the detected hadron: favored processes involve the creation of at most one $q\bar{q}$ pair. If the final hadron is a kaon, we further distinguish a favored process initiated by a strange quark/antiquark from a favored process initiated by an up quark/antiquark.

For simplicity, we assume charge conjugation and isospin symmetries. The latter is often imposed also in the parametrization of collinear FFs [240], but not always [241]. In practice, we consider four different Gaussian shapes:

$$\langle \boldsymbol{P}^2_{\perp,u\to\pi^+} \rangle = \langle \boldsymbol{P}^2_{\perp,\bar{d}\to\pi^+} \rangle = \langle \boldsymbol{P}^2_{\perp,\bar{u}\to\pi^-} \rangle = \langle \boldsymbol{P}^2_{\perp,d\to\pi^-} \rangle \equiv \langle \boldsymbol{P}^2_{\perp,\text{fav}} \rangle \,, \tag{5.2.17}$$

$$\langle \boldsymbol{P}^2_{\perp,u\to K^+} \rangle = \langle \boldsymbol{P}^2_{\perp,\bar{u}\to K^-} \rangle \equiv \langle \boldsymbol{P}^2_{\perp,uK} \rangle \,, \tag{5.2.18}$$

$$\langle \boldsymbol{P}^2_{\perp,\bar{s}\to K^+} \rangle = \langle \boldsymbol{P}^2_{\perp,s\to K^-} \rangle \equiv \langle \boldsymbol{P}^2_{\perp,sK} \rangle \,, \tag{5.2.19}$$

$$\langle \boldsymbol{P}^2_{\perp,\text{all others}} \rangle \equiv \langle \boldsymbol{P}^2_{\perp,\text{unf}} \rangle \,. \tag{5.2.20}$$

The last assumption is made mainly to keep the number of parameters under control, though it could be argued that unfavored fragmentation into kaons is different from unfavored fragmentation into pions.

As for TMD PDFs, also for TMD FFs we introduce a dependence of the average square transverse momentum on the longitudinal momentum fraction z, as done in several models or phenomenological extractions (see, e.g., [180, 224, 230, 242–244]). We choose the functional form

$$\langle \boldsymbol{P}^2_{\perp,a\to h} \rangle(z) = \langle \hat{\boldsymbol{P}}^2_{\perp,a\to h} \rangle \frac{(z^\beta + \delta)\ (1-z)^\gamma}{(\hat{z}^\beta + \delta)\ (1-\hat{z})^\gamma} \tag{5.2.21}$$

$$\text{where } \langle \hat{\boldsymbol{P}}^2_{\perp,a\to h} \rangle \equiv \langle \boldsymbol{P}^2_{\perp,a\to h} \rangle(\hat{z}), \text{ and } \hat{z} = 0.5. \tag{5.2.22}$$

The free parameters β, γ, and δ are equal for all kinds of fragmentation functions.

In conclusion, we use seven different parameters to describe all the TMD FFs.

5.3 Analysis procedure

5.3.1 Data selection

The HERMES collaboration collected a total of 2688 data points (336 points for each of the 8 combination of target and final-state hadrons), with the average values of (x, Q^2) ranging from about $(0.04, 1.25\ \text{GeV}^2)$ to about $(0.4, 9.2\ \text{GeV}^2)$, $0.1 \leq z \leq 0.9$, and $0.1\ \text{GeV} \leq |\boldsymbol{P}_{hT}| \leq 1\ \text{GeV}$. The collaboration presented two distinct data sets, including or neglecting vector meson contributions. Here, we use the data set where the vector meson contributions have been subtracted. In all cases, we sum in quadrature statistical and systematic errors and we ignore correlations. We always use the average values of the kinematic variables in each bin.

Our analysis relies on the assumption that the transverse-momentum-integrated multiplicities, $m_N^h(x, z, Q^2)$, are well described by currently available parametrizations of collinear PDFs and FFs. However, this is not always true. In order to identify the range of applicability of the collinear results, we compared the multiplicities as functions of x and z with the leading-order (LO) theoretical predictions obtained using the MSTW08LO PDF set [218] and the DSS LO FF set [241]. In the comparison, we neglected the uncertainties affecting the PDFs but we included the ones affecting the FFs, obtaining the latter from the plots in [245]. They are of the order of 5-10% for light quarks fragmenting into pions, of 10-15% for favored kaon FFs, of 50% for all the other cases, and they are larger at higher z.

In Tab. 5.1, we quote the χ^2 per degree of freedom (χ^2/d.o.f.) obtained in our comparison. Our results are different from the ones quoted in Tabs. IV and VIII of [241] for a few reasons: i) we used the final HERMES data, in particular the set with x and z binning; ii) we included also the lowest z bin ($z < 0.2$); iii) we did not include any overall normalization constant; iv) we included the theoretical errors on the extracted fragmentation functions. The comparison shows that in general the theoretical predictions do not describe the HERMES data very well. The agreement is particularly bad for π^- and K^-. However, this is not surprising because: i) the MSTW set of PDFs does not take into account semi-inclusive DIS data, ii) as mentioned above, the DSS set of FFs [241] was deduced using only a preliminary version of the HERMES multiplicities, iii) the HERMES data give very large contributions to the χ^2 of the global DSS analysis. Nevertheless, in our analysis we decided to restrict the ranges to $Q^2 > 1.4\ \text{GeV}^2$ and $0.1 < z < 0.8$, i.e., excluding the first bin in Q^2 (equivalent also to the lowest x) and the last bin in z. Inclusion of decays from exclusive vector-mesons markedly degrades the χ^2 of the pion channels and increases the global χ^2 (cf. the first and second columns of

χ^2/d.o.f.				
	$Q^2 > 1.4$ GeV^2	$Q^2 > 1.4$ GeV^2 (no VM subtr.)	$Q^2 > 1.4$ GeV^2 (with evolution)	$Q^2 > 1.6$ GeV^2
global	2.86	3.90	3.55	2.29
$p \to K^-$	2.25	2.27	1.38	2.38
$p \to \pi^-$	3.39	6.58	5.03	2.70
$p \to \pi^+$	1.87	2.45	2.74	1.16
$p \to K^+$	0.89	0.85	1.13	0.59
$D \to K^-$	4.26	4.22	2.81	4.45
$D \to \pi^-$	5.05	8.66	7.96	3.42
$D \to \pi^+$	3.33	4.61	5.19	2.29
$D \to K^+$	1.80	1.57	2.17	1.31

Table 5.1. Values of χ^2/d.o.f. obtained from the comparison of the HERMES multiplicities $m_N^h(x, z, Q^2)$ with the theoretical prediction using the MSTW08LO collinear PDFs [218] and the DSS LO collinear FFs [241]. In all cases, the range $0.1 \leq z \leq 0.8$ was included.

Tab. 5.1). Hence we will present results for only the fits to vector-meson subtracted multiplicities. We checked that our basic conclusions do not change when using data without vector-meson subtraction.

We also noted that a description of data of comparable quality could be achieved by turning off the Q^2 dependence of both collinear PDFs and FFs, and by computing them at the fixed value of $Q^2 = 2.4$ GeV^2 (cf. the first and third columns of Tab. 5.1). Therefore, we decided to systematically neglect any contribution of QCD evolution and to compute all theoretical quantities at the average value of $Q^2 = 2.4$ GeV^2.

When considering also the transverse-momentum dependence, the TMD formalism is valid only when $\boldsymbol{P}_{hT}^2 \ll Q^2$. In order not to exclude too many data points, we apply the loose requirement $\boldsymbol{P}_{hT}^2 < Q^2/3$. This leads to the exclusion of at most two bins at high $\boldsymbol{P}_{hT}^2$ and low Q^2.

Finally, we exclude also the data points with the lowest $|\boldsymbol{P}_{hT}|$ ($|\boldsymbol{P}_{hT}| < 0.15$ GeV). A priori, there is no reason to exclude them, but in our attempts we found them particularly difficult to fit, mainly because they often do not follow the trend of the other data points and at the same time they have small errors. In order to be able to fit them, we need to increase the flexibility of our functional forms. We leave this task to future studies.

In summary, we use a total of 1538 data points, approximately 190 for each of the 8 combinations of target and final-state hadrons, which correspond to about 60% of the total 2688 points measured by the HERMES collaboration.

5.3.2 The replica method

The fit and the error analysis were carried out using a similar Monte Carlo approach as in [246], and taking inspiration from the work of the NNPDF collaboration (see, e.g., [247–249]). The approach consists in creating $\mathcal{M}$ replicas of the data points. In each replica (denoted by the index r), each data point i is shifted by a Gaussian noise with the same variance as the measurement. Each replica, therefore, represents a possible outcome of an independent experimental measurement, which we denote by $m^h_{N,r}(x, z, \boldsymbol{P}^2_{hT}, Q^2)$. The number of replicas is chosen so that the mean and standard deviation of the set of replicas accurately reproduces the original data points. In our case, we have found that 200 replicas are more than sufficient.

The standard minimization procedure is applied to each replica separately, by minimizing the following error function [1]

$$E^2_r(\{p\}) = \sum_i \frac{\left[m^h_{N,r}(x_i, z_i, \boldsymbol{P}^2_{hTi}, Q^2_i) - m^h_{N,\text{theo}}(x_i, z_i, \boldsymbol{P}^2_{hTi}; \{p\})\right]^2}{\left[\Delta m^{h\,2}_{N,\text{stat}} + \Delta m^{h\,2}_{N,\text{sys}}\right](x_i, z_i, \boldsymbol{P}^2_{hTi}, Q^2_i) + \left[\Delta m^h_{N,\text{theo}}(x_i, z_i, \boldsymbol{P}^2_{hTi})\right]^2}. \tag{5.3.1}$$

The sum runs over the i experimental points, including all species of targets N and final-state hadrons h. The theoretical multiplicities $m^h_{N,\text{theo}}$ and their error $\Delta m^h_{N,\text{theo}}$ do not depend on Q^2, as explained in the previous section. They are computed at the fixed value $Q^2 = 2.4$ GeV^2 using the formula in (5.2.13). However, in each z bin for each replica the value of $D_1^{a\to h}$ is independently modified with a Gaussian noise with standard deviation equal to the theoretical error $\Delta D_1^{a\to h}$. The latter is estimated from the plots in [245] and it represents the main source of uncertainty in $\Delta m^h_{N,\text{theo}}$. Finally, the symbol $\{p\}$ denotes the vector of fitting parameters.

The minimization was carried out using the MINUIT code. The final outcome is a set of $\mathcal{M}$ different vectors of best-fit parameters, $\{p_{0r}\}$, $r = 1, \dots \mathcal{M}$, with which we can calculate any observable, its mean, and its standard deviation. The distribution of these values needs not to be necessarily Gaussian. In this case, the 1σ confidence interval is different from the 68% interval. The 68% confidence interval can simply be computed for each experimental point by rejecting the largest and the lowest 16% of the $\mathcal{M}$ values.

Although the minimization is performed on the function defined in (5.3.1), the agreement of the $\mathcal{M}$ replicas with the original data is better expressed in terms of a χ^2 function defined as in (5.3.1) but with the replacement $m^h_{N,r} \to m^h_N$, i.e., with respect to the original data set. If the model is able to give a good description of the data, the distribution of the $\mathcal{M}$ values of χ^2/d.o.f. should be peaked around 1.

[1] Note that the error for each replica is taken to be equal to the error on the original data points. This is consistent with the fact that the variance of the $\mathcal{M}$ replicas should reproduce the variance of the original data points.

In practice, the rigidity of our functional form leads to higher χ^2 values.

5.4 Results

In this section, we describe the results obtained by fitting the HERMES multiplicities with the theoretical formula of (5.2.13) and using the Monte Carlo method outlined in the previous section. We performed different kinds of fits with different assumptions. The first one, conventionally named "default fit", includes all the 1538 data points selected according to the criteria described in Sec. 5.3.1. In the second one, we excluded data also for the second lowest Q^2 bin, i.e., by selecting $Q^2 > 1.6$ GeV^2. This cut reduces the number of data points to 1274. The third scenario corresponds to neglecting kaons in the final state and taking only multiplicities for pions. The last scenario is a fit of the default selection using a flavor-independent (but kinematic dependent) Gaussian ansatz. Before discussing each different scenario, here below we list their common features.

As repeatedly mentioned above, in our analysis we neglected completely the effect of Q^2 evolution, even in the collinear PDFs and FFs, and we evaluated all observables at the fixed value $Q^2 = 2.4$ GeV^2.

As for the dependence of the TMD average transverse momentum on x, we noticed that the fit is weakly sensitive to the exponents in (5.2.15). We tried fits with $\alpha = \sigma = 0$ and obtained good results. However, in order to stress the fact that present data do not constrain these parameters very well, we decided to assign random values extracted from uniform distributions to both the exponents: we consider α as a random number between 0 and 2 and σ as a random number between -0.3 and 0.1. Better determinations of these parameters require an extended range in x, together with uncorrelated x and Q^2 binnings. The dependence of the TMD FF average transverse momentum on z is governed by (5.2.21); in this case, we decided to keep all three parameters free. The $\langle \hat{\boldsymbol{P}}^2_{\perp,a\to h} \rangle$ parameters are free, apart from $\langle \hat{\boldsymbol{P}}^2_{\perp,sK} \rangle$, whose values are extracted from a uniform distribution between 0.125 GeV^2 and 0.25 GeV^2.

For each scenario, we performed 200 replicas of the fit. In this section, we present the 68% confidence intervals of the parameters over the replicas, computed by rejecting the largest and the lowest 16% of the replicated parameter values. We quote the values as $A \pm B$, where A is the average of the upper and lower limits of the 68% confidence interval and B is their semi-difference. It is understood that much more information is available by scrutinizing the full set of 200 values for each of them.[2] In Tab. 5.2, we list the 68% confidence intervals of the χ^2/d.o.f. for the different scenarios, including the global result and the outcome for each target-hadron combination, separately. In Tabs. 5.3 and 5.4, we list the 68% confidence

[2]The results are available via the TMD project and TMDlib or upon request.

χ^2/d.o.f.				
	Default	$Q^2 > 1.6$ GeV^2	Pions only	Flavor-indep.
global	1.63 ± 0.12	1.37 ± 0.12	2.04 ± 0.16	1.72 ± 0.11
$p \to K^-$	0.78 ± 0.15	0.77 ± 0.14	-	0.87 ± 0.16
$p \to \pi^-$	1.80 ± 0.27	1.50 ± 0.24	1.68 ± 0.24	1.83 ± 0.25
$p \to \pi^+$	2.64 ± 0.21	1.91 ± 0.30	2.70 ± 0.22	2.89 ± 0.23
$p \to K^+$	0.46 ± 0.07	0.49 ± 0.07	-	0.43 ± 0.07
$D \to K^-$	2.77 ± 0.56	2.78 ± 0.52	-	3.15 ± 0.62
$D \to \pi^-$	1.65 ± 0.20	1.28 ± 0.19	1.50 ± 0.18	1.66 ± 0.20
$D \to \pi^+$	2.16 ± 0.21	1.64 ± 0.25	2.22 ± 0.22	2.21 ± 0.22
$D \to K^+$	0.71 ± 0.15	0.58 ± 0.12	-	0.71 ± 0.15

Table 5.2. 68% confidence intervals of χ^2/d.o.f. values (global result and for every available target-hadron combination $N \to h$) for each of the considered four scenarios.

Parameters for TMD PDFs				
	Default	$Q^2 > 1.6$ GeV^2	Pions only	Flavor-indep.
$\langle \hat{\boldsymbol{k}}^2_{\perp,d_v} \rangle$ [GeV^2]	0.30 ± 0.17	0.33 ± 0.19	0.34 ± 0.12	0.30 ± 0.10
$\langle \hat{\boldsymbol{k}}^2_{\perp,u_v} \rangle$ [GeV^2]	0.36 ± 0.14	0.37 ± 0.17	0.35 ± 0.12	0.30 ± 0.10
$\langle \hat{\boldsymbol{k}}^2_{\perp,\text{sea}} \rangle$ [GeV^2]	0.41 ± 0.16	0.31 ± 0.18	0.29 ± 0.13	0.30 ± 0.10
α (random)	0.95 ± 0.72	0.93 ± 0.70	0.95 ± 0.68	1.03 ± 0.64
σ (random)	-0.10 ± 0.13	-0.10 ± 0.13	-0.09 ± 0.14	-0.12 ± 0.12

Table 5.3. 68% confidence intervals of best-fit parameters for TMD PDFs in the different scenarios.

intervals for the five fitting parameters for TMD PDFs and for the seven fitting parameters for TMD FFs[3], respectively.

In all fits, we observe a strong anticorrelation between the distribution and fragmentation transverse momenta. This is not surprising, since the width of the observed $\boldsymbol{P}_{hT}$ distribution is given by (5.2.12). To better pin down the values of $\langle \boldsymbol{k}^2_{\perp,a} \rangle$ and $\langle \boldsymbol{P}^2_{\perp,a\to h} \rangle$ separately for the various flavors a, it will be essential to include also data from electron-positron annihilation and DY processes. A common feature of all scenarios is that the $\langle \hat{\boldsymbol{k}}^2_{\perp,a} \rangle$ (namely, the average squared transverse momenta of TMD PDFs at $x = 0.1$) have average values around 0.3 GeV^2, while the

[3]In Tab. 4 in [174] γ and δ have been accidentally exchanged.

Parameters for TMD FFs				
	Default	$Q^2 > 1.6$ GeV^2	Pions only	Flavor-indep.
$\langle \hat{\boldsymbol{P}}^2_{\perp,\mathrm{fav}} \rangle$ [GeV^2]	0.15 ± 0.04	0.15 ± 0.04	0.16 ± 0.03	0.18 ± 0.03
$\langle \hat{\boldsymbol{P}}^2_{\perp,\mathrm{unf}} \rangle$ [GeV^2]	0.19 ± 0.04	0.19 ± 0.05	0.19 ± 0.04	0.18 ± 0.03
$\langle \hat{\boldsymbol{P}}^2_{\perp,sK} \rangle$ [GeV^2]	0.19 ± 0.04	0.19 ± 0.04	-	0.18 ± 0.03
$\langle \hat{\boldsymbol{P}}^2_{\perp,uK} \rangle$ [GeV^2]	0.18 ± 0.05	0.18 ± 0.05	-	0.18 ± 0.03
β	1.43 ± 0.43	1.59 ± 0.45	1.55 ± 0.27	1.30 ± 0.30
γ	1.29 ± 0.95	1.41 ± 1.06	1.20 ± 0.63	0.76 ± 0.40
δ	0.17 ± 0.09	0.16 ± 0.10	0.15 ± 0.05	0.22 ± 0.06

Table 5.4. 68% confidence intervals of best-fit parameters for TMD FFs in the different scenarios.

$\langle \hat{\boldsymbol{P}}^2_{\perp,a\to h} \rangle$ (namely the average square transverse momenta of TMD FFs at $z = 0.5$) have average values around 0.18 GeV^2. Moreover, the fits prefer large values of the exponents β and γ for TMD FFs, but with large uncertainties; the parameter δ is usually small. Below, we discuss in detail the results for the four different scenarios.

5.4.1 Default fit

In this scenario, we consider all 1538 data points selected according to the criteria explained in Sec. 5.3.1. The quality of the fit is fairly good. The global χ^2/d.o.f. is 1.63 ± 0.13. In Fig. 5.2, the distribution of the χ^2/d.o.f. over the 200 replicas is shown. Many replicas have χ^2/d.o.f. > 1.5. This indicates some difficulty to reproduce the data correctly. It is not surprising if we take into account that the description of the collinear multiplicities was already difficult (see Tab. 5.1). It may actually seem contradicting that our fit is able to describe the transverse-momentum-dependent multiplicities relatively well. This is probably simply due to the fact that the multidimensional binning has many more data points but with much larger statistical errors.

In Tab. 5.2, we list the 68% confidence intervals of the χ^2/d.o.f. also for each target-hadron combination $N \to h$, separately. The worst result is for $D \to K^-$. This may be a bit surprising, also because $p \to K^-$ is described very well. However, this may be due to the fact that the collinear description of this channel is poor (see Tab. 5.1). We point out also that the systematic errors in $D \to K^-$ are significantly smaller than $p \to K^-$ [29]. The second worst agreement is for $p \to \pi^+$, which is not unexpected since statistical errors are smallest in this channel. The π^- channels are described decently, which is at odds with the poor description of their collinear multiplicities (see Tab. 5.1). We do not have a reasonable explanation for this

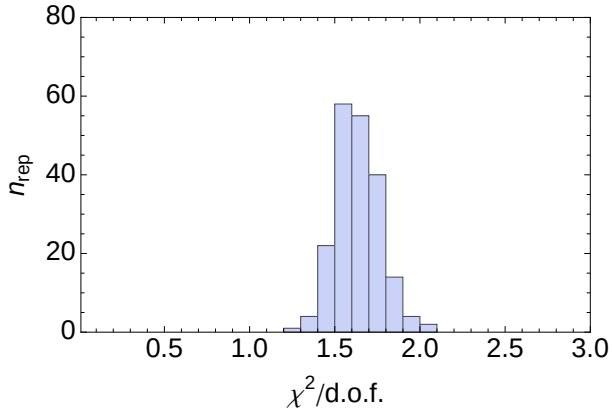

Figure 5.2. Distribution of the values of χ^2/d.o.f. for the default fit. On the vertical axis, the number of replicas with χ^2/d.o.f. inside the bin. The bin width is 0.1.

feature yet. Maybe, it could be ascribed to the cuts in $\boldsymbol{P}_{hT}$ that we implemented in our fit.

Figs. 5.3 and 5.4 illustrate the agreement between our fit and the HERMES data. For each figure, the upper panels display the results for pions (π^- on the left and π^+ on the right), the lower panels for kaons. The results show the multiplicities $m_N^h(x, z, \boldsymbol{P}_{hT}^2, Q^2)$ for $N = p$ proton and $N = D$ deuteron targets, respectively, as functions of $\boldsymbol{P}_{hT}^2$ for one selected bin $\langle x \rangle \sim 0.15$ and $\langle Q^2 \rangle \sim 2.9$ GeV^2 (out of the total five x bins we used), and for four different z bins (out of the total seven z bins we used). The lowest $\boldsymbol{P}_{hT}^2$ bin was excluded from the fit, as explained in Sec. 5.3.1. The theoretical band is obtained by rejecting the largest and lowest 16% of the replicas for each $\boldsymbol{P}_{hT}^2$ bin. The theoretical uncertainty is dominated by the error on the collinear fragmentation functions $D_1(z)$, which induces an overall normalization uncertainty in each z bin. The different values of the fit parameters in each replica are responsible for the slight differences in the slopes of the upper and lower borders of the bands.

In Tab. 5.3, the values of the fit parameters for TMD PDFs are listed. We note that the average square transverse momenta can range between 0.13 and 0.57 GeV^2 within the 68% confidence interval.

In the left panel of Fig. 5.5, the ratios $\langle \boldsymbol{k}_{\perp,d_v}^2 \rangle / \langle \boldsymbol{k}_{\perp,u_v}^2 \rangle$ vs. $\langle \boldsymbol{k}_{\perp,\text{sea}}^2 \rangle / \langle \boldsymbol{k}_{\perp,u_v}^2 \rangle$ for 200 replicas are compared. The white box represents the point at the center of each one-dimensional 68% confidence interval of the two ratios. The shaded area represents the two-dimensional 68% confidence region, it contains 68% of the points with the shortest distance from the white box. Since for each flavor the x dependence of the average square transverse momenta is the same (see (5.2.15)), these ratios are x-independent. The dashed lines correspond to the ratios being

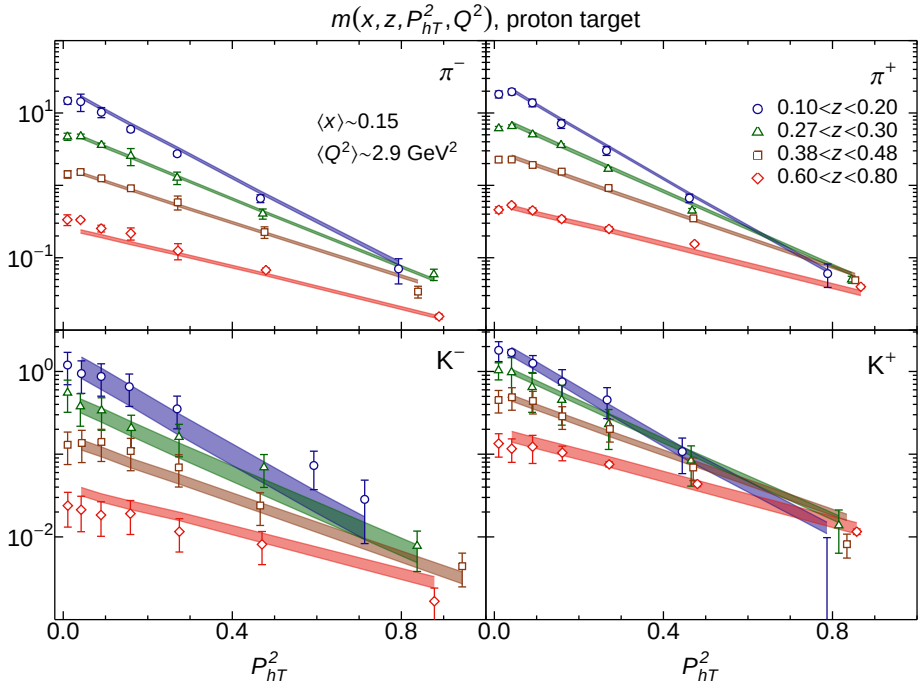

Figure 5.3. Data points: HERMES multiplicities $m_p^h(x, z, \boldsymbol{P}_{hT}^2; Q^2)$ for pions and kaons off a proton target as functions of $\boldsymbol{P}_{hT}^2$ for one selected x and Q^2 bin and few selected z bins. Shaded bands: 68% confidence intervals obtained from fitting 200 replicas of the original data points in the scenario of the default fit. The bands include also the uncertainty on the collinear fragmentation functions. The lowest $\boldsymbol{P}_{hT}^2$ bin has not been included in the fit.

unity and divide the plane into four quadrants. Most of the replicas are in the upper left quadrant, i.e., we have $\langle \boldsymbol{k}_{\perp,d_v}^2 \rangle < \langle \boldsymbol{k}_{\perp,u_v}^2 \rangle < \langle \boldsymbol{k}_{\perp,\text{sea}}^2 \rangle$. The white box shows that d_v is on average about 20% narrower than u_v, which is in turn about 10% narrower than the sea. The crossing of the dashed lines corresponds to a flavor-independent distribution of transverse momenta. This crossing point lies at the limit of the 68% confidence region. In a relevant number of replicas d_v can be more than 40% narrower than the u_v, and the sea can be more than 30% wider than u_v. From this fit, it seems possible that the sea is narrower than u_v, but unlikely that d_v is wider than u_v.

In the right panel of Fig. 5.5, we compare the ratio $\langle \boldsymbol{P}_{\perp,\text{unf}}^2 \rangle / \langle \boldsymbol{P}_{\perp,\text{fav}}^2 \rangle$ vs. $\langle \boldsymbol{P}_{\perp,uK}^2 \rangle / \langle \boldsymbol{P}_{\perp,\text{fav}}^2 \rangle$ in the same conditions as before. All points are clustered in the upper right quadrant and close to its bisectrix, i.e., we have the stable outcome that $\langle \boldsymbol{P}_{\perp,\text{fav}}^2 \rangle < \langle \boldsymbol{P}_{\perp,\text{unf}}^2 \rangle \sim \langle \boldsymbol{P}_{\perp,uK}^2 \rangle$. The width of unfavored and $u \to K^+$ fragmentations are about 20% larger than the widht of favored ones.

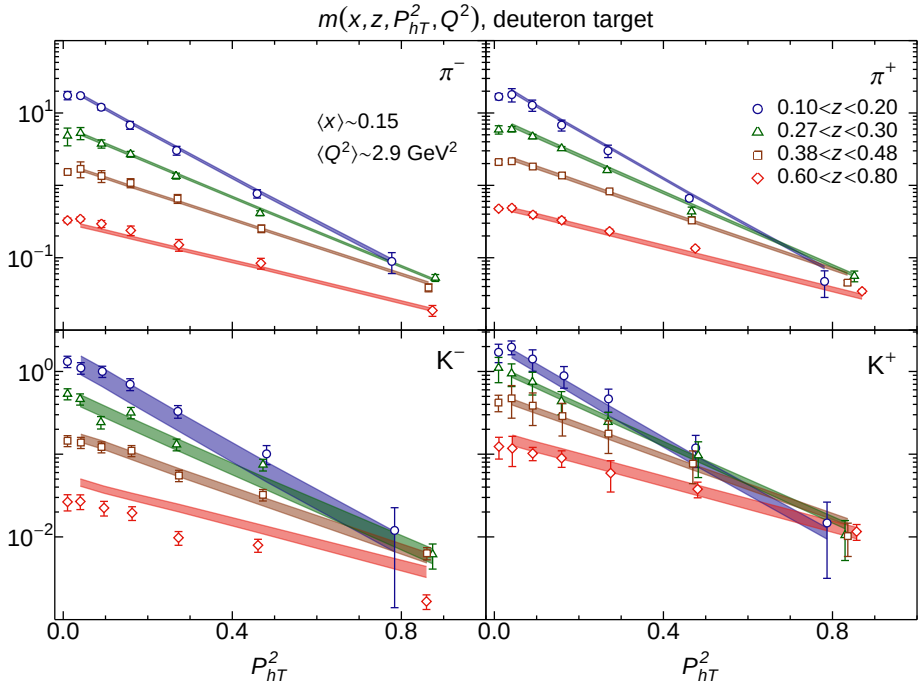

Figure 5.4. Same content and notation as in the previous figure, but for a deuteron target.

5.4.2 Fit with $Q^2 > 1.6$ GeV^2

In this scenario, we restrict the Q^2 range compared to the default fit by imposing the cut $Q^2 > 1.6$ GeV^2. The set of data is reduced to 1274 points. The mean value of the χ^2/d.o.f is smaller, since we are fitting less data. Moreover, the disregarded Q^2 bin contains high statistics. As for the default fit, the behavior of transverse momenta over the 200 replicas is summarized in Fig. 5.6. The exclusion of low-Q^2 data leads to partial differences in the features of the extracted TMD PDFs: the average width of valence quarks slightly increases, while the distribution for sea quarks becomes narrower.

In the left panel, most of the replicas are in the lower left quadrant, i.e., we have $\langle \boldsymbol{k}_{\perp,\mathrm{sea}}^2\rangle \lesssim \langle \boldsymbol{k}_{\perp,d_v}^2\rangle < \langle \boldsymbol{k}_{\perp,u_v}^2\rangle$. On average, d_v quarks are 15% narrower than u_v quarks, which are in turn more than 20% wider than sea quarks. In a relevant number of replicas d_v can be more than 40% narrower than the u_v, and the sea can be even 50% narrower than u_v. In this scenario, it is unlikely that the sea is wider than u_v, but it is possible that d_v is wider than u_v.

In the right panel, the behavior of transverse momenta in fragmentation processes is qualitatively unchanged with respect to the default fit, apart from the fact

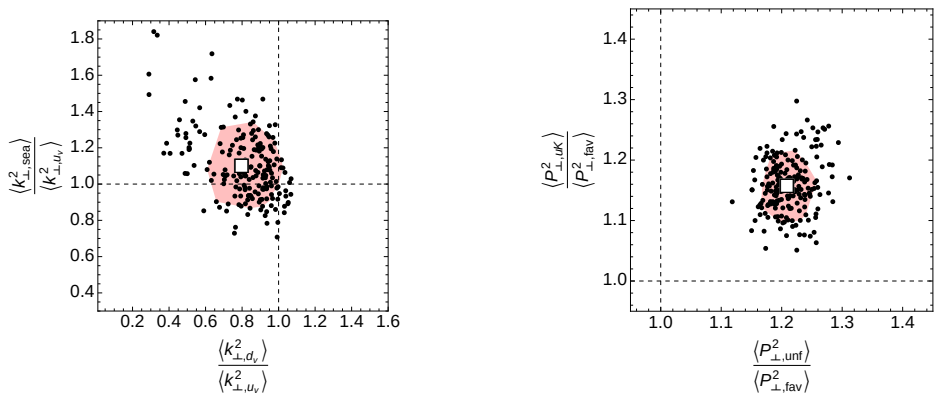

(a) (b)

Figure 5.5. (a) Distribution of the values of the ratios $\langle \boldsymbol{k}^2_{\perp,d_v}\rangle/\langle \boldsymbol{k}^2_{\perp,u_v}\rangle$ vs. $\langle \boldsymbol{k}^2_{\perp,\text{sea}}\rangle/\langle \boldsymbol{k}^2_{\perp,u_v}\rangle$ obtained from fitting 200 replicas of the original data points in the scenario of the default fit. The white squared box indicates the center of the 68% confidence interval for each ratio. The shaded area represents the two-dimensional 68% confidence region around the white box. The dashed lines correspond to the ratios being unity; their crossing point corresponds to the result with no flavor dependence. For most of the points, $\langle \boldsymbol{k}^2_{\perp,d_v}\rangle < \langle \boldsymbol{k}^2_{\perp,u_v}\rangle < \langle \boldsymbol{k}^2_{\perp,\text{sea}}\rangle$. (b) Same as previous panel, but for the distribution of the values of the ratios $\langle \boldsymbol{P}^2_{\perp,\text{unf}}\rangle/\langle \boldsymbol{P}^2_{\perp,\text{fav}}\rangle$ vs. $\langle \boldsymbol{P}^2_{\perp,uK}\rangle/\langle \boldsymbol{P}^2_{\perp,\text{fav}}\rangle$. For all points, $\langle \boldsymbol{P}^2_{\perp,\text{fav}}\rangle < \langle \boldsymbol{P}^2_{\perp,\text{unf}}\rangle \sim \langle \boldsymbol{P}^2_{\perp,uK}\rangle$.

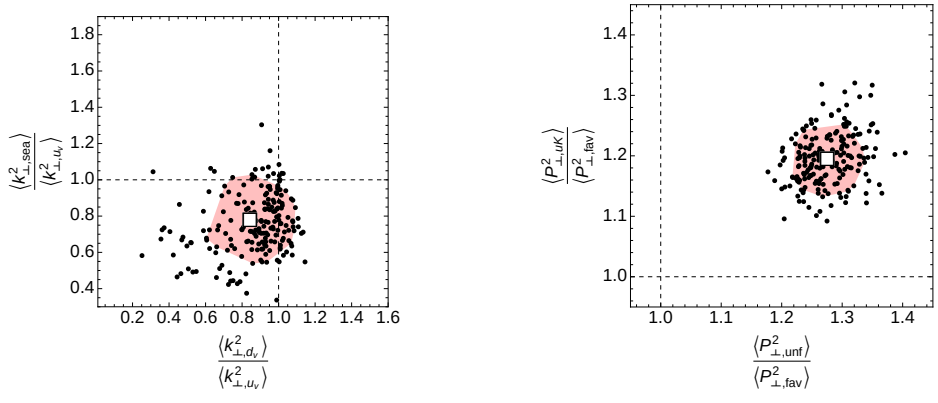

(a) (b)

Figure 5.6. Same content and notation as in the previous figure, but for the scenario with the cut $Q^2 > 1.6$.

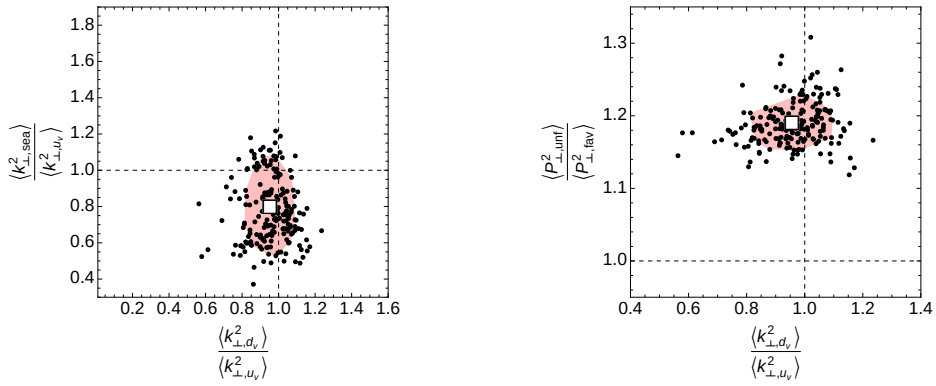

(a) (b)

Figure 5.7. (a) Same content and notation as in Fig. 5.5a) but for the scenario with only pions in the final state. For most of the points, $\langle \boldsymbol{k}^2_{\perp,\mathrm{sea}}\rangle < \langle \boldsymbol{k}^2_{\perp,d_v}\rangle \lesssim \langle \boldsymbol{k}^2_{\perp,u_v}\rangle$. (b) Distribution of the values of the ratios $\langle \boldsymbol{P}^2_{\perp,\mathrm{unf}}\rangle/\langle \boldsymbol{P}^2_{\perp,\mathrm{fav}}\rangle$ vs. $\langle \boldsymbol{k}^2_{\perp,d_v}\rangle/\langle \boldsymbol{k}^2_{\perp,u_v}\rangle$ obtained in the same conditions as in the previous case. For all points $\langle \boldsymbol{P}^2_{\perp,\mathrm{fav}}\rangle < \langle \boldsymbol{P}^2_{\perp,\mathrm{unf}}\rangle$.

that the unfavored Gaussian function becomes now more than 25% larger than the favored one.

The crossing point again indicates no flavor dependence and lies just outside the 68% confidence region for TMD PDFs and completely outside the same region for TMD FFs.

We conclude that the low-Q^2 data, being also characterized by low x, can have a significant impact on the analysis of TMD PDFs, in particular the sea components. More data at low x (but possibly at high Q^2) are necessary to better constrain the sea quarks TMD PDFs [17, 30, 250].

5.4.3 Fit with pions only

We also choose to fit data related only to pions in the final state, in order to explore the importance of the kaons data set. In this framework, we are left with two independent fragmentation processes: favored and unfavored ones. Accordingly, the number of fit parameters for TMD FFs reduces from 7 to 5 ($\langle \hat{\boldsymbol{P}}^2_{\perp,\mathrm{fav}}\rangle$, $\langle \hat{\boldsymbol{P}}^2_{\perp,\mathrm{unf}}\rangle$, β, δ, γ; see (5.2.17)-(5.2.21)).

The agreement between data and the model is the worst (see Tab. 5.1). This is due to at least two reasons. First of all, the fit of collinear multiplicities was poor in all the target-hadron combinations involving pions in the final state. Moreover, the high statistics collected for pions (mostly in the low-Q^2 region) leads to higher values of χ^2.

Fig. 5.7 shows the behavior of transverse momenta over the 200 replicas. As for TMD PDFs, in the left panel most of the replicas are in the lower part, i.e., we have $\langle \boldsymbol{k}^2_{\perp,\mathrm{sea}} \rangle < \langle \boldsymbol{k}^2_{\perp,d_v} \rangle \lesssim \langle \boldsymbol{k}^2_{\perp,u_v} \rangle$. On average, d_v quarks are equally distributed as u_v quarks, which are in turn more than 20% wider than sea quarks. In the default fit sea quarks were wider than valence ones and there was a remarkable difference between u_v and d_v, not evident in this scenario. In any case, in a relevant number of replicas d_v can be more than 15% narrower than the u_v, but also more than 10% wider than u_v. The sea can be even 50% narrower than u_v, but it is also not unlikely that the sea is wider than u_v. Once again, the crossing point for flavor independence lies at the boundary of the 68% confidence region, due to the difference between the distributions of sea quarks and valence quarks.

As in the other scenarios, TMD FFs for unfavored processes are wider than favored ones. The difference is comparable to the default fit, with unfavored functions about 20% larger than favored ones.

Similar fits have been performed in [33, 35], but using data averaged over z, which renders it particularly difficult to disentangle the distribution and fragmentation contributions. To overcome this problem, both fits included also indirect information from the azimuthal $\cos\phi_h$ dependence. The fit of [35] obtained a small value for the distribution mean square transverse momenta of up quarks, $\langle \boldsymbol{k}^2_{\perp,u} \rangle = 0.07 \pm 0.03$ GeV^2, while the down quark mean transverse momentum was compatible with zero, $\langle \boldsymbol{k}^2_{\perp,d} \rangle = -0.01 \pm 0.05$ GeV^2 (sea quarks were neglected). The previous fit [33] obtained a somewhat different behavior, with a mean transverse momentum of the up quark compatible with zero and $\langle \boldsymbol{k}^2_{\perp,d} \rangle = 0.11 \pm 0.13$ GeV^2. In both fits, the average values of the width of the TMD FFs are compatible with our results, but, contrary to our findings, a slight tendency for the favored FF to be larger than unfavored was found. In any case, we remark that the average kinematics of the experiment taken into consideration in [33, 35] are different from HERMES (see also the discussion in [167]).

Overall, we conclude that kaon data have an important impact in a flavor-dependent analysis, due to the large role played by strange quarks and antiquarks in kaon multiplicities.

5.4.4 Flavor-independent fit

In this scenario, we assume a Gaussian ansatz for unpolarized TMD PDFs and TMD FFs with flavor-independent widths, i.e., we neglect any flavor dependence in (5.2.10):

$$\left\langle \hat{\boldsymbol{k}}^2_{\perp,u_v} \right\rangle = \left\langle \hat{\boldsymbol{k}}^2_{\perp,d_v} \right\rangle = \left\langle \hat{\boldsymbol{k}}^2_{\perp,\mathrm{sea}} \right\rangle \equiv \left\langle \hat{\boldsymbol{k}}^2_{\perp} \right\rangle , \tag{5.4.1}$$

$$\left\langle \hat{\boldsymbol{P}}^2_{\perp,\mathrm{fav}} \right\rangle = \left\langle \hat{\boldsymbol{P}}^2_{\perp,\mathrm{unf}} \right\rangle = \left\langle \hat{\boldsymbol{P}}^2_{\perp,uK} \right\rangle = \left\langle \hat{\boldsymbol{P}}^2_{\perp,sK} \right\rangle \equiv \left\langle \hat{\boldsymbol{P}}^2_{\perp} \right\rangle . \tag{5.4.2}$$

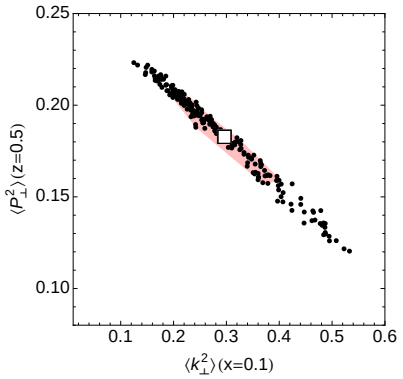

Figure 5.8. Distribution of the values of $\langle \boldsymbol{k}_\perp^2 \rangle$ (at $x = 0.1$) and $\langle \boldsymbol{P}_\perp^2 \rangle$ (at $z = 0.5$) obtained from fitting 200 replicas of the original data points in the scenario of the flavor-independent fit. The white squared box indicates the center of the one-dimensional 68% confidence interval for each parameter. The shaded area represents the two-dimensional 68% confidence region around the white box. The transverse momenta are manifestly anti-correlated.

Accordingly, the number of fit parameters reduces to 3 for TMD PDFs ($\langle \hat{\boldsymbol{k}}_\perp^2 \rangle$, α, σ) and 4 for TMD FFs ($\langle \hat{\boldsymbol{P}}_\perp^2 \rangle$, β, δ, γ). Their values are summarized in Tab. 5.3 and 5.4. The expression (5.2.13) for the multiplicities considerably simplifies and the $\boldsymbol{P}_{hT}$ width is the same for every target-hadron combination:

$$\left\langle \boldsymbol{P}_{hT}^2 \right\rangle = z^2 \left\langle \boldsymbol{k}_\perp^2 \right\rangle + \left\langle \boldsymbol{P}_\perp^2 \right\rangle . \tag{5.4.3}$$

The agreement between data and the flavor-independent model is poorer than in the (flavor-dependent) default fit: the central value of the χ^2/d.o.f. is 1.73 (see Tab. 5.2). This is not surprising, since we are fitting with the same function data for all the available target-hadron combinations, which display sensibly different behaviors. However, these results do not rule out the flavor-independent ansatz.

Fig. 5.8 clearly shows the anti-correlation between $\langle \hat{\boldsymbol{k}}_\perp^2 \rangle$ and $\langle \hat{\boldsymbol{P}}_\perp^2 \rangle$ induced by Eq. (5.4.3).

Similar fits have been performed in the past for SIDIS and DY processes [167, 180], also including the effect of transverse momentum resummation. The values of our mean square transverse momenta at $x = 0.1$ and $z = 0.5$ are consistent with the values obtained without considering x and z dependence in [167] ($\langle \boldsymbol{k}_\perp^2 \rangle = 0.38 \pm 0.06$ GeV^2 and $\langle \boldsymbol{P}_\perp^2 \rangle = 0.16 \pm 0.01$ GeV^2) and in [178] ($\langle \boldsymbol{k}_\perp^2 \rangle = 0.25$ GeV^2 and $\langle \boldsymbol{P}_\perp^2 \rangle = 0.20$ GeV^2) using a different approach based on the Cahn effect [251]. In the HERMES Monte Carlo generator GMC$_{\text{TRANS}}$, the following flavor-independent parametrization of the mean square transverse momenta, which were tuned to HER-

MES pion-multiplicity data, has been implemented:

$$\langle \boldsymbol{k}_\perp^2 \rangle = 0.14 \text{ GeV}^2, \qquad \langle \boldsymbol{P}_\perp^2 \rangle = 0.42\, z^{0.54}(1-z)^{0.37} \text{ GeV}^2. \tag{5.4.4}$$

The latter functional form is not much different from the one we obtained. The value of the distribution transverse momentum is slightly smaller than our average value, which is compensated by the fact that the fragmentation transverse momentum is slightly higher. Other fits that explored the z dependence in the Gaussian width of TMD FFs can be found in [180,242]. A combined analysis of HERMES and COMPASS data has been presented in [252]. It relies on a flavor and kinematic independent Gaussian ansatz and a standard fit procedure. Results can be compatible with the ones presented here considering the anticorrelation of momenta in distributions and fragmentations. Additional comments are presented in Sec. 5.5.

Comparison with extractions from DY experiments (see, e.g., [167, 180–182, 253]) is not straightforward, due to the different kinematic conditions and the difficulty to extrapolate the results obtained in the CSS formalism (see also the discussion in [191]). The mean square transverse momentum obtained from Gaussian fits without TMD evolution [167,180] is larger than in our case, $\langle \boldsymbol{k}_\perp^2 \rangle \gtrsim 0.7$ GeV^2.

5.5 Summary

Using the recently published HERMES data on semi-inclusive DIS multiplicities [29], we explored for the first time the flavor dependence of the transverse momenta of both the unpolarized parton distributions (TMD PDFs) and fragmentation functions (TMD FFs). We adopted a simplified framework based on the parton model and neglecting the effects of QCD evolution. Using a flavor-dependent Gaussian ansatz, we obtained different results for multiplicities in eight different target–hadron combinations. We performed several fits of the data in different scenarios: including all bins as described in Sec. 5.3.1 (the "default fit"), excluding data with $Q^2 \leq 1.6$ GeV^2 (equivalent to excluding partons at low x), selecting only pions in the final state, or neglecting any flavor dependence.

Comparing the default fit and the flavor-independent one, we conclude that the flavor-dependent Gaussian ansatz performs better. The difference between the average χ^2/d.o.f. in the two cases is not striking but, nonetheless, appreciable. We find convincing indications that the unfavored fragmentation functions have larger average transverse momenta with respect to pion favored fragmentation functions. We get weaker indications of flavor dependence for the TMD PDFs. It is very likely to find fits of the available data with differences of the order of 20% in the mean square transverse momenta of different flavors. In particular, our default fit shows a tendency for valence down quarks to have a narrower distribution than the one of valence up quarks, which in turn is narrower than the one for sea quarks. These

features have a potentially large impact on the extraction of polarized TMDs, where usual flavor-independent transverse momentum parametrizations are assumed in the fragmentation, as even the normalizations extracted for those TMDs depend, directly or indirectly, on the widths of the polarization-averaged TMD FFs.

Apart from the ratios among different flavors, the absolute values of the mean square transverse momenta are compatible with results quoted in the literature. However, it should be kept in mind that there exist strong anti-correlations between mean squared transverse momenta of distribution and fragmentation functions.

This work is a first step in the exploration of the flavor structure in the transverse momentum dependence of partons inside hadrons. First of all, it needs to be updated by implementing evolution equations in the TMD framework. Secondly, the data set needs to be enlarged to include the recently released COMPASS data in a wider kinematical domain [30], and, in the following step, to include also data from e^+e^- annihilations and Drell-Yan processes. Finally, other functional forms different from the Gaussian ansatz should be explored.

Phenomenological impact

Despite the χ^2 being compatible with other less flexible parametrization, the phenomenological relevance of this study is two-fold. Considering SIDIS, the flavor-dependent Gaussian ansatz is, in a sense, less biased than the flavor-independent one. We saw that the 200 replicas have qualitatively similar χ^2 values, compatible also with a flavor independent fit. For this reason, from the physical point, there is no reason to prefer a flavor independent approach, apart from its simplicity. A more general approach is to consider an ensemble of flavor-dependent parameters describing data equally well; this is well represented by the philosophy of the replica method.

Moreover, choosing a flavor-independent model automatically excludes potentially interesting physical effects on other processes, such as e^+e^- annihilation and $Z/W^\pm$ production in hadronic collisions, that will be presented in the next two chapters.

CHAPTER 6

ELECTRON-POSITRON ANNIHILATION

In this Chapter we present a study of the combined effect of TMD evolution and flavor dependence of partonic transverse momentum on e^+e^- annihilation into two almost back-to-back hadrons. Text and results are based on [139, 214, 254]. The convention for labeling partonic and hadronic momenta is specified in Fig. 6.1.

6.1 Introduction

In Chap. 5 the dependence of the intrinsic transverse-momentum distribution of both unpolarized TMD PDFs and TMD FFs upon the flavor and the longitudinal momentum of the parton involved was discussed using the data published by the HERMES collaboration [29] on multiplicities for pions and kaons produced in SIDIS off proton and deuteron targets. Although the flavor-independent fit of the data was not statistically excluded, a clear indication was found that different quark flavors produce different transverse-momentum distributions of final hadrons, especially when comparing different species of final hadrons. This feature corresponds quite naturally to the well known strong flavor dependence of integrated PDFs (see Sec. 4.3.1), and to indications from some models [104, 220, 221, 223–225] and lattice calculations of TMD objects [229]. The SIDIS process is useful because it gives simultaneous access to TMD PDFs and TMD FFs. But the factorized cross section always involves a convolution of transverse momenta of the initial and the fragmenting partons: anticorrelation hinders a separate investigation of the two intrinsic distributions. Moreover, the HERMES data were collected at such a limited range in the hard scale that the statistical analysis in Chap. 5 was reasonably performed without involving modifications due to evolution effects.

In this Chapter, we consider the production of two back-to-back hadrons in electron-positron annihilation. In analogy with the SIDIS process, we define the multiplicities in e^+e^- annihilation as the differential number of back-to-back pairs of hadrons produced per corresponding single-hadron production. Then, we study their transverse momentum distribution at large values of the center-of-mass (cm) energy, starting from an input expression for TMD FFs taken from the analysis of HERMES SIDIS multiplicities at low energy performed in Chap. 5. Within this framework, we extract uncontaminated details on the transverse-momentum dependence of the unpolarized TMD FF, which is a fundamental ingredient of any spin asymmetry in SIDIS and, therefore, it affects the extraction also of polarized TMD distributions (see [255] for a recent analysis of the Collins asymmetry when including TMD evolution effects). Moreover, we make realistic tests on the sensitivity to various implementations of TMD evolution available in the literature, due to the fact that the hard scales involved in e^+e^- annihilation are much larger than the average values explored in SIDIS by the HERMES experiment, which are assumed as the starting reference scale.

This Chapter is organized as follows. In Sec. 6.2, we outline the theoretical tools needed to work out the cross sections for annihilation in two hadrons and define the e^+e^- multiplicities. In Sec. 6.3, relying on the concepts introduced in Chap. 3, we specify the QCD evolution for TMD FFs at LO-NLL and describe some procedures to separate perturbative from nonperturbative domains of transverse momenta. We also provide some prescriptions to parametrize the nonperturbative contributions to the evolution kernel and the resummation of soft gluon radiation. In Sec. 6.4, we introduce the flavor decomposition of fragmentation processes. In Sec. 6.5, we make predictions for the spectrum in transverse momentum of e^+e^- multiplicities for production of two back-to-back hadrons, focusing on the sensitivity of results to the flavor of the fragmenting parton and to the different prescriptions for describing TMD evolution. Comments, remarks and an outlook of possible future analyses are summarized in Sec. 6.6.

6.2 Multiplicities for e^+e^- annihilation into two hadrons

We consider the process $e^+e^- \to h_1 h_2 X$ depicted in Fig. 6.1. An electron e^- and a positron e^+ annihilate producing a vector boson with time-like momentum transfer $q^2 \equiv Q^2 \geq 0$. A quark and an antiquark are then emitted, each one fragmenting into a residual jet containing a leading hadron that for simplicity we will consider unpolarized: the hadron h_1 with momentum and mass P_1, M_1, and the hadron h_2 with momentum and mass P_2, M_2. The two hadrons belong to two back-to-back jets, *i.e.* we have $P_1 \cdot P_2 \approx Q^2$. In the following, we will limit Q^2 values to a range where the vector boson can be safely identified with a virtual photon. Using the standard notations for the light-cone components of a 4-vector, we define the

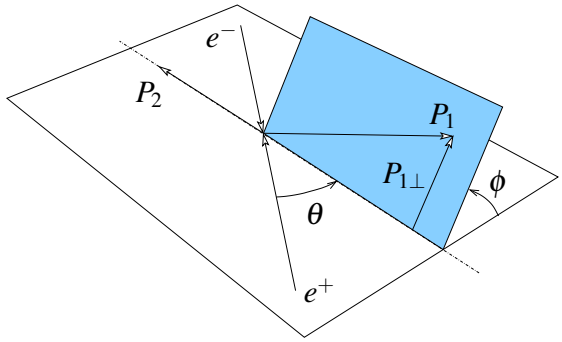

Figure 6.1. Kinematics for the e^+e^- annihilation leading to two back-to-back hadrons with momenta P_1 and P_2.

following invariants

$$z_1 = \frac{2P_1\cdot q}{Q^2} \approx \frac{P_1^-}{q^-} \approx \frac{P_1\cdot P_2}{q\cdot P_2}\ , \qquad (6.2.1)$$
$$z_2 = \frac{2P_2\cdot q}{Q^2} \approx \frac{P_2^+}{q^+} \approx \frac{P_2\cdot P_1}{q\cdot P_1}\ , \quad y = \frac{P_2\cdot \ell}{P_2\cdot q}\ ,$$

where ℓ is the electron momentum. The z_1 is the fraction of parton momentum carried by the hadron h_1, and similarly for z_2 referred to the hadron h_2. Covariantly, we can define the normalized time-like and space-like directions

$$\hat{t}^\mu = \frac{q^\mu}{Q} \quad \text{and} \quad \hat{z}^\mu = \frac{Q}{P_2\cdot q}P_2^\mu - \hat{t}^\mu = \frac{2}{z_2 Q}P_2^\mu - \hat{t}^\mu\ . \qquad (6.2.2)$$

Correspondingly, we can define the projector into the space orthogonal to $\hat{z}$ and $\hat{t}$:

$$g_\perp^{\mu\nu} = g^{\mu\nu} - \hat{t}^\mu\hat{t}^\nu + \hat{z}^\mu\hat{z}^\nu = g^{\mu\nu} - \frac{P_2^\mu q^\nu + q^\mu P_2^\nu}{P_2\cdot q} + O\left(\frac{M^2}{Q^2}\right)\ . \qquad (6.2.3)$$

The lepton momentum is then given by

$$\ell^\mu = \tfrac{1}{2}q^\mu + \left(y-\tfrac{1}{2}\right)Q\hat{z}^\mu + Q\sqrt{y(1-y)}\,\hat{\ell}_\perp^\mu\ , \qquad (6.2.4)$$

where $\hat{\ell}_\perp^\mu = \ell_\perp^\mu/|\boldsymbol{\ell}_\perp|$ and $\ell_\perp^\mu = g_\perp^{\mu\nu}\ell_\nu$.

The $g_\perp^{\mu\nu}$ projects onto the space orthogonal to q and P_2. The projector onto the space orthogonal to P_1 and P_2, namely in the hadron cm frame where P_1 and P_2 have no transverse components, is given by

$$g_T^{\mu\nu} = g^{\mu\nu} - \frac{P_1^\mu P_2^\nu + P_2^\mu P_1^\nu}{P_1\cdot P_2} + O\left(\frac{M^2}{Q^2}\right)$$

$$= g_\perp^{\mu\nu} + \tfrac{P_2^\mu q_T^\nu + q_T^\mu P_2^\nu}{P_2\cdot q} + O\left(\tfrac{M^2}{Q^2}\right) , \tag{6.2.5}$$

where the non-collinearity is defined as

$$\begin{aligned} q_T^\mu &= q^\mu - \frac{P_1^\mu}{z_1} - \frac{P_2^\mu}{z_2} = g_T^{\mu\nu} q_\nu \\ &= -\frac{P_{1\perp}^\mu}{z_1} + O\left(\frac{M^2}{Q^2}\right) = -g_\perp^{\mu\nu}\frac{P_{1\nu}}{z_1} + O\left(\frac{M^2}{Q^2}\right) . \end{aligned} \tag{6.2.6}$$

In the electron-positron cm frame of Fig. 6.1, we define the angle $\theta = \arccos(\boldsymbol{\ell}\cdot\hat{\boldsymbol{z}}/|\boldsymbol{\ell}|)$ where $\hat{\boldsymbol{z}} = -\boldsymbol{P}_2$. It is related to the invariant $y \approx (1+\cos\theta)/2$. In analogy to the Trento conventions [166], we define the azimuthal angle

$$\cos\phi = \frac{\boldsymbol{P}_2\times\boldsymbol{\ell}}{|\boldsymbol{P}_2\times\boldsymbol{\ell}|}\cdot\frac{\boldsymbol{P}_{1\perp}\times\boldsymbol{P}_2}{|\boldsymbol{P}_{1\perp}\times\boldsymbol{P}_2|} , \tag{6.2.7}$$

so that $P_1^\mu = (0, |\boldsymbol{P}_{1\perp}|\cos\phi, |\boldsymbol{P}_{1\perp}|\sin\phi, 0)$ in this frame, and in any frame obtained from this one by a boost along $\hat{\boldsymbol{z}}$. In general, the covariant definition is $\cos\phi = -q_T\cdot\hat{\ell}_\perp/|\boldsymbol{q}_T|$.

The cross section for the e^+e^- annihilation into back-to-back pairs of unpolarized hadrons can be written in a factorized formula at low transverse momenta [20, 26, 96, 256]:

$$\begin{aligned} \frac{d\sigma^{h_1h_2}}{dz_1\,dz_2\,dq_T^2\,dy} &= \frac{6\pi\alpha^2}{Q^2}\,A(y)\,\mathcal{H}(Q^2,\mu) \\ &\times\sum_q e_q^2\int_0^\infty db_T\,b_T\,J_0\left[z_1^2\,D_1^{q\to h_1}(z_1,b_T;\,\zeta_1,\,\mu)\,z_2^2\,D_1^{\bar q\to h_2}(z_2,b_T;\,\zeta_2,\,\mu) + (q\leftrightarrow\bar q)\right] \\ &+ Y(q_T^2/Q^2) + \mathcal{O}(M^2/Q^2) , \end{aligned} \tag{6.2.8}$$

where $J_0 \equiv J_0(q_T b_T)$, $q_T \equiv |\boldsymbol{q}_T|$ and $A(y) = \frac{1}{2} - y + y^2$. The $\mathcal{H}$ is the hard annihilation part. The $D_1^{q\to h}(z, b_T;\,\zeta,\,\mu)$ is the TMD FF in impact parameter space for an unpolarized quark with flavor q fragmenting into an unpolarized hadron h and carrying light-cone momentum fraction z and transverse momentum conjugated to b_T [129]. Both $\mathcal{H}$ and $D_1^{q\to h}$ depend on the renormalization/factorization scale μ and evolve with it through renormalization group equations. The $D_1^{q\to h}$ depends also on the scale ζ (with $\zeta_1\zeta_2 = Q^4$) and evolves with it via a process-independent soft factor. The term $Y(q_T^2/Q^2)$ ensures the matching with perturbative calculations at large transverse momenta.

In this chapter, we will consider a kinematics where $q_T^2 \ll Q^2$ and $M^2 \ll Q^2$. Hence, in Eq. (6.2.8) the $Y(q_T^2/Q^2)$ term and corrections from higher twists of order M^2/Q^2 or higher will be neglected. Moreover, the soft gluon radiation is here

resummed into the TMD FF at the Next-to-Leading-Log level (NLL). It implies that the hard annihilation part is consistently calculated at leading order (LO) in α_s, namely $\mathcal{H}(Q^2,\mu) \approx 1$. Equation (6.2.8) then simplifies to

$$\frac{d\sigma^{h_1 h_2}}{dz_1\, dz_2\, dq_T^2\, dy} \approx \frac{6\pi\alpha^2}{Q^2}\, A(y) \tag{6.2.9}$$
$$\times \sum_q e_q^2 \int_0^\infty db_T\, b_T\, J_0\, \Big[z_1^2\, D_1^{q\to h_1}(z_1, b_T;\, \zeta_1,\, \mu)\, z_2^2\, D_1^{\bar{q}\to h_2}(z_2, b_T;\, \zeta_2,\, \mu) + (q \leftrightarrow \bar{q}) \Big] \,.$$

In Sec. 6.5, we present our results for the q_T spectrum of hadron pair multiplicities in e^+e^- annihilation. In strict analogy with the SIDIS definition [29], we construct the e^+e^- multiplicities as the differential number of back-to-back pairs of hadrons produced per corresponding single-hadron production after the e^+e^- annihilation. In terms of cross sections, we have

$$M^{h_1 h_2}(z_1, z_2, q_T^2, y) = \frac{d\sigma^{h_1 h_2}}{dz_1\, dz_2\, dq_T^2\, dy} \Big/ \frac{d\sigma^{h_1}}{dz_1\, dy} \,, \tag{6.2.10}$$

where $d\sigma^{h_1 h_2}$ is the differential cross section of Eq. (6.2.9). The $d\sigma^{h_1}$ describes the production of a single hadron h_1 from the e^+e^- annihilation and it is obtained from the previous cross section by summing over all hadrons produced in one hemisphere [256]:

$$\frac{d\sigma^{h_1}}{dz_1 dy} = \frac{12\pi\alpha^2}{Q^2}\, A(y) \sum_q e_q^2\, D_1^{q\to h_1}(z_1) \,. \tag{6.2.11}$$

6.3 TMD evolution of fragmentation functions

In the following, we describe in more detail the dependence of the fragmentation functions $D_1^{q\to h}$ of (6.2.9) upon the renormalization/factorization scale μ and the scale ζ (see also Chap. 3). As outlined in Chap. 3, different scenarios are possible according to the choice of the initial starting value for the factorization scale, and of the low-energy model describing the nonperturbative part of the evolution kernel. We first describe the structure of the input $D_1^{q\to h}$ at the starting scale.

6.3.1 Input fragmentation functions at the starting scale

We consider the unpolarized TMD FF extracted by fitting the hadron multiplicities in SIDIS data at low energy from HERMES [29]. The assumed functional form displays a transverse-momentum dependent part which is described in impact pa-

rameter space by the following fixed-scale flavor-dependent Gaussian ansatz[1]:

$$D_1^{a\to h}(z, b_T;\, Q^2) = d_1^{a\to h}(z;\, Q^2)\, \frac{1}{z^2}\, \exp\left[-\frac{1}{4z^2}\, \left\langle \boldsymbol{P}_\perp^2 \right\rangle^{a\to h}(z)\, b_T^2\right] , \tag{6.3.1}$$

where $\left\langle \boldsymbol{P}_\perp^2 \right\rangle^{a\to h}(z)$ with $a = q, \bar{q}$, is the flavor- and z-dependent Gaussian width at some starting scale Q_0^2 [174–176]. The choice of having separate Gaussian functions for different flavors is motivated by the significant differences displayed by the HERMES data between pion and kaon final-state hadrons [29]. The factorized collinear dependent part $d_1^{a\to h}(z;\, Q^2)$ is described by using the DSS parametrization [241].

Following [181, 253], a possible energy dependence of the Gaussian distribution was taken into account introducing the logarithmic term

$$\exp\left\{ -\, g_2\, \frac{b_T^2}{4}\, \ln\frac{Q^2}{Q_0^2} \right\} , \tag{6.3.2}$$

with g_2 a free parameter. Choosing $Q_0^2 = 1$ GeV^2, it was soon realized that the best-fit value for g_2 was compatible with zero. As a matter of fact, the Q^2 range spanned by HERMES is small and the obtained experimental data for multiplicities are not sensitive to evolution effects. For this reason, the fit was performed by using (6.3.1) at a scale fixed to the experimental average value, namely $Q^2 = Q_0^2 = 2.4$ GeV^2. With this choice, the possible energy dependence of (6.3.2) is automatically eliminated.

In summary, the input to our studies on the evolution of $D_1^{a\to h}$ with the scales μ and ζ is referred to the expression in (6.3.1) to be considered at the starting scale $Q_0^2 = 2.4$ GeV^2. However, depending on the choice of the initial value of the factorization scale this identification is not always straightforward, as will be explained in the following sections.

6.3.2 The μ_b prescription

As shown in (6.2.9), the TMD FFs generally depend on the factorization scale μ and on the rapidity scale ζ. The TMD FFs satisfy evolution equations with respect to both of them (see Chap. 3).

The functional form of TMD FFs at small b_T can be calculated in perturbative QCD. Conversely, the nonperturbative part at large b_T must be constrained by fitting experimental data. At the medium/large energies of the BES III and BELLE experiments, the perturbative tail of TMD FFs needs to be taken into account. As explained in Sec. 3.6, using the technique of Operator Product Expansion (OPE), it

[1] The $1/z^2$ factors appearing in (6.3.1) are due to b_T being conjugated to the partonic transverse momentum $\boldsymbol{k}_T$, whereas the TMD FFs in [174] and Chap. 5 are defined and normalized in momentum space with respect to the hadronic transverse momentum $\boldsymbol{K}_T = -z\boldsymbol{k}_T$.

can be represented as a convolution of (perturbatively calculable) Wilson coefficients C with the (nonperturbative) collinear fragmentation functions d_1 (see (3.6.1)).

For a TMD FFs, the convolution in (3.6.1) is defined as

$$[C \otimes d_1^{a\to h}](z, b_T; \zeta, \mu) = \sum_{j=q,\bar{q},g} \int_z^1 \frac{ds}{s}\, C_{j\to a}\left(\frac{z}{s}, b_T; \zeta, \mu\right)\, d_1^{j\to h}(s;\mu)\,. \tag{6.3.3}$$

Via the CS evolution kernel (3.5.1), (3.5.2), the dependence of the coefficients upon both factorization and rapidity scales can be represented in a factorized form:

$$C_{j\to a}(z, b_T; \zeta, \mu) = \left(\frac{\zeta}{\mu_b^2}\right)^{-K(b_T;\mu)} C_{j\to a}(z, b_T; \mu_b^2, \mu)\,, \tag{6.3.4}$$

where we made the *natural* choice $\zeta_i = \mu_b$ (see Chap. 3), the latter being defined in (3.5.9) as

$$\mu_b = \frac{2e^{-\gamma_E}}{b_T}\,, \tag{6.3.5}$$

and γ_E is the Euler constant. The K function in Eq. (6.3.4) [2] arises from the process-independent soft factor that is necessary to proof the factorization theorem leading to the definition of the TMD FFs; it drives the evolution of TMD FFs in the ζ variable. The convolution in Eq. (6.3.3) is only valid for small b_T, namely $b_T \ll 1/\Lambda_{\rm QCD}$. Moreover, the expression of the C coefficients consists in a power series in α_s ln (μ^2/μ_b^2) (including also double logarithms of the same argument). This motivates us to choose the *natural* value $\mu = \mu_b$ to maximize the convergence of the perturbative series. Accordingly, we can write the TMD FF as

$$D^{a\to h}(z, b_T; \zeta, \mu_b) = \left(\frac{\zeta}{\mu_b^2}\right)^{-K(b_T;\mu_b)} \sum_{j=q,\bar{q},g} \int_z^1 \frac{ds}{s}\, C_{j\to a}\left(\frac{z}{s}, b_T; \mu_b^2, \mu_b\right)\, d_1^{j\to h}(s;\mu_b) \times \mathcal{O}(b_T\Lambda_{\rm QCD})\,. \tag{6.3.6}$$

The evolution of this fragmentation function from μ_b to another value of μ (e.g., $\mu = Q$) is driven by RGE equations. Instead, the evolution from an initial rapidity scale ζ_i to ζ is controlled by the K function. The final expression of the TMD FF at the scales $\mu = Q$ and ζ is

$$D^{a\to h}(z, b_T; \zeta, Q) = \exp\left\{\int_{\mu_b}^{\mu=Q} \frac{d\bar{\mu}}{\bar{\mu}}\gamma_{FF}\right\}\left(\frac{\zeta}{\zeta_i}\right)^{-K(b_T;\mu_b)}$$

[2] Our K function corresponds to the D function in [122], and to the $\tilde{K}$ function in [20] but for a factor $-1/2$.

$$\times \left(\frac{\zeta_i}{\mu_b^2}\right)^{-K(b_T;\mu_b)} \sum_{j=q,\bar{q},g} \int_z^1 \frac{ds}{s}\, C_{j\to a}\left(\frac{z}{s}, b_T; \mu_b^2, \mu_b\right)\, d_1^{j\to h}(s;\mu_b)$$
$$\times +\mathcal{O}(b_T \Lambda_{\rm QCD})\,, \tag{6.3.7}$$

where the anomalous dimension γ_{FF} reads (for more details see Chap. 3)

$$\gamma_{FF} = -\left(\Gamma_{\rm cusp}\, \ln\frac{\zeta}{\mu^2} + \gamma^V\right)\,, \tag{6.3.8}$$

and $\Gamma_{\rm cusp}$ and γ^V are also power series in α_s (see Chap. 3).

As explained in Sec. 3.7.3, the above procedure is valid up to a maximum value of b_T, named $b_{\rm max}$, beyond which we do not trust the perturbative calculation. Hence, it is convenient to reconsider the OPE by introducing the variable $\hat{b}_T$ defined in (3.7.7) that freezes at $b_{\rm max}$ when b_T becomes large.

By adding the decomposition in (3.7.8) and the intrinsic transverse distribution at the starting scale (6.3.1), (6.3.7) becomes

$$D^{a\to h}(z, b_T; \zeta, Q) = \exp\left\{\int_{\mu_{\hat{b}}}^{Q} \frac{d\bar{\mu}}{\bar{\mu}} \gamma_{FF}\right\} \left(\frac{\zeta}{\zeta_i}\right)^{-K(\hat{b}_T;\mu_{\hat{b}}) - g_{\rm np}(b_T)}$$
$$\times \left(\frac{\zeta_i}{\mu_{\hat{b}}^2}\right)^{-K(\hat{b}_T;\mu_{\hat{b}}) - g_{\rm np}(b_T)} \sum_{j=q,\bar{q},g} \int_x^1 \frac{ds}{s} C_{j\to a}\left(\frac{z}{s}, \hat{b}_T; \mu_{\hat{b}}^2, \mu_{\hat{b}}\right)\, d_1^{a\to h}(s;\mu_{\hat{b}})$$
$$\times \frac{1}{z^2}\, e^{-\frac{\langle \boldsymbol{P}_\perp^2 \rangle^{a\to h}(z)}{4z^2} b_T^2} \left(\frac{\zeta_i}{Q_0^2}\right)^{-g_{\rm np}(b_T)}\,. \tag{6.3.9}$$

If we insert $\zeta_i = \mu_{\hat{b}}^2$ and $\zeta = \mu^2 = Q^2$, the above equation reduces to

$$D^{a\to h}(z, b_T; Q^2, Q) = \exp\left\{\int_{\mu_{\hat{b}}}^{Q} \frac{d\bar{\mu}}{\bar{\mu}} \gamma_{FF}\right\} \left(\frac{Q^2}{\mu_{\hat{b}}^2}\right)^{-K(\hat{b}_T;\mu_{\hat{b}}) - g_{\rm np}(b_T)}$$
$$\times \sum_{j=q,\bar{q},g} \int_z^1 \frac{ds}{s}\, C_{j\to a}\left(\frac{z}{s}, \hat{b}_T; \mu_{\hat{b}}^2, \mu_{\hat{b}}\right)\, d_1^{j\to h}(s;\mu_{\hat{b}})$$
$$\times \frac{1}{z^2}\, e^{-\frac{\langle \boldsymbol{P}_\perp^2 \rangle^{a\to h}(z)}{4z^2}\, b_T^2} \left(\frac{\mu_{\hat{b}}^2}{Q_0^2}\right)^{-g_{\rm np}(b_T)}$$
$$\equiv R(b_T; Q^2, Q, \mu_{\hat{b}}^2, \mu_{\hat{b}})\; D^{a\to h}(z, b_T; \mu_{\hat{b}}^2, \mu_{\hat{b}})\,. \tag{6.3.10}$$

Hence, the net effect of evolution can be represented as the action of the evolution operator R (3.5.7) on the input TMD FF evaluated at the scale $\mu_{\hat{b}}$, which is running with $\hat{b}_T$. This peculiar feature grants that there is a smooth matching between the

perturbative domain at small b_T and the nonperturbative domain at large b_T. As mentioned in Sec. 3.7.3, from (6.3.9) and (6.3.10) we deduce that modeling the nonperturbative part affects the whole b_T spectrum, not only the large b_T region.

In this analysis, we resum the soft gluon radiation up to NLL contributions in $\ln(\mu/\mu_b)$, which corresponds to include terms linear in α_s in the perturbative expansion of K and γ^V, and quadratic in the expansion of $\Gamma_{\rm cusp}$ (see Sec. 3.7.2):

$$\begin{aligned} K(b_T;\mu) &= \frac{C_F}{2\pi}\ \alpha_s\ \ln\frac{\mu^2}{\mu_b^2}\ , \\ \gamma^V &= -\frac{3C_F}{2\pi}\ \alpha_s\ , \\ \Gamma_{\rm cusp} &= \frac{C_F}{\pi}\alpha_s\left\{1+\frac{\alpha_s}{4\pi}\left[\left(\frac{67}{9}-\frac{\pi^2}{3}\right)C_A-\frac{20}{9}\ T_F\ n_f\right]\right\}\ , \end{aligned} \tag{6.3.11}$$

where $C_A = N_c$, $C_F = (N_c^2-1)/2N_c$, are the usual Casimir operators for the gluon and fermion representations of the color group $\mathrm{SU}(N_c)$ with N_c colors, and $T_F = n_f/2$ with n_f the number of active quark flavors. The coefficients C are computed at LO in α_s (see Tab. 3.1), namely they reduce to δ functions such that (6.3.10) simplifies to

$$\begin{aligned} D^{a\to h}(z,b_T;Q) = \exp\left\{\int_{\mu_{\hat b}}^{Q}\frac{d\bar\mu}{\bar\mu}\gamma_{FF}\Big|_{\rm NLL}\right\}\left(\frac{Q^2}{\mu_{\hat b}^2}\right)^{-K_{\rm NLL}(\hat b_T;\mu_{\hat b})-g_{\rm np}(b_T)} \\ \times\ d_1^{a\to h}(z;\mu_{\hat b})\ \frac{1}{z^2}\ \exp\left\{-\frac{\langle \boldsymbol{P}_\perp^2\rangle^{a\to h}(z)}{4z^2}b_T^2\right\}\left(\frac{\mu_{\hat b}^2}{Q_0^2}\right)^{-g_{\rm np}(b_T)}\ . \end{aligned} \tag{6.3.12}$$

The definition of $g_{\rm np}(b_T)$ in (3.7.8) obviously implies that this function depends on $b_{\rm max}$, i.e. on the value of the impact parameter that sets the separation between the perturbative and nonperturbative regimes. Indeed, by perturbatively expanding $K(b_T;\mu_b)$ at lowest order we have [128]

$$g_{\rm np}(b_T) \approx \frac{\alpha_s(\mu_{\hat b})\,C_F}{\pi}\ln\left(1+\frac{b_T^2}{b_{\rm max}^2}\right)\ . \tag{6.3.13}$$

For $b_T \ll b_{\rm max}$, this expression recovers the quadratic parametrization $\frac{1}{2}g_2 b_T^2$ adopted in the fits of [181] and [182], and it suggests that the parameter g_2 is not free but anticorrelated to $b_{\rm max}$, and proportional to $b_{\rm max}^2$ through a perturbatively calculable coefficient. The $g_{\rm np}$ function accounts for the radiation of soft gluons emitted from a parton at high b_T. A small (large) value of $b_{\rm max}$ implies that the QCD perturbative description is valid up to relatively small (large) b_T values.

Consequently, the amount of soft gluons emission is larger (smaller) and we expect a large (small) value for g_2. More generally, this anticorrelation is motivated by the fact that both the exact function $K(b_T;\mu_b)$ and the TMD FF itself must not depend on the arbitrary choice of $b_{\max}$. So, $b_{\max}$ should not be regarded as a free parameter to be fitted to data, but it should be considered as an arbitrary scale that separates perturbative from nonperturbative regimes: changing $b_{\max}$ implies a rearrangement of all terms in Eq. (6.3.9) such that the TMD FF does not change [128].

For the purpose of this work, we will consider anticorrelated pairs of values for $\{b_{\max}, g_2\}$, inspired to the values adopted in [181] and [182]. We will also explore different expressions for each one of the $\hat{b}_T$ and $g_{\rm np}$ functions. For $\hat{b}_T$, our first choice is the socalled "b-star" prescription [20, 181]

$$\hat{b}_T \equiv b_T^* = \frac{b_T}{\sqrt{1+\frac{b_T^2}{b_{\max}^2}}} \,. \tag{6.3.14}$$

The second choice is based on the exponential function

$$\hat{b}_T \equiv b_T^\dagger = b_{\max}\left\{1-\exp\left[-\frac{b_T^4}{b_{\max}^4}\right]\right\}^{\frac{1}{4}} \,, \tag{6.3.15}$$

that is steeper and it approaches the asymptotic constant $b_{\max}$ more quickly. For $g_{\rm np}$, we choose a linear function of b_T^2 similarly to [181, 182, 253] (see also (6.3.2)):

$$g_{\rm np}^{\rm lin}(b_T) = \frac{g_2}{4}\, b_T^2 \,. \tag{6.3.16}$$

The second choice is suggested by (6.3.13):

$$g_{\rm np}^{\rm log}(b_T) = g_2\, \bar{b}_T^2\, \ln\left(1+\frac{b_T^2}{4\bar{b}_T^2}\right) \,, \quad \bar{b}_T = 1\ {\rm GeV}^{-1} \,. \tag{6.3.17}$$

This expression was considered also in [179], and it reduces to (6.3.16) for small b_T.

In principle, we have four different combinations of prescriptions: $\{b_T^*, g_{\rm np}^{\rm lin}\}$, $\{b_T^*, g_{\rm np}^{\rm log}\}$, $\{b_T^\dagger, g_{\rm np}^{\rm lin}\}$, and $\{b_T^\dagger, g_{\rm np}^{\rm log}\}$. However, after some preliminary exploration we realized that some of them were producing redundant results. Therefore, they have been neglected. In summary, the transverse-momentum spectrum of the multiplicities in Eq. (6.2.10) will be analyzed by varying the anticorrelated pair of parameters $\{b_{\max}, g_2\}$, and by considering only the two combinations $\{b_T^*, g_{\rm np}^{\rm lin}\}$ and $\{b_T^\dagger, g_{\rm np}^{\rm log}\}$.

Finally, we remark that if we choose $Q = \mu_{\hat{b}}$ in Eq. (6.3.12), *i.e.* if we switch off evolution effects, we should recover the Gaussian model expression of Eq. (6.3.1) for the TMD FF at the initial scale Q_0. Formally, this is not the case because in the

second line the collinear d_1 is evaluated at $\mu_{\hat{b}}$ and the term $(\mu_{\hat{b}}^2/Q_0^2)^{-g_{\rm np}(b_T)}$ survives. However, the Gaussian model of (6.3.1)) is deduced by fitting the HERMES SIDIS data, whose kinematics overlaps the domain of very large $b_T \gg b_{\rm max}$, namely where $\hat{b}_T \approx b_{\rm max}$. If we use the prescription $\hat{b}_T \equiv b_T^*$ of (6.3.14)), it is easy to check that for $b_{\rm max} = 0.7$ GeV^{-1} we have $\mu_{\hat{b}}^2 \approx Q_0^2 = 2.4$ GeV^2. Hence, the $D^{a\to h}(z, b_T; \mu_{\hat{b}})$ of (6.3.12) at $Q = \mu_{\hat{b}}$ actually behaves like the $D^{a\to h}(z, b_T; Q_0)$ of (6.3.1) at the scale Q_0 and at very large b_T values, or equivalently for very small parton transverse momenta.

6.3.3 The fixed-scale prescription

Alternatively, we can fix the initial scales ζ_i and μ_b^2 at the value $Q_i^2 = Q_0^2 = 2.4$ GeV^2 for the whole b_T distribution:

$$D^{a\to h}(z, b_T; Q) = R(b_T; Q, Q_i)\; D^{a\to h}(z, b_T; Q_i)\;. \tag{6.3.18}$$

With this choice, it is not possible to apply the OPE for calculating a perturbative tail to which the TMD FF should match at low b_T, because the logarithms in the perturbative expression are not minimized by the natural choices. For this reason, we need a model input over the whole b_T spectrum. In our case, it is now very easy to identify the input TMD FF at the starting scale Q_i with the Gaussian parametrization of (6.3.1) at Q_0. Then, for $\mu_i^2 = \zeta_i = Q_i^2 = Q_0^2 = 2.4$ GeV^2 the TMD FF evolved at NLL up to a final scale $\mu^2 = \zeta \equiv Q^2$ becomes

$$\begin{aligned} D^{a\to h}(z, b_T; Q) = \exp\left\{\int_{Q_i}^{Q} \frac{d\bar{\mu}}{\bar{\mu}} \gamma_{FF}\big|_{\rm NLL}\right\} \left(\frac{Q^2}{Q_i^2}\right)^{-K_{\rm NLL}(b_T; Q_i)} \\ \times\, d_1^{a\to h}(z; Q_i)\; \frac{1}{z^2}\; \exp\left\{-\frac{\langle \boldsymbol{P}_\perp^2 \rangle^{a\to h}(z)}{4z^2} b_T^2\right\}\;. \end{aligned} \tag{6.3.19}$$

The contribution from the $g_{\rm np}$ term in the input distribution does not appear because of the choice of the starting scale $\zeta_i = Q_i^2 = Q_0^2$.

The choice $\mu_i = Q_i$ of identifying the starting factorization scale with a fixed scale for the whole b_T spectrum has important consequences also on the function K. From Eq. (6.3.11), we can expand K in powers of ln (μ/μ_b): if $\mu_i \neq \mu_b$, the series may not converge. One possible workaround is to apply the resummation technique to the K function itself [122]. Here, we will discuss two different approaches: computing K from [20] at a fixed order in α_s; or dressing K by resumming large logarithms of the kind ln (μ/μ_b) [122]. In the first case, K is expanded in powers of α_s; in the second case, the expansion is in α_s ln (μ/μ_b). If $\mu_i = \mu_b$, the two expansions are the same.

We will refer to the first choice as the "fixed-scale" prescription. The function

K is evolved from $\mu_{\hat{b}}$ to Q_i through its anomalous dimension:

$$K(b_T;Q_i) = K(\hat{b}_T;\mu_{\hat{b}}) + \int_{\mu_{\hat{b}}}^{Q_i} \frac{d\bar{\mu}}{\bar{\mu}}\, \Gamma_{\rm cusp} + g_{\rm np}(b_T)$$
$$\overset{\approx}{_{\rm NLL}} \int_{\mu_{\hat{b}}}^{Q_i} \frac{d\bar{\mu}}{\bar{\mu}}\, \Gamma_{\rm cusp} + g_{\rm np}(b_T)\ , \tag{6.3.20}$$

where $g_{\rm np}(b_T)$ can get either the expression in (6.3.16) or in (6.3.17). The perturbative contributions are calculated at NLL as in Eq. (6.3.11), according to which we have $K_{\rm NLL}(\hat{b}_T;\mu_{\hat{b}}) = 0$.

The second choice is connected to the results of [122] and has already been outlined in Sec. 3.7.3. There large logarithms of the kind ln (μ/μ_b) are resummed in the perturbative part:

$$K(b_T;Q_i) = D^R(b_T;Q_i)\ \theta(b_{T,c} - b_T) + \bar{g}_{\rm np}(b_T)\ \theta(b_T - b_{T,c})\ , \tag{6.3.21}$$

where D^R is the resummed contribution (computed, e.g., in [122]), and $b_{T,c}$ is the convergence radius of the perturbative expression. Apart from the resummation of logarithms, the main difference with (6.3.20) is the presence of the θ functions: no $\hat{b}_T$ prescription is used to connect the perturbative and nonperturbative domains. As explained in Sec. 3.7.3, the nonperturbative contribution acts differently: while $g_{\rm np}$ in (6.3.20) applies to the whole b_T spectrum, in (6.3.21) it does only for $b_T > b_{T,c}$. Here we use the notation $\bar{g}_{\rm np}$ to account for this difference. For example, the K function must be at least continuous at $b_T = b_{T,c}$. We can match this constraint by defining the nonperturbative contribution at $b_T > b_{T,c}$ as

$$\bar{g}_{\rm np}(b_T) = D^R(b_{T,c})\ \left[1 + g_{\rm np}(b_T - b_{T,c})\right]\ , \tag{6.3.22}$$

where $g_{\rm np}$ can be again either the $g_{\rm np}^{\rm lin}$ prescription of (6.3.16) or the $g_{\rm np}^{\rm log}$ prescription of (6.3.17).

For $Q_i \ll Q$, the perturbative component D^R in (6.3.21) diverges for $b_T < b_{T,c}$. Hence, its contribution to the evolution of the fragmentation function becomes negligible, being of the kind $(Q/Q_i)^{-D^R}$. Since K is a smooth function in b_T, also the contribution of the nonperturbative part $\bar{g}_{\rm np}$ for $b_T > b_{T,c}$ becomes numerically negligible [122]. However, this result cannot be generalized to any value of Q. Since we will make explorative calculations also at the BES III scale $Q = \sqrt{14.6}$ GeV which cannot be considered to be much larger than the initial scale $Q_0 = \sqrt{2.4}$ GeV of our input TMD FF, we will consider only the "fixed-scale" prescription of (6.3.20).

6.3.4 Summary of evolution kernels

In summary, we consider two possible ways of evolving the TMD FF, according to the choice of the initial factorization scale μ_i. It is understood that all formulae are computed at the NLL level of accuracy, according to (6.3.11) and Sec. 3.7.2.

$\mathcal{A}$ The "μ_b" prescription: then $\mu_i^2 = \mu_{\hat{b}}^2 = \zeta_i,\ \zeta = \mu^2 = Q^2$, and we have

$$D^{a\to h}(z, b_T; Q) = \exp\left\{\int_{\mu_{\hat{b}}}^{Q} \frac{d\bar{\mu}}{\bar{\mu}}\gamma_{FF}\right\} \left(\frac{Q^2}{\mu_{\hat{b}}^2}\right)^{-K(\hat{b}_T;\mu_{\hat{b}})-g_{\rm np}(b_T)} \times d_1^{a\to h}(z;\mu_{\hat{b}})\ \frac{1}{z^2}\ \exp\left\{-\frac{\langle \boldsymbol{P}_\perp^2\rangle^{a\to h}(z)}{4z^2} b_T^2\right\} \left(\frac{\mu_{\hat{b}}^2}{Q_0^2}\right)^{-g_{\rm np}(b_T)}, \tag{6.3.23}$$

where γ_{FF} and K are described by (6.3.8) and (6.3.11), $\mu_{\hat{b}}$ is given by (3.5.9) with (6.3.14) and (6.3.15), and $g_{\rm np}$ is described in (6.3.16) and (6.3.17).

$\mathcal{B}$ The "fixed-scale" prescription: then $\mu_i^2 = Q_i^2 = \zeta_i,\ \zeta = \mu^2 = Q^2$, and we have

$$D^{a\to h}(z, b_T; Q) = \exp\left\{\int_{Q_i}^{Q} \frac{d\bar{\mu}}{\bar{\mu}}\gamma_{FF}\right\} \left(\frac{Q^2}{Q_i^2}\right)^{-K(\hat{b}_T;\mu_{\hat{b}})-\int_{\mu_{\hat{b}}}^{Q_i}\frac{d\bar{\mu}}{\bar{\mu}}\Gamma_{\rm cusp}-g_{\rm np}(b_T)} \times d_1^{a\to h}(z;Q_i)\ \frac{1}{z^2}\ \exp\left\{-\frac{\langle \boldsymbol{P}_\perp^2\rangle^{a\to h}(z)}{4z^2} b_T^2\right\}, \tag{6.3.24}$$

where γ_{FF}, $\mu_{\hat{b}}$, $g_{\rm np}$ are defined in the same equations as above, while K is given in (6.3.20).

6.4 Flavor dependence of fragmentation functions

The flavor sum in (6.2.9) can be made explicit and further simplified using the symmetry upon charge-conjugation transformations:

$$D_1^{q\to h}(z, b_T;\, Q^2) = D_1^{\bar{q}\to \bar{h}}(z, b_T;\, Q^2)\ . \tag{6.4.1}$$

At the starting scale Q_0, we distinguish the *favored* fragmentation where the fragmenting parton is in the valence content of the final hadron h. All the other channels are classified as *unfavored* fragmentation and are characterized by the fact that the detected hadron is produced by exciting more than one $q\bar{q}$ pair from the vacuum. If the final hadron is a kaon, we further distinguish a favored fragmentation initiated by an up quark/antiquark from the one initiated by a strange quark/antiquark. See also Sec. 5.2.2. We limit the sum to three flavors u, d, s, and the corresponding

antiquark partners. For an analysis of the impact of this decomposition on the production of $\{\pi^{\pm}, K^{\pm}\}$ combinations, see Sec. 4 in [139].

Flavor dependent TMD Gaussian ansatz

The starting input to our analysis are the TMD FFs extracted by fitting the hadron multiplicities in SIDIS data from HERMES at $Q_0^2 = 2.4$ GeV^2 [174]. The assumed functional form displays a transverse-momentum dependent part which is described in impact parameter space by the following flavor-dependent Gaussian ansatz:

$$\begin{aligned} D_1^{q\to h}(z, b_T; Q_0^2) &= d_1^{q\to h}(z; Q_0^2)\, \frac{1}{z^2}\, \exp\left[-\frac{1}{4z^2}\, \langle \boldsymbol{P}_{\perp}^2 \rangle^{q\to h}(z)\, b_T^2\right] \\ &\equiv d_1^{q\to h}(z; Q_0^2)\, G_q^h(z, b_T^2)\ . \end{aligned} \tag{6.4.2}$$

The cross section of (6.2.9) (and, in turn, the multiplicity in (6.2.10)) is then a sum of Gaussians, and thus no longer a simple Gaussian. The width of the Gaussian depends also on the fractional momentum z as in (5.2.21).

Isospin and charge-conjugation symmetries suggest four different Gaussian shapes, as in (5.2.17), (5.2.18), (5.2.19), (5.2.20).Correspondingly, we have four different Gaussian functions in (6.4.2):

$$G_u^{\pi^+} = G_{\bar{d}}^{\pi^+} = G_{\bar{u}}^{\pi^-} = G_d^{\pi^-} \equiv G_{\rm fav}(z, b_T^2)\ , \tag{6.4.3}$$

$$G_u^{K^+} = G_{\bar{u}}^{K^-} \equiv G_{uK}(z, b_T^2)\ , \tag{6.4.4}$$

$$G_{\bar{s}}^{K^+} = G_s^{K^-} \equiv G_{sK}(z, b_T^2)\ , \tag{6.4.5}$$

$$\begin{aligned} G_u^{\pi^-} = G_u^{K^-} = G_d^{\pi^+} = G_d^{K^\pm} = G_s^{\pi^\pm} = G_s^{K^+} = G_{\bar{u}}^{\pi^+} = G_{\bar{u}}^{K^+} \\ = G_{\bar{d}}^{\pi^-} = G_{\bar{d}}^{K^\pm} = G_{\bar{s}}^{\pi^\pm} = G_{\bar{s}}^{K^-} \equiv G_{\rm unf}(z, b_T^2)\ . \end{aligned} \tag{6.4.6}$$

Each one of these four functions depends on the same fitting parameters β, δ, γ, of (5.2.21) (see Sec. 5.2.2).

Collinear fragmentation functions

For the collinear functions $d_1^{q\to h}(z; Q_0^2)$, we adopt the same assumptions of [241]:

- isospin symmetry of the sea quarks

- for $h = \pi^+$, a direct proportionality between the $(d + \bar{d})$ and $(u + \bar{u})$ combinations, *i.e.* $(d + \bar{d}) = N(u + \bar{u})$.

For more details concerning their implementation, together with the flavor dependent Gaussian ansatz, we refer to Sec. 4 in [139].

6.5 Predictions for multiplicities

In this section, we present our results as normalized multiplicities

$$M^{h_1 h_2}(z_1, z_2, q_T^2, y)/M^{h_1 h_2}(z_1, z_2, 0, y) \tag{6.5.1}$$

for the hadron pair (h_1, h_2), where $M^{h_1 h_2}(z_1, z_2, q_T^2, y)$ is defined in Eq. (6.2.10). In such way, we are able to directly compare the genuine trend in q_T^2 for each different case. If not explicitly specified, we choose $y = 0.2$. For selected values of $\{z_1, z_2\}$, the results are displayed as a function of $\boldsymbol{P}_{1\perp}^2 = z_1^2 \boldsymbol{q}_T^2$. Hence, the useful range in $\boldsymbol{P}_{1\perp}^2$ depends on z_1 in order to fulfill the condition $q_T^2 \ll Q^2$. The range obviously depends also on the choice of the hard scale; we consider $Q^2 = 100$ GeV^2, as in the Belle experiment, and $Q^2 = 14.6$ GeV^2, as in the BES III one. For each specific case, the results are displayed as uncertainty bands: they represent the 68% of the envelope of 200 different values for the intrinsic parameters in (5.2.21) for the $D_1(z, b_T; Q_0^2)$ at the starting scale Q_0^2, obtained by rejecting the largest and lowest 16% of them. The 200 values are obtained by fitting 200 replicas of SIDIS multiplicities measured by the Hermes collaboration [29]. If the 200 values for each parameter were distributed as a Gaussian, the 68% band would correspond to the usual 1σ confidence interval (for more details, see Ref. [174]).

The results are organized as follows. In Sec. 6.5.1, we show the sensitivity of the normalized multiplicity to different values of the evolution parameters $\{b_{\max}, g_2\}$ described in Sec. 6.3.2 for a final hadron pair $(h_1 h_2) = (\pi^+\pi^-)$. In Sec. 6.5.2, we compare normalized multiplicities for the two different evolution schemes described in Secs. 6.3.2 and 6.3.3. In Sec. 6.5.3, we discuss the capability of discriminating among the various prescriptions illustrated in Sec. 6.3.2 for the nonperturbative evolution effects. In Sec. 6.5.4, we concentrate on the sensitivity of the normalized multiplicities upon varying the fractional energy z of final hadrons. In Sec. 6.5.5, we show how the results get modified when lowering Q^2 from the Belle scale to the BES III scale. Finally, in Sec. 6.5.6 we discuss the sensitivity of ratios of normalized multiplicities for different final states to the flavor structure of the intrinsic transverse-momentum-dependent part of the input TMD FF at the starting scale of evolution.

6.5.1 Sensitivity to nonperturbative evolution parameters

As already remarked in Sec. 6.3.2, for a specific evolution scheme the nonperturbative part of the TMD evolution depends on the choice of a prescription for describing the transition from perturbative to nonperturbative regimes, which in turn depends on the two parameters $b_{\max}$ and g_2. In this section, we explore the sensitivity of our predictions to different values of the pair $\{b_{\max}, g_2\}$. Units of measure $\{\text{GeV}^{-1}, \text{GeV}^2\}$ will be intended. We adopt as limiting cases the choices

$\{b_{\max} = 1.5,\, g_2 = 0.18\}$ and $\{b_{\max} = 0.5,\, g_2 = 0.68\}$, that were deduced in [182] and [181], respectively, by fitting the transverse-momentum distribution of lepton pairs produced in Drell-Yan processes. If not explicitly specified, the first choice is described by uncertainty bands with dot-dashed borders while the second choice is linked to bands with solid borders. As explained in Sec. 6.3.2, the two parameters are anticorrelated. In the following, we show results also for the interpolating choice $\{b_{\max} = 1,\, g_2 = 0.43\}$. The corresponding results are displayed as uncertainty bands with dashed borders.

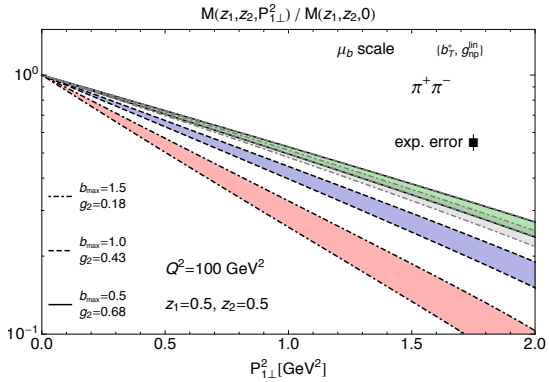

Figure 6.2. The normalized multiplicity at $z_1 = z_2 = 0.5$ as a function of $\boldsymbol{P}_{1\perp}^2 = z_1^2 \boldsymbol{q}_T^2 \equiv (0.5)^2 \boldsymbol{q}_T^2$ at the BELLE scale $Q^2 = 100$ GeV^2 for the "μ_b scale" evolution scheme and with the $\{b_T^*,\, g_{\rm np}^{\rm lin}\}$ prescription for the transition to the nonperturbative regime (see text). The uncertainty bands correspond to various choices of the nonperturbative parameters of evolution: $\{b_{\max} = 1.5,\, g_2 = 0.18\}$ for the band with dot-dashed borders, $\{b_{\max} = 1,\, g_2 = 0.43\}$ for the one with dashed borders, $\{b_{\max} = 0.5,\, g_2 = 0.68\}$ for the one with solid borders. The latter is accompanied by a light-gray band with dot-dashed borders, that represents the result with the same parameters but with the choice $\mu_b/2$ for the arbitrary matching scale, and by an overlapping light-gray band with dashed borders for the choice $2\mu_b$. An experimental error of 7% is also indicated.

In Fig. 6.2, the normalized multiplicity

$$M^{\pi^+\pi^-}(z_1 = 0.5, z_2 = 0.5, q_T^2, y = 0.2)/M^{\pi^+\pi^-}(z_1 = 0.5, z_2 = 0.5, 0, y = 0.2) \tag{6.5.2}$$

is shown as a function of $\boldsymbol{P}_{1\perp}^2 = z_1^2 \boldsymbol{q}_T^2 \equiv (0.5)^2 \boldsymbol{q}_T^2$ at the BELLE scale $Q^2 = 100$ GeV^2 for the "μ_b scale" evolution scheme and with the $\{b_T^*,\, g_{\rm np}^{\rm lin}\}$ prescription for the transition to the nonperturbative regime, as explained in Sec. 6.3.2. The explored range in $\boldsymbol{P}_{1\perp}^2$ is such that for $z_1 = 0.5$ the maximum $\boldsymbol{q}_T^2$ satisfies the condition $\boldsymbol{q}_T^2 \ll Q^2$. The three uncertainty bands, corresponding to the three different choices $\{b_{\max} = 1.5,\, g_2 = 0.18\}$ (dot-dashed borders), $\{b_{\max} = 1,\, g_2 = 0.43\}$ (dashed borders), and $\{b_{\max} = 0.5,\, g_2 = 0.68\}$ (solid borders), are well separated. The

squared box with error bar indicates an experimental error of 7%. We fix it by propagating to the normalized multiplicity the typical experimental error of 3% for single-hadron production data in e^+e^- annihilation at $Q^2 = 100$ GeV^2 and $z = 0.5$, from which the collinear $d_1^q(z;\, Q^2)$ are extracted [241]. This expected experimental error of 7% seems small enough to discriminate among predictions produced with different choices of $\{b_{\rm max},\, g_2\}$.

Two additional light-gray bands are shown, which are partially overlapped (dot-dashed borders) or completely overlapped (dashed borders) to the band with solid borders corresponding to the choice $\{b_{\rm max} = 0.5,\, g_2 = 0.68\}$. These bands reproduce the outcome of calculations performed in the same conditions but for different (arbitrary) choices of the scale μ_b. If the band with solid borders corresponds to calculations with the choice of Eq. (6.3.5) for μ_b, then the light-gray band with dot-dashed borders corresponds to the choice $\mu_b/2$, and the one with dashed borders to $2\mu_b$. The almost complete overlap of these results shows that for the selected observable, the normalized multiplicity, the theoretical uncertainty in determining the matching scale μ_b (that describes the transition from perturbative to nonperturbative regimes) is negligible with respect to the sensitivity to the parameters describing the nonperturbative effects in the evolution.

6.5.2 Sensitivity to evolution schemes

In this section, we explore the sensitivity of our normalized multiplicity to the choice of the evolution scheme. In Sec. 6.3, we described two different schemes, the "μ_b scale" and the "fixed scale". They differ mainly in the fact that in the latter the whole distribution in impact parameter space b_T of the TMD FF D_1^q at beginning of evolution is computed at a fixed scale Q_0, namely there is no impact parameter that describes the transition from low (perturbative) b_T to high (nonperturbative) b_T. Actually, one would expect that for small values of g_2 and corresponding not too large values of $b_{\rm max}$ (*i.e.*, where the perturbative description of the evolution of the b_T distribution is still applicable and gives the predominant contribution) the predictions from the different schemes should tend to a common result, determined mainly by a fully perturbative calculation. However, the complexity of the evolution kernels, described in Secs. 6.3.2 and 6.3.3, indicates that this is too a naïve expectation.

In fact, in Fig. 6.3 the normalized multiplicity of Eq. (6.5.2) is shown as a function of $\boldsymbol{P}_{1\perp}^2 = z_1^2 \boldsymbol{q}_T^2 \equiv (0.5)^2 \boldsymbol{q}_T^2$ at the BELLE scale $Q^2 = 100$ GeV^2 with the $\{b_T^*,\, g_{\rm np}^{\rm lin}\}$ prescription. There are two groups of uncertainty bands. The former one displays the results for the "fixed scale" evolution scheme in the standard notation, *i.e.* for $\{b_{\rm max} = 1.5,\, g_2 = 0.18\}$ (dot-dashed borders), $\{b_{\rm max} = 1,\, g_2 = 0.43\}$ (dashed borders), and $\{b_{\rm max} = 0.5,\, g_2 = 0.68\}$ (solid borders). Then, two additional light-gray bands are shown that correspond to the results with the "μ_b

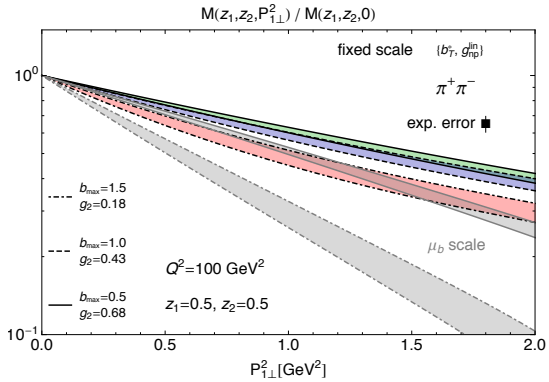

Figure 6.3. The normalized multiplicity at $z_1 = z_2 = 0.5$ as a function of $\boldsymbol{P}_{1\perp}^2 = z_1^2 \boldsymbol{q}_T^2 \equiv (0.5)^2 \boldsymbol{q}_T^2$ in the same conditions and with the same notation as in Fig. 6.2, but for the "fixed scale" evolution scheme. The additional light-gray bands with dot-dashed and solid borders are the result related to the "μ_b scale" evolution scheme for $\{b_{\max} = 1.5,\ g_2 = 0.18\}$ and $\{b_{\max} = 0.5,\ g_2 = 0.68\}$, respectively.

scale" evolution scheme for $\{b_{\max} = 1.5,\ g_2 = 0.18\}$ (dot-dashed borders) and $\{b_{\max} = 0.5,\ g_2 = 0.68\}$ (solid borders).

It is evident that for the maximum (minimum) $b_{\max}$ (g_2) the band with dot-dashed borders in the "fixed scale" scheme is not similar to the light-gray band with dot-dashed borders in the "μ_b scale" scheme. Actually, all the results in the "fixed scale" scheme show a much larger distribution in $\boldsymbol{P}_{1\perp}^2$, somewhat pointing to stronger evolution effects of perturbative origin that seem to be absent in the "μ_b scale" scheme (where the scale choice minimizes the effect of large logarithms in the perturbative coefficients). It is important to notice that there is a significant overlap between the band with dot-dashed borders in the "fixed scale" scheme and the light-gray band with solid borders in the "μ_b scale" scheme. Apparently, the normalized multiplicity seems not to be enough sensitive to discriminate among different evolution schemes, since two different choices of them can produce similar results with different evolution parameters $\{b_{\max}, g_2\}$. However, this result is observed at a specific value of fractional energies of the final hadrons, namely $z_1 = z_2 = 0.5$.

In Fig. 6.4, we show the $\boldsymbol{P}_{1\perp}^2$ distribution of normalized multiplicities calculated in the same conditions, notation and conventions as in the previous figure, but at $z_1 = 0.3$ and $z_2 = 0.5$. The band with dot-dashed borders in the "fixed scale" scheme can now be easily separated from the light-gray band with solid borders in the "μ_b scale" scheme if the estimated experimental error is around 7%. Therefore, only when combining the study of the z and $\boldsymbol{P}_{1\perp}^2$ dependencies in the normalized multiplicity we may be able to discriminate among different evolution schemes.

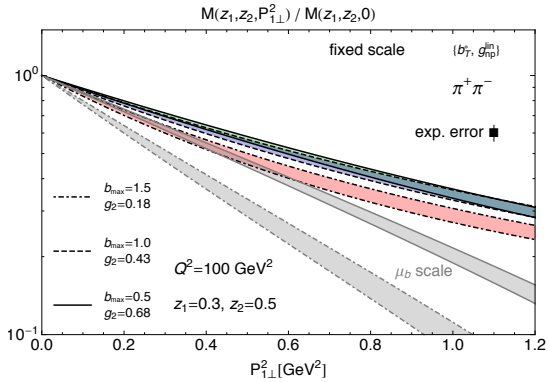

Figure 6.4. The same as in the previous figure, but at $z_1 = 0.3$.

6.5.3 Sensitivity to prescriptions for the transition to nonperturbative transverse momenta

We now focus on exploring the possibility of discriminating among different prescriptions that describe the functional dependence in b_T of the nonperturbative Sudakov evolution factor (see Eqs. (6.3.16) and (6.3.17)) or the transition from the perturbative low$-b_T$ domain to the nonperturbative high$-b_T$ one (see Eqs. (6.3.14) and (6.3.15)).

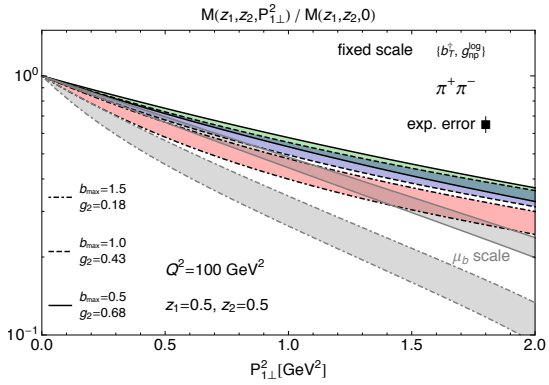

Figure 6.5. The normalized multiplicity at $z_1 = z_2 = 0.5$ as a function of $\boldsymbol{P}_{1\perp}^2 = z_1^2 \boldsymbol{q}_T^2 \equiv (0.5)^2 \boldsymbol{q}_T^2$ at the BELLE scale $Q^2 = 100$ GeV^2 for the "fixed scale" evolution scheme and with the $\{b_T^\dagger, g_{\rm np}^{\rm log}\}$ prescription for the transition to the nonperturbative regime (see text). Notation and conventions for the uncertainty bands as in Fig. 6.3.

In Fig. 6.5, the normalized multiplicity of Eq. (6.5.2) is shown as a function of $\boldsymbol{P}_{1\perp}^2 = z_1^2 \boldsymbol{q}_T^2 \equiv (0.5)^2 \boldsymbol{q}_T^2$ at the BELLE scale $Q^2 = 100$ GeV^2 with the $\{b_T^\dagger, g_{\rm np}^{\rm log}\}$ prescription. Again, as in Fig. 6.3 there are two groups of uncertainty bands. The

former one displays the results for the "fixed scale" evolution scheme in the standard notation, *i.e.* for $\{b_{\max} = 1.5,\, g_2 = 0.18\}$ (dot-dashed borders), $\{b_{\max} = 1,\, g_2 = 0.43\}$ (dashed borders), and $\{b_{\max} = 0.5,\, g_2 = 0.68\}$ (solid borders). The two additional light-gray bands correspond to the results with the "μ_b scale" evolution scheme for $\{b_{\max} = 1.5,\, g_2 = 0.18\}$ (dot-dashed borders) and $\{b_{\max} = 0.5,\, g_2 = 0.68\}$ (solid borders). So, also for the $\{b_T^{\dagger},\, g_{\rm np}^{\rm log}\}$ prescription we find the same ambiguity as for the $\{b_T^{*},\, g_{\rm np}^{\rm lin}\}$ one in Fig. 6.3: the overlap of the light-gray band with solid borders and of the band with dot-dashed borders indicates that two different evolution schemes give similar results with different evolution parameters $\{b_{\max},\, g_2\}$. Hence, we wonder if this similar trend suggests that it might not be possible to distinguish between the two schemes. Again, the possible way out is to look at the dependence of the results upon the fractional energy of the final hadrons.

In Fig. 6.6, the normalized multiplicity of Eq. (6.5.1) is shown as a function of $\boldsymbol{P}_{1\perp}^2 = z_1^2 \boldsymbol{q}_T^2$ at the BELLE scale $Q^2 = 100$ GeV^2 for the "μ_b scale" evolution scheme. Also in this plot, there are two groups of uncertainty bands. A group displays the results for the $\{b_T^{\dagger},\, g_{\rm np}^{\rm log}\}$ prescription in the standard notation, *i.e.* for $\{b_{\max} = 1.5,\, g_2 = 0.18\}$ (dot-dashed borders), $\{b_{\max} = 1,\, g_2 = 0.43\}$ (dashed borders), and $\{b_{\max} = 0.5,\, g_2 = 0.68\}$ (solid borders). The group of two light-gray bands correspond to the results with the $\{b_T^{*},\, g_{\rm np}^{\rm lin}\}$ prescription for $\{b_{\max} = 1.5,\, g_2 = 0.18\}$ (dot-dashed borders) and $\{b_{\max} = 0.5,\, g_2 = 0.68\}$ (solid borders). If we focus on the left panel where calculations are performed at $z_1 = z_2 = 0.5$, the two bands with dot-dashed borders are substantially overlapped, thus reinforcing the suspect that it might not be possible to discriminate between the $\{b_T^{*},\, g_{\rm np}^{\rm lin}\}$ and $\{b_T^{\dagger},\, g_{\rm np}^{\rm log}\}$ prescriptions. But if we now turn to the right panel, where the same calculation is performed at $z_1 = 0.3$, $z_2 = 0.5$, we may hope to have a sufficiently small experimental error that discriminates between the two bands with dot-dashed borders. Unfortunately, the plot suggests also that this option seems possible only for the $\{b_{\max} = 1.5,\, g_2 = 0.18\}$ case. And further explorations show that the same calculation, when performed in the "fixed scale" evolution scheme, produces more confusing results. In summary, a combined study of the z and $\boldsymbol{P}_{1\perp}^2$ dependencies in the normalized multiplicity might be able to discriminate among different prescriptions for the nonperturbative effects in the evolution only for a selected set of evolution parameters and schemes.

6.5.4 Sensitivity to hadron fractional-energy dependence

In the previous sections, we found that in several occasions only the combined study of the z and $\boldsymbol{P}_{1\perp}^2$ dependencies of the normalized multiplicity allows for discerning results obtained from different parametrizations and prescriptions in the description of nonperturbative effects in the TMD evolution. This is not accidental. With the approximations adopted in this work, the main difference between the two consid-

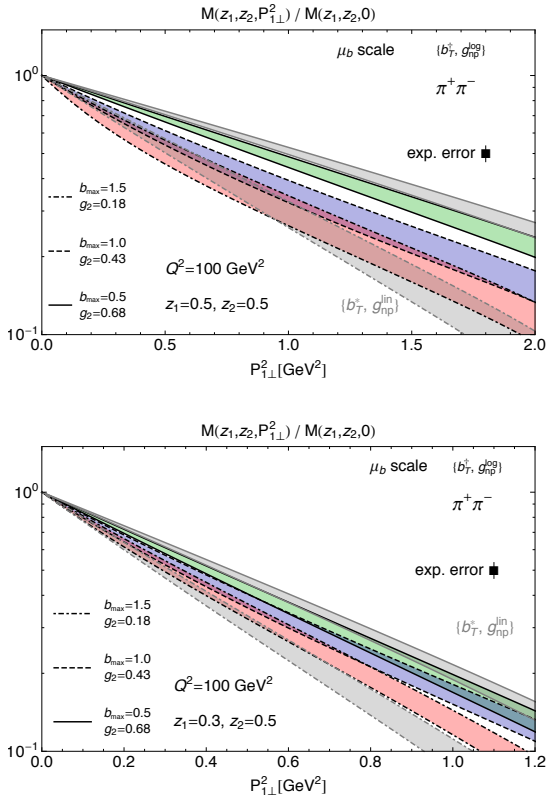

Figure 6.6. The normalized multiplicity at $z_2 = 0.5$ as a function of $\boldsymbol{P}_{1\perp}^2 = z_1^2 \boldsymbol{q}_T^2$ at the BELLE scale $Q^2 = 100$ GeV^2 for the "μ_b scale" evolution scheme and with the $\{b_T^\dagger, g_{\rm np}^{\rm log}\}$ prescription for the transition to the nonperturbative regime (see text). Notation for the uncertainty bands as in previous figure. The additional light-gray bands with dot-dashed and solid borders are the result with the $\{b_T^*, g_{\rm np}^{\rm lin}\}$ matching prescription for $\{b_{\rm max} = 1.5,\, g_2 = 0.18\}$ and $\{b_{\rm max} = 0.5,\, g_2 = 0.68\}$, respectively. Left panel for $z_1 = 0.5$, right panel for $z_1 = 0.3$.

ered evolution schemes lies in fact in the z dependence of the collinear fragmentation function d_1, as it can be deduced by comparing Eqs. (6.3.23) and (6.3.24).

The plots in Fig. 6.7 seem to confirm this finding. In the left panel, the normalized multiplicity of Eq. (6.5.1) is shown as a function of $\boldsymbol{P}_{1\perp}^2 = z_1^2 \boldsymbol{q}_T^2$ at the BELLE scale $Q^2 = 100$ GeV^2 for the "μ_b scale" evolution scheme, the $\{b_T^*, g_{\rm np}^{\rm lin}\}$ prescription, and the choice $\{b_{\rm max} = 1.5,\, g_2 = 0.18\}$. The bands display results for the values $z_1 = 0.3$, $z_2 = 0.5$ (band with dot-dashed borders), $z_1 = z_2 = 0.5$ (dashed borders), and $z_1 = 0.7$, $z_2 = 0.5$ (solid borders). In the right panel, we show the results of the calculations performed in the same conditions but for the "fixed scale" evolution scheme. It is quite evident that the latter scheme produces

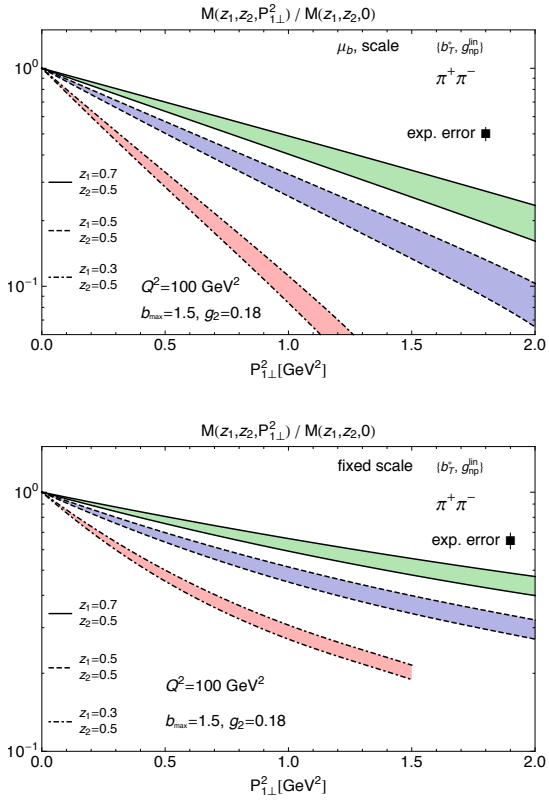

Figure 6.7. The normalized multiplicity at $z_2 = 0.5$ as a function of $\boldsymbol{P}_{1\perp}^2 = z_1^2 \boldsymbol{q}_T^2$ at the BELLE scale $Q^2 = 100$ GeV^2 for the evolution parameters $\{b_{\max} = 1.5,\, g_2 = 0.18\}$ and with the $\{b_T^*,\, g_{\rm np}^{\rm lin}\}$ prescription for the transition to the nonperturbative regime (see text). Uncertainty band with dot-dashed borders for $z_1 = 0.3$, with dashed borders for $z_1 = 0.5$, with solid borders for $z_1 = 0.7$. The squared box with error bar corresponds to an experimental error of 7%. Left panel for the "μ_b scale" evolution scheme, right panel for the "fixed scale" one.

$\boldsymbol{P}_{1\perp}^2$ distributions that are systematically larger for any combination of $\{z_1, z_2\}$. This finding holds true also for other choices of the evolution parameters $\{b_{\max},\, g_2\}$ and for the $\{b_T^\dagger,\, g_{\rm np}^{\rm log}\}$ prescription.

6.5.5 Sensitivity to the hard scale: from BELLE to BES III

All previous results have been obtained at the BELLE scale of $Q^2 = 100$ GeV^2. We may wonder what happens when reducing the "evolution path" to lower scales, like, e.g., the BES III scale $Q^2 = 14.6$ GeV^2.

In Fig. 6.8, the normalized multiplicity of Eq. (6.5.2) is shown as a function of $\boldsymbol{P}_{1\perp}^2 = z_1^2 \boldsymbol{q}_T^2 \equiv (0.5)^2 \boldsymbol{q}_T^2$ in the same conditions and notation as in Fig. 6.2

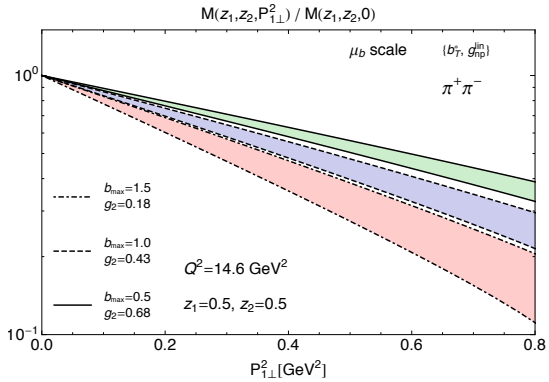

Figure 6.8. The normalized multiplicity of Eq. (6.5.2) as a function of $\boldsymbol{P}_{1\perp}^2 = z_1^2 \boldsymbol{q}_T^2 \equiv (0.5)^2 \boldsymbol{q}_T^2$ at the BES III scale $Q^2 = 14.6$ GeV^2 for the "μ_b scale" evolution scheme and with the $\{b_T^*, g_{\rm np}^{\rm lin}\}$ prescription for the transition to the nonperturbative regime (see text). Notation and conventions for the uncertainty bands as in Fig. 6.2.

but at the BES III scale $Q^2 = 14.6$ GeV^2. By comparing these results with the ones in Fig. 6.2, we deduce that the net effect is a systematic enlargement of the uncertainty bands. This finding occurs also for other combinations of evolutions schemes and nonperturbative prescriptions. Hence, we deduce that working at the BES III scale is not useful if we want to discriminate among different evolution parameters $\{b_{\rm max}, g_2\}$, or between the $\{b_T^*, g_{\rm np}^{\rm lin}\}$ and $\{b_T^\dagger, g_{\rm np}^{\rm log}\}$ prescriptions, or between the "fixed scale" and "μ_b scale" evolution schemes.

However, we recall that each uncertainty band is the envelope of the 68% of 200 different curves, each one corresponding to a specific replica of the intrinsic parameters entering the Gaussian widths $\langle \boldsymbol{P}_\perp^2 \rangle^{a\to h}(z)$ of Eq. (6.3.1) for the b_T distribution of the D_1^a at the starting scale in the evolution. Then, we might envisage that the experimental error is sufficiently smaller than the band width such that it is able to discriminate some of the replicas, in order to narrow the uncertainty on the intrinsic parameters. In any case, this goal will be achieved only by performing additional more precise measurements of SIDIS multiplicities for different final hadron species and on different targets.

6.5.6 Sensitivity to partonic flavor

The sensitivity to the nonperturbative intrinsic parameters, that describe the b_T distribution of the TMD FF at the initial scale of evolution, is an important issue. The analysis of SIDIS multiplicities at low Q^2 suggests that some of these parameters are different for different flavors [174]. Hence, we expect that also the distribution in transverse momentum space of the evolved TMD FF will depend on the flavor of the fragmenting partons. However, the cross section in Eq. (6.2.9)

mixes all flavors in the sum. Therefore, it is useful to define an observable that is well suited to explore the effect of flavor in the TMD evolution.

In the following, we will show results for the $\boldsymbol{P}_{1\perp}^2$ distribution of ratios of normalized multiplicities corresponding to different final states:

$$M^{h_1h_2}(z_1, z_2, q_T^2, y)/M^{h_1h_2}(z_1, z_2, 0, y) \times \left[M^{h_1'h_2'}(z_1, z_2, q_T^2, y)/M^{h_1'h_2'}(z_1, z_2, 0, y)\right]^{-1} . \tag{6.5.3}$$

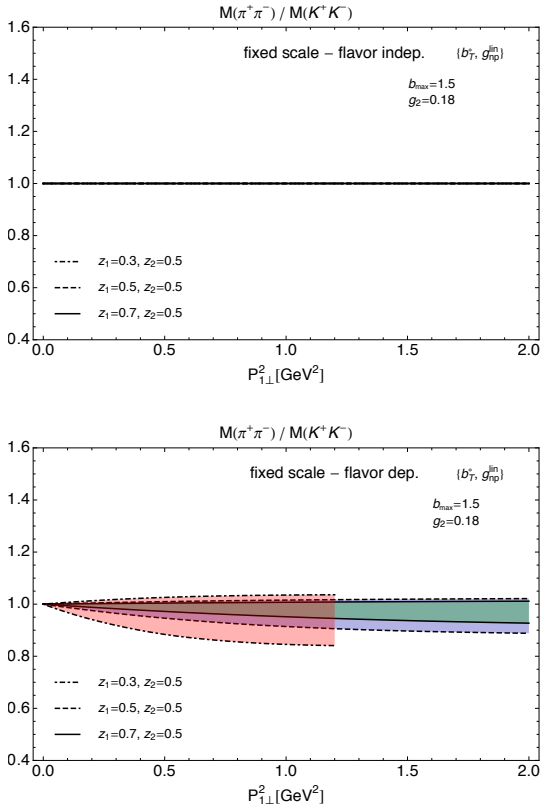

Figure 6.9. Tha ratio of normalized multiplicities in Eq. (6.5.3) between the $\{\pi^+\pi^-\}$ final state and the $\{K^+K^-\}$ final state at $z_2 = 0.5$ and $y = 0.2$ as a function of $\boldsymbol{P}_{1\perp}^2 = z_1^2\boldsymbol{q}_T^2$ at the BELLE scale $Q^2 = 100$ GeV^2 for the "fixed scale" evolution scheme, for the evolution parameters $\{b_{\max} = 1.5,\ g_2 = 0.18\}$, and with the $\{b_T^*,\ g_{\rm np}^{\rm lin}\}$ prescription for the transition to the nonperturbative regime (see text). Uncertainty bands with dot-dashed, dashed, and solid borders for $z_1 = 0.3,\ 0.5,\ 0.7$, respectively. Left panel for flavor independent intrinsic parameters of input TMD FF, right panel for flavor dependent ones (see text).

In Fig. 6.9, we show the ratio of Eq. (6.5.3) between the normalized multiplicity for $\{\pi^+\pi^-\}$ and the one for $\{K^+K^-\}$ at $z_2 = 0.5$ and $y = 0.2$ as a function of $\boldsymbol{P}_{1\perp}^2 =$

$z_1^2 \boldsymbol{q}_T^2$ at the BELLE scale $Q^2 = 100$ GeV^2 for the "fixed scale" evolution scheme, for the evolution parameters $\{b_{\max} = 1.5, g_2 = 0.18\}$, and with the $\{b_T^*, g_{\rm np}^{\rm lin}\}$ prescription for the transition to the nonperturbative regime.

If we suppose to switch off the flavor dependence of the intrinsic parameters, the b_T distribution of the TMD FF in Eq. (6.3.24) is controlled by the same Gaussian width $\langle \boldsymbol{P}_\perp^2 \rangle(z)$ for all channels. This feature remains valid when performing the Bessel transform to momentum space, such that the $\boldsymbol{q}_T^2$ distribution of the cross section can be factorized out of the flavor sum. Therefore, if we take the ratio of normalized multiplicities at the same z_1 we expect the latter to be independent of $\boldsymbol{P}_{1\perp}^2 = z_1^2 \boldsymbol{q}_T^2$. This is indeed the result displayed in the left panel of Fig. 6.9. It is a systematic feature of the "fixed scale" evolution scheme: it holds true for other values of z_1, as shown in the panel, but also for other combinations of nonperturbative evolution parameters and nonperturbative prescriptions.

If we account for the flavor dependence of the Gaussian widths $\langle \boldsymbol{P}_\perp^2 \rangle^{q\to h}(z)$, then the b_T distribution is different for the $\{\pi^+\pi^-\}$ final state from the one for $\{K^+K^-\}$. Consequently, the ratio of normalized multiplicities has a specific $\boldsymbol{P}_{1\perp}^2 = z_1^2 \boldsymbol{q}_T^2$ distribution that, of course, changes with z_1. This is indeed the content of the right panel in Fig. 6.9: the uncertainty band of the 68% of 200 replicas of Gaussian widths with dot-dashed borders corresponds to $z_1 = 0.3$, the band with dashed borders to $z_1 = 0.5$, the band with solid borders to $z_1 = 0.7$.

Almost all the ratios are smaller than unity because in our approximations the fragmentation into kaons has two favoured channels while the fragmentation into pions only one and the $\boldsymbol{P}_{1\perp}^2$ distribution of the fragmentation into kaons seems to be larger than the corresponding one for pions (see the analysis in [174]). In any case, we believe that the inspection of the $\boldsymbol{P}_{1\perp}^2$ distribution of ratios of normalized multiplicities for different final hadrons produced in future e^+e^- annihilation experiments is a useful tool to discriminate among different scenarios in TMD evolution. For example, if future data for this observable will lie well above unity, the "fixed scale" evolution scheme would be ruled out, independently of the flavor dependence of the intrinsic parameters in the TMD FF at the initial scale of evolution.

In Fig. 6.10, in the two panels of the upper row we show the same ratio of normalized multiplicities in the same conditions and notation as in the previous figure but for the "μ_b scale" evolution scheme. The left panel still corresponds to the case when the flavor dependence of the intrinsic parameters is neglected. However, in the "μ_b scale" scheme the b_T distribution of the TMD FF is influenced also by the collinear part of the fragmentation function: the $d_1^{q\to h}$ in (6.3.23) is evaluated at the running scale $\mu_{\hat{b}}$ which is related to b_T via (3.7.7), (6.3.14), (6.3.15). Hence, when performing the Bessel transform of D_1^q in the cross section, the resulting $\boldsymbol{q}_T^2$ distribution depends on the flavor of the fragmenting parton even if the intrinsic parameters do not. This "perturbative" flavor dependence, induced by RGE acting on the evolved collinear part of the TMD FF, mixes with the possible flavor depen-

dence of the intrinsic parameters, making it rather difficult to disentangle the two effects. The left panel in the upper row shows the ratio of normalized multiplicities as a function of $\boldsymbol{P}_{1\perp}^2 = z_1^2 \boldsymbol{q}_T^2$ for three different values of z_1. As in the previous figure, the band with dot-dashed borders corresponds to $z_1 = 0.3$, the band with dashed borders to $z_1 = 0.5$, and the band with solid borders to $z_1 = 0.7$. Suprisingly, all the ratios are larger than unity. When including also the flavor dependence in the intrinsic parameters, the uncertainty bands become larger because there is a marked sensitivity to all possible replica values of the intrinsic parameters themselves. Again, as in the previous section we can argue that experimental data will have a sufficiently small error to discriminate among the various replicas.

A further constraint can be achieved by considering a different combination of final state hadrons in the ratio of normalized multiplicities in Eq. (6.5.3). The lower panel in Fig. 6.10 shows the results for the ratio between a $\{\pi^+\pi^-\}$ final state and a $\{\pi^+K^-\}$ final state when neglecting the flavor dependence of intrinsic parameters of the TMD FF at the initial scale. The notation and conventions are the same as in the other panels. All the ratios are now lower than unity. Hence, combining this result with the content of the upper left panel could represent a very selective test of the "μ_b scale" evolution scheme. In fact, when neglecting the flavor dependence of intrinsic parameters the $\boldsymbol{P}_{1\perp}^2$ distribution of normalized multiplicities for the $\{\pi^+\pi^-\}$ final state should be larger than the one for $\{K^+K^-\}$ at any z_1, while at the same time it should turn out narrower than the one for $\{\pi^+K^-\}$ at any z_1. Moreover, if future data for the $\{\pi^+\pi^-\}$ back-to-back production in e^+e^- annihilation will display a much narrower $\boldsymbol{P}_{1\perp}^2$ distribution than for the $\{K^+K^-\}$ production, at least by 20%, this will represent a further selective test for calculations performed in this evolution scheme, as it can be deduced by combining the results in the panels of the upper row.

Finally, we notice that because of charge conjugation symmetry (see (6.4.1)) we predict that the ratio between normalized multiplicities leading to (π^+, K^-) and (π^-, K^+) final states should be equal to unity, irrespective of the choice of evolution schemes, nonperturbative evolution parameters and prescriptions. It would be interesting to cross-check this prediction by measuring this ratio as a function of $\boldsymbol{P}_{1\perp}^2$.

6.6 Summary

In this chapter, we consider the semi-inclusive production of two back-to-back hadrons in electron-positron annihilation. We study the transverse momentum distribution of such pairs of hadrons by observing the mismatch between their collinear momenta, and we focus on charge-separated combinations of pions and kaons. We conveniently define the multiplicities in electron-positron annihilation as the differential number of back-to-back pairs of hadrons produced per corre-

sponding single-hadron production, in analogy to the definition of multiplicity in SIDIS process. In particular, we analyze the multiplicities normalized to the point of vanishing transverse momentum in order to extract clean and uncontaminated details on the transverse momentum dependence of the functions describing the fragmentation process (transverse-momentum dependent fragmentation functions - TMD FFs). The normalized multiplicities are advantageous also because they turn out to be almost insensitive to the theoretical uncertainty related to the arbitrary choice of the renormalization scale.

We consider electron-positron annihilation at large values of the center-of-mass (cm) energy, namely in the experimental conditions of the Belle and BES III experiments. We study how TMD FFs evolve with the hard scale. The input expression for TMD FFs is taken from a previous analysis of SIDIS multiplicities measured by Hermes at low energy, which is assumed as the starting scale. Since the hard scale in annihilation processes is much larger, we perform realistic tests on the sensitivity to various implementations of TMD evolution available in the literature.

We find that within a specific evolution scheme the transverse momentum distribution of normalized multiplicities at the Belle scale can be very sensitive to the choice of the parameters describing the nonperturbative part of the evolution kernel. An estimated 7% error in such data (compatible with the observed experimental error in collinear back-to-back emissions in electron-positron annihilation) could discriminate among different choices of parameters that are justified and adopted in the literature.

But we observe also that at the same Belle scale different evolution schemes with different nonperturbative parameters can give overlapping transverse momentum distributions. Our global results indicate that different evolution schemes can be discriminated only by considering the combined dependence of normalized multiplicities on both the transverse momentum and the fractional energy carried by the final hadrons. And this finding holds true (with some limitations) also for the purpose of discriminating among different prescriptions for describing the transition from nonperturbative to perturbative regimes in transverse momentum.

The dependence on the fractional energy of the final hadrons is contained in the collinear part of the TMD FFs. Different evolution schemes produce different evolution effects also in the collinear fragmentation functions, which in turn emphasize the differences in the final transverse momentum distribution of evolved TMD FFs. The dependence on the fractional energy is contained also in the average squared transverse momenta that describe the width of the input distribution of the TMD FFs at the starting scale. Therefore, by studying this dependence it may be possible to reduce the uncertainty on the intrinsic parameters that describe these input distributions.

To this purpose, focusing on the normalized multiplicities at the BES III scale

looks more promising. In fact, we observe that in stepping down from Belle to BES III scale the transverse momentum distributions of normalized multiplicities become much more sensitive to the details of the input distribution at the starting scale. The uncertainty in the determination of the intrinsic parameters needed to fit the Hermes SIDIS multiplicities reflects in a larger spread of normalized multiplicities as functions of transverse momentum. At the BES III scale, an expected experimental error of 7% does not discriminate among results coming from different nonperturbative evolution parameters or from different evolution schemes. But within a specific choice of evolution scheme it can discriminate among results that come from different values of the intrinsic parameters.

The Hermes results allow energy show significant differences between SIDIS multiplicities for final-state pions and kaons. Hence, these data were fitted using transverse momentum distributions for the input TMD FFs that contain flavor dependent parameters. Here, we explore also how the final results for normalized multiplicities at Belle and BES III scales are sensitive to the details of this flavor dependence at the starting scale. In doing so, we find that the most convenient observable is represented by the ratio of normalized multiplicities for different final hadron species, particularly at the Belle scale.

The most striking evidence is for evolution schemes where the flavor dependence is strictly localized only in the intrinsic parameters of the input TMD FFs at the starting scale. If we switch off such flavor dependence, the transverse momentum distribution of normalized multiplicities is always the same, irrespective of the species of final hadrons. So, if we select for example pions and kaons, the ratio of the corresponding normalized multiplicities is constant and equal to unity. If the flavor dependence of the intrinsic parameters is switched on, then the ratio deviates to values (mostly) lower than unity, in agreement with general expectations that kaons have a larger distribution in transverse momentum.

The situation is more confused for evolution schemes where the flavor dependence is indirectly contained also in the initial conditions of the evolution equations through the (flavor dependent) collinear part of the fragmentation functions. In this case, this effect mixes up with the flavor dependence contained in the intrinsic transverse momentum distribution, and it is difficult to disentangle one from the other. At variance with the previous class of evolution schemes, in this case the ratio of normalized multiplicities for pions with respect to kaons turns out to be (mostly) larger than unity. Fortunately, more selective criteria are offered by considering a variety of species of final hadrons. If we consider ratios of normalized multiplicities for pions with respect to mixed pion-kaon pairs, the results are (mostly) lower than unity. By combining the results for various final states all together, one would hope to constrain the arbitrary ingredients of TMD FFs as much as possible.

We conclude by stressing that all the results and remarks above refer to the unpolarized TMD FFs that describe the fragmentation of an unpolarized parton

into an unpolarized hadron. However, this function is an essential ingredient in all the (spin) azimuthal asymmetries extracted in hard processes like electron-positron annihilation, hadronic collision, and SIDIS. Hence, a better control on the transverse momentum dependence of unpolarized TMD FFs implies also a better knowledge of polarized TMD FFs as well as of (un)polarized TMD parton distributions. For this reason, we are looking forward to a multidimensional analysis of data accumulated by the BELLE and BES III collaborations, possibly including a study of normalized multiplicities for various hadron species as suggested in this work.

Phenomenological impact

Finally, we summarize some of the results relevant for phenomenology, emerging from the analysis presented in this Chapter. First of all, the way QCD evolution is implemented (both via the perturbative accuracy and the nonperturbative models) affects the extraction of nonperturbative information. This needs to be carefully considered when comparing different extractions. Ideally, one should act in such a way to minimize the need for nonperturbative information, where possible. On the other hand, models at low energy need to be as flexible and physically rich as possible.

The evolution of cross sections and multiplicities can help in studying nonperturbative parameters. At higher energies (e.g. the BELLE scale $Q^2 = 100$ GeV^2) it is useful to discriminate among different evolution schemes (Sec. 6.5.2) and pin down parameters related to the evolution itself (here $b_{\max}$ and g_2, see Sec. 6.5.1). At lower energy (e.g. the BES III scale $Q^2 = 14.6$ GeV^2) it is useful to constrain the parameters involved in the intrinsic part of TMD FFs (Sec. 6.5.4). Moreover, considering multiplicities normalized at $q_T = 0$ (Sec. 6.5), we can reduce the sensitivity of the predictions to variations of the renormalization scale (see Fig. 6.2). This is a way of reducing the theoretical error alternative to adding $\mathcal{O}(\alpha_s^n)$ corrections, of relevance in the region of low transverse momentum. At the experimental level, though, this might produce larger systematic errors, which should be kept under control.

Annihilation to final states including pions and kaons simultaneously can be useful to constrain the flavor dependence of the TMD part of FFs (Sec. 6.5.6). Extra care is needed due to the potential mixing of flavor dependence of nonperturbative and perturbative origin, the first related to intrinsic transverse momentum of quarks and the second to different initial conditions for RG evolution equations.

In general, deepening the knowledge of unpolarized FFs is very useful to improve potential extractions of polarized TMDs too via spin asymmetries (see Chap. 4).

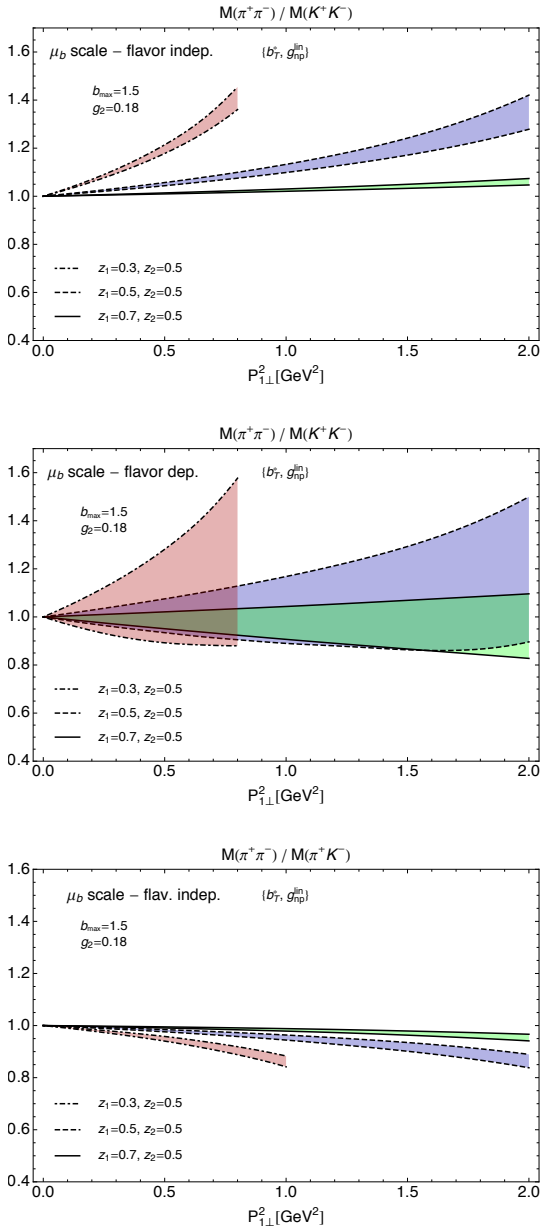

Figure 6.10. Upper panels: same as in previous figure but for the "μ_b scale" evolution scheme. Lower panel: the ratio between the normalized multiplicities $M^{\pi^+\pi^-}(z_1, z_2 = 0.5, q_T^2, y = 0.2)/M^{\pi^+\pi^-}(z_1, z_2 = 0.5, 0, y = 0.2)$ and $M^{\pi^+K^-}(z_1, z_2 = 0.5, q_T^2, y = 0.2)/M^{\pi^+K^-}(z_1, z_2 = 0.5, 0, y = 0.2)$ as a function of $\boldsymbol{P}_{1\perp}^2 = z_1^2 \boldsymbol{q}_T^2$ at the Belle scale $Q^2 = 100$ GeV^2 in the same conditions and with the same notation as in the upper panels, but for flavor independent intrinsic parameters of input TMD FF (see text).

CHAPTER 7

ELECTROWEAK BOSON PRODUCTION

The aim of science is not open
the door to infinite wisdom,
but to set a limit on infinite error.
B. Brecht

In this Chapter we present a study of the impact of the flavor dependence of partonic transverse momentum extracted from SIDIS data and presented in Chap. 5 on the q_T spectrum of electroweak gauge bosons produced in proton-proton collisions at the LHC. In Sec. 7.1 we outline some motivations for such a study. In Sec. 7.2 we review some determinations of the mass of the W boson and the associated uncertainties. In Sec. 7.3 we review the flavor-dependent Gaussian formalism to account for the intrinsic transverse motion of quarks. In Sec. 7.4 we estimate the impact of different physical effects on the position of the peak for the q_T spectrum of electroweak bosons. In Sec. 7.5 we summarize the results and outline possible future directions. Text and results are partly based on [257].

7.1 Introduction and motivation

Electroweak precision observables are highly sensitive to loop contributions, also from potential new physics. For this reason, these observables are interesting benchmarks to test the limits of the Standard Model and to discriminate between different possible scenarios of new physics (see, e.g. [258]). The mass of the W boson, m_W, is an example of such an observable. Its value and the associated uncertainties can potentially help in discriminating among scenarios for new physics. The most precise determination of m_W has been performed by Tevatron (see Sec. 7.2) and further

improvements are expected from LHC measurements. In order to maximally benefit of its precise determination, we need to control all the sources of uncertainties. The q_T spectrum (and in particular the bulk of the cross section, concentrated around the peak) of $W^\pm$ and Z is among the observables relevant for the determination of the W mass.

In this chapter, we focus on the error components coming from the q_T distribution of $W^\pm$, on estimating the uncertainties associated to a flavor dependent treatment of the intrinsic transverse momentum of quarks and on comparing it to other sources. In Sec. 7.4 we look at the impact of the flavor dependence on the position of the peak for the q_T spectra of $W^\pm$ and Z and we find that it is non negligible.

Following the same philosophy, the impact of uncertainties associated to collinear PDFs on the determination of m_W was presented in [259]. Detailed studies of non-perturbative effects in Drell-Yan processes and Higgs production have also been presented in [189, 190].

7.2 Measurements and uncertainties

The most precise determination of m_W has been performed at Tevatron from $p\bar{p}$ collisions. The CDF collaboration [260] measured $m_W = 80.387 \pm 0.019$ GeV. The D0 collaboration [261] obtained $m_W = 80.375 \pm 0.023$ GeV. An extraction from e^+e^- annihilation has been performed by the DELPHI collaboration at LEP, obtaining $m_W = 80.336 \pm 0.055 \pm 0.039$ GeV [6, 262]. An overview of other determinations is available on the Particle Data Group (PDG) website. The LEP and Tevatron average is $m_W = 80.385 \pm 0.015$ GeV, as reported by the PDG 2014 [6].

Let us focus on the hadronic channels. Both analyses at Tevatron did not include the flavor structure in the transverse momentum dependence. In the analysis of CDF, the impact of the g_2 and g_3 parameters[1] of the BLNY model [181] and of the coupling constant α_s have been considered. Fitting Z data, they found that the uncertainty on m_W due to the modeling of the q_T^W distribution via the aforementioned variables are:

$$\delta m_W = 3 \text{ MeV, via } m_T \,, \tag{7.2.1}$$

$$\delta m_W = 9 \text{ MeV, via } p_T^\ell \,, \tag{7.2.2}$$

$$\delta m_W = 4 \text{ MeV, via } p_T^\nu \,, \tag{7.2.3}$$

where m_T is the transverse mass of the W, p_T^ℓ is the transverse momentum of the lepton in the final state and p_T^ν is the transverse momentum of the (anti)neutrino. For convenience, we report Tab. 7.1 from [260], which summarizes the uncertainties

[1] Similar to the ones in (7.3.2).

on m_W via p_T^ℓ. The same overview for m_T and p_T^ν is available in [260]. From Tab. 7.1

Uncertainties on m_W [MeV] from p_T^ℓ fit

Source	$W \to \mu\nu$	$W \to e\nu$	Common
Lepton energy scale	7	10	5
Lepton energy resolution	1	4	0
Lepton efficiency	1	2	0
Lepton tower removal	0	0	0
Recoil scale	6	6	6
Recoil resolution	5	5	5
Backgrounds	5	3	0
PDFs	9	9	9
W boson q_T	9	9	9
Photon radiation	4	4	4
Statistical	18	21	0
Total	25	28	16

Table 7.1. Uncertainties on m_W (in MeV) as resulting from charged-lepton transverse-momentum fits in the $W \to \mu\nu$ and $W \to e\nu$ samples. "W boson q_T" refers to sources discussed before (7.2.1). The last column reports the portion of the uncertainty that is common in the $\mu\nu$ and $e\nu$ results. Original version and definitions in [260].

we see that the uncertainty propagating from the q_T spectrum of the W to its mass via p_T^ℓ is among the largest sources of error, together with the one coming from the collinear distribution functions. In essence, the proton structure and its evolution largely contribute to the uncertainties on m_W. Similar results hold for the analysis of the D0 collaboration [261]. With this work, we want to emphasize the sensitivity of the peak of the q_T spectrum of the $W^\pm$ bosons to the flavor dependence of the intrinsic transverse momentum, which could potentially result in an increase of the uncertainty mentioned in (7.2.1), (7.2.2), (7.2.3).

This could be important in view of a possible study of m_W at the LHC. The ATLAS collaboration published measurement of transverse momentum distributions for W and Z/γ^* bosons from pp collisions [263, 264]. Also CMS published results on the q_T-differential cross section of the Z boson in [265, 266]. For an overview of the measurements available from the Tevatron and the LHC see App. F.

7.3 Formalism

At the LHC, the transverse momentum spectrum of the EW gauge bosons at $q_T \sim m$ (where m is the mass of the produced boson) is described by collinear factorization, by means of unpolarized collinear PDFs dressed with parton showers. In order to describe the low-q_T spectrum and the peak, transverse momentum resummation is included and the intrinsic transverse momentum of partons is modelled with a Gaussian distribution (see e.g. [107]). We stress that a treatment based on TMD factorization describing the full q_T spectrum (Chap. 3) is potentially richer and can introduce also other terms, as the $h_1^\perp$ Boer-Mulders TMD PDF, whose effects at the LHC are yet unconstrained.

The goal of this work is to show that the uncertainties arising from the present level of ignorance about the structure of the proton in momentum space should not be excluded from precision physics programs at hadron colliders like the LHC. Here we focus on the impact of the simplest 3D structure, the unpolarized TMD PDF. A complete study, though, should include all the spin-spin and spin-orbit correlations encoded in TMDs, both for quarks and gluons (Chap. 2).

The Sudakov form factor needs to be dressed with a model to describe the high b_T part of the evolution. The same holds for the TMD PDF, to account for the low intrinsic transverse momentum spectrum. A flavor and kinematic dependent Gaussian model has been recently presented and discussed in [174–177, 214]. As explained in Sec. 5.5, this model is statistically richer than other analyses (e.g. [252]) and we investigate how this additional uncertainties arising from the flavor structure propagate to physical observables.

The tools available on the market, which have been used to compute and analyze the q_T spectra of $W^\pm/Z$ (e.g. ResBos), rely on fits of nonperturbative parameters for the low b_T behavior tuned on world data for Z production. The partonic channels involved in Z production are of the type $q_i\bar{q}_i$. The same information is then used to analyze cross sections for $W^\pm$ production, despite the partonic content is different from the one in Z production, namely $q_i\bar{q}_j$, $i \neq j$. This is equivalent to neglecting the flavor dependence of partonic transverse momentum. The cross section is proportional to the convolution of two TMD PDFs. Assuming Gaussian behavior in the intrinsic transverse momentum and for the high b_T part of the evolution, it reads:

$$\frac{d\sigma}{dq_T}(Z/W^\pm) \sim \sum_{i,j} \exp\left\{ - g_{ij} b_T^2 \right\} , \tag{7.3.1}$$

$$g_{ij} \doteq \frac{\langle k_T^2 \rangle_{q_i}}{4} + \frac{\langle k_T^2 \rangle_{\bar{q}_j}}{4} + 2 g_2 \ln Q^2 \ , \text{ with } i \equiv j \text{ for } Z \text{ and } i \neq j \text{ for } W^\pm \ , \tag{7.3.2}$$

where $\langle k_T^2 \rangle_{q_i}$ is the average square transverse momentum of the quark with flavor i

and g_2 is a nonperturbative parameter governing the strength of evolution at high b_T. In our analysis we take the flavor dependence of $\langle k_T^2 \rangle_{q_i}$ into account, building replicas of $\langle k_T^2 \rangle_{q_i}$, whose values are compatible with the ratios fitted in Chap. 5[2]. The goal is to combine flavor dependent parameters in such a way to respect the values g_{ii} fitted on the Z data, generating at the same time different values g_{ij} to be employed in calculating the transverse momentum distribution for $W^{\pm}$:

$$\begin{aligned} [\text{GeV}]^2 \quad g_{ii}(Z) &\stackrel{\text{fit}}{=} 0.7 = u + \bar{u} = 0.2 + 0.5 \\ &= d + \bar{d} = 0.3 + 0.4 \\ &= \cdots = 0.6 + 0.1 = \cdots \ , \end{aligned} \tag{7.3.3}$$

$$[\text{GeV}]^2 \quad g_{u\bar{d}}(W^+) \equiv u + \bar{d} = 0.2 + 0.4 = 0.6 \ , \tag{7.3.4}$$

and similarly for different flavor configurations[3]. In essence, we study flavor dependent configurations that respect the experimental constraint on Z, producing different distributions for $W^{\pm}$. The impact of g_{ij} on the q_T spectrum of the Z boson has already been addressed in [267], see also Fig. 7.1. The g_{ij} control the position of the peak and affect the low q_T part of the distribution.

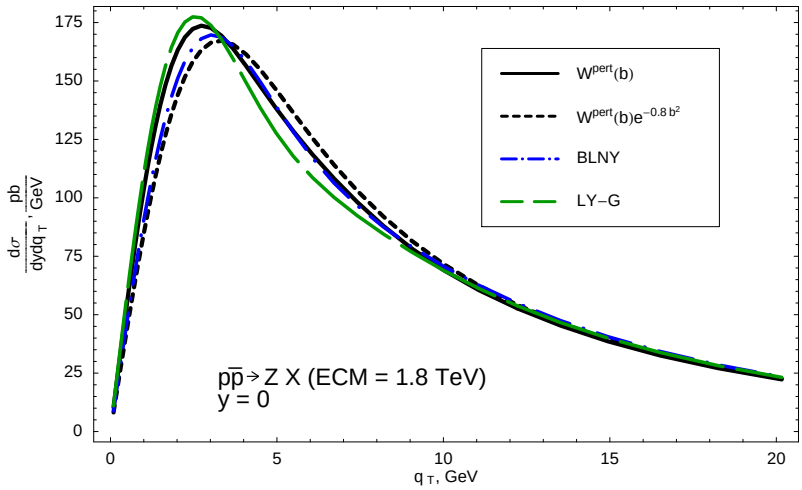

Figure 7.1. Impact of nonperturbative parameters on the Z q_T spectrum at Tevatron. The black line represents the perturbative result, without any nonperturbative smearing. The dashed black line includes a Gaussian factor in momentum space with $g_{ij} = 0.8$ GeV^2. The dot-dashed blue line is generated by means of the BLNY model [181]. The dashed-green line implements the LY model [268]. This plot is from [267].

[2]We neglect the kinematic dependence in this analysis.
[3]The values in (7.3.3) and (7.3.4) are only for illustrative purpose.

From (7.3.2) we see that g_{ij} receives contribution both from the intrinsic transverse momentum of quarks and from soft gluon emissions. In the following we will neglect the latter contribution and decompose the whole g_{ij} by means of flavor dependent ratios. This is both because there are no experimental determinations of g_2 compatible with the perturbative accuracy of the computational tools, and also because the flavor dependence has been investigated in an energy range where the soft gluon radiation is almost negligible. A more complete treatment is left for future works.

Perturbative accuracy

The impact of nonperturbative effects diminishes with increasing the invariant mass of the final states Q. Nonetheless, here we will show that at the $Z/W^{\pm}$ pole they are not negligible: flavor effects introduce an uncertainty on the q_T spectrum comparable to the one originating from the imperfect knowledge of the collinear PDFs. As already explained in Chap. 3, the impact of nonperturbative models changes depending on the perturbative accuracy. Studying precision observable, it is important to use high perturbative accuracy in order to precisely evaluate theoretical uncertainties and avoid misinterpretations of perturbative effects by means of nonperturbative models.

We use three different computational tools to calculate the full q_T spectra: CuTe [108], DyqT [106] and DYRes [107]. CuTe is based on the SCET formalism and produces the transverse momentum spectrum of on-shell electroweak bosons at NLO accuracy in α_s at small-q_T (in the Wilson coefficients) and NNLL[4] in the resummed part (Chap. 3). Resummation is performed in momentum space, namely $\mu = q_T + q^\star$, where $q^\star$ is a cutoff to avoid the Landau pole. DyqT and DYRes are based on the QCD calculation of [106, 107]. The first can describe the production of on-shell electroweak gauge bosons, the second computes the decay products including off-shell effects. Their accuracy is NNLO at small q_T (in the Wilson coefficients) and NNLL in the resummed part. Here transverse momentum resummation is performed in position space, namely $\mu = \mu_{\hat{b}}$ (see Chap. 3). Note that DyqT implements the minimal (complex-b) prescription to distinguish between hard and soft transverse momenta, so its dependence on nonperturbative effects has been minimized. DyRes, instead, relies on the $b^\star$ prescription (see Chap. 3), mainly for computational reasons.

[4]Strictly speaking, CuTe is labelled NNLL in the SCET language and NNLL′ in standard pQCD language. This is because the Wilson coefficients are chosen at NLO, despite the accuracy of the anomalous dimension being the same. In pQCD literature, NNLL′ is considered lower than the NNLL accuracy, which combines with NNLO Wilson coefficients.

7.4 Effects on the peak position

In this section we compare the impact of different effects on the position of the q_T spectrum for Z and $W^{\pm}$ bosons. We consider: changes in the renormalization scale (Sec. 7.4.2), uncertainties from the PDFs (Sec. 7.4.3), changes of α_s (Sec. 7.4.4) and flavor (in)dependent variations of the intrinsic average square transverse momenta on Z and $W^{\pm}$ (Sec. 7.4.5 and 7.4.6). We begin with Tab. 7.2, summarizing all the uncertainties. For more details, see the relevant sections. We choose the tool CuTe to be able to compare with [269]. The relation between different notations for the nonperturbative parameters (e.g. Λ_{NP} and $\langle \mathbf{k}_T^2 \rangle$) is outlined in App. E.

7.4.1 Summary of peak position shifts

In Tab. 7.2 we collect the uncertainties on the position of the peak for $d\sigma/dq_T$ in GeV. "F.i." and "f.d." stand for flavor independent and dependent, respectively. For other definitions and abbreviations see the relevant subsections.

The conclusion we can safely draw is that the uncertainty from scale variation, choice of α_s and the nonperturbative parameter Λ_{NP} (see App. E and [108] for its definition) are all comparable.

The shift in the peak position from f.d. $\langle \mathbf{k}_T^2 \rangle$ is smaller than each of scale variation, α_s and f.i. $\langle \mathbf{k}_T^2 \rangle$, but not by much. It is also bigger than the uncertainty from the pdf set which is the only other uncertainty where the shifts are *not* almost perfectly correlated between the three vector bosons. The f.i variation $\langle \mathbf{k}_T^2 \rangle =$

	W^+		W^-		Z	
$\mu_R = \mu_c/2, 2\mu_c$	$+0.30$	-0.09	$+0.29$	-0.06	$+0.23$	-0.05
pdf (90% cl)	$+0.03$	-0.05	$+0.06$	-0.02	$+0.05$	-0.02
$\alpha_S = 0.121, 0.115$	$+0.14$	-0.12	$+0.14$	-0.14	$+0.15$	-0.15
f.i. $\langle \mathbf{k}_T^2 \rangle = 1.0, 1.96$	$+0.16$	-0.16	$+0.16$	-0.14	$+0.16$	-0.15
f.d. $\langle \mathbf{k}_T^2 \rangle$ (max W^+ effect)	$+0.09$			-0.06	± 0	
f.d. $\langle \mathbf{k}_T^2 \rangle$ (max W^- effect)		-0.03	$+0.05$		± 0	

Table 7.2. Summary of the shifts in GeV for the peak position for q_T spectra of $W^{\pm}/Z$ arising from different sources. The colors for the flavor dependent (f.d.) and independent (f.i.) variations match the ones in Sec. 7.4.6.

$1.0, 1.96$ corresponds to a f.i. variation $\Lambda_{NP} = 0.5, 0.7$ of the parameter relevant for CuTe (see App. E).

7.4.2 Renormalization scale uncertainty

Here we look at how the q_T distribution changes when we vary the renormalization scale between $1/2(q_T + q^\star)$ and $2(q_T + q^\star)$. We are in particular interested in how much the peak of $\mathrm{d}\sigma/\mathrm{d}q_T$ shifts. The scale for the hard part (with the default at $m_{W/Z}$) has not been varied.

The shifts of the peak positions (denoted as q_p in all the figures) are given in Tab. 7.3 in GeV. Shifts of the peak positions are also displayed in Fig. 7.2, 7.3, 7.4.

	Z	W^+	W^-
$\mu = 1/2\,\mu_c$	$+0.23$	$+0.30$	$+0.29$
$\mu = 2\,\mu_c$	-0.05	-0.09	-0.06

Table 7.3. Shifts of the peak positions in GeV induced by μ_r variations.

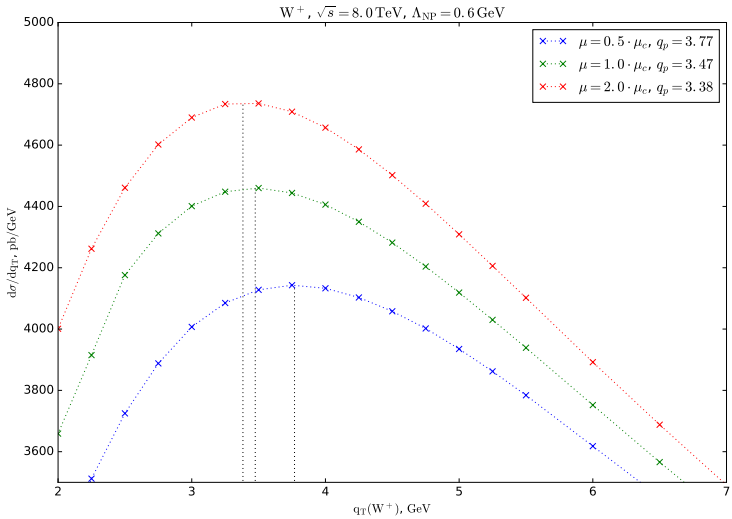

Figure 7.2. Impact of variations of the renormalization scale μ_R by a factor 2 on the peak position in the q_T spectrum of W^+. Calculated by means of CuTe with $\sqrt{s} = 8$ TeV, $\Lambda_{NP} = 0.6$ GeV^2.

7.4.3 PDF uncertainty

Here we look at how the q_T distributions change from one pdf member to the next, using Neural-Network PDFs (NNPDF) 3.0 with $\alpha_S = 0.118$. NNPDF are based

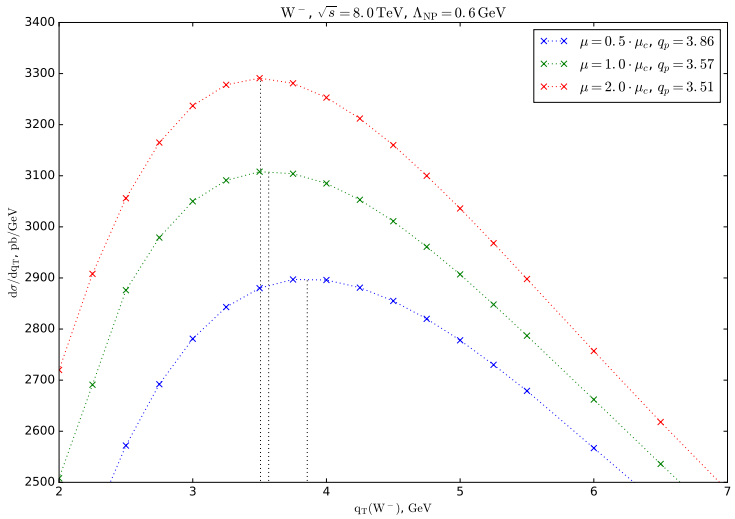

Figure 7.3. Impact of variations of the renormalization scale μ_R by a factor 2 on the peak position in the q_T spectrum of W^-. Calculated by means of CuTe with $\sqrt{s} = 8$ TeV, $\Lambda_{NP} = 0.6$ GeV^2.

on a replica methodology and we will use this feature to test the uncertainty. We determine the position of the peak for every pdf member, then we determine the smallest interval which contains 68% or 90% of the peak positions. The boundaries of the interval determine the lower and upper shifts of the peak position in GeV. In GeV, results are summarized in Tab. 7.4. Impact on the peak positions are also

	90% (lower)	68% (lower)	68% (upper)	90% (upper)
Z	-0.02	-0.02	$+0.03$	$+0.05$
W^+	-0.05	$+0.03$	$+0.03$	$+0.03$
W^-	-0.02	$+0.00$	$+0.04$	$+0.06$

Table 7.4. Shifts of the peak positions in GeV induced by the PDFs.

presented in Fig. 7.5, 7.6, 7.7.

7.4.4 α_s uncertainty

Here we use the NNPDF 3.0 set with $\alpha_s = 0.115$, $\alpha_s = 0.121$, corresponding to variations of 0.03 of the world average value $\alpha_s(m_Z) = 0.118 \pm 0.0007$ [6,270]. The

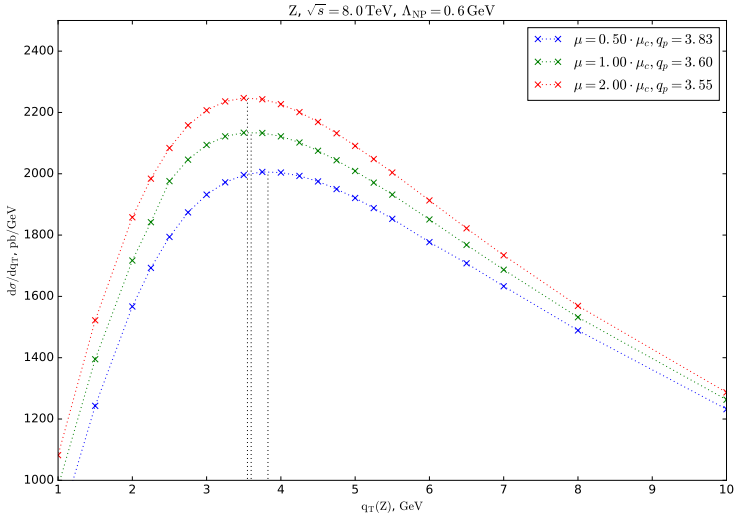

Figure 7.4. Impact of variations of the renormalization scale μ_R by a factor 2 on the peak position in the q_T spectrum of Z. Calculated by means of CuTe with $\sqrt{s} = 8$ TeV, $\Lambda_{NP} = 0.6$ GeV^2.

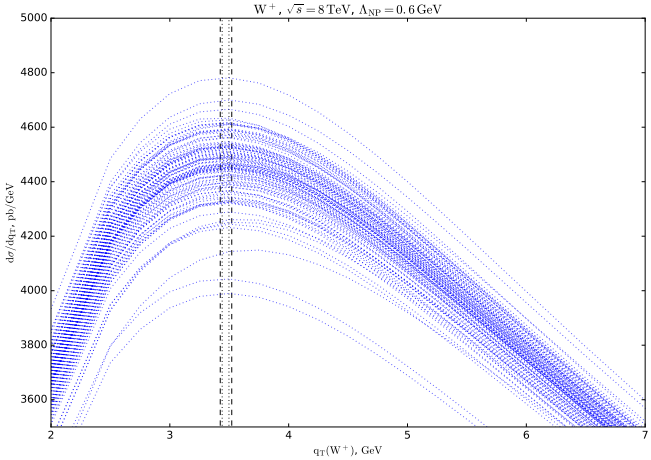

Figure 7.5. Impact of variations of the equally likely PDF members on the peak position in the q_T spectrum of W^+. Calculated by means of CuTe with $\sqrt{s} = 8$ TeV, $\Lambda_{NP} = 0.6$ GeV^2. Tab. 7.4 indicates the ranges (in GeV) in which the peak shifts.

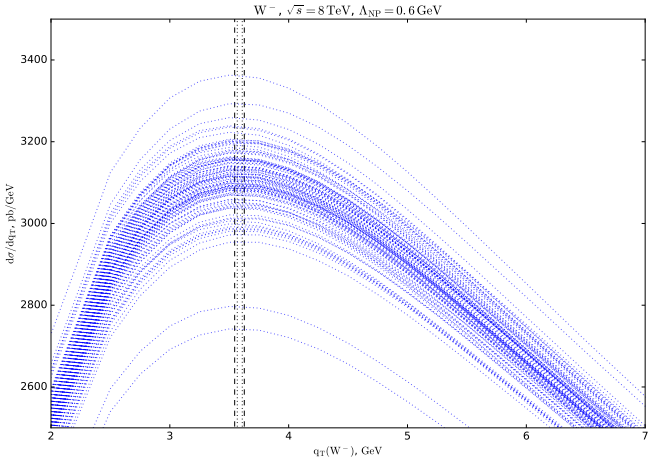

Figure 7.6. Impact of variations of the equally likely PDF members on the peak position in the q_T spectrum of W^-. Calculated by means of CuTe with $\sqrt{s} = 8$ TeV, $\Lambda_{NP} = 0.6$ GeV^2. Numbers in the legenda indicate the ranges (in GeV) in which the peak shifts.

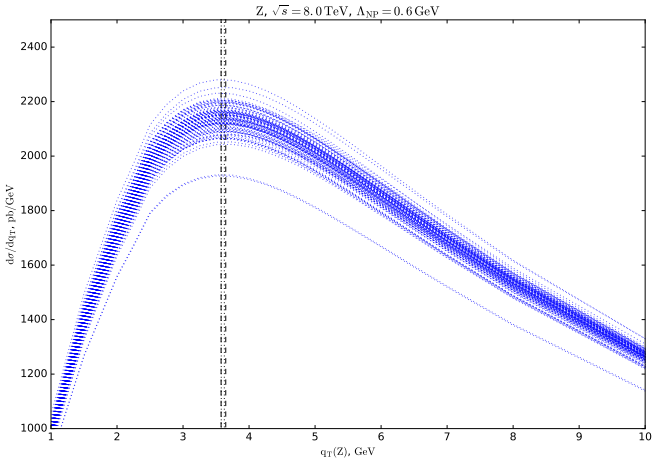

Figure 7.7. Impact of variations of the equally likely PDF members on the peak position in the q_T spectrum of Z. Calculated by means of CuTe with $\sqrt{s} = 8$ TeV, $\Lambda_{NP} = 0.6$ GeV^2. Numbers in the legenda indicate the ranges (in GeV) in which the peak shifts.

shifts of the peaks of the vector boson transverse momentum spectra in GeV are collected in Tab. 7.5. Results for peak positions are also presented in Fig. 7.8, 7.9, 7.10.

	Z	W^+	W^-
$\alpha_s = 0.115$	-0.15	-0.12	-0.14
$\alpha_s = 0.121$	$+0.15$	$+0.14$	$+0.14$

Table 7.5. Shifts of the peak positions in GeV induced by α_s.

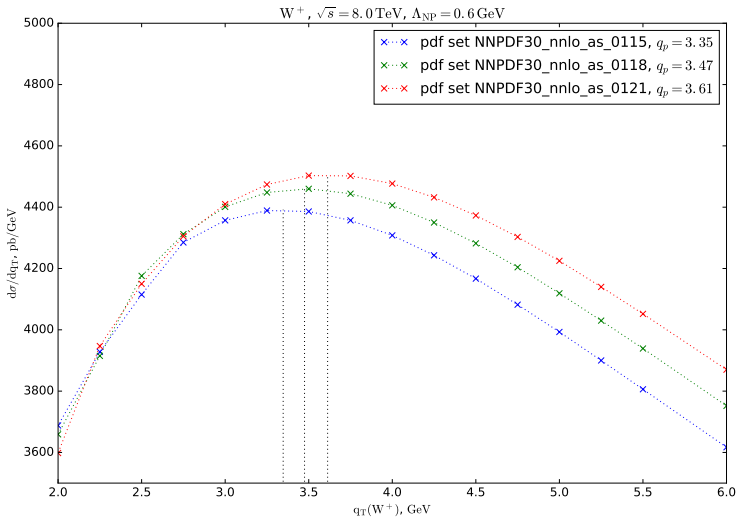

Figure 7.8. Impact of variations of $\alpha_s(m_Z)$ on the peak position in the q_T spectrum of W^+. Calculated by means of CuTe with $\sqrt{s} = 8$ TeV, $\Lambda_{NP} = 0.6$ GeV^2.

7.4.5 Impact of $\langle \mathbf{k}_T^2 \rangle$ on Z peak

Here we are interested in which changes to $\langle \mathbf{k}_T^2 \rangle$ leave the q_T spectrum of Z mostly unchanged. First we look at the ranges for peak positions, using flavor independent variations. The default value is $\langle \mathbf{k}_T^2 \rangle = 1.44$ GeV^2 (corresponding to $\Lambda_{NP} = 0.6$ GeV). In the plot legends we use the abbreviated form $u_v = 1.44$ for $\langle \mathbf{k}_T^2 \rangle_{u_v} = 1.44$ GeV^2. Allowing for a shift in the peak position of about 0.05 GeV, we have

$$\Delta_{\text{peak}} \approx 0.05 \text{ GeV} \;\Rightarrow \Delta\left(\langle \mathbf{k}_T^2 \rangle\right) \approx 0.14 \text{ GeV}^2 \,, \tag{7.4.1}$$

namely the nonperturbative parameter can change up to 10% of its value. The effect is presented in Fig. 7.11. Furthermore, we determine flavor dependent variations of $\langle \mathbf{k}_T^2 \rangle$ such that the Z is slightly affected, maximizing the impact on the peak position for both W^+ and W^-. The results are presented in Fig. 7.12. In Fig. 7.13, we present the same analysis for variations of $\langle \mathbf{k}_T^2 \rangle$ that leave the Z peak completely

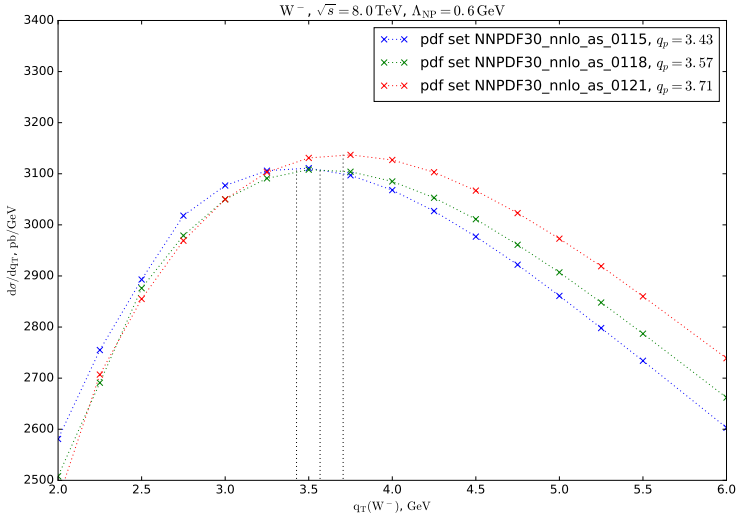

Figure 7.9. Impact of variations of $\alpha_s(m_Z)$ on the peak position in the q_T spectrum of W^-. Calculated by means of CuTe with $\sqrt{s} = 8$ TeV, $\Lambda_{NP} = 0.6$ GeV^2.

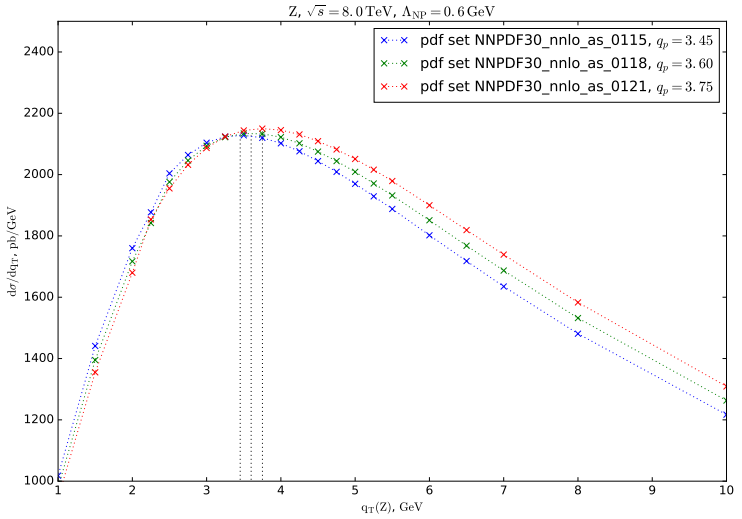

Figure 7.10. Impact of variations of $\alpha_s(m_Z)$ on the peak position in the q_T spectrum of Z. Calculated by means of CuTe with $\sqrt{s} = 8$ TeV, $\Lambda_{NP} = 0.6$ GeV^2.

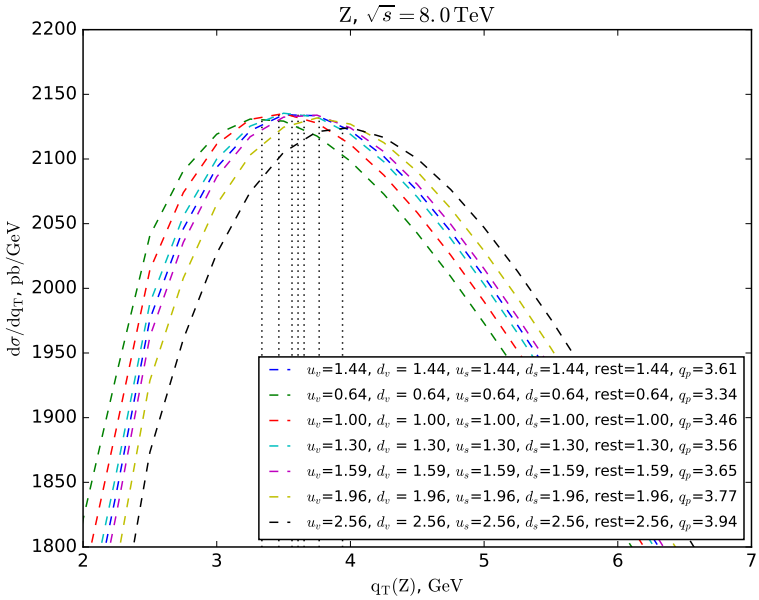

Figure 7.11. Impact of flavor independent variations of the intrinsic momentum of the quarks on the Z peak. Allowing for a shift of the peak around $\pm$ 0.05 GeV, the $\langle \mathbf{k}_T^2 \rangle$ can shift of ± 0.14 GeV^2. The blue (first from top in legenda) line is the reference curve. The light-blue and purple ones (fourth and fifth from top in legenda) correspond to variations of the peak of $\pm$ 0.05 GeV.

unchanged. Among the possible configurations for the flavor dependent $\langle \mathbf{k}_T^2 \rangle$ values, we choose the ones respecting the features of the fit in [174], together with an additional arbitrary constraint on sea quarks. In particular:

$$\begin{aligned} 0.6\, u_v &\leq d_v \leq u_v \\ 0.8\, u_v &\leq 1/2\, (u_s + d_s) \\ 0.5\, u_s &\leq d_s \leq 2\, u_s \\ u_s &\leq 2 u_v \\ d_s &\leq 2 u_v \ . \end{aligned} \tag{7.4.2}$$

The first two conditions reproduces the 68% c.l. intervals in the mentioned fit. The last two ones are compatible with the fit, considering 100% c.l. intervals for the values of the parameters. The third one is an arbitrary condition imposed on the ratio between down and up quarks in the sea, which turns out to be important in the analysis.

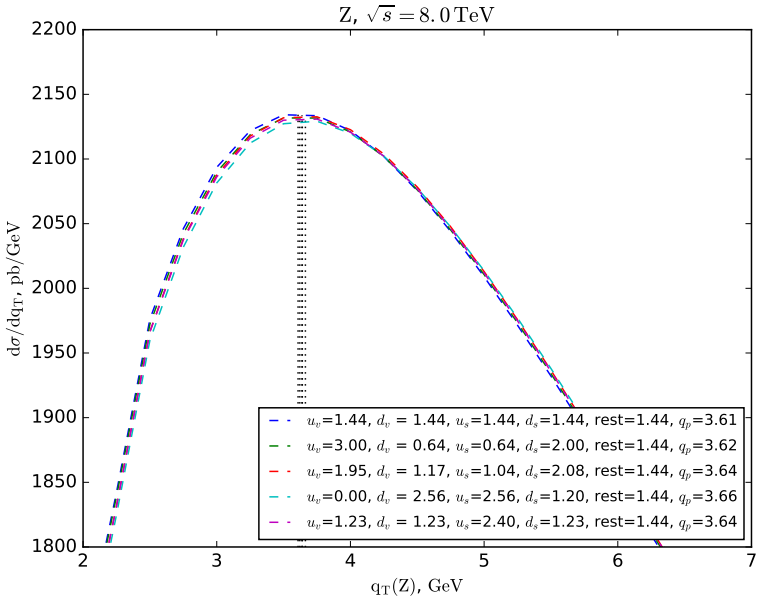

Figure 7.12. Impact of flavor dependent variations of the intrinsic momentum of the quarks on the Z peak. The red (third from top in legenda) and purple (fifth from top in legenda) curves leave the Z peak almost unchanged (with respect to the blue curve, first in legenda) and respect the conditions on the parameter in (7.4.2), which resemble the fit [174] results.

7.4.6 Impact of $\langle \mathbf{k}_T^2 \rangle$ on $W^\pm$ peak

Here we use the flavor dependent parameters which have resulted in a small shift of the Z q_T and apply them to the $W^\pm$. Results are presented in Tab. 7.7 (plots are available via http://tmd.hepforge.org). Then we study the impact on $W^\pm$ for the flavor dependent parameters that leave the Z peak unchanged. Results are collected in Fig. 7.14 and 7.15 and in Tab. 7.8.

Summarizing, using a flavor independent shift in $\langle \mathbf{k}_T^2 \rangle$, the peak positions of Z, W^+ and W^- change in the same way (plots for the impact of flavor independent changes are available via http://tmd.hepforge.org/): see Tab. 7.6.

Allowing for flavor dependent parameters, the correlation among the shifts is lost: see Tab. 7.7. Moreover, we can further tune the parameters by hand such that the Z peak is left perfectly unchanged. We can still have an effect on the $W^\pm$ though: see Tab. 7.8. It is not accidental that the peaks of the W^+ and W^- shift in different directions. Since we select the $\langle \mathbf{k}_T^2 \rangle$ parameters under the constraint that the Z should not be affected, the channels for W^+ and W^- move in different directions necessarily.

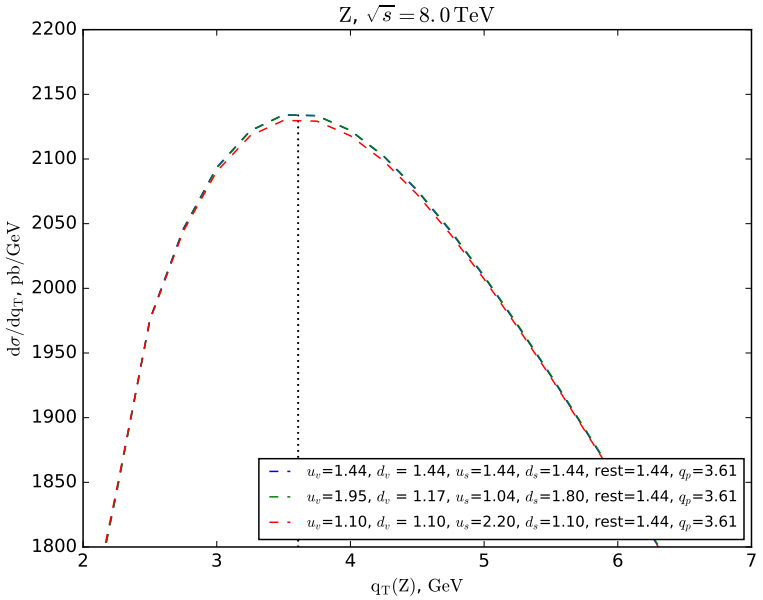

Figure 7.13. Impact of flavor dependent variations of the intrinsic momentum of the quarks on the Z peak. The green (second from top in legenda) and red (third from top in legenda) curves leave the Z peak completely unchanged (with respect to the blue curve, first in legenda) and respect the conditions on the parameter in (7.4.2), which resemble the fit [174] results. Green and red colors correspond to the ones used in Tab. 7.2.

	$\Delta(\langle \mathbf{k}_T^2 \rangle) = -0.14\ \mathrm{GeV}^2$	$\Delta(\langle \mathbf{k}_T^2 \rangle) = +0.14\ \mathrm{GeV}^2$
$\Delta(q_{\mathrm{peak}})\, W^+$	-0.05	+0.05
$\Delta(q_{\mathrm{peak}})\, W^-$	-0.04	+0.05
$\Delta(q_{\mathrm{peak}})\, Z$	-0.05	+0.04

Table 7.6. Peak shifts in GeV from flavor independent variations of $\langle \mathbf{k}_T^2 \rangle$.

	maximise W^+	maximise W^-
$\Delta(q_{\mathrm{peak}})\, W^+$	+0.10	-0.02
$\Delta(q_{\mathrm{peak}})\, W^-$	-0.01	+0.07
$\Delta(q_{\mathrm{peak}})\, Z$	+0.03	+0.03

Table 7.7. Peak shifts in GeV for $W^{\pm}$ from flavor dependent variations of $\langle \mathbf{k}_T^2 \rangle$.

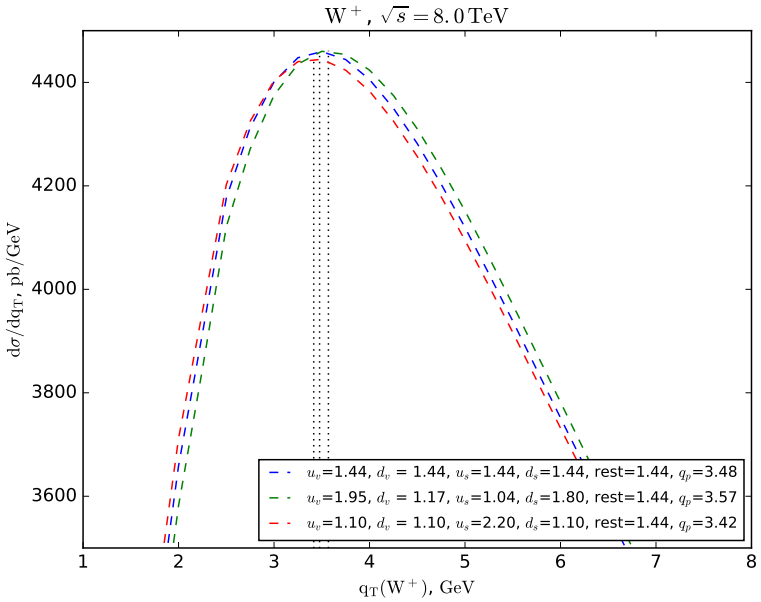

Figure 7.14. Maximal shift for W^+ peak as a result of flavor dependent changes of $\langle \mathbf{k}_T^2 \rangle$ parameters leaving the Z peak unchanged. The green (second from top in the legenda) maximizes the shift for W^+, the red (third from top in the legenda) maximizes the shift for W^-.

	maximise W^+	maximise W^-
$\Delta(q_{\text{peak}})\, W^+$	+0.09	-0.06
$\Delta(q_{\text{peak}})\, W^-$	-0.03	+0.05

Table 7.8. Maximal peak shifts in GeV for $W^\pm$ from flavor independent variations of $\langle \mathbf{k}_T^2 \rangle$ which leave the Z peak unchanged.

The *anticorrelation* of the shifts between W^+ and W^- is one of the most interesting features of this analysis, a peculiarity of this source of uncertainty. With this study, as anticipated by Tab. 7.2, we proved that the uncertainty on the peak position for $W^\pm$ bosons arising from the flavor dependence in the intrinsic transverse momentum is not negligible with respect to the other sources of uncertainties and comparable in magnitude with the errors arising from the collinear PDFs. A similar study has been performed using DyqT at NNLL order of accuracy, obtaining qualitatively similar results.

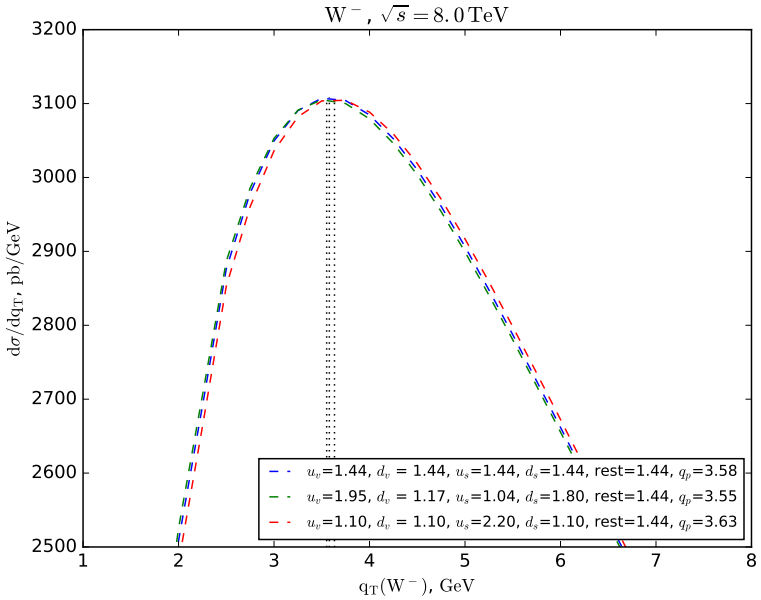

Figure 7.15. Maximal shift for W^- peak as a result of flavor dependent changes of $\langle \mathbf{k}_T^2 \rangle$ parameters leaving the Z peak unchanged. The green (second from top in the legenda) maximizes the shift for W^+, the red (third from top in the legenda) maximizes the shift for W^-.

7.5 Outlook and future developments

Within the framework of transverse-momentum-dependent (TMD) factorization we estimated the impact of flavor-dependent intrinsic transverse momentum on the production of electroweak gauge bosons $W^{\pm}/Z$ at the Large Hadron Collider (LHC) with $\sqrt{s} = 8$ TeV. We evaluate the uncertainty on the position of the peak in the cross section differential with respect to the transverse momentum q_T of the produced boson arising from the intrinsic transverse momentum of quarks, in particular from its flavor dependence. We compare it with other sources of uncertainty and we observe that its magnitude is comparable with the others, thus being not negligible (contrary to the approaches available in literature).

The next step is to investigate a potential impact of the flavor dependence of the quark intrinsic transverse momentum on the value and the uncertainty of m_W. Effort in this direction is currently in progress. In particular, we are comparing the magnitude of the smearing induced on the cross section by the Gaussian intrinsic $\boldsymbol{k}_T$ with the smearing produced by a Breit-Wigner distribution peaked on $m_W = m_W^{PDG}$.

The determination via hadronic collisions of the properties of the W boson, such as the mass m_W, is sensitive to the q_T^W spectrum, in particular the position and the height of its peak. This proves that a detailed knowledge of TMD distributions is important not only for nucleon tomography, but also to constrain fundamental parameters of the Standard Model. In light of the result presented in this chapter, we call for improved investigations of the impact of nonperturbative effects linked to the proton structure at hadron colliders. Following the same philosophy and approach, it would be interesting to perform a study focused on the flavor dependence in the intrinsic transverse momentum of the unpolarized TMD FFs, in order to address production of W^+W^- pairs from e^+e^- annihilation. Such a study could be potentially interesting for the physics program of the future International Linear Collider (ILC).

CHAPTER 8

QUARKONIUM PRODUCTION

The goal of this chapter is to investigate the impact of (un)polarized gluon TMD PDFs in hadronic collisions, for example at the LHC and at A Fixed Target Experiment at the LHC (AFTER@LHC [36]). In the context of high energy proton-proton collisions, we look at final states with low mass (e.g. η_b quarkonium) in order to be able to investigate the nonperturbative part of TMD PDFs. We study the factorization theorem for the q_T spectrum of η_b produced in proton-proton collisions relying on the effective field theory approach, defining the tools to perform phenomenological investigations at next-to-next-to-leading log (NNLL[1]) and next-to-leading order (NLO) accuracy in perturbation theory (see Chap. 3). We provide predictions for the unpolarized cross section and comment on the possibility of extracting nonperturbative information about the gluon content of the proton once data at low transverse momentum are available. For the unpolarized case, we investigate the matching with the high q_T region. Text and results are partly based on [271] and on ongoing research [98].

8.1 Introduction and motivation

In order to have a good sensitivity on nonperturbative effects from the proton structure, we study final states with low invariant mass, such as quarkonium bound states. According to non-relativistic QCD (NRQCD), the latter can be produced in a color-singlet or in a color-octet configuration, which eventually evolves into a physical color-singlet state radiating gluons. For $C = +$ states, NRQCD predicts [272]

[1]From the standard pQCD point of view, this accuracy level is named NNLL′. See the remark in Sec. 7.3.

that color-octet contributions are suppressed with respect to the singlet contributions at least by factors v^2, where v is the relative velocity of the quark-antiquark pair in the bound state. In particular, color-octet contributions can be neglected for $C = +$ bottomonium states [36, 273, 274]. For the $PC = -+$ charmonium state η_c, instead, complications may arise at high transverse momentum [275, 276]. A recent analysis [277], though, shows that LHCb data for η_c production at high q_T are well described by the color-singlet configuration only.

Assuming that the initial gluons are on shell, the Landau-Yang theorem [278, 279] forbids the production of spin 1 states. Since the impact of linearly polarized gluons is heavily suppressed in production of $J = 2$ states [201], we focus on the $J = 0$ case. In the TMD formalism, $J^{PC} = 0^{++}$ (scalar) states have been treated in [125, 201] and 0^{-+} (pseudoscalars) in [201] in a parton model approach.

Here we investigate production of the 0^{-+} state $\eta_b(1S)$ including TMD evolution effects. The value of its mass (9.39 GeV [6]) is low enough in order for the nonperturbative effects to be appreciable (see Fig. 8.1). At the same time, it is high enough, compared to the one of $\eta_c(1S)$ (2.98 GeV), in order to avoid potential pollution from power corrections to the factorization formula. Moreover, the impact of the very small b_T region ($b_T < 1/M_h$, see Sec. 3.7.4) is reduced in the case of η_b.

Phenomenology of q_T spectra for quarkonium production has already been addressed in the literature. For example, in [280] the authors factorize the q_T spectrum of quarkonium production at the LHC in terms of TMD PDFs defined off-the-light-cone. They do not consider the non-relativistic wave function of the bound state, usually calculated by means of NRQCD. In [281] the authors elaborate on the results in [280] and show the breakdown of TMD factorization for P-wave quarkonium states. The authors in [282] suggest that the associated production of a quarkonium state and a photon is a powerful processes to access gluon TMDs at the LHC. The presence of the photon allows for the variation of the invariant mass of the final states and the applicability of TMD evolution over a potentially wide energy range. Within the effective field theory methodology, [283–287] address quarkonium production from the combined SCET+NRQCD point of view, but do not treat the small q_T region. Factorization theorem has been addressed also in [288, 289]. The large q_T region has been studied in [290, 291]. Transverse momentum resummation for heavy-quark hadroproduction in full QCD has been presented in [292]. A review on NRQCD is available in [293].

The novelties of this work rely in studying the factorization theorem for the q_T spectrum of a pseudoscalar quarkonium bound state from an effective field theory point of view, on the possibility of extracting nonperturbative information at low transverse momentum for (un)polarized gluon TMDs and on the calculation of the matching to the high q_T part (Y term, see Sec. 3.3.3).

Linearly polarized gluons at the LHC

At the LHC with unpolarized proton beams, two gluon TMD PDFs play a role: the unpolarized distribution $f_1^g(x, \boldsymbol{k}_T^2)$ and the distribution of linearly polarized gluons $h_1^{\perp g}(x, \boldsymbol{k}_T^2)$ (see Tab. 2.3). The situation is simpler than in the quark case, because $h_1^{\perp g}$ is matched onto twist-2 unpolarized collinear distributions $f_1^{g,q}$ (contrary to the Boer-Mulders TMD PDF $h_1^\perp(x, \boldsymbol{k}_T^2)$, which is matched onto twist-3 collinear matrix elements).

So far no experimental extractions of $h_1^{\perp g}(x, \boldsymbol{k}_T^2)$ have been performed. It would be possible to access it from investigations of spin asymmetries at EIC and LHeC [294, 295] and at RHIC and LHC [296]. Model calculations suggest that this distributions reaches its maximal size in the small-x regime [76, 297, 298]. This has been recently confirmed via the operator analysis in [78]. The impact of linearly polarized gluons in Higgs production has been addressed, e.g., in [89,125,199,299,300]. Their impact has been predicted for gluon fusion to two photons in [296, 301], for quarkonium production in [125, 201], for Higgs plus jet production in [200]. Associated production of quarkonium and Z boson has been investigated in [302].

In order to understand how relevant linearly polarized gluons in unpolarized proton-proton collisions are, it is useful to look at the ratio[2] [89, 125]:

$$\mathcal{R}(x_A, x_B, q_T; Q) \doteq \frac{\int d^2\boldsymbol{b}_T e^{-i\boldsymbol{q}_T\cdot\boldsymbol{b}_T} \tilde{h}_1^{\perp(2)g/A}(x_A, b_T^2; Q)\tilde{h}_1^{\perp(2)g/B}(x_B, b_T^2; Q)}{\int d^2\boldsymbol{b}_T e^{-i\boldsymbol{q}_T\cdot\boldsymbol{b}_T} \tilde{f}_1^{g/A}(x_A, b_T^2; Q)\tilde{f}_1^{g/B}(x_B, b_T^2; Q)} \,. \tag{8.1.1}$$

The involved TMD distributions are defined in App. D, A, B label the two interacting protons and the renormalization and rapidity scales have been fixed to $\mu^2 = \zeta = Q^2$. The ratio in (8.1.1) is presented in Fig. 8.1 at $Q = m_H = 125$ GeV and $Q = m_{\eta_b} = 9.39$ GeV, for different values of the nonperturbative parameters discussed in [89]. For a definition of the nonperturbative parameters λ_Q and $\lambda_{f,h}$ see Sec. 8.3. From Fig. 8.1 we can draw interesting observations. Depending on the value of the nonperturbative parameters chosen in [89], the impact of $h_1^{\perp g}$ ranges between 10% and 70% at low-medium energy of quarkonium production. Their impact at the scale of the Higgs mass, instead, does not exceed 10%. At low and medium energy there is more sensitivity to the values of the nonperturbative parameters as compared to the high-energy case. In agreement with the discussion in Chap. 3 and 4, we conclude that quarkonium production at medium energy is an ideal process to quantify the nonperturbative effects associated to linearly polarized gluons. The latter could then be used to refine predictions also at higher energies, e.g. for the q_T spectrum of the Higgs boson. This holds true also for the nonperturbative effects in the unpolarized gluon TMD PDF f_1. An analogous study for quarks has been presented in Chap. 7, in which the flavor dependence of intrinsic

[2] Considering a pseudoscalar final state, (8.1.1) needs an overall minus sign [201].

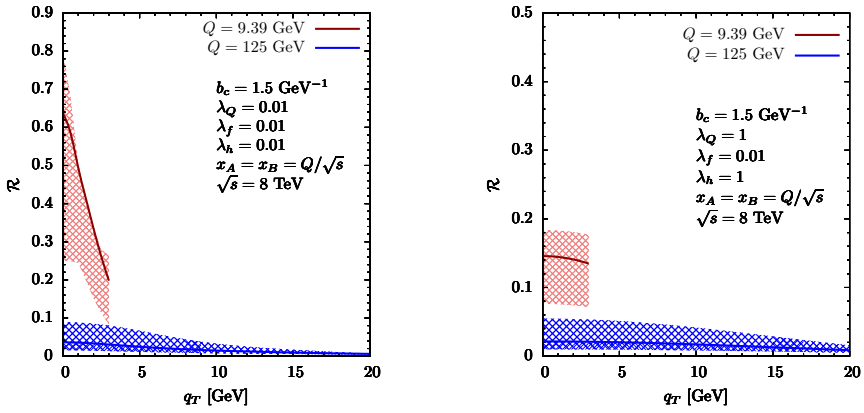

(a) (b)

Figure 8.1. The ratio of linearly polarized to unpolarized gluons at LHC, for different invariant mass in the final state Q and values of nonperturbative parameters. The red line corresponds to cross section for η_b production. The red band arises from variations by a factor of 2 of the renormalization and rapidity scales. The blue line corresponds to cross section for Higgs production. The blue is conceptually identical to the red one. b_c is a cut-off parameter similar to $b_{\max}$ (see Sec. 3.7.3) defined in [89]. λ_Q is the nonperturbative parameter introduced to avoid the Landau pole upon evolution and $\lambda_{f,h}$ represent the intrinsic transverse momenta of unpolarized and linearly polarized gluons (see Sec. 8.3). Figure from [89].

transverse momentum of quarks extracted at low energy reveals to have an impact on $Z/W^{\pm}$ boson production at the LHC.

8.2 Effective description

Let us consider the process

$$p(P_A, S_A) \ + \ p(P_B, S_B) \to \{Q\bar{Q}\}[^{2S+1}L_J^{(1)}](q) \ + \ X \ , \tag{8.2.1}$$

where the colliding protons have mass M, four-momenta P_A and P_B, spin vectors S_A and S_B, with $S_{A,B}^2 = -1$ and $S_A \cdot P_A = S_B \cdot P_B = 0$. We assume that a colorless heavy quark-antiquark pair $Q\bar{Q}[^{2S+1}L_J^{(1)}]$ with four-momentum q is produced and forms a bound state described by a nonrelativistic wave function with spin S, orbital angular momentum L and total angular momentum J. The S, L, J quantum numbers are indicated in the spectroscopic notation, while the color assignment of the pair is specified by the singlet or octet superscript, (1) or (8). Following the color-singlet model, we assume that the two quarks are produced in a color-singlet

state. The squared invariant mass of the resonance is $M_h^2 = q^2$ and M_h is twice the heavy quark mass, up to relativistic corrections (which are usually neglected).

To lowest order in perturbative QCD (pQCD), we have only[3] the gluon fusion process

$$g(p_a) \; + \; g(p_b) \; \to \; \{Q\bar{Q}\}[^{2S+1}L_J^{(1)}](q) \; , \tag{8.2.2}$$

described by the Feynman diagrams in Fig. 8.2.

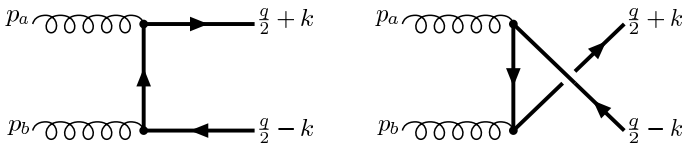

Figure 8.2. Feynman diagrams for the process $gg \to Q\bar{Q}$ at leading order (LO) in pQCD.

8.2.1 Parton model structure

Following the diagrammatic approach (Sec. 2.4), we assume that at sufficiently high energies TMD factorization holds. Using the point of view of frame "A" in Sec. 2.6, the cross section for the process in (8.2.2) can be written as

$$d\sigma = \frac{1}{2s}\,\frac{d^3\boldsymbol{q}}{(2\pi)^3\,2q^0}\int dx_a\,dx_b\,d^2\boldsymbol{p}_{Ta}\,d^2\boldsymbol{p}_{Tb}\,(2\pi)^4\delta^{(4)}(p_a+p_b-q)\times \\ \overline{\sum}_{\text{colors}}\,\Gamma_g^{\mu\nu}(x_a,\boldsymbol{p}_{Ta})\,\Gamma_g^{\rho\sigma}(x_b,\boldsymbol{p}_{Tb})\,\mathcal{A}_{\mu\rho}\,(\mathcal{A}_{\nu\sigma})^* \; , \tag{8.2.3}$$

where $\mathcal{A}$ is the Feynman amplitude for the partonic subprocess [201, 303–305] and Γ_g is a TMD correlator for gluons introduced in Sec. 2.6. In particular, the form in (D.0.12) is used. $s = (P_A + P_B)^2$ is the total energy squared in the hadronic center of mass frame. In the following we consider $p_a^- = p_b^+ = 0$. In the rest frame of the bound state, the relative momentum $2k$ of the two quarks is small compared to their mass M_q, which justifies a nonrelativistic approach.

We consider the production of the quarkonium state $\eta_Q = Q\bar{Q}$, where $Q = b, c$ in particular the spin-color configuration $^{2S+1}L_J^{(1)} = {}^1S_0^{(1)}$. Expanding the expression for $\mathcal{A}$, the cross section depends on NRQCD matrix elements describing the wavefunction of the bound state. The most relevant matrix element for the η_Q is related to the η_Q radial wave function at the origin [272]:

$$\langle 0|\mathcal{O}_1^{\eta_Q}(^1S_0)|0\rangle = \frac{N_c}{2\pi}\,|R_0(0)|^2[1+\mathcal{O}(v^4)]\,, \tag{8.2.4}$$

[3]We neglect t-channel interactions initiated by a $c\bar{c}$ or $b\bar{b}$ pair.

with $N_c = 3$ and valid for production of $J = 0$ states[4]. R_0 is the radial wavefunction of the quarkonium with quantum numbers $n = l = 0$, v is the relative velocity of Q and $\bar{Q}$. The subscript 1 in $\mathcal{O}_1^{\eta_Q}$ represents the color-singlet configuration and v is the velocity of the heavy quarks inside the $Q\bar{Q}$ bound state. The color-octet contribution ${}^1S_0^{(8)}$ is, according to the NRQCD counting rules, suppressed by v^4 [272, 307] with respect to the leading color-singlet term and will not be included. Considering (8.2.3) with correlators for unpolarized protons (D.0.12), evaluating $\mathcal{A}$ for $\eta_Q({}^1S_0^{(1)})$ [201, 303–305], the leading-order cross section at low q_T reads:

$$\frac{d\sigma_{UU}(\eta_Q)}{dy\, d^2\boldsymbol{q}_T} = \frac{2}{9}\frac{\pi^3\alpha_s^2}{M_h^3\, s}\,\langle 0|\mathcal{O}_1^{\eta_Q}({}^1S_0)|0\rangle\,\Big\{\mathcal{C}\,[f_1^g\, f_1^g] \,-\, \mathcal{C}\,\Big[w_{UU}\, h_1^{\perp\, g}\, h_1^{\perp\, g}\Big]\Big\}\,, \tag{8.2.5}$$

Corrections of order $\mathcal{O}(q_T/M_h)$ and $\mathcal{O}(v^2)$ are neglected. The convolutions of TMD PDFs are defined as:

$$\mathcal{C}[w\, f\, f] \equiv \int d^2\boldsymbol{p}_{Ta} \int d^2\boldsymbol{p}_{Tb}\, \delta^2(\boldsymbol{p}_{Ta} + \boldsymbol{p}_{Tb} - \boldsymbol{q}_T)\, w(\boldsymbol{p}_{Ta}, \boldsymbol{p}_{Tb})\, f(x_a, \boldsymbol{p}_{Ta}^2)\, f(x_b, \boldsymbol{p}_{Tb}^2)\,, \tag{8.2.6}$$

In (8.2.5), the transverse momentum weight is [201]:

$$w_{UU} = \frac{p_{Ta}^{\mu\nu}\; p_{Tb\;\mu\nu}}{2M^4}\;. \tag{8.2.7}$$

y is the rapidity of the produced bound state along the direction of the incoming hadrons and, neglecting corrections related to small transverse momenta, the collinear momentum fractions are

$$x_a = \frac{M_h}{\sqrt{s}}\, e^{y}\;, \qquad x_b = \frac{M_h}{\sqrt{s}}\, e^{-y}\;. \tag{8.2.8}$$

Outline of the effective description

Eq. (8.2.3) represents the standard approach to the process in (8.2.1) via the diagrams in Fig. 8.2. In this context, we can introduce an *effective* description, through an effective operator representing the coupling of the gluons to the quarkonium bound state. In particular, the gluons in the initial states will be described by SCET, while the description of the quark-antiquark pair as a color-singlet quarkonium will be described by NRQCD.

TMD factorization (Sec. 3.1 and 3.2) can be viewed as a multi-step matching procedure. For this process:

$$\text{QCD} \to \text{NRQCD} \oplus \text{SCET}_{q_T} \to \text{NRQCD} \oplus \text{SCET}_{\Lambda_{\text{QCD}}}. \tag{8.2.9}$$

[4]For $J \neq 0$ an additional $(2J+1)^{-1}$ factor is needed in (8.2.4) [306].

In the first step, the hard scale M_h associated with the process is integrated out and we perform the matching of full QCD onto a combination of SCET$_{q_T}$ and NRQCD operators. This step, valid when M_h is bigger than any other scale, already factorizes the cross section in terms of TMDs (describing the initial state), a NRQCD matrix element (describing the transition into the quarkonium) and a spin-independent matching coefficient. In the second step, valid when $\Lambda_{\rm QCD} \ll q_T \ll M_h$, the TMDs are further factorized in terms of the collinear PDFs. This matching is performed by means of spin-dependent Wilson coefficients.

The first step has already been investigated at NLO in [280], but with TMDs defined off the light-cone and with rapidity divergences. Here we investigate TMD factorization on the light-cone [96]. Another recent study can be found in [308]. In order to check if TMD factorization holds (or, following the SCET terminology, in order to "establish" TMD factorization) at NLO, we need to check that the cross section expressed in terms of TMDs has the same infrared behavior as the cross section evaluated with $\mathcal{O}(\alpha_s)$ corrections in pQCD.

8.2.2 Effective structure at LO

For the convention regarding light-cone expansions in SCET see App. A (the $\perp$ symbol indicates the transverse components in such a basis). As mentioned in Sec. 3.2, the advantage of SCET$_{q_T}$ is the separation of (anti)collinear and soft modes at the level of the Lagrangian. Subscripts n, $\bar{n}$, s indicate the relevant modes [89].

We define an effective operator for the partonic process as:

$$\mathcal{O}(\xi) = C_H(-q^2;\mu^2)\ \{\chi^\dagger\ \Gamma^{(\eta)}_{\mu\nu}\ \psi\ \mathcal{B}^{\mu,a}_{n\perp}(\xi)\ (\mathcal{S}^\dagger_n \mathcal{S}_{\bar{n}})^{ab}(\xi)\ \mathcal{B}^{\nu,b}_{\bar{n}\perp}(\xi)\}\ , \tag{8.2.10}$$

where C_H is the spin-independent matching coefficient used to integrate out the hard scale of the process (and to match the effective description to the QCD one beyond LO), a, b are the gauge group indexes, $\Gamma^{(\eta)}$ is a Lorentz matrix which incorporates the Lorentz structure of the NRQCD amplitude. It also matches the effective description to the QCD one at leading-order (see (8.2.22)). Concerning the fields, χ and ψ are the spinors describing the $Q\bar{Q}$ state, $\mathcal{B}_{n\perp}$ is the gluon field in SCET (including collinear Wilson lines W_n), $\mathcal{S}_n$ is the SCET soft Wilson line. The latter quantities are defined as [89, 98]:

$$W_n(x) = \mathbb{P}\exp\left[ig\int_{-\infty}^{0} ds\ \bar{n}\cdot A^a_n(x+\bar{n}s)t^a\right]\ , \tag{8.2.11}$$

$$S_n(x) = \mathbb{P}\exp\left[ig\int_{-\infty}^{0} ds\ n\cdot A^a_s(x+ns)t^a\right]\ , \tag{8.2.12}$$

$$\mathcal{B}^\mu_{n\perp}(y) = \frac{i}{p_n\cdot\bar{n}}\ \bar{n}_\alpha\ g^\mu_{\perp\beta}\ W^\dagger_n(y)\ F^{\alpha\beta,a}_n(y)\ W_n(y)\ , \tag{8.2.13}$$

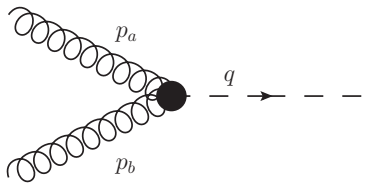

Figure 8.3. Effective vertex for the process $gg \to Q\bar{Q}$ at leading order in pQCD. The two gluons couple directly to the quarkonium, see also (8.2.10). The matching of the effective vertex to the diagrams in Fig. 8.2 is performed via $\Gamma^{(\eta)}_{\mu\nu}$ and the spin-independent coefficient C_H.

where p_n is the partonic four-momentum.

The operator in (8.2.10) describes a vertex where the two gluons directly interact with the quarkonium, as in Fig. 8.3. The amplitude for the process can be described via the matrix element of the effective operator

$$\langle X, \eta |\ \mathcal{O}(\xi)\ | P_A S_A, P_B S_B \rangle\ . \tag{8.2.14}$$

In SCET the Lagrangians for (anti)collinear and soft modes are decoupled. The final hadron is generated by a NRQCD interaction. Accordingly, we can decompose the final state as a product of states

$$|X, h\rangle = |X_n\rangle \otimes |X_{\bar{n}}\rangle \otimes |X_s\rangle \otimes |\eta\rangle\ . \tag{8.2.15}$$

A similar decomposition applies to the initial state, considering proton A collinear and proton B anticollinear. Combining (8.2.14) with its complex conjugate, we can write the cross section for the process in (8.2.1) in terms of the following correlators [89, 98]:

$$\begin{aligned} J_n^{(0)\mu\nu}(x_A, \boldsymbol{k}_{n\perp}, S_A; \mu) \doteq \frac{x_A P_A^+}{2} \int \frac{dy^- d^2\boldsymbol{y}_\perp}{(2\pi)^3}\ e^{-i(\frac{1}{2} x_A y^- P_A^+ - \boldsymbol{y}_\perp \cdot \boldsymbol{k}_{n\perp})} \\ \times \sum_{X_n} \langle P_A S_A | \mathcal{B}^{\mu,a}_{n\perp}(y^-, \boldsymbol{y}_\perp) | X_n \rangle \langle X_n | \mathcal{B}^{\nu,a}_{n\perp}(0) | P_A S_A \rangle\ . \end{aligned} \tag{8.2.16}$$

A similar definition[5] holds for the proton B, replacing $n \to \bar{n}$, $A \to B$ and $+ \to -$. Soft modes are combined in

$$\begin{aligned} S(\boldsymbol{k}_{\boldsymbol{s}\perp}; \mu) \doteq \frac{1}{N_c^2 - 1} \sum_{X_s} \int \frac{d^2\boldsymbol{y}_\perp}{(2\pi)^2}\ e^{i \boldsymbol{y}_\perp \cdot \boldsymbol{k}_{n\perp}} \\ \times \langle 0 | (S_n^\dagger S_{\bar{n}})^{ab}(\boldsymbol{y}_\perp) | X_s \rangle \langle X_s | (S_{\bar{n}}^\dagger S_n)^{ba}(0) | 0 \rangle\ . \end{aligned} \tag{8.2.17}$$

[5] For the meaning of the superscript (0) we refer to [89].

Combining the Fourier transformed matrix elements in (8.2.16) and (8.2.17), it is possible to define a TMD correlator for gluons which is free of rapidity divergences. Following to the general procedure outlined in Sec. 3.4, we can introduce the gluon-gluon correlator (for the details we refer to [89]):

$$G^{\mu\nu}_{U\ g/A}(x_A, \boldsymbol{k}_{n\perp}; \mu, \zeta_A) \equiv \frac{1}{2}\left[-g_\perp^{\mu\nu}\ f_1^g(x_A, \boldsymbol{k}_{n\perp}; \mu, \zeta_A) + 2\frac{k^{\mu\nu}_{n\perp}}{\boldsymbol{k}^2_{n\perp}}\ h_1^{\perp g}(x_A, \boldsymbol{k}_{n\perp}; \mu, \zeta_A)\right] . \tag{8.2.18}$$

Note that the TMD PDFs depend also on the renormalization scale and the rapidity scale, introduced upon cancellations of the RDs (see Sec. 3.4). Comparing with (2.6.31) and with (D.0.12), we see that

$$f_1^{g\ \{G\}} \equiv -f_1^{g\ \{\Gamma\}}\ , \quad h_1^{\perp g\ \{G\}} \equiv -\frac{\boldsymbol{p}_T^2}{2M^2} h_1^{\perp g\ \{\Gamma\}}\ , \tag{8.2.19}$$

where the superscripts refer to the type of correlator[6]. For a version of (8.2.18) in b_T space see [89] and eq.(2.20) therein.

Relying on (8.2.18) and its Fourier transform, we can write the cross section for the process in (8.2.1) with unpolarized protons as

$$\begin{aligned}\frac{d\sigma_{UU}}{dyd^2\boldsymbol{q}_T} &= \frac{(2\pi)^7(N_c^2-1)}{sM_h^2}\ \langle\mathcal{O}(\eta)\rangle\ |C_H(-q^2;\mu^2)|^2\ \Gamma^*_{\alpha\mu}\Gamma_{\nu\beta} \\ &\times \int \frac{d^2\boldsymbol{b}_T}{(2\pi)^2}\ e^{i\boldsymbol{b}_T\cdot\boldsymbol{q}_T}\left[\tilde{G}^{\mu\nu\ [U]}_{g/A}(x_a, \boldsymbol{b}_T; \mu, \zeta_a)\ \tilde{G}^{\alpha\beta\ [U]}_{g/B}(x_b, \boldsymbol{b}_T, S_B; \mu, \zeta_b)\right] \\ &+ Y(q_T; M_h) + \mathcal{O}(\Lambda_{\rm QCD}/M_h)\ ,\end{aligned} \tag{8.2.20}$$

where η is the produced resonance, $|C_H|^2$ is the hard function and $\langle\mathcal{O}(\eta)\rangle$ refers to the NRQCD matrix element:

$$\langle\mathcal{O}(\eta)\rangle \doteq |\langle 0|\chi^\dagger\psi(y)|h\rangle|^2 = \frac{N_c}{2\pi}|R_{nl}(0)|^2[1+\mathcal{O}(v^4)]\ , \tag{8.2.21}$$

which coincides with (8.2.4). In (8.2.20), Y represents corrections for large q_T (see Sec. 3.3.3 and 8.3.3). In order for this effective description to be valid, we enforce it to reproduce the leading order QCD result for production of pseudoscalar $\eta_{b,c}({}^1S_0^{(1)})$ quarkonium [201] by fixing Γ. Its expression is:

$$\Gamma_{\mu\nu} = \frac{i\alpha_s\epsilon_{\perp\mu\nu}}{12\pi^2\sqrt{2M_h(N_c^2-1)}}\ , \tag{8.2.22}$$

where M_h is the mass of the produced hadron and $\epsilon_\perp^{\mu\nu} = \frac{1}{2}\epsilon^{n\bar{n}\mu\nu}$.

[6]The minus sign is due to the sign difference between the operator definitions of Γ and G.

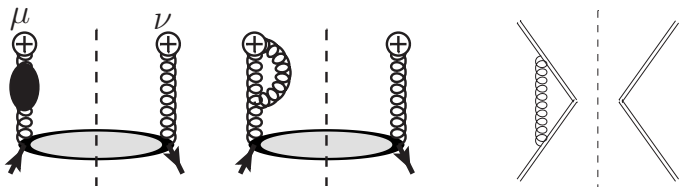

(a) (b)

Figure 8.4. One-loop virtual diagrams that introduce $\mathcal{O}(\alpha_s)$ corrections to the collinear J_n (8.2.16) (a) and soft S (8.2.17) (b) matrix elements, entering the definition of the gluon TMD PDFs. Hermitean conjugates diagrams are not shown. The cross represents a collinear Wilson lines, double lines are soft Wilson lines. The black blob is the gluon self-energy.

8.2.3 NLO structure

Now we investigate how legitimate (8.2.20) is beyond the leading order of QCD, namely if it reproduces the structure of infrared poles of the QCD calculation at NLO, that is adding $\mathcal{O}(\alpha_s)$ corrections. Diagrams in Fig. 8.2 plus the emission of a real gluon do not suffer of infrared divergences because the transverse momentum of the emitted gluon is fixed and finite. For this reason, we focus only on virtual diagrams:

$$\sigma^{(1)}_{\rm virt} \overset{\rm IR}{\longleftrightarrow} \left[\tilde{f}_1^{g/A}\tilde{f}_1^{g/B}\right]^{(1)}_{\rm virt} . \tag{8.2.23}$$

If the IR poles of the NLO calculation for the virtual part of the cross section (LHS of (8.2.23)) are the same as the ones generated by the two TMD PDFs (RHS of (8.2.23)), TMD factorization is established at NLO. This means that the factorized form based on SCET and NRQCD reproduces the physical (QCD) result, up to a finite matching coefficient that can be calculated subtracting the RHS from the LHS of (8.2.23). The result for the cross section in (8.2.23) is [309, 310]:

$$\begin{aligned}\frac{\sigma^{\rm virt(1)}}{\sigma_{\rm Born}} = \frac{\alpha_s}{2\pi}\Bigg[&-2\frac{C_A}{\epsilon^2_{\rm IR}} - \frac{2}{\epsilon_{\rm IR}}\left(\frac{\beta_0}{2} + C_A \ln\frac{\mu^2}{M_h^2}\right) + 2C_F\frac{\pi^2}{2v} \\ &- C_A \ln^2\frac{\mu^2}{M_h^2} + 2C_A\left(1+\frac{\pi^2}{3}\right) + 2C_F\left(-5+\frac{\pi^2}{4}\right)\Bigg] ,\end{aligned} \tag{8.2.24}$$

where in red we highlighted the infrared (IR) singularities, in blue the Coulomb singularity absorbed by the NRQCD long-distance matrix element and in black the finite contributions. Ultraviolet (UV) divergences have been cured by means of the on-shell renormalization scheme [309, 310].

For the TMD PDFs, we need to consider $\mathcal{O}(\alpha_s)$ corrections to both the collinear J_n (8.2.16) and the soft S (8.2.17) matrix elements (see Fig. 8.4). According to [89],

combining J_n and S, the pole structure for an unpolarized TMD PDF is:

$$\tilde{f}_1^{g(1)} = \frac{\alpha_s}{2\pi}\left[\frac{C_A}{\epsilon_{\rm UV}^2} + \frac{1}{\epsilon_{\rm UV}}\left(\frac{\beta_0}{2} + C_A \ln\frac{\mu^2}{\zeta_A}\right) - \frac{C_A}{\epsilon_{\rm IR}^2} - \frac{1}{\epsilon_{\rm IR}}\left(\frac{\beta_0}{2} + C_A \ln\frac{\mu^2}{\zeta_A}\right)\right] , \quad (8.2.25)$$

where in red we have the IR singularities, in black the UV poles. Considering two TMD PDFs, we can see that the structure of the IR poles match, thus TMD factorization holds at this perturbative order, namely SCET reproduced the IR physics in QCD at NLO. The finite matching coefficient (hard part) can then be calculated by subtraction:

$$\begin{aligned}\mathcal{H} = |C_H|^2 = \sigma_{\rm virt}^{(1)} - \left[\tilde{f}_1^{g/A}\tilde{f}_1^{g/B}\right]_{\rm virt}^{(1)} = \\ = 1 + \frac{\alpha_S}{2\pi}\left[- C_A \ln^2\frac{\mu^2}{M_h^2} + 2C_A\left(1 + \frac{\pi^2}{3}\right) + 2C_F\left(- 5 + \frac{\pi^2}{4}\right)\right] .\end{aligned} \quad (8.2.26)$$

This is a byproduct of the factorization theorem and it is fundamental for phenomenology.

8.2.4 Matching TMD and collinear distributions

The second matching step in (8.2.9) consists in expanding the TMD PDFs onto a basis of collinear PDFs by means of perturbatively calculable coefficients:

$$\tilde{T}_g(x, b_T; \mu, \zeta) = \left\{ \sum_{j=q,\bar{q},g} \tilde{C}_{g/j}^T(x, b_T; \mu, \zeta) \otimes t_j(x; \mu) \right\} \tilde{T}_g^{\rm NP}(x, b_T, Q; \{\boldsymbol{\lambda}\}) , \quad (8.2.27)$$

where the summation runs over quarks, antiquarks and gluons, $\tilde{T}_g$ is a generic gluon TMD PDF in b_T-space, t_j is the collinear distribution for parton j and $\tilde{C}_{g/j}^T$ are the calculable Wilson coefficients which match the TMD $\tilde{T}_g$ onto the PDFs t_j. The expansion is only valid at low values of b_T, corresponding to high values of partonic transverse momentum (see Sec. 3.6). At low transverse momentum (high b_T), due to the divergence of the coupling constant, a nonperturbative factor $\tilde{T}_g^{\rm NP}$ is needed. As explained in Sec. 3.7.3 and 3.7.5, it can depend on the kinematic variables and on a set of parameters $\{\boldsymbol{\lambda}\}$ to be fixed from the experimental data.

For completeness, we report the Wilson coefficients for the leading-twist gluon TMD PDFs in an unpolarized proton, f_1^g and $h_1^{\perp g}$ [89]. The coefficient for the gluon-gluon channel for f_1^g is:

$$\begin{aligned}\tilde{C}_{g/g}^{f_1} = \delta(1-x) + \frac{\alpha_s}{2\pi}\Bigg[C_A\delta(1-x)\left(- \frac{1}{2}L_T^2 + L_T \ln\frac{\mu^2}{Q^2} - \frac{\pi^2}{12}\right) \\ - L_T\left(\mathcal{P}_{g/g} - \delta(1-x)\frac{\beta_0}{2}\right)\Bigg] ,\end{aligned} \quad (8.2.28)$$

where $C_A = N_c$ is the Casimir factor for gluons, $L_T \doteq \ln(\mu^2/\mu_b^2)$ (see also (3.5.9)), $\mathcal{P}_{g/g}$ is the DGLAP kernel for a gluon splitting into a gluon [4] and β_0 is a constant related to the running coupling $\alpha_s(\mu)$ [4]. The coefficient for the quark-gluon channel for f_1^g is:

$$\tilde{C}_{g/q}^{f_1} = \frac{\alpha_s}{2\pi}\Big[- L_T \mathcal{P}_{g/q} + C_F x\Big] \ , \tag{8.2.29}$$

where $C_F = (N_c^2 - 1)/2N_c$ is the Casimir factor for quarks and $\mathcal{P}_{g/q}$ is the DGLAP kernel for a quark splitting into a gluon [4]. The coefficient for the gluon-gluon channel for $h_1^{\perp g}$ is:

$$\tilde{C}_{g/g}^{h_1^\perp} = \frac{\alpha_s}{\pi} C_A \ \frac{1-x}{x} \tag{8.2.30}$$

and the coefficient for the quark-gluon channel for $h_1^{\perp g}$ is:

$$\tilde{C}_{g/q}^{h_1^\perp} = \frac{\alpha_s}{\pi} C_F \ \frac{1-x}{x} \ , \tag{8.2.31}$$

where x is the collinear momentum fraction of the parton extracted from the proton.

As explained in Chap. 3, these coefficients account for perturbative components of the partonic transverse momentum and are phenomenologically relevant in the regime $\Lambda_{\rm QCD} \ll q_T \ll M_h$, where M_h is the hard scale.

8.3 Phenomenology

Knowing the hard part of the process (8.2.26) and the Wilson coefficients (8.2.28), (8.2.29), (8.2.30), (8.2.31) for the gluon TMD PDFs in unpolarized protons, we can predict the q_T-spectrum of the unpolarized cross section σ_{UU} (8.2.20) for η ($^1S_0^{(1)}$) production with NLO and NNLL accuracy (see Sec. 3.7.2).

We focus on η_b production at the kinematics of AFTER@LHC [36]. In Sec. 8.3.1 we focus on the low q_T part of the spectrum[7]. In Sec. 8.3.2 and 8.3.3 we address the problem of the matching between the low and the high q_T regions (see also Chap. 3).

8.3.1 Low q_T unpolarized cross section

Substituting (8.2.18) in (8.2.20), we get:

$$\frac{d\sigma_{UU}}{dyd^2\boldsymbol{q}_T} = \frac{2\pi^3\alpha_s^2}{9sM_h^3}\,\mathcal{H}(\mu,M_h)\,\langle\mathcal{O}(\eta_b)\rangle\int\frac{d^2\boldsymbol{b}_T}{(2\pi)^2}e^{i\boldsymbol{q}_T\cdot\boldsymbol{b}_T} \left[\tilde{f}_{1\;g/A}^{\{G\}}(x_a,b_T;\mu,\zeta_a)\;\tilde{f}_{1\;g/B}^{\{G\}}(x_b,b_T;\mu,\zeta_b) - \tilde{h}_{1\;g/A}^{\perp(2)\;\{G\}}(x_a,b_T;\mu,\zeta_a)\;h_{1\;g/B}^{\perp(2)\;\{G\}}(x_b,b_T;\mu,\zeta_b)\right] . \tag{8.3.1}$$

For the TMDs in b_T space for the correlator G, see App. D. (8.3.1) coincides with (8.2.5) but it contains NLO corrections in the hard part $\mathcal{H}$ and in the Wilson coefficients for the TMD PDFs. Sudakov form factors are also considered.

We implement (8.2.27) for f_1^g and $h_1^{\perp g}$ at NNLL+NLO, consistently with the accuracy for (8.2.26), and we fix the value of the radial wavefunction from [274] to:

$$|R_0|^2 = 7.33\ \text{GeV}^3\ . \tag{8.3.2}$$

As explained in Sec. 3.7.3, we need a prescription to separate low and high b_T values. We define $\hat{b}_T$ in (3.7.7) as:

$$\hat{b}_T(b_T) \doteq b_c\left(1-e^{-(b_T/b_c)^2}\right)^{1/2}\ ,\ \text{with}\ b_c \equiv b_{\max} \doteq 1.5\ \text{GeV}^{-1}\ . \tag{8.3.3}$$

We choose a Gaussian model in transverse momentum to describe the high b_T behavior of $\tilde{f}_1^g$:

$$\tilde{f}_1^{g\;\text{NP}}(b_T,Q;\lambda_f) = \exp[-b_T^2\;\lambda_f]\ . \tag{8.3.4}$$

We use the same model for $\tilde{h}_1^{\perp g\;\text{NP}}$, with λ_f replaced by λ_h, where $4\lambda_{f/h}$ represent the average square intrinsic transverse momenta of gluons. To parametrize the high

[7] All the plots have been labeled as "preliminary" since they do not appear in the final publication(s) yet.

b_T behavior of the Collins-Soper kernel we choose (cf. (3.7.8) and (6.3.16)):

$$g_{\rm np}(b_T;\lambda_Q) \doteq \lambda_Q\ b_T^2\ , \tag{8.3.5}$$

where λ_Q is the nonperturbative parameter encoding the soft gluon emissions at high b_T. The values of $\lambda_{f/h}$ and λ_Q are not well known yet. Experimental data at low q_T are needed to better constrain them. We set initial values of rapidity and renormalization scales to $\mu_{\hat{b}}^2$, combining (3.5.9) with (8.3.3), whereas final values for both scales are set equal to the hard scale:

$$\zeta_i = \mu_i^2 = \mu_{\hat{b}}^2 \tag{8.3.6}$$

$$\zeta_f = \mu_f^2 = M_h^2\ , \tag{8.3.7}$$

which hold for both proton A and B. Note that the final values of rapidity scales satisfy the constraint $\zeta_A\zeta_B = M_h^4$. Comparing with (6.3.23) for a distribution function, numerically the action of $g_{\rm np}$ is combined in a single term with $Q_0^2 = 1$ GeV^2 and $Q^2 = M_h^2$.

Because of the medium value of its mass (9.39 GeV), η_b production is an ideal process to extract information about the nonperturbative part of gluon TMD PDFs (see the discussion in Sec. 8.1). The cross section in (8.3.1) (without Y term) is displayed in Figs. 8.5, 8.6 for different choices of the nonperturbative parameters and the energy in the center of mass.

Fig. 8.5 and 8.6 show the sensitivity of the cross section to nonperturbative parameters at the kinematics of AFTER@LHC. We choose $q_T < M_h/2$, $\sqrt{s} = 115$ GeV and the rapidity of the quarkonium is integrated over the range $y_{\rm min} = -\ln 1/\tau$, $y_{\rm max} = +\ln 1/\tau$, where $\tau \doteq M_h/\sqrt{s}$. From Fig. 8.5 we notice a marked sensitivity of the unpolarized cross section at low q_T to the parameter λ_Q, which controls TMD evolution at high b_T. Comparing plots (a) in Fig. 8.5 and 8.6, we see that the sensitivity to the intrinsic transverse momenta $\lambda_{f,h}$ is still evident but less marked with respect to λ_Q. From Fig. 8.6 and Fig. 8.5 (a), we can see that the effect of the intrinsic transverse momentum of linearly polarized gluons in unpolarized protons on the cross section at low q_T with fixed λ_Q is small with respect to variations of λ_Q (cf. Fig. 8.5) and with respect to combined variations of λ_f and λ_h (cf. Fig. 8.5 (a) and Fig. 8.6 (a)). In order to appreciate the effect of $h_1^{\perp g}$, we need to reduce the theoretical error (increasing the perturbative accuracy and/or looking at variables which are less sensitive to the variations of the scales - see, e.g., the normalized multiplicities in Chap. 6) and to have multidifferential data sets at low q_T (see the discussion in Chap. 5 and 4). Constrain first λ_f and λ_Q would help in quantifying λ_h.

Repeating the analyses presented in Fig. 8.5 and 8.6 at the kinematics of LHCb ($\sqrt{s} = 8$ TeV and rapidity of the quarkonium integrated over the range $y_{\rm min} =$

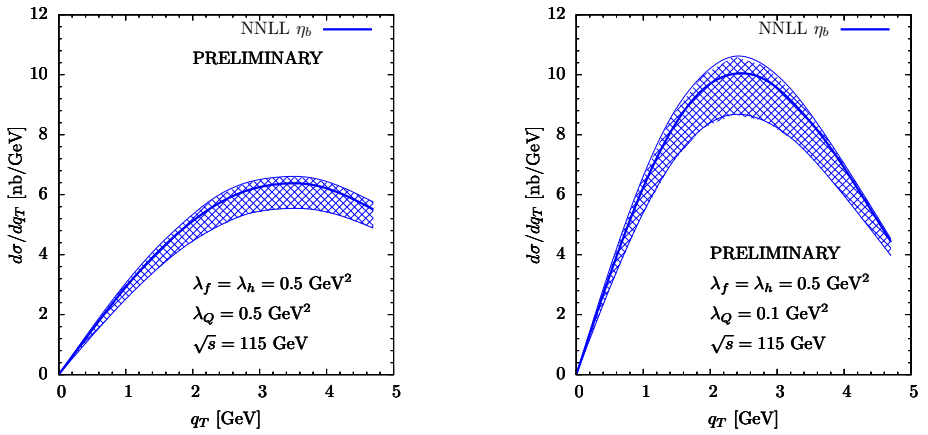

(a) (b)

Figure 8.5. Here we present the sensitivity of the cross section for production of η_b at AFTER@LHC with unpolarized protons (8.3.1) to the parameter λ_Q controlling TMD evolution at high b_T. We compare cross sections with fixed intrinsic transverse momenta $\lambda_f = \lambda_h = 0.5$ GeV^2 and $\lambda_Q = 0.5$ GeV^2 (a), $\lambda_Q = 0.1$ GeV^2 (b). We notice a marked sensitivity on λ_Q with respect to the impact of intrinsic transverse momenta (cf. Fig. 8.6). The blue line represents the choices in (8.3.6) and (8.3.7). The band comes from variations of μ_f and $\zeta_{f\ A/B}$ by a factor of 2.

2, $y_{\max} = 5$ determined by the detector), we obtain qualitatively similar results with respect to the case of AFTER@LHC for what concerns the sensitivity to the nonperturbative parameters. Notably, the peak of the cross section governed by transverse momentum resummation does not lie in the low q_T region ($q_T < M_h/2$ in our case), a feature that deserves further investigations. We notice the same behavior for $\eta_c({}^1S_0^{(1)})$ production at AFTER@LHC kinematics.

8.3.2 Fixed order calculation

At large transverse momentum ($q_T \geq M_h$) the cross section is described by collinear factorization (see Sec. 3.1 and Fig. 3.1). For the unpolarized case, consistently with the α_s accuracy at low q_T, we describe the cross section at fixed $\mathcal{O}(\alpha_s^3)$ order (see also Sec. 3.3.1). At $q_T \geq M_h$ the hard scale is given by the transverse mass $m_T \doteq \sqrt{M_h^2 + q_T^2}$ and the cross section is given by [92][8]

$$\frac{d\sigma}{dyd^2\boldsymbol{q}_T} = \sum_{a,b} \int dx_a dx_b \; f_1^{a/A}(x_a;\mu) f_1^{b/B}(x_b;\mu) \; \delta(\hat{s}+\hat{t}+\hat{u}-M_h^2) \; \frac{\hat{s}}{\pi} \; \frac{d\sigma}{d\hat{t}}(ab \to hd) \; , \tag{8.3.8}$$

[8]Note that we generalize the result in [92] to the massive case.

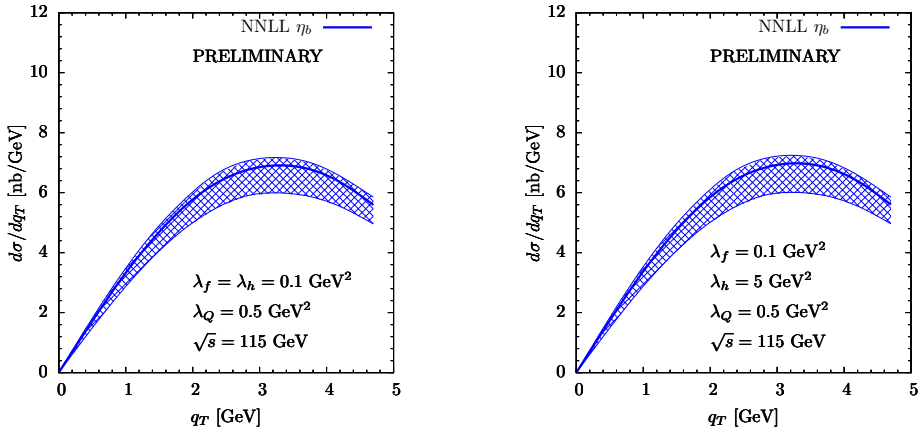

(a) (b)

Figure 8.6. Here we present the sensitivity of the cross section for production of η_b at AFTER@LHC with unpolarized protons (8.3.1) to the parameter λ_h controlling the intrinsic transverse momentum in $h_1^{\perp g}$. We compare cross sections with fixed λ_Q, fixed λ_f and $\lambda_h = 0.1$ GeV^2 (a), $\lambda_h = 5$ GeV^2 (b). We notice a poor sensitivity on λ_h with respect to the sensitivity to λ_Q (cf. Fig. 8.5) and the combined sensitivity to λ_f and λ_h (cf. Fig. 8.5 (a) and Fig. 8.6 (a)).

where a, b are partons in the initial state, h is the produced hadron and d a parton radiated in the final state. $\hat{s}$, $\hat{t}$, $\hat{u}$ are the partonic Mandelstram variables [4] and the partonic cross section $d\sigma/d\hat{t}$ is given at $\mathcal{O}(\alpha_s^3)$ in [305, 309] for different channels. Considering only the contributions initiated by two gluons, we can reasonably reproduce the data for η_c production collected by the LHCb collaboration [311] at high q_T [98].

8.3.3 Matching low and high q_T

In this section we comment on the prescription presented in Sec. 3.3.3 to match the low q_T and high q_T regimes. The simplest way to match the two regions is to introduce a term which, in principle, should

- be negligible at low q_T, where the cross section should be described by the resummed term (W-term)
- approach the fixed-order calculation for $q_T \geq M_h$
- bridge the two descriptions in the intermediate region $q_T \lesssim M_h$.

As explained in (3.3.3), a possibility is to introduce the so-called Y-term, defined as the difference between the fixed-order calculation and the expansion of the re-

summed term at the same perturbative order:

$$Y(q_T, M_h) \doteq \frac{d\sigma}{dq_T}_{|\text{f.o.}} - \frac{d\sigma}{dq_T}_{|\text{ASY}} \ . \tag{8.3.9}$$

If the Y-term behaves as described above, the cross section over the complete q_T spectrum should be given by:

$$\frac{d\sigma}{dq_T}(q_T, M_h) = W(\text{ small } q_T) + Y(q_T, M_h) \ . \tag{8.3.10}$$

We implement the Y as given in (8.3.9) with the fixed order calculation at NLO (neglecting the very small contribution from the channels initiated by quarks) and NLO corrections for the unpolarized cross section at low q_T [98], as described in Sec. 8.3.1. We operate at Tevatron energy, $\sqrt{s} = 1.96$ TeV. We compute the cross section in (8.3.10) for production of a fake quarkonium with mass $m = 100$ GeV and for η_b production ($M_h = 9.39$ GeV). We verify that in both cases this method does not work as expected and different prescriptions to perform the matching need to be explored.

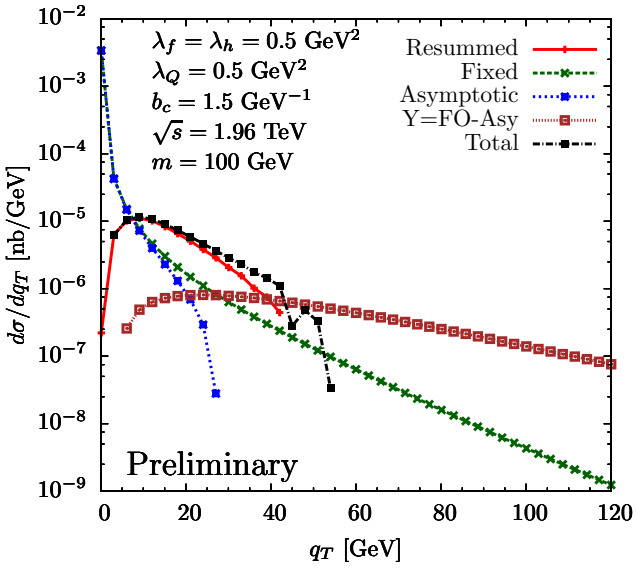

Figure 8.7. Different contributions to the q_T spectrum for the production of a quarkonium with mass $m = 100$ GeV. The black curve represents the sum of the resummed and the Y-term, as in (8.3.10). At low q_T the Y-term behaves as expected, at high q_T it does not converge to the fixed order.

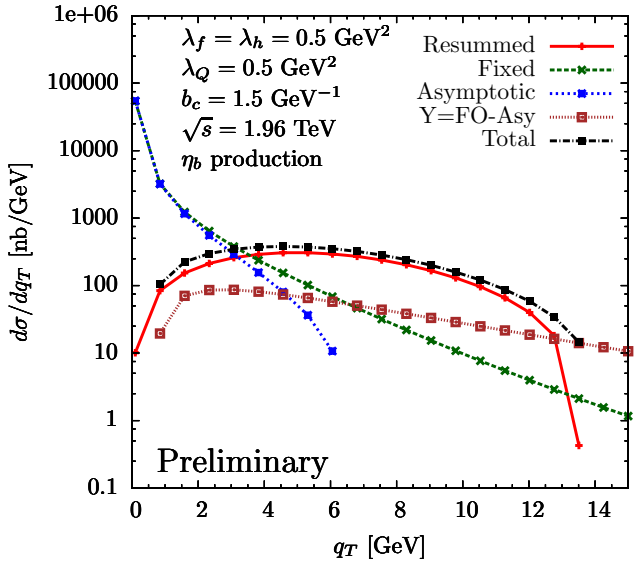

Figure 8.8. Different contributions to the q_T spectrum for the production of $\eta_b(^1S_0^{(1)})$, with $M_h = 9.39$ GeV. The black curve represents the sum of the resummed and the Y-term, as in (8.3.10). At low q_T the Y-term is not negligible with respect to the resummed part and at high q_T it does not converge to the fixed order.

At low q_T, in the high energy ($m = 100$ GeV) case (see Fig. 8.7), the total (namely $W + Y$) cross section is well described by the resummed term and the Y-term is negligible with respect to the resummed (as it should). At low energy (η_b production, Fig. 8.8), the Y-term is not negligible with respect to the resummed and contributes significantly to the cross section: at $q_T = 1$ GeV it is more than 10% of the resummed, at $q_T = 2$ GeV it is $\sim 60\%$ of the resummed[9]. This problem persists lowering the scale, as pointed out for the SIDIS case in [112, 113].

At high q_T there are problems in both cases. At low energy the expansion of the resummed becomes negative for $q_T < M_h$ and, as a result, the Y-term gets larger than the fixed order. At higher q_T we see no convergence of the Y to the fixed order. At high energy the same happens. In this case, also $W + Y$ becomes negative around $q_T \sim m/2$. This feature is not evident from the results presented, e.g., in [108, 109], but there the fixed order calculation is not explicitly shown and it is not possible to understand if the Y-term, despite being a smooth decreasing function as in Fig. 8.7 and 8.8, converges to the fixed order or not.

[9]The sensitivity of these percentages to the numerical accuracy of the computation needs to be further tested.

In the intermediate region we do not know yet how the prescription performs. Modifications are needed in order to reproduce the correct behaviors at small and large q_T and a proposal has been recently presented in [113]. It might be that also the intermediate region is affected by those corrections: further investigations are necessary.

Looking at Fig. 8.8, we see that the resummed part (TMDs) extends till $q_T > M_h$. The applicability of TMD factorization, though, is limited to $q_T \ll M_h$ and one should be careful in trusting the resummed description outside such a limit. The fact that the cross-section is driven by the resummed piece might be an artifact of the low value for the hard scale M_h.

The treatment of the $b_T \to 0$ limit of the Sudakov form factor (described in Sec. 3.7.4) is left to future investigations.

8.3.4 Polarized cross sections

Let us briefly comment on the case when the target proton is polarized, a peculiar setting of the AFTER@LHC which allows investigations of polarized TMDs.

If the spin of the target proton is longitudinally oriented, contracting the gluon-gluon twist-2 correlators with the Feynman amplitudes $\mathcal{A}$ as in (8.2.3), the cross section vanishes:

$$\frac{d\sigma_{UL}}{dyd^2\boldsymbol{q}_T} = 0 \ . \tag{8.3.11}$$

This result can be understood also via the following argument: in this configuration, the only correlation involving the spin of the target, the momentum of the beam and the transverse momentum of the final state hadron which respects parity invariance of the theory is:[10]

$$(\boldsymbol{q}_T \times \boldsymbol{S}) \cdot \boldsymbol{P} \ , \tag{8.3.12}$$

where $\boldsymbol{P}$ and $\boldsymbol{S}$ are, respectively, the three-momentum of the proton in the beam and the spin vector of the proton in the target. $\boldsymbol{q}_T$ is the transverse momentum of the quarkonium in the final state. Checks of (8.3.11) at sub-leading twist are required.

If the target proton is transversely polarized with polarization vector $\boldsymbol{S}_{TB}$ and the colliding proton beam is unpolarized, the cross section involves convolutions of different TMD PDFs. At parton model level, it reads:

$$\frac{d\sigma_{UT}(\eta_b)}{dyd^2\boldsymbol{q}_T} = \frac{2}{9}\frac{\pi^3\alpha_s^2}{M_h^3\, s}\,\langle 0|\mathcal{O}_1^{\eta_b}(^1S_0)|0\rangle\,|\boldsymbol{S}_{TB}|\sin\phi_S\,\times \tag{8.3.13}$$
$$\left\{\mathcal{C}\left[w_{UT}^{(A)}\ f_1^g\ f_{1T}^{\perp g}\right] - \mathcal{C}\left[w_{UT}^{(B)}\ h_1^{\perp g}\, h_1^g\right] - \mathcal{C}\left[w_{UT}^{(C)}\ h_1^{\perp g}\, h_{1T}^{\perp g}\right]\right\} \ ,$$

[10] This argument holds true with a single spin and one hadron only in the final state.

where ϕ_S is the azimuthal angle of the transverse spin vector $\boldsymbol{S}_{TB}$ with respect to $\boldsymbol{q}_T$ and the expression of the $w_{UT}^{(i)}$ coefficients is given in [98]. This equation has already been presented in [308] with a different notation. For a comparison with the unpolarized case, see (8.2.5). In (8.3.13), the TMD PDFs of the unpolarized proton beam couple to the definite-rank T-odd functions $f_{1T}^{\perp g}$, h_1^g, $h_{1T}^{\perp g}$ (see Tab. 2.3). Experimental investigations could shed light on the size of these functions[11]. The Wilson coefficients for the three T-odd gluon TMDs are not known yet. These functions are matched onto collinear twist-3 matrix elements, a feature that complicates NLO investigations according to (3.6.1) and (8.2.27). At the moment, a possible accuracy level is LO in the Wilson coefficients and NNLL in the resummation (see Tab. 3.1).

8.4 Outlook and future developments

In this Chapter we discussed TMD factorization at NLO for the q_T-spectrum of color-singlet quarkonium production in terms of gluon TMDs, using an effective field theory (SCET and NRQCD) approach. With the tools available from the factorization theorem, we presented accurate predictions for unpolarized cross sections at AFTER@LHC. Polarization studies are in progress. Concerning nonperturbative parameters, we noticed a marked sensitivity to the parameter governing the emission of soft gluons in the high b_T region. We also investigated the matching between the low and the high q_T regions, pointing out the behavior of the Y-term prescription as presented in Sec. 3.3.3.

Once experimental data will be available at low q_T, this formalism will allow the extraction of the nonperturbative part of (un)polarized gluon TMD PDFs. Especially the distribution of linearly polarized gluons in unpolarized protons ($h_1^{\perp g}$) will be addressed in forthcoming studies at hadron colliders [28].

[11] Note that the TMD PDFs in (8.3.13) are the ones in the Γ^{ij} correlator.

CHAPTER 9

CONCLUSIONS AND OUTLOOKS

A poem, a symphony, a painting,
a mathematical truth, a new scientific fact,
all bear in themselves all the justification that universities,
colleges and institutes of research need or require.
A. Flexner

Transverse-momentum-dependent parton distribution functions (TMD PDFs) and fragmentation functions (TMD FFs) give a multidimensional description of partonic structure in momentum space. They are functions of the longitudinal and transverse momentum of partons, with respect to the reference hadron momentum. As such, they offer richer information compared to standard collinear PDFs and FFs, which depend only on the longitudinal momentum.

In the last decade, TMD PDFs and TMD FFs have gained increasing attention especially because of emerging data from experiments on semi-inclusive processes [16–18]. The knowledge of the unpolarized distribution and fragmentation functions is a fundamental ingredient for TMD phenomenology: a detailed understanding of their structure can improve the description of unpolarized processes and provide a reliable baseline to address effects arising from the polarization of partons and/or hadrons. Despite many efforts, though, our level of knowledge is still limited compared to the one available for collinear distributions. Nonetheless, thanks to improvements on both the theoretical and the experimental side (Sec. 4.4), we are moving from an exploratory phase to a precision and consolidation phase.

In this thesis we explored strategies to improve this basic but fundamental knowledge, focusing, in particular, on the flavor structure of the TMD part in unpolarized distribution and fragmentation functions and on its interplay with TMD

evolution. To test the impact on LHC physics, in Chap. 7 we investigated the role of the flavor dependence of the intrinsic transverse momentum on the q_T spectra of the Z and $W^{\pm}$ bosons. These observables are directly related to one of the fundamental parameters in the Standard Model, namely the mass of W bosons. This is just an example of the potential role of quark TMDs in high-energy hadronic collisions. Considering gluons, instead, the distribution of linearly polarized gluons in unpolarized protons $h_1^{\perp g}$ (Sec. 2.6) plays a role at the LHC. Along this line, in Chap. 8 we presented a strategy to extract its nonperturbative content at medium energy, in order to be be able to test its impact on processes at higher energy (see Sec. 8.1).

For extended descriptions of the research results, we refer to Sec. 5.5, 6.6, 7.5, 8.4. Here we summarize the most important points addressed in the various analyses.

Results

In this thesis, we first presented the framework in which TMD distributions are defined. Then, we outlined the role of factorization theorems and the emergence of QCD evolution equations. In the second part of the thesis, we put the given definitions at work, aiming at improving the knowledge of unpolarized structures and at giving a quantitative estimate of their impact on medium/high-energy physics.

Considering the operator definition, in Chap. 2 we presented a notation for TMD correlators based on symmetric traceless tensors (STTs) built with transverse momentum vectors (see also App. B). Among the main advantages: a clean correspondence with Fourier transformed functions (useful for TMD evolution purposes) and a potential insight into the angular dependence in structure functions and spin asymmetries (see also Chap. 4).

QCD evolution is needed in order to match descriptions at different energy scales: in Chap. 3 we described it both from a theoretical and phenomenological point of view. Different prescriptions have been introduced and some of them have been implemented in the subsequent Chapters.

The phenomenological part of the thesis begins in Chap. 4 with an overview of the advantages presented by different observables (namely cross sections and asymmetries). Moreover, a summary of the current knowledge for unpolarized quark and gluon TMDs has been presented, outlining also possible strategies for improvement.

In Chap. 5 we investigated the flavor and kinematic dependence of the average square intrinsic transverse momentum of quarks from SIDIS data collected by the HERMES collaboration. We presented a fit based on the replica method, which generates *distributions* of equally probable best-fit values. This allows to estimate

physical observables computing expectation values and uncertainties based on the distributions of best-fit values. Summarizing, we found that the TMD PDF for sea quarks is wider (in transverse momentum) than the distribution for up valence quarks, which in turn is wider than the distribution for down valence quarks. Considering TMD FFs, the width in transverse momentum associated to unfavored fragmentation processes is wider than the width for favored fragmentation into pions. The latter is also narrower than the TMD FF of up quarks into kaons (for more details see Chap. 5). Considering the kinematic dependence, the z-dependence of the average intrinsic transverse momentum in fragmentation functions is crucial to fit HERMES data. The x-dependence in distributions, instead, is not well constrained by the fit. These results are quite sensitive to the kinematic cuts considered and to the combination of target and final state hadrons. For this reason, further investigations on larger data sets are needed. Moreover, to shed more light on these open questions, it will be crucial to include TMD evolution and to allow for more flexible functional forms describing the nonperturbative contributions.

In order to test the impact of the flavor and kinematic dependence of partonic transverse momentum, we started in Chap. 6 from the case of TMD FFs, for which the flavor dependence is more evident. In particular, we investigated the impact of the flavor dependent replicas on multiplicities for e^+e^- annihilation into two hadrons. We combined this with the impact of TMD evolution, exploring different phenomenological implementations of the nonperturbative part of the kernel. We illustrated how measurements of TMD observables at higher energies can be useful in order to constrain parameters encoded in the evolution schemes, while measurements at lower energies are essential to investigate the parameters related to the nonperturbative hadron structure. Measurements with different hadrons in the final state (e.g. kaons and pions) can help in zooming on the flavor dependence of the intrinsic transverse momentum of quarks.

In Chap. 7 we tested the impact of flavor-dependent TMD PDFs in proton-proton collisions. In this way, we also investigated the phenomenological relevance of quark TMDs at the LHC. We found that the flavor structure extracted in Chap. 5 introduces an additional uncertainty on the position of the peak in q_T spectra of $W^\pm$ bosons, comparable to the error associated to the choice of the collinear distribution functions. This is the first study which quantitatively addresses the role of nonperturbative contributions in q_T spectra at the LHC. Moreover, further investigations are needed to directly estimate the impact of this effect on the uncertainties associated to the W boson mass.

In Chap. 8, using an effective theory point of view, we established TMD factorization for production of ${}^1S_0^{(1)}$ quarkonium in hadronic collisions at NLO accuracy.

As a byproduct, we obtained the hard part of the process, in agreement with other derivations presented in literature. The perturbative ingredients (the hard part, the Sudakov form factor and the Wilson coefficients), allowed to compute predictions for the q_T spectrum, for which we reached a NLO-NNLL order of accuracy. This is important in order to assess the theoretical errors arising from variations of renormalization and rapidity scales in the process. For unpolarized cross sections, we presented predictions for the low q_T spectrum at the kinematics of AFTER@LHC, testing the impact of nonperturbative parameters on the predictions. We found that the cross section is quite sensitive to the parameter encoding evolution at high b_T. The effect of intrinsic transverse momenta is still relevant but not crucial. At Tevatron energies, we investigated the matching between low and high q_T, revealing critical points in the Y-term prescription introduced to bridge TMD and collinear factorization. Eventually, we presented the gluon TMD PDFs involved in collisions of an unpolarized proton beam with a transversely polarized fixed target.

A path along the road of TMD phenomenology to reconstruct the TMDs for the proton constituents involves several challenges, ranging from the applicability of factorization theorems, to the implementation of QCD evolution and the validation of phenomenological models. As explained in Chap. 4, improvements from the theoretical, experimental and phenomenological points of view will all be crucial for such a program.

The analyses presented in this thesis (and the strategies to improve them) help in quantifying the impact of our ignorance about hadron structure on the description of high-energy physics observables. Keeping under control and progressively reducing these uncertainties is a major goal in order to draw maps of hadron structure which could be, step by step, more accurate and less out of focus. The ultimate goal is the possibility of benefiting from reliable and precise maps, a task that needs collective efforts and shared long-range plans from both the theoretical and the experimental communities.

APPENDIX A

NOTATIONS AND CONVENTIONS

You must be very careful.
P.J. Mulders

Metric

We use the metric tensor given in [4]:

$$g^{\mu\nu} \doteq \mathrm{diag}(1, -1, -1, -1) \ .$$

Greek letters will indicate Lorentz indexes, running from 0 to 3. Roman indexes will refer to Euclidean vectors. Bold-face vectors live in Euclidean space.

Light-cone coordinates

An introduction to light-cone coordinates is given in [312]. Given a Cartesian basis $\{\hat{e}_0, \hat{e}_1, \hat{e}_2, \hat{e}_3\}$ we can introduce a light-cone basis as:

$$n_+ \doteq \frac{1}{\sqrt{2}}(\hat{e}_0 + \hat{e}_3), \quad n_- \doteq \frac{1}{\sqrt{2}}(\hat{e}_0 - \hat{e}_3), \quad \hat{e}_T \doteq (\hat{e}_1, \hat{e}_2)$$

such that

$$n_+ \cdot n_- = 1, \quad n_+^2 = n_-^2 = 0 \ .$$

Light-cone coordinates for a generic vector V are:

$$\begin{aligned} V^+ &= \frac{1}{\sqrt{2}}(V^0 + V^3) \equiv V \cdot n_- \\ V^- &= \frac{1}{\sqrt{2}}(V^0 - V^3) \equiv V \cdot n_+ \\ V_{\scriptscriptstyle T} &= (V^1, V^2) \ , \end{aligned}$$

where $\{0, 1, 2, 3\}$ are the standard Cartesian coordinates. In particular

$$V_{\scriptscriptstyle T}^2 = -\boldsymbol{V}_{\scriptscriptstyle T}^2 \ .$$

The symmetric projector onto the transverse plane is defined as:

$$g_{\scriptscriptstyle T}^{\mu\nu} \doteq g^{\mu\nu} - n_+^{\{\mu} n_-^{\nu\}} \ .$$

In components $g_{\scriptscriptstyle T}^{11} = g_{\scriptscriptstyle T}^{22} = -1$. The antisymmetric projector onto the transverse plane is:

$$\epsilon_{\scriptscriptstyle T}^{\mu\nu} \doteq \epsilon^{\rho\sigma\mu\nu} n_{+\rho} n_{-\sigma} = \epsilon^{-+\mu\nu} \equiv \epsilon^{n_+ n_- \mu\nu} \ ,$$

We choose $\epsilon^{0123} = 1$ so that $\epsilon_{\scriptscriptstyle T}^{12} = -\epsilon_{\scriptscriptstyle T}^{21} = 1$. We also use the following notation:

$$a^{b\nu} \doteq a^{\mu\nu} b_\mu \ .$$

An example of convention for light-cone coordinates in SCET is given in [93].

Dirac matrices

Dirac matrices [4] satisfy the anticommutation relation:

$$\{\gamma^\mu, \gamma^\nu\} = 2g^{\mu\nu}\mathbb{I} \ ,$$

where $\mathbb{I}$ is the identity in Dirac space. A fifth matrix is defined as:

$$\gamma_5 \doteq i\gamma^0\gamma^1\gamma^2\gamma^3 \ .$$

We define an antisymmetric structure:

$$\sigma^{\mu\nu} \doteq \frac{i}{2} \, [\gamma^\mu, \gamma^\nu] \ .$$

APPENDIX B

SYMMETRIC TRACELESS TENSORS

Here we point out some reasons in support of using a symmetric traceless tensor (STT) form for the p_T structures involved in distribution and fragmentation correlators:

1 functions with definite rank in p_T are naturally used in rank expansions of the correlator;

2 there exists a 1-1 correspondence between TMDs in b_T and p_T space. This is useful especially when translating a cross section to b_T space in order to implement transverse momentum resummation (TMD evolution). In a non-STT form, the functions with no definite rank are not mapped in a 1-1 way via the Fourier transform;

3 using a STT form in p_T, it is easy to check that only the rank-0 structures in p_T in the TMD correlator survive integration over transverse momentum;

4 a potential advantage of using distribution and fragmentation TMD correlators of definite rank is the possibility of linking the rank of the functions to the angular dependence with which they contribute to structure functions and azimuthal asymmetries (see Sec. 4.2.3).

Here we list the symmetric traceless tensors $p_T^{i_1 \cdots i_n}$ that are built from the partonic four-momentum p_T. For a spin-1/2 target, a quark-quark correlator involves terms up to rank-2. For gluons up to rank-3. In a spin-1 target also terms with

rank-4 are considered [78]:

$$p_T^{ij} \equiv p_T^i p_T^j - \frac{1}{2} p_T^2 g_T^{ij}, \tag{B.0.1}$$

$$p_T^{ijk} \equiv p_T^i p_T^j p_T^k - \frac{1}{4} p_T^2 \left(g_T^{ij} p_T^k + g_T^{ik} p_T^j + g_T^{jk} p_T^i \right), \tag{B.0.2}$$

$$\begin{aligned} p_T^{ijkl} \equiv\ & p_T^i p_T^j p_T^k p_T^l - \frac{1}{6} p_T^2 \left(g_T^{ij} p_T^{kl} + g_T^{ik} p_T^{jl} + g_T^{il} p_T^{jk} + g_T^{jk} p_T^{il} + g_T^{jl} p_T^{ik} + g_T^{kl} p_T^{ij} \right) \\ & - \frac{1}{8} p_T^4 \left(g_T^{ij} g_T^{kl} + g_T^{ik} g_T^{jl} + g_T^{il} g_T^{jk} \right), \end{aligned} \tag{B.0.3}$$

satisfying

$$g_{T\,ij} p_T^{ij} = g_{T\,ij} p_T^{ijk} = g_{T\,ij} p_T^{ijkl} = 0 \tag{B.0.4}$$

for every pair of indexes. Products of p_T vectors can be decomposed into symmetric traceless tensors as follows:

$$p_T^i p_T^\alpha = p_T^{i\alpha} + \frac{1}{2} p_T^2 g_T^{i\alpha}, \tag{B.0.5}$$

$$p_T^i p_T^{\alpha\beta} = p_T^{i\alpha\beta} + \frac{1}{4} p_T^2 \left(g_T^{i\alpha} p_T^\beta + g_T^{i\beta} p_T^\alpha - g_T^{\alpha\beta} p_T^i \right), \tag{B.0.6}$$

$$\begin{aligned} p_T^{ij} p_T^{\alpha\beta} =\ & p_T^{ij\alpha\beta} + \frac{1}{6} p_T^2 \left(g_T^{i\alpha} p_T^{j\beta} + g_T^{i\beta} p_T^{j\alpha} + g_T^{j\alpha} p_T^{i\beta} + g_T^{j\beta} p_T^{i\alpha} - 2 g_T^{ij} p_T^{\alpha\beta} - 2 g_T^{\alpha\beta} p_T^{ij} \right) \\ & + \frac{1}{8} p_T^4 \left(g_T^{i\alpha} g_T^{j\beta} + g_T^{i\beta} g_T^{j\alpha} - g_T^{ij} g_T^{\alpha\beta} \right). \end{aligned} \tag{B.0.7}$$

Every symmetric traceless tensor $p_T^{i_1 \cdots i_n}$ of rank n (for $n \geq 1$) only has two independent components, which allows for the identification:

$$p_T^{i_1 \cdots i_n} \equiv \frac{p_T^n}{2^{n-1}} e^{\pm i n \varphi}, \tag{B.0.8}$$

in terms of the two numbers $p_T \equiv |\boldsymbol{p}_T|$ and φ, the azimuthal angle of p_T.

APPENDIX C

TIME REVERSAL

The quark Sivers function

Let us investigate the interplay between gauge symmetry and time reversal for the specific case of the quark Sivers function $f_{1T}^{\perp}$ (Tab. 2.1). The density of unpolarized quarks in a proton is defined through a trace of the quark distribution correlator with the γ^+ matrix:

$$\Phi^{[U]}_{[\gamma^+]} \doteq \frac{1}{2}\mathrm{Tr}^{\mathrm{D}}\big\{\Phi^{[U]}\gamma^+\big\} = f_1^{[U]}(x,p_T^2) - \frac{(\hat{\boldsymbol{P}}\times\boldsymbol{p}_T)\cdot\boldsymbol{S}_T}{M}\; f_{1T}^{\perp[U]}(x,p_T^2)\;. \qquad \text{(C.0.1)}$$

Applying the definitions of P and T in (2.8.3) to the specific case of $\Phi^{[+]}_{[\gamma^+]}$, we can see that it transforms as:

$$P \;:\; \Phi^{[+]}_{[\gamma^+]}(p,P,S;n_\pm) = \Phi^{[+]}_{[\bar{\gamma}^+]}(\bar{p},\bar{P},-\bar{S};\bar{n}_\pm) \qquad \text{(C.0.2)}$$

$$T \;:\; \Phi^{[+]}_{[\gamma^+]}(p,P,S;n_\pm) = \Phi^{[-]}_{[\bar{\gamma}^+]}(\bar{p},\bar{P},\bar{S};\bar{n}_\pm)^*\;, \qquad \text{(C.0.3)}$$

where $n_\pm$ vectors are the light-cone basis vectors. The P, T behavior of the Dirac fields, the matrices and the states is determined in order for the transformations to be symmetry of QCD [4, 79]. Accordingly, both (C.0.2) and (C.0.3) encode parity invariance and time reversal invariance, but display a crucial difference: under time reversal the gauge link $[+]$ is exchanged into $[-]$ (and viceversa). Considering (C.0.3), we can decompose $\Phi^{[\pm]}_{[\gamma^+]}$ in T-even and T-odd parts in the following way

(omitting the basis):

$$\Phi^{\text{T-even}}_{[\gamma^+]}(p,P,S) = \frac{1}{2}\left[\Phi^{[+]}_{[\gamma^+]}(p,P,S) + \Phi^{[-]}_{[\gamma^+]}(p,P,S)\right] \tag{C.0.4}$$

$$\Phi^{\text{T-odd}}_{[\gamma^+]}(p,P,S) = \frac{1}{2}\left[\Phi^{[+]}_{[\gamma^+]}(p,P,S) - \Phi^{[-]}_{[\gamma^+]}(p,P,S)\right] . \tag{C.0.5}$$

The previous equations imply the possibility to decompose $\Phi^{[\pm]}_{[\gamma^+]}$ in a sum of T-even and T-odd parts:

$$\Phi^{[+]}_{[\gamma^+]}(p,P,S) = \Phi^{\text{T-even}}_{[\gamma^+]}(p,P,S) + \Phi^{\text{T-odd}}_{[\gamma^+]}(p,P,S) \tag{C.0.6}$$

$$\Phi^{[-]}_{[\gamma^+]}(p,P,S) = \Phi^{\text{T-even}}_{[\gamma^+]}(p,P,S) - \Phi^{\text{T-odd}}_{[\gamma^+]}(p,P,S) . \tag{C.0.7}$$

Combining (C.0.1), (C.0.3) and (C.0.7) we see that $f_1^{[\pm]}$ is the T-even part of $\Phi^{[\pm]}_{[\gamma^+]}$, whereas the term proportional to $f_{1T}^{\perp[\pm]}$ is the T-odd one; in particular, from (C.0.3) we get:

$$f_1^{[+]}(x,p_T^2) = f_1^{[-]}(x,p_T^2) \tag{C.0.8}$$

$$f_{1T}^{\perp[+]}(x,p_T^2) = -f_{1T}^{\perp[-]}(x,p_T^2) , \tag{C.0.9}$$

which represents the process dependence of the quark Sivers function between SIDIS and DY. This sign change is considered one of the striking predictions of the TMD formalism and is among the key experimental measurements to be (hopefully) completed in the near future by means of polarized DY and SIDIS programs by the COMPASS collaboration at CERN and the STAR collaboration at RHIC in BNL (see App. F). T-odd effects coming from the proton structure in the TMD formalism are essentially due to the transverse separation in the gauge links: if we had no transverse separation, the staple links would reduce to a straight line and the two collinear integration to and from infinity would cancel, eliminating the possibility of interchanging the paths and defining T-odd correlators.

Since in (C.0.2) there is no interchange betwenn the staple links, there is no way to define P-odd terms. For this reason, arguments considering T-oddness are equivalent to ones dealing with PT-oddness, as in [20].

The quark Boer-Mulders function

The case of the T-odd quark TMD PDF $h_1^\perp$ (Boer-Mulders) (Tab. 2.1) is similar to the Sivers one, but related to a different Dirac projection of the correlator. The projection of the correlator related to transversely polarized quarks is $\Phi_{[i\sigma^{k+}\gamma_5]}$. Tracing the TMD quark distribution correlator with $i\sigma^{k+}\gamma_5$ and introducing time

reversal transformations we get:

$$T \quad : \quad \Phi^{[+]}_{[i\sigma^{k+}\gamma_5]}(p,P,S;n_\pm) = -\Phi^{[-]}_{\overline{[i\sigma^{k+}\gamma_5]}}(\bar{p},\bar{P},\bar{S};\bar{n}_\pm)^* \ . \tag{C.0.10}$$

As in (C.0.3), the interchange of the staple links allows the decomposition of $\Phi_{[i\sigma^{k+}\gamma_5]}$ into T-even and T-odd pieces:

$$\Phi^{\text{T-even}}_{[i\sigma^{k+}\gamma_5]}(p,P,S) = \frac{1}{2}\left[\Phi^{[+]}_{[i\sigma^{k+}\gamma_5]}(p,P,S) - \Phi^{[-]}_{[i\sigma^{k+}\gamma_5]}(p,P,S)\right] \tag{C.0.11}$$

$$\Phi^{\text{T-odd}}_{[i\sigma^{k+}\gamma_5]}(p,P,S) = \frac{1}{2}\left[\Phi^{[+]}_{[i\sigma^{k+}\gamma_5]}(p,P,S) + \Phi^{[-]}_{[i\sigma^{k+}\gamma_5]}(p,P,S)\right] \ , \tag{C.0.12}$$

Note the different signs with respect to the Sivers case. h_1, $h_{1L}^\perp$, $h_{1T}^\perp$ are the functions entering the T-even part of $\Phi_{[i\sigma^{k+}\gamma_5]}$ (Tab. 2.1). The Boer-Mulder function $h_1^\perp$ enters the T-odd part and, as the Sivers, is subject to a sign change between SIDIS and DY:

$$h_1^{\perp[+]}(x,p_T^2) = -h_1^{\perp[-]}(x,p_T^2) \ . \tag{C.0.13}$$

This is another peculiarity of the TMD formalism that will be experimentally investigated.

T-odd TMD PDFs and gluonic poles

Leading twist T-odd TMD PDFs are very interesting objects from the phenomenological point of view, but difficult to be accessed since they are matched onto higher twist collinear functions. In [74] it has been shown that the first moment of the quark Sivers function is linked to a twist-3 collinear Qiu-Sterman matrix element T_F [161]:

$$2Mf_{1T}^{\perp(1)}(x) = -g_s T_F(x) \ , \tag{C.0.14}$$

where the first moment of a generic TMD PDF f is defined as:

$$f^{(1)}(x) \doteq \int d^2\boldsymbol{p}_T \frac{\boldsymbol{p}_T^2}{2M^2} f(x,p_T^2) \ . \tag{C.0.15}$$

The first transverse moment of the quark-quark correlator is defined as:

$$\Phi_\partial^{[U]\alpha}(x) \doteq \int d^2\boldsymbol{p}_T p_T^\alpha \ \Phi^{[U]}(x,\boldsymbol{p}_T) \ . \tag{C.0.16}$$

Because of the explicit gauge link dependence, in the case of staple-like links $\Phi_\partial^{[U]\alpha}(x)$ can be decomposed in T-even and T-odd parts as:

$$\Phi_\partial^{[\pm]\alpha}(x) = \tilde{\Phi}_\partial^\alpha(x) \pm \pi\Phi_G^\alpha(x,x) \ , \tag{C.0.17}$$

where $\tilde{\Phi}^{\alpha}_{\partial}$ is T-even and Φ^{α}_{G} is T-odd. In $\Phi^{[\pm]\alpha}_{\partial}(x)$ the process dependence is not washed out, as for the integrated (collinear) correlator $\Phi(x)$, but survives only in the $\pm$ sign in front of Φ^{α}_{G} in (C.0.17). The latter is called *gluonic pole*[1] matrix element and is proportional to a Qiu-Sterman matrix element [74, 152].

A similar treatment holds for T-odd gluon TMD PDFs, but with two gluonic poles matrix elements, due to the presence of two links in the definition of the correlator [88]:

$$\begin{aligned}\Gamma^{\alpha[U]}_{\partial}(x) &\doteq \int d^2p_T p_T^{\alpha}\ \Gamma^{[U]}(x,p_T) \\ &= \tilde{\Gamma}^{\alpha}_{\partial}(x) + C^{[U]}_{G,1}\Gamma^{\alpha}_{G,1}(x) + C^{[U]}_{G,2}\Gamma^{\alpha}_{G,2}(x)\ ,\end{aligned} \tag{C.0.18}$$

where the calculable process dependence is encoded in the gluonic pole factors $C^{[U]}_{G,i}$ (the analogue of $\pm$ in (C.0.17)). The first term in the RHS is T-even, the last two are T-odd. (C.0.18) implies that the T-odd gluon Sivers function is built out of two universal TMD PDFs (cf. eq.(46) in [88]).

The collinear case

T-odd effects coming from the interplay with the gauge link structure are only due to the transverse separation in the links at infinity ($A_T(\infty)$). Without this separation, the staple links would reduce to a straight line along the light cone direction n_- and the two collinear integration to and from infinity would cancel, eliminating the possibility of interchanging the paths and defining T-odd correlators. As a consequence, the twist-2 integrated correlator consists only of a T-even part:

$$\Phi(x) = \Phi^{[\text{T-even}]}(x)\ . \tag{C.0.19}$$

This is true for both quarks and gluons. For a spin 1/2 hadron, this coincides with the fact that all the T-odd TMDs are not rank-0 structures, so they do not survive integration over transverse momentum. For a spin-1 hadron, instead, there is one T-odd TMD structure, namely the one related to the Bacchetta function $h_{1LT}(x,p_T^2)$ describing a transversely polarized quark in a LT-polarized hadron, which is rank-0 in p_T. Despite surviving transverse momentum integration, $h_{1LT}(x)$ is zero[2] because of the combined effect of hermiticity and time reversal. The generalization of (C.0.10) to the spin 1 case, with no links, is:

$$\Phi_{[i\sigma^{k+}\gamma_5]}(p,P,S,T;n_\pm) = -\Phi_{\overline{[i\sigma^{k+}\gamma_5]}}(\bar{p},\bar{P},\bar{S},\bar{T};\bar{n}_\pm)^*\ , \tag{C.0.20}$$

[1] Since it is a quark matrix element that contains an additional zero momentum gluon.
[2] In contrast with what claimed in [75, 83].

where T is the tensor representing the tensor polarizations in spin 1 [75, 78], transforming under parity as $\bar{T}^{\mu\nu} \equiv \delta^{\mu\rho}\delta^{\nu\sigma}T_{\rho\sigma}$. Specifying (C.0.20) to a proton with T-polarization and to a deuteron with LT-polarization we have [75]:

$$\mathrm{T} \ : \ [S_T^k h_1(x)]^* = S_T^k h_1(x) \tag{C.0.21}$$

$$\mathrm{LT} \ : \ [\epsilon_T^{kj} S_{LTj} h_{1LT}(x)]^* = -\epsilon_T^{kj} S_{LTj} h_{1LT}(x) \ . \tag{C.0.22}$$

Hermiticity requires functions to be real. Thus, being the components of S and T real, $h_{1LT}(x)$ must vanish.

TMD fragmentation functions

As for distribution correlators, in the case of fragmentation correlators, the interplay between gauge symmetry and time reversal properties does not impose constraints but defines relations between different correlators with $[\pm]$ links [79]. The situation for fragmentation, though, is more involved due to the difference between initial and final states in the correlator:

$$\text{Time reversal:} \quad \Delta_{\text{out}}^{[\pm]\dagger}(p; P, S) = i\gamma^1\gamma^3 \Delta_{\text{in}}^{[\mp]}(\bar{p}; \bar{P}, \bar{S}) i\gamma^1\gamma^3 \ , \tag{C.0.23}$$

where we took into account that T also interchanges initial and final states. Keeping the same notation as in [74], we can distinguish two different sources of behavior under T: the interchange in $\longleftrightarrow$ out (denoted by the label FSI) and the interchange of link structure (denoted by O). Thus, fixing a configuration of initial and final states, from (C.0.23) we can decompose a TMD fragmentation correlator in T-even and T-odd parts as [74]:

$$\Delta_{\text{out}}^{[\pm]}(z, k_T) = \left[\Delta_{\text{O}}^{[\text{T-even}]}(z, k_T) + \Delta_{\text{FSI}}^{[\text{T-odd}]}(z, k_T)\right] \pm \left[\Delta_{\text{O}}^{[\text{T-odd}]}(z, k_T) + \Delta_{\text{FSI}}^{[\text{T-even}]}(z, k_T)\right] . \tag{C.0.24}$$

Looking at the k_T-weighted correlator, (C.0.24) can be translated to:

$$\Delta_{\partial\ \text{out}}^{[\pm]\alpha}(z) = \left[\Delta_{\partial\ \text{O}}^{\alpha[\text{T-even}]}(z) + \Delta_{\partial\ \text{FSI}}^{\alpha[\text{T-odd}]}(z)\right] \pm \pi \left[\Delta_{G\ \text{O}}^{\alpha[\text{T-odd}]}(z, z) + \Delta_{G\ \text{FSI}}^{\alpha[\text{T-even}]}(z, z)\right] , \tag{C.0.25}$$

where the last two terms are two gluonic pole matrix elements for quark fragmentations. In [313–315] it has been shown, in model-(in)dependent ways, that partonic poles vanish, for fragmentation of both quarks and gluons. Thus, (C.0.24) and (C.0.25), respectively, reduces to

$$\Delta_{\text{out}}^{[\pm]}(z, k_T) = \left[\Delta_{\text{O}}^{[\text{T-even}]}(z, k_T) + \Delta_{\text{FSI}}^{[\text{T-odd}]}(z, k_T)\right] \tag{C.0.26}$$

$$\Delta^{[\pm]\alpha}_{\partial\ \mathrm{out}}(z) = \left[\Delta^{\alpha[\text{T-even}]}_{\partial\ \mathrm{O}}(z) + \Delta^{\alpha[\text{T-odd}]}_{\partial\ \mathrm{FSI}}(z)\right] . \tag{C.0.27}$$

This means that, in general, T-odd fragmentation functions exist and are due to the interchange of initial and final states, but not to the interplay with the link structure. For this reason, quark/gluon TMD FFs are *strictly universal*, namely T-odd TMD FFs (like the Collins function $H_1^\perp(z, k_T^2)$) are the same in all processes [316].

T-oddness has a different physical origin in distribution and fragmentation correlators: this is a crucial difference with respect to T-odd quark/gluon TMD PDFs. This reflects also onto the collinear fragmentation correlator, where we can have also T-odd terms with FSI source:

$$\Delta_{\mathrm{out}}(z) = \left[\Delta^{[\text{T-even}]}_{\mathrm{O}}(z) + \Delta^{[\text{T-odd}]}_{\mathrm{FSI}}(z)\right] . \tag{C.0.28}$$

Collinear T-odd terms appear at twist-3 in spin 1/2 hadrons, for quark [56] and gluon [57] fragmentations. In spin-1 hadrons, T-odd terms appear at twist-2 for quark fragmentation. This is the fragmentation analogue of the collinear Bacchetta function, which does not vanish beacuse T does not impose constraints on the correlator, due to the interchange of initial and final states.

APPENDIX D

CORRELATORS AND FOURIER TRANSFORMS

Factorization and TMD evolution are implemented in $\boldsymbol{b}_T$ space, so it is useful to write the correlator on the light-front as a function of $\boldsymbol{b}_T$. Here we present results for the gluon-gluon distribution correlator for the proton, but the procedure is general. We assume that the correlator in $\boldsymbol{b}_T$ space can be derived from the TMD one in $\boldsymbol{p}_T$ space via a Fourier transform. Moreover, we define TMD functions in $\boldsymbol{b}_T$ space as Fourier transform of the functions in $\boldsymbol{p}_T$ space:

$$\Gamma^{ij}(x, \boldsymbol{b}_T) \equiv \int d^2\boldsymbol{k}_T \; e^{i\boldsymbol{p}_T\cdot\boldsymbol{b}_T} \; \Gamma^{ij}(x, \boldsymbol{p}_T) \tag{D.0.1}$$

$$\tilde{f}(x, b_T^2) \equiv \int d^2\boldsymbol{p}_T \; e^{i\boldsymbol{p}_T\cdot\boldsymbol{b}_T} \; \tilde{f}(x, p_T^2) \; . \tag{D.0.2}$$

These two equations set the relations between the dimensions of the correlator and the functions in $\boldsymbol{p}_T$ and $\boldsymbol{b}_T$ space.

Computing (D.0.1), we can see that the functions entering the parametrizations of $\Gamma(x, \boldsymbol{b}_T)$ are not the ones in (D.0.2), but their n^{th}-derivatives with respect to $\boldsymbol{b}_T^2$, n being the rank of the function in $\boldsymbol{p}_T$ space:

$$\tilde{f}^{(n)}(x, b_T^2) \equiv n!\bigg(- \frac{2}{M^2}\frac{\partial}{\partial \boldsymbol{b}_T^2}\bigg)^n \; \tilde{f}(x, b_T^2) \tag{D.0.3}$$

$$= \frac{2\pi n!}{M^{2n}} \int_0^{+\infty} d|\boldsymbol{p}_T||\boldsymbol{p}_T| \bigg(\frac{|\boldsymbol{p}_T|}{|\boldsymbol{b}_T|}\bigg)^n J_n(|\boldsymbol{p}_T||\boldsymbol{b}_T|) f(x, p_T^2) \; , \tag{D.0.4}$$

where we have used the property:

$$\int_0^{2\pi} d\phi_p e^{in\phi_p} e^{ix\cos(\phi_b-\phi_p)} = 2\pi\ i^n J_n(x)\ e^{in\phi_b}\ . \tag{D.0.5}$$

$J_n(z)$ is the Bessel function of the first kind of order n, defined as:

$$J_n(z) = \frac{1}{2\pi i^n}\ \int_0^{2\pi} d\varphi\ e^{in\varphi}\ e^{iz\cos\varphi}\ . \tag{D.0.6}$$

The coefficient M^{-2n} renders the derivative operator adimensional. The $n!$ is to match with the conventions set in [129]. (D.0.3) can be derived from the property:

$$\left(\frac{1}{z}\frac{d}{dz}\right)^k \left(z^{-\nu} J_\nu(z)\right) = (-)^k z^{-\nu-k} J_{\nu+k}(z)\ , \tag{D.0.7}$$

considering $\nu = 0$, $k = n$ and $z = |\boldsymbol{p}_T||\boldsymbol{b}_T|$ with $|\boldsymbol{p}_T|$ fixed.

Since we have expanded the light-front correlators in terms of symmetric traceless tensors built from p_T, it follows from (D.0.3) that there is a one-to-one correspondence between the TMDs in $\boldsymbol{b}_T$- and in $\boldsymbol{p}_T$-space. Below we give an overview of correlators in $\boldsymbol{b}_T$ space obtained with this method. Expression for the gluon-gluon and the Wilson loop correlators including spin-1 terms can be found in [78].

Gluon-gluon correlator

$$\Gamma_U^{ij}(x,\boldsymbol{b}_T) = \frac{xP^+}{2}\left[-g_T^{ij}\,\tilde{f}_1(x,\boldsymbol{b}_T^2) - \frac{M^2}{2} b_T^{ij}\,\tilde{h}_1^{\perp(2)}(x,\boldsymbol{b}_T^2)\right], \tag{D.0.8}$$

$$\Gamma_L^{ij}(x,\boldsymbol{b}_T) = \frac{xP^+}{2}\left[i\epsilon_T^{ij} S_L\,\tilde{g}_1(x,\boldsymbol{b}_T^2) - S_L\frac{M^2}{4}\,\epsilon_{T\alpha}^{\{i} b_T^{j\}\alpha}\,\tilde{h}_{1L}^{\perp(2)}(x,\boldsymbol{b}_T^2)\right], \tag{D.0.9}$$

$$\begin{aligned}\Gamma_T^{ij}(x,\boldsymbol{b}_T) = \frac{xP^+}{2}\Big[&-i\,M g_T^{ij}\epsilon_T^{S_T b_T}\,\tilde{f}_{1T}^{\perp(1)}(x,\boldsymbol{b}_T^2) - M\epsilon_T^{ij}(\boldsymbol{b}_T\cdot\boldsymbol{S}_T)\,\tilde{g}_{1T}^{(1)}(x,\boldsymbol{b}_T^2)\\ &-\frac{iM}{4}\left(\epsilon_T^{b_T\{i} S_T^{j\}} + \epsilon_T^{S_T\{i} b_T^{j\}}\right)\tilde{h}_1^{(1)}(x,\boldsymbol{b}_T^2)\\ &+\frac{iM^3}{12}\epsilon_T^{\{i}{}_\alpha\, b_T^{j\}\alpha S_T}\,\tilde{h}_{1T}^{\perp(3)}(x,\boldsymbol{b}_T^2)\Big].\end{aligned} \tag{D.0.10}$$

Alternative form for the gluon correlator

The following definition and parametrization of the gluon-gluon correlator are equivalent to the ones given in Chap. 2 in frame A (see Sec. 2.6). They will be used in

Chap. 8:

$$\Gamma_g^{\mu\nu}(x,\boldsymbol{p}_T) = \frac{n_\rho\, n_\sigma}{(p\cdot n)^2}\int \frac{d(\xi\cdot P)\, d^2\xi_T}{(2\pi)^3}\; e^{ip\cdot\xi}\, \langle P|\ \mathrm{Tr}\left[\, F^{\mu\rho}(0)\, U_{[0,\xi]} F^{\nu\sigma}(\xi)\, U'_{[\xi,o]}\,\right] |P\rangle\,\big\rfloor_{\mathrm{LF}}\,, \tag{D.0.11}$$

$$\begin{aligned}
\Gamma_U^{\mu\nu}(x,\boldsymbol{p}_T) &= \frac{1}{2x}\left\{ -\, g_T^{\mu\nu}\, f_1^g(x,\boldsymbol{p}_T^2) + \left(\frac{p_T^\mu p_T^\nu}{M_h^2} + g_T^{\mu\nu}\frac{\boldsymbol{p}_T^2}{2M_h^2}\right) h_1^{\perp\, g}(x,\boldsymbol{p}_T^2)\right\},\\
\Gamma_L^{\mu\nu}(x,\boldsymbol{p}_T) &= \frac{1}{2x}\, S_L\, \left\{ i\epsilon_T^{\mu\nu}\, g_{1L}^g(x,\boldsymbol{p}_T^2) \,+\, \frac{\epsilon_T^{p_T\{\mu} p_T^{\nu\}}}{M_h^2}\, h_{1L}^{\perp g}(x,\boldsymbol{p}_T^2)\right\}\,,\\
\Gamma_T^{\mu\nu}(x,\boldsymbol{p}_T) &= \frac{1}{2x}\left\{ g_T^{\mu\nu}\, \frac{\epsilon_T^{p_T S_T}}{M_h}\, f_{1T}^{\perp\, g}(x,\boldsymbol{p}_T^2) \,+\, i\epsilon_T^{\mu\nu}\, \frac{p_T\cdot S_T}{M_h}\, g_{1T}^{\perp\, g}(x,\boldsymbol{p}_T^2)\right.\\
&\quad -\, \frac{\epsilon_T^{p_T\{\mu} S_T^{\nu\}} \,+\, \epsilon_T^{S_T\{\mu} p_T^{\nu\}}}{4M_h}\, h_1^g(x,\boldsymbol{p}_T^2)\\
&\quad \left. -\, \frac{1}{2M_h^3}\, \epsilon_{T\alpha}^{\{\mu} p_T^{\nu\}\alpha\beta} S_{T\beta}\; h_{1T}^{\perp\, g}(x,\boldsymbol{p}_T^2)\right\}.
\end{aligned} \tag{D.0.12}$$

Note that despite integrating over $\xi\cdot P$ in (D.0.11), $P^+ \neq 1$.

APPENDIX E

CONVENTIONS FOR NONPERTURBATIVE PARAMETERS

For convenience, we collect the naive translation of the nonperturbative parameters here. In the conventions of [139, 174], the nonperturbative parameters appear as:

$$\mathrm{d}\sigma \propto \exp\left(-\frac{1}{4}\left(\langle k_T^2\rangle_{q_1} + \langle k_T^2\rangle_{q_2}\right) b_T^2\right) \ . \tag{E.0.1}$$

In CuTe [108] only nonperturbative parameter enters the cross section:

$$\mathrm{d}\sigma \propto \exp\left(-2\Lambda_{NP}^2 b_T^2\right) \ . \tag{E.0.2}$$

The same happens in DyqT [106] and DYRes [107], in terms of the nonperturbative parameter g_{NP}:

$$\mathrm{d}\sigma \propto \exp\left(-g_{NP} b_T^2\right) \ . \tag{E.0.3}$$

We obtain the parameter employed in CuTe as:

$$\begin{aligned} \Lambda_{NP} &= \sqrt{\frac{1}{8}\left(\langle k_T^2\rangle_{q_1} + \langle k_T^2\rangle_{q_2}\right)} \ , \\ \Lambda_{NP} &= \sqrt{g_{NP}/2} \ . \end{aligned} \tag{E.0.4}$$

The same applies to the DYqT parameter:

$$\begin{aligned} g_{NP} &= \frac{1}{4}\left(\langle k_T^2\rangle_{q_1} + \langle k_T^2\rangle_{q_2}\right) \ , \\ g_{NP} &= 2\Lambda_{NP}^2 \ . \end{aligned} \tag{E.0.5}$$

The scaling between the parameters related to a single quark is:

$$\Lambda_{\mathrm{DyRes}} = \frac{\Lambda_{\mathrm{CuTe}}}{4}\frac{1.2}{0.72} \,. \tag{E.0.6}$$

Here we report the most important values:

	$\langle k_T^2 \rangle (q_1 = q_2)$	Λ_{NP} CuTe	g_{NP} DYqT
CuTe default	1.44	0.60	0.72
DYqT conservative estimate	2.40	0.77	1.2

APPENDIX F

LINKS

Here we collect links to websites and projects dealing with particle physics in general and phenomenology of TMDs in particular, ranging from low-energy to high-energy physics.

Experimental collaborations

- HERA: `http://www.desy.de/research/facilities__projects/hera/index_eng.html`
- HERMES: `http://www-hermes.desy.de/`
- COMPASS: `https://wwwcompass.cern.ch/`
- JLab 12 GeV: `https://www.jlab.org/12-gev-upgrade`
- LHeC: `http://lhec.web.cern.ch/`
- EIC - eRHIC: `https://wiki.bnl.gov/eic/index.php/Main_Page`
- EIC - MEIC/JLEIC: `https://eic.jlab.org/wiki/index.php/Main_Page`
- BaBar: `http://www.slac.stanford.edu/BFROOT/`
- BES-III: `http://bes3.ihep.ac.cn/index.htm`
- Belle: `http://belle.kek.jp/`
- Belle II: `https://www.belle2.org/`
- ILC: `https://www.linearcollider.org/`

- LHC: http://home.cern/topics/large-hadron-collider
- RHIC: https://www.bnl.gov/rhic/eic.asp
- STAR: https://www.star.bnl.gov/
- AFTER@LHC: http://after.in2p3.fr/after/index.php/Main_Page
- JPARC: http://j-parc.jp/index-e.html

Data repositories

- The Particle Data Group : http://pdg.lbl.gov/
- The Durham HepData Project : http://hepdata.cedar.ac.uk/
- Hermes multiplicities: http://hermesmults.appspot.com/
- Tevatron electroweak working group: http://tevewwg.fnal.gov/wz/
- CERN Open Data Portal: http://opendata.cern.ch/
- ATLAS experiment, Standard Model results: https://twiki.cern.ch/twiki/bin/view/AtlasPublic/StandardModelPublicResults

Software

- LHAPDF: http://lhapdf.hepforge.org/
- database of collinear fragmentation functions: http://www2.pv.infn.it/~radici/FFdatabase/
- The TMD project: http://tmd.hepforge.org/
- TMDlib: https://tmdlib.hepforge.org/
- TMDplotter: http://tmdplotter.desy.de/
- GMCTRANS : https://wiki.bnl.gov/eic/index.php/Gmc_trans
- ResBos : http://hep.pa.msu.edu/resum/
- Cascade: https://cascade.hepforge.org/
- HeraFitter: https://www.herafitter.org

APPENDIX G

SUMMARY

If you want to build a ship,
don't drum up people to collect wood
and don't assign them tasks and work,
but rather teach them to long
for the endless immensity of the sea.
Antoine de Saint-Exupéry

A beautiful landscape

Protons and neutrons are among the building blocks of matter and they account for almost all the mass of our world. Even if many efforts have been made to deepen our knowledge about them, we are still far from a complete understanding of their inner structure. Over the past few years, thanks to a fruitful synergy of theoretical and experimental progress, we have opened the study of new multidimensional images of the structure of the proton, investigating the behavior of its fundamental constituents, the quarks and gluons (collectively called partons). The internal structure of the proton is shaped by Quantum Chromodynamics (QCD) and it is one of the most fascinating and yet unexplored natural landscapes. Despite not being directly accessible by our eyes, we can still appreciate its beauty by means of particle accelerators, which are the most powerful microscopes in the world. The procedure described in Chap. 5 of this thesis works, in essence, as if we are taking a photograph of the proton structure in momentum space. The energy transferred by the flash is so high that the proton breaks and we can reconstruct pictures of the proton structure by looking at the fragments.

Confinement

When we shoot pictures with extremely high resolution, the constituents of the proton appear almost free. Instead, due to the nature of the strong force in QCD, when we look at the proton with lower resolutions, quarks and gluons are inescapably *confined* inside the proton. At present we are not able yet to fully understand mathematically the transition to this confined phase. Confinement is the most crucial characteristic of QCD and represents one of the hardest physics problems of today, listed as one of the Millenium Prize Problems by the Clay Mathematics Institute. It also prevents us from calculating maps of the proton structure (and of hadron structure more in general) from the first principles of the theory. One of the options we are left with in order to study the proton is shooting "subatomic photographs" employing the exchange of photons, which we can fully control.

Multidimensional maps of the proton

Studying the internal landscape of the proton and drawing maps of its structure is one of the hot topics in particle physics. It is complementary to the searches of new physics at the Large Hadron Collider (LHC) and it is not less important. Not only it responds to our desire of knowledge and understanding the world, but it will also have crucial impacts on some of the open problems in particle physics, such as to unravel the various contributions to the proton spin [13, 77, 317].

The knowledge of the multidimensional structure of protons allows for the analysis of properties otherwise inaccessible. Diagnostic studies provide an effective analogy: electrocardiography, for example, gives us one-dimensional information about the heart activity. It is of great importance, but it does not give detailed information about the multidimensional inner structure. Instead, more refined tomographies can open windows on the multidimensional structure and provide fundamental additional information.

Concerning the proton tomography, we know with good accuracy one-dimensional maps in momentum space (see Fig. 1.2 and Chap. 4), the collinear parton distribution functions (PDFs). They are the prime ingredient for studying any process involving hadrons (such as the proton-proton collisions taking place at the LHC), but from the point of view of nucleon tomography they are rather limited. They describe the distribution of partons in a single dimension in momentum space, namely assuming that the constituents move collinear with the parent hadron. More informative objects are the so-called transverse-momentum-dependent distributions (TMDs), which represent three-dimensional pictures in momentum space (see Chap. 2).

The coordinates used to parametrize these maps are the momentum components (usually divided in collinear and transverse) of the constituents and the energy at which the picture of the proton has been shot. Fortunately, we can (almost

completely) calculate the energy dependence of the map by means of QCD evolution equations (see Chap. 3) and this allows us, for example, to use at the LHC the pictures of the proton structure measured at the Hadron-Electron Ring Accelerator (HERA). To this extent, one should be careful about the transverse momentum dependence, which introduces a calculable process dependence for the maps [24].

Open questions

To first approximation, we can introduce eight different types of three-dimensional maps for quarks and gluons in momentum space (see Chap. 2). This richness emerges from all the possible correlations between the momenta and the spins of the constituents and the proton itself. From a theoretical point of view, we know how to define these maps by means of operators in QCD. Nonetheless, there are many nontrivial questions concerning the TMDs that do not have a complete answer yet. For example: "What does the transverse momentum dependence look like?".

This thesis is focused on this question, in particular for the simplest three-dimensional map for quarks, the unpolarized distribution. At present, we know that experimental data from proton-proton and lepton-proton collisions point towards Gaussian functional forms at low transverse momentum. Until recently, we did not have any information on their flavor dependence, though (see Fig. G.1). Namely, are up quarks moving in the nucleon with greater velocity than the down ones, or vice versa? What about sea quarks? Are they faster than the other ones? The study presented in Chap. 5 addresses these questions. From analyses of lepton-proton and lepton-deuteron scattering data, we now know that sea quarks are likely to be faster than up quarks, which are in turn faster than down ones. This result is interesting also in order to describe other reactions where hadrons play a role, for example electron-positron annihilation into pions and kaons (see Chap. 6) and proton-proton collisions at the LHC (see Chap. 7). New effects have been observed in both cases.

Concerning gluons instead, in Chap. 8 we investigate the interplay between two of the three-dimensional distributions, namely the ones for unpolarized and for linearly polarized gluons in unpolarized protons. For both, we study their definition and the impact of evolution equations, selecting a process useful to better constrain their properties.

Impact and outlook

In general, the interpretation of the huge amount of data collected at hadron colliders like the LHC relies on the knowledge of parton distribution functions, both in one dimension (the PDFs) and in three dimensions (the TMDs). Until now, data analysis of high-energy particle reactions has been performed assuming that all the quarks move with the same average transverse momentum. Now that we know that more general flavor-dependent scenarios are also likely, it will be important to test

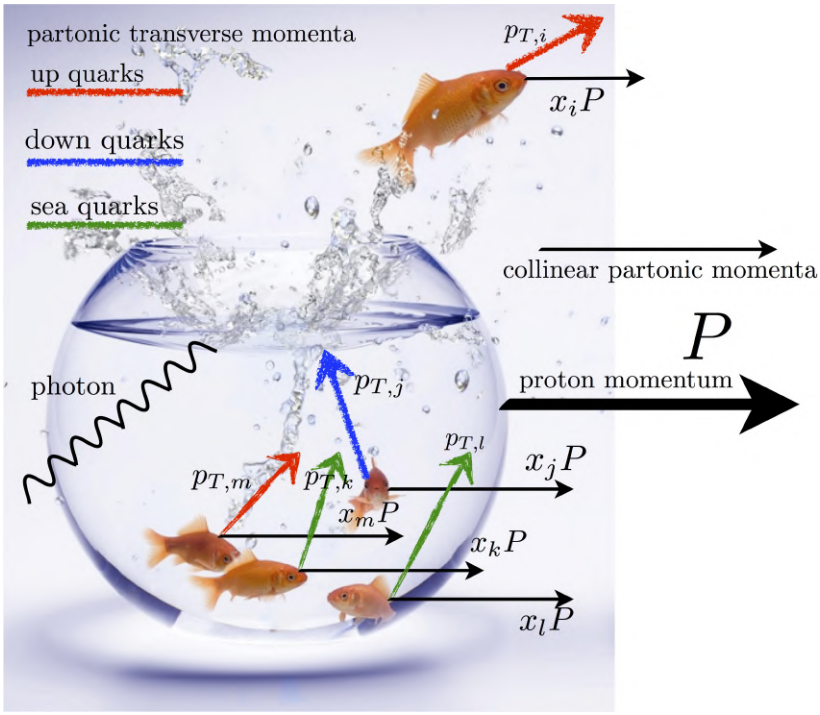

Figure G.1. Quarks and gluons are like fishes confined inside a fishbowl (the proton). Each parton has its own collinear and transverse velocity, indicated by black and colored arrows respectively. Different colors indicate different flavors for quarks and external excitations (like photons) can extract partons from inside the proton.

their impact, as done in Chapters 6 and 7. Refining the knowledge of the proton structure will also improve the accuracy of searches for new physics at hadron colliders.

Unpolarized TMDs for quarks and gluons are also interesting in order to study all the other polarized distributions, because they affect their phenomenological investigation. The possibility of accessing the orbital angular momentum of the partons makes the tomography of hadron structure in momentum space a valuable starting point to solve the spin puzzle of the proton.

New experimental programs, among which A Fixed Target Experiment at the LHC (AFTER@LHC) in Europe and the Electron-Ion Collider (EIC) in the United States, will provide us with the possibility of taking more powerful and precise pictures of the proton inner landscape, helping in completing our knowledge of its structure. Exciting times for physicists dealing with hadron physics are just ahead.

For further introductory discussions on the open puzzles in hadronic physics see, e.g., [13, 318], "The proton in 3D" (A. Bacchetta, M. Contalbrigo) and "Femtostrutture: e pluribus unum" (A. Bacchetta, A. Signori; Italian only). Outreach contributions about particle physics are available on Quantum Diaries, the blog of the Interactions collaboration.

APPENDIX H

SAMENVATTING

Een prachtig landschap

Protonen en neutronen zijn bouwstenen van materie en verantwoordelijk voor bijna alle massa in onze wereld. Ondanks vele inspanningen om onze kennis over deze deeltjes te vergroten, is een volledig begrip van hun interne structuur nog ver weg. Vrij recentelijk worden er dankzij een synergie van theoretisch en experimenteel onderzoek pogingen gedaan om een multidimensionaal beeld van de interne structuur van het proton te krijgen en het dynamische gedrag van de fundamentele quarks en gluonen (collectief partonen genoemd) te bestuderen. De interne structuur van het proton wordt theoretisch beschreven met de kwantumchromodynamica (QCD), een fascinerend terrein in de natuurkunde met nog veel onbekende stukken. Ondanks dat de wereld van QCD niet direct met onze ogen waarneembaar is, kunnen we haar schoonheid waarderen gebruikmakend van deeltjesversnellers, de krachtigste microscopen ter wereld. De procedure die in H. 5 van dit proefschrift wordt beschreven, kan in essentie worden opgevat als het nemen van een foto van het proton in impulsruimte. De energie-overdracht bij een dergelijke lichtflits is dermate hoog dat het proton uiteenvalt. De brokstukken kunnen vervolgens worden gebruikt om de protonstructuur te reconstrueren.

Confinement

Wanneer we foto's maken met een extreem hoge resolutie, lijken de bouwstenen van het proton zich nagenoeg als vrije deeltjes te gedragen. Als we daarentegen naar het proton kijken met lagere resoluties, dan blijken de quarks en gluonen opgesloten te zitten in het proton als gevolg van de sterke kernkracht in QCD. Dit wordt *confinement* genoemd. Vandaag de dag bestaat er nog geen volledige wis-

kundige beschrijving voor de overgang naar confinement. Het is een van de meest kenmerkende eigenschappen van QCD en tevens een openstaand natuurkundeproblemen. Een wiskundige beschrijving van confinement in QCD is daarom ook niet voor niets een van de Millenium Prize Problems van het Clay Mathematics Institute. Ons beperkte begrip van confinement heeft als gevolg dat de protonstructuur (of de structuur van hadronen meer in het algemeen) niet berekend kan worden met de QCD theorie. Een andere optie, echter, is het maken van "subatomaire foto's" van het proton gebruikmakende van de uitwisseling van fotonen waarmee experimentatoren gemakkelijk kunnen werken.

Multidimensionale afbeeldingen van het proton

De studie van de interne structuur van het proton is een van de "hot topics" in de deeltjesfysica. Het is een aanvulling op de zoektochten naar nieuwe fysica in de Large Hadron Collider (LHC) en zeker niet minder belangrijk. Het draagt niet alleen bij aan onze kennis en ons begrip van de wereld om ons heen, maar het zal ook invloed hebben op openstaande vragen in de deeltjesfysica zoals het ontrafelen van de verschillende bijdragen aan de spin van het proton [13, 77, 317].

Kennis van de multidimensionale protonstructuur maakt de analyse mogelijk van eigenschappen die anders ontoegankelijk zouden zijn. Een goede analogie is het volgende voorbeeld: elektrocardiografie geeft eendimensionale informatie over de hartactiviteit, maar geeft geen gedetailleerde informatie over de multidimensionale interne structuur van het hart. Meer verfijnde tomografie opent deuren naar die multidimensionale structuur en levert nieuwe fundamentele informatie op.

Wat betreft protontomografie beschikken we over goede kennis van eendimensionale afbeeldingen in impulsruimte (zie Fig. 1.2 en H. 4), de collineaire partondistributiefuncties (PDFs). Hoewel deze functies zeer nuttig zijn voor het bestuderen van processen waar hadronen bij betrokken zijn (zoals de proton-proton botsingen die plaatsvinden in de LHC), zijn ze beperkt in gebruik vanuit het oogpunt van nucleontomografie, omdat ze de verdeling van partonen beschrijven in één enkele dimensie in impulsruimte vanwege de aanname dat de partonen collineair bewegen, parallel aan de impuls van het proton. Meer informatief zijn de zogenaamde transversale-impulsafhankelijke distributies (TMDs), driedimensionale afbeeldingen in impulsruimte (zie H. 2).

De coördinaten die worden gebruikt om deze afbeeldingen te parametriseren zijn de impulscomponenten (deze worden gebruikelijk opgesplitst in collineair en transversaal) van de partonen, maar ook de energie van het overgedragen foton waarmee een foto van het proton is gemaakt. De energie-afhankelijkheid van de distributies kan nagenoeg volledig worden berekend met behulp van de QCD evolutievergelijkingen (zie H. 3), waardoor we bijvoorbeeld de afbeeldingen van het proton verkregen met de Hadron-Electron Ring Accelerator (HERA) bij DESY ook kunnen gebruiken voor LHC experimenten bij CERN. Voorzichtigheid is echter ge-

boden betreffende de afhankelijkheid van transversale impuls. Dit geeft aanleiding tot een berekenbare procesafhankelijkheid van de distributies [24].

Open vragen

In eerste benadering zijn er acht verschillende types van driedimensionale afbeeldingen van quarks en gluonen in impulsruimte (zie H. 2). Dit volgt uit de mogelijke correlaties tussen impulsen en spins van de partonen. Vanuit een theoretisch oogpunt weten we hoe we dit soort afbeeldingen kunnen definiëren door middel van operatoren in QCD. Niettemin zijn er nog steeds veel belangrijke vragen met betrekking tot TMDs waarbij een volledig antwoord ontbreekt, bijvoorbeeld: "Hoe ziet de afhankelijkheid van de transversale impuls er nou precies uit?".

Deze vraag staat centraal in dit proefschrift en wel in het bijzonder voor het geval van de simpelste driedimensionale afbeelding voor quarks, de ongepolariseerde distributie. Experimentele data afkomstig van proton-proton en lepton-proton botsingen lijkt de wijzen op een Gauss-achtige afhankelijkheid voor kleine transversale impulsen. Het ontbreekt ons echter nog aan informatie over de precieze afhankelijkheid van de quarksmaken (zie Fig. G.1). Bewegen de up-quarks bijvoorbeeld sneller in het nucleon dan de down-quarks, of juist andersom? En hoe zit het met de 'zee'-quarks behorend bij de zee van quark-antiquark paren? Bewegen deze sneller dan de anderen? De laatste vraag wordt besproken in H. 5. Uit analyses van lepton-proton en lepton-deuteron data volgt dat zee-quarks waarschijnlijk sneller bewegen dan up-quarks, welke weer sneller bewegen dan down-quarks. Dit resultaat is tevens interessant voor de beschrijving van andere reacties waarbij hadronen een rol spelen, zoals bij elektron-positron annihilatie waarbij pionen en kaonen gemaakt worden (zie H. 6), alsook bij proton-proton botsingen in de LHC (zie H. 7). In beide gevallen zijn er nieuwe effecten waargenomen.

In H. 8 onderzoeken we de wisselwerking tussen twee driedimensionale distributies, namelijk die voor ongepolariseerde en lineair gepolariseerde gluonen in ongepolariseerde protonen. Voor beide distributies bestuderen we hun precieze definities en de invloed van evolutievergelijkingen, waarbij we een proces selecteren om hun eigenschappen beter te kunnen onderzoeken.

Invloed en vooruitzichten

De interpretatie van de enorme hoeveelheid data afkomstig van hadronversnellers zoals de LHC hangt over het algemeen af van onze kennis van partondistributiefuncties, zowel in één dimensie (de PDFs) als in drie dimensies (de TMDs). Tot nu toe is er voor de data-analyse van hoogenergetische processen aangenomen dat alle quarks bewegen met dezelfde gemiddelde transversale impuls. Nu we weten dat meer algemene, quarksmaakafhankelijke scenario's ook mogelijk zijn, is het belangrijk om de impact hiervan te testen, zoals wordt beschreven in H. 6 en 7. Het

verfijnen van onze kennis van de protonstructuur zal ook de nauwkeurigheid van het zoeken naar nieuwe fysica in hadronversnellers vergroten.

Goede kennis van de ongepolariseerde TMDs voor quarks en gluonen is belangrijk om de andere gepolariseerde distributies nauwkeurig te kunnen bestuderen, vanwege hun invloed op het fenomenologische onderzoek. De mogelijkheid om het baanimpulsmoment van partonen te meten, maakt de hadrontomografie in impulsruimte een waardevol startpunt om de spinopbouw van het proton beter te begrijpen.

Nieuwe experimentele programma's zoals in Europa het 'A Fixed Target Experiment' in de LHC (AFTER@LHC) en in de Verenigde Staten de Electron-Ion Collider (EIC) zullen ons in staat stellen om nog krachtigere en preciezere foto's te maken van de interne structuur van het proton. Voor fysici werkzaam op het gebied van de hadronfysica worden het spannende tijden.

Voor meer inleidende informatie over de openstaande problemen in de hadronfysica, zie bijvoorbeeld [13,318], "The proton in 3D" (A. Bacchetta, M. Contalbrigo) en "Femtostrutture: e pluribus unum" (A. Bacchetta, A. Signori; alleen in het Italiaans). Bijdrages aan outreachprogramma's over deeltjesfysica zijn beschikbaar op Quantum Diaries, het blog van de Interactions collaboratie.

ACKNOWLEDGMENTS

The first words of gratitude are for Piet Mulders, my supervisor and promotor. Thank you for your patient guidance, for being always available and eager to broaden my horizons. I enjoyed the atmosphere in our group, it has been friendly, lively and stimulating. I strongly believe that your effort in educating and inspiring young researchers is invaluable.

I also wish to thank the members of the reading committee (Alessandro Bacchetta, Daniël Boer, Eric Laenen, Gerhard Raven, Raimond Snellings) and my co-promotor Marco Radici for the careful examination of this thesis, and Marja Herronen for her precious and precise support with all the administrative matters in the last four years.

I am deeply indebted to the people who devoted time and energies to educate me, especially Alessandro Bacchetta and Marco Radici in Pavia and Miguel Echevarria, Tomas Kasemets, Cristian Pisano, and Mathias Ritzmann at Nikhef. Thank you! I will do my best to be as valuable as you have been for me in these years.

Along my PhD program I also benefited from the expertise of many other researchers, with whom I collaborated (directly and indirectly) and exchanged ideas. Listing everybody would be impossible, but special thanks go to Daniël Boer, Maria Elena Boglione, Charlotte van Hulse, Hannes Jung, Jean-Philippe Lansberg, Emanuele Nocera, Barbara Pasquini, Ted Rogers, Gunar Schnell, Jian Zhou, and Ya-Jin Zhou. I enjoyed working and discussing with you, especially during conferences and workshops.

Thanks to my PhD-mates, Maarten Buffing, Sabrina Cotogno and Tom van Daal, for sharing everything of the PhD-life with me. I always appreciate both the human and scientific support that we manage to give to each other. A special mention also for my office mates in these years, Giuseppe d'Ambrosi, Maarten

Buffing and Sabrina Cotogno. You made our messy room a colorful, lively and tea-friendly place: thanks! Moreover, I enjoyed every day a bit more the Nikhef Theory Group. Thanks to all the present and past members that I met, for contributing to such a rich environment.

Living abroad is a challenging experience. I wish to thank in particular Maarten Buffing, Tom van Daal, Rob Knegjens, Palmira Lieuw, Sander Mooij, Claudio Pollice, Robbert Rietkerk, Jorinde van de Vis, Jan Weenink for helping me get acquainted a bit more with the Dutch culture and language and to the Italian crew (Mario Daprà, Nicoletta Liguori, Domenico Bonocore, Sabrina Cotogno, Jacopo Fumagalli, Francesca Ferrari, Paolo Rosi, Natascia Pinzani, Edoardo Fantechi, Giuseppe d'Ambrosi, Elisa Mariani, Sara Oliveira) for all the times that we managed to feel at home together. Thanks also to you, Walter Cannizzo, for helping me settle down in Amsterdam and for sharing our experiences and feelings.

Mamma, papà, grazie per avermi sostenuto in questi anni, per avermi incoraggiato e guidato. Quello che riesco a fare oggi, lo devo a quanto avete fatto (e continuate a fare) voi con me. Thanks also to my sister Federica, and to Cristiano. Despite having been scattered around Europe, I always felt your support. Thanks for sharing your thoughts, your enthusiasm and your fears. Even if we do not really know where our roads will lead us, I am sure we will always be close to each other.

I always enjoyed from a distance the support from my friends in Italy. Too many to list everyone, but special thoughts go to Mattia, Sara, Franci, Paolino, Betta, Francesco, Paco, Paolotto, Giuba, Diana. Thanks, you have always been a second family for me.

Finally, I wish to thank the person that always accompanied me during these years, first from a distance and then at my side. Carlotta, thank you. Your presence is such a precious gift, and I am delighted that it will be a lighthouse for the future.

Amsterdam, October 17$^{\text{th}}$ 2016

LIST OF FIGURES

LIST OF TABLES

BIBLIOGRAPHY

[1] C.-N. Yang and R. L. Mills, *Conservation of isotopic spin and isotopic gauge invariance*, Phys. Rev. **96** (1954) 191–195.

[2] M. Nakahara, *Geometry, topology and physics*. Boca Raton, USA: Taylor and Francis (2003) 573 p, 2003.

[3] J. Jost, *Riemannian geometry and geometric analysis*. Universitext. Springer, Berlin, 2002.

[4] M. E. Peskin and D. V. Schroeder, *An introduction to quantum field theory*. Addison-Wesley, Reading, MA, USA, 1995.

[5] T. Muta, *Foundations of Quantum Chromodynamics: An Introduction to Perturbative Methods in Gauge Theories, (3rd ed.)*, vol. 78 of *World scientific Lecture Notes in Physics*. World Scientific, Hackensack, N.J., 2010.

[6] Particle Data Group, K. A. Olive et al., *Review of Particle Physics*, Chin. Phys. **C38** (2014) 090001.

[7] X.-S. Chen, X.-F. Lu, W.-M. Sun, F. Wang, and T. Goldman, *Spin and orbital angular momentum in gauge theories: Nucleon spin structure and multipole radiation revisited*, Phys.Rev.Lett. **100** (2008) 232002, [arXiv:0806.3166].

[8] M. Wakamatsu, *On Gauge-Invariant Decomposition of Nucleon Spin*, Phys.Rev. **D81** (2010) 114010, [arXiv:1004.0268].

[9] Y. Hatta, *Gluon polarization in the nucleon demystified*, Phys.Rev. **D84** (2011) 041701, [arXiv:1101.5989].

[10] Y. Hatta, *Notes on the orbital angular momentum of quarks in the nucleon*, [arXiv:1111.3547].

[11] Y. Hatta and S. Yoshida, *Twist analysis of the nucleon spin in QCD*, JHEP **10** (2012) 080, [arXiv:1207.5332].

[12] C. Lorcé, *Gauge-covariant canonical formalism revisited with application to the proton spin decomposition*, Phys. Rev. **D88** (2013) 044037, [arXiv:1302.5515].

[13] A. Bacchetta, *Where do we stand with a 3-D picture of the proton?*, Eur. Phys. J. **A52** (2016), no. 6, 163.

[14] A. Bacchetta and M. Radici, *Constraining quark angular momentum through semi-inclusive measurements*, Phys.Rev.Lett. **107** (2011) 212001, [arXiv:1107.5755].

[15] A. Bacchetta, M. Diehl, K. Goeke, A. Metz, P. J. Mulders, and M. Schlegel, *Semi-inclusive deep inelastic scattering at small transverse momentum*, JHEP **02** (2007) 093, [hep-ph/0611265].

[16] V. Barone, F. Bradamante, and A. Martin, *Transverse-spin and transverse-momentum effects in high-energy processes*, Prog. Part. Nucl. Phys. **65** (2010) 267–333.

[17] D. Boer, M. Diehl, R. Milner, R. Venugopalan, W. Vogelsang, et al., *Gluons and the quark sea at high energies: distributions, polarization, tomography*, [arXiv:1108.1713].

[18] C. A. Aidala, S. D. Bass, D. Hasch, and G. K. Mallot, *The spin structure of the nucleon*, Rev. Mod. Phys. **85** (2013) 655–691, [arXiv:1209.2803].

[19] X. Ji, J.-P. Ma, and F. Yuan, *QCD factorization for semi-inclusive deep-inelastic scattering at low transverse momentum*, Phys. Rev. **D71** (2005) 034005, [hep-ph/0404183].

[20] J. Collins, *Foundations of perturbative QCD*. Cambridge University Press, 2011.

[21] S. J. Brodsky, D. S. Hwang, and I. Schmidt, *Final-state interactions and single-spin asymmetries in semi-inclusive deep inelastic scattering*, Phys. Lett. **B530** (2002) 99–107, [http://arXiv.org/abs/hep-ph/0201296].

[22] X. Ji and F. Yuan, *Parton distributions in light-cone gauge: where are the final-state interactions?*, Phys. Lett. **B543** (2002) 66–72, [hep-ph/0206057].

[23] A. V. Belitsky, X. Ji, and F. Yuan, *Final state interactions and gauge invariant parton distributions*, Nucl. Phys. **B656** (2003) 165–198, [hep-ph/0208038].

[24] M. G. A. Buffing, *Color and TMD Universality in Hadronic Interactions*, PhD thesis, NIKHEF, Amsterdam, 2015-09-02.

[25] J. Collins, *Different approaches to TMD Evolution with scale*, EPJ Web Conf. **85** (2015) 01002, [arXiv:1409.5408].

[26] M. G. Echevarria, A. Idilbi, and I. Scimemi, *Unified treatment of the QCD evolution of all (un-)polarized transverse momentum dependent functions: Collins function as a study case*, Phys. Rev. **D90** (2014), no. 1, 014003, [arXiv:1402.0869].

[27] Z.-B. Kang, A. Prokudin, P. Sun, and F. Yuan, *Nucleon tensor charge from Collins azimuthal asymmetry measurements*, Phys.Rev. **D91** (2015), no. 7, 071501, [arXiv:1410.4877].

[28] R. Angeles-Martinez et al., *Transverse Momentum Dependent (TMD) parton distribution functions: status and prospects*, Acta Phys. Polon. **B46** (2015), no. 12, 2501–2534, [arXiv:1507.05267].

[29] HERMES, A. Airapetian et al., *Multiplicities of charged pions and kaons from semi-inclusive deep-inelastic scattering by the proton and the deuteron*, Phys. Rev. **D87** (2013) 074029, [arXiv:1212.5407].

[30] COMPASS, C. Adolph et al., *Hadron transverse momentum distributions in muon deep inelastic scattering at 160 GeV/c*, [arXiv:1305.7317].

[31] EMC, M. Arneodo et al., *Transverse momentum and its compensation in current and target jets in deep-inelastic muon-proton scattering*, Phys. Lett. **B149** (1984) 415.

[32] H1, C. Adloff et al., *Measurement of charged particle transverse momentum spectra in deep-inelastic scattering*, Nucl. Phys. **B485** (1997) 3–24, [hep-ex/9610006].

[33] H. Mkrtchyan et al., *Transverse momentum dependence of semi-inclusive pion production*, Phys. Lett. **B665** (2008) 20–25, [arXiv:0709.3020].

[34] CLAS, M. Osipenko et al., *Measurement of unpolarized semi-inclusive π^+ electroproduction off the proton*, Phys. Rev. **D80** (2009) 032004, [arXiv:0809.1153].

[35] R. Asaturyan, R. Ent, H. Mkrtchyan, T. Navasardyan, V. Tadevosyan, et al., *Semi-inclusive charged-pion electroproduction off protons and deuterons: Cross sections, ratios and access to the quark-parton model at low energies*, Phys. Rev. **C85** (2012) 015202, [arXiv:1103.1649].

[36] S. J. Brodsky, F. Fleuret, C. Hadjidakis, and J. P. Lansberg, *Physics Opportunities of a Fixed-Target Experiment using the LHC Beams*, Phys. Rept. **522** (2013) 239–255, [arXiv:1202.6585].

[37] J.-P. Lansberg et al., *Physics case for a polarised target for AFTER@LHC*, PoS **PSTP2015** (2016) 042, [arXiv:1602.06857].

[38] H. Geiger and E. Marsden, *On a diffuse reflection of the α-particles*, Proceedings of the Royal Society of London A: Mathematical, Physical and Engineering Sciences **82** (1909), no. 557, 495–500, [http://rspa.royalsocietypublishing.org/content/82/557/495.full.pdf].

[39] E. M. Riordan, *The Discovery of quarks*, Science **256** (1992) 1287–1293.

[40] M. Gell-Mann, *The Eightfold Way: A Theory of strong interaction symmetry*, [inspirehep 44998].

[41] M. Gell-Mann and Y. Neemam, *The Eightfold way: a review with a collection of reprints*, [inspirehep 44629].

[42] M. Gell-Mann, *A Schematic Model of Baryons and Mesons*, Phys. Lett. **8** (1964) 214–215.

[43] G. Zweig, *An SU(3) model for strong interaction symmetry and its breaking. Version 1*, [inspirehep 11881].

[44] J. D. Bjorken, *PARTONS*, in *In *Bjorken, J.D.: A collection of summary talks in high energy physics* 77-92*, 1971.

[45] J. D. Bjorken, *Asymptotic Sum Rules at Infinite Momentum*, Phys. Rev. **179** (1969) 1547–1553.

[46] C. G. Callan, Jr. and D. J. Gross, *High-energy electroproduction and the constitution of the electric current*, Phys. Rev. Lett. **22** (1969) 156–159.

[47] W. B. Atwood, E. D. Bloom, R. L. Cottrell, H. C. DeStaebler, M. D. Mestayer, C. Y. Prescott, L. S. Rochester, S. Stein, R. E. Taylor, and D. Trines, *Inelastic electron Scattering from Hydrogen at 50-Degrees and 60-Degrees*, Phys. Lett. **B64** (1976) 479.

[48] F. E. Close, *An Introduction to Quarks and Partons*. 1979.

[49] D. J. Gross and F. Wilczek, *Ultraviolet behavior of non-abelian gauge theories*, Phys. Rev. Lett. **30** (1973) 1343–1346.

[50] D. J. Gross and F. Wilczek, *Asymptotically free gauge theories. i*, Phys. Rev. **D8** (1973) 3633–3652.

[51] H. D. Politzer, *Reliable perturbative results for strong interactions?*, Phys. Rev. Lett. **30** (1973) 1346–1349.

[52] H. Fritzsch and M. Gell-Mann, *Current algebra: Quarks and what else?*, eConf **C720906V2** (1972) 135–165, [hep-ph/0208010].

[53] H. Fritzsch, M. Gell-Mann, and H. Leutwyler, *Advantages of the Color Octet Gluon Picture*, Phys. Lett. **B47** (1973) 365–368.

[54] G. 't Hooft, *The birth of asymptotic freedom*, Nucl. Phys. **B254** (1985) 11–18.

[55] CMS, V. Khachatryan et al., *Measurement of the inclusive 3-jet production differential cross section in proton–proton collisions at 7 TeV and determination of the strong coupling constant in the TeV range*, Eur. Phys. J. **C75** (2015), no. 5, 186, [arXiv:1412.1633].

[56] F. Pijlman, *Single spin asymmetries and gauge invariance in hard scattering processes*, PhD thesis, Vrije U., Amsterdam, 2006, [hep-ph/0604226].

[57] P. J. Mulders, *Transverse momentum dependence in high-energy scattering processes.* Unpublished lecture notes, 2016.

[58] K. G. Wilson, *Nonlagrangian models of current algebra*, Phys. Rev. **179** (1969) 1499–1512.

[59] H. D. Politzer, *Power Corrections at Short Distances*, Nucl. Phys. **B172** (1980) 349.

[60] K. G. Wilson and W. Zimmermann, *Operator product expansions and composite field operators in the general framework of quantum field theory*, Commun. Math. Phys. **24** (1972) 87–106.

[61] S. Weinberg, *The quantum theory of fields. Vol. 2: Modern applications.* Cambridge University Press, 2013.

[62] R. L. Jaffe, *Spin, twist and hadron structure in deep inelastic processes*, [hep-ph/9602236].

[63] W. Zimmermann, *Normal products and the short distance expansion in the perturbation theory of renormalizable interactions*, Annals Phys. **77** (1973) 570–601, [Lect. Notes Phys.558,278(2000)].

[64] D. J. Gross and S. B. Treiman, *Light cone structure of current commutators in the gluon quark model*, Phys. Rev. **D4** (1971) 1059–1072.

[65] M. Radici, *Lectures notes - hadronic physics.* Unpublished notes - Master course at University of Pavia.

[66] R. K. Ellis, W. Furmanski, and R. Petronzio, *Unraveling Higher Twists*, Nucl. Phys. **B212** (1983) 29.

[67] R. K. Ellis, W. Furmanski, and R. Petronzio, *Power Corrections to the Parton Model in QCD*, Nucl. Phys. **B207** (1982) 1.

[68] J.-W. Qiu and G. F. Sterman, *Power corrections to hadronic scattering. 2. Factorization*, Nucl. Phys. **B353** (1991) 137–164.

[69] J.-W. Qiu and G. F. Sterman, *Power corrections in hadronic scattering. 1. Leading $1/Q^2$ corrections to the Drell-Yan cross section*, Nucl. Phys. **B353** (1991) 105–136.

[70] J.-W. Qiu and G. F. Sterman, *Single transverse spin asymmetries in hadronic pion production*, Phys. Rev. **D59** (1999) 014004, [hep-ph/9806356].

[71] R. D. Tangerman and P. J. Mulders, *Intrinsic transverse momentum and the polarized Drell-Yan process*, Phys. Rev. **D51** (1995) 3357–3372, [hep-ph/9403227].

[72] P. J. Mulders and J. Rodrigues, *Transverse momentum dependence in gluon distribution and fragmentation functions*, Phys.Rev. **D63** (2001) 094021, [hep-ph/0009343].

[73] P. J. Mulders and R. Tangerman, *The Complete tree level result up to order $1/Q$ for polarized deep inelastic leptoproduction*, Nucl.Phys. **B461** (1996) 197–237, [hep-ph/9510301].

[74] D. Boer, P. J. Mulders, and F. Pijlman, *Universality of T-odd effects in single spin and azimuthal asymmetries*, Nucl.Phys. **B667** (2003) 201–241, [hep-ph/0303034].

[75] A. Bacchetta and P. J. Mulders, *Deep inelastic leptoproduction of spin-one hadrons*, Phys. Rev. **D62** (2000) 114004, [http://arXiv.org/abs/hep-ph/0007120].

[76] S. Meissner, A. Metz, and K. Goeke, *Relations between generalized and transverse momentum dependent parton distributions*, Phys.Rev. **D76** (2007) 034002, [hep-ph/0703176].

[77] A. Accardi, J. Albacete, M. Anselmino, N. Armesto, E. Aschenauer, et al., *Electron Ion Collider: The Next QCD Frontier - Understanding the glue that binds us all*, [arXiv:1212.1701].

[78] D. Boer, S. Cotogno, T. van Daal, P. J. Mulders, A. Signori, and Y.-J. Zhou, *Gluon and Wilson loop TMDs for hadrons of spin* ≤ 1, [arXiv:1607.01654].

[79] M. S. Sozzi, *Discrete symmetries and CP violation - From experiment to theory*. Oxford University Press, 2008.

[80] K. Goeke, A. Metz, and M. Schlegel, *Parameterization of the quark-quark correlator of a spin-1/2 hadron*, Phys. Lett. **B618** (2005) 90–96, [hep-ph/0504130].

[81] J. P. Ralston and D. E. Soper, *Production of Dimuons from High-Energy Polarized Proton Proton Collisions*, Nucl.Phys. **B152** (1979) 109.

[82] A. Kotzinian, *New quark distributions and semi-inclusive electroproduction on the polarized nucleons*, Nucl. Phys. **B441** (1995) 234–248, [hep-ph/9412283].

[83] A. Bacchetta, *Probing the Transverse Spin of Quarks in Deep Inelastic Scattering*, PhD thesis, Vrije U., Amsterdam, 2002, [hep-ph/0212025].

[84] R. D. Tangerman, *Higher twist correlations in polarized hadrons*, PhD thesis, Vrije U., Amsterdam, 1996.

[85] J. Pereira-Resina-Rodrigues, *Modeling quark and gluon correlation functions*, PhD thesis, Vrije U., Amsterdam, 2001.

[86] D. Boer, *Azimuthal asymmetries in hard scattering processes*, PhD thesis, Vrije U., Amsterdam, 1998.

[87] D. Boer, C. Lorcé, C. Pisano, and J. Zhou, *The gluon Sivers distribution: status and future prospects*, Adv. High Energy Phys. **2015** (2015) 371396, [arXiv:1504.04332].

[88] M. G. A. Buffing, A. Mukherjee, and P. J. Mulders, *Generalized Universality of Definite Rank Gluon Transverse Momentum Dependent Correlators*, Phys.Rev. **D88** (2013) 054027, [arXiv:1306.5897].

[89] M. G. Echevarria, T. Kasemets, P. J. Mulders, and C. Pisano, *QCD evolution of (un)polarized gluon TMDPDFs and the Higgs* q_T*-distribution*, [arXiv:1502.05354].

[90] D. Boer, M. G. Echevarria, P. J. Mulders, and J. Zhou, *Single spin asymmetries from a single Wilson loop*, Phys. Rev. Lett. **116** (2016), no. 12, 122001, [arXiv:1511.03485].

[91] J. C. Collins, D. E. Soper, and G. Sterman, *Factorization of hard processes in QCD*, Adv. Ser. Direct. High Energy Phys. **5** (1988) 1–91, [hep-ph/0409313].

[92] CTEQ, R. Brock et al., *Handbook of perturbative QCD: Version 1.0*, Rev. Mod. Phys. **67** (1995) 157–248.

[93] T. Becher, A. Broggio, and A. Ferroglia, *Introduction to Soft-Collinear Effective Theory*, [arXiv:1410.1892].

[94] X. Ji, J.-P. Ma, and F. Yuan, *QCD factorization for spin-dependent cross sections in DIS and Drell-Yan processes at low transverse momentum*, Phys. Lett. **B597** (2004) 299–308, [hep-ph/0405085].

[95] P. Sun, B.-W. Xiao, and F. Yuan, *Gluon Distribution Functions and Higgs Boson Production at Moderate Transverse Momentum*, Phys. Rev. **D84** (2011) 094005, [arXiv:1109.1354].

[96] M. G. Echevarria, A. Idilbi, and I. Scimemi, *Factorization theorem for Drell-Yan at low* q_T *and Transverse Momentum Distributions on-the-light-cone*, JHEP **1207** (2012) 002, [arXiv:1111.4996].

[97] M. Diehl, J. R. Gaunt, D. Ostermeier, P. Plößl, and A. Schäfer, *Cancellation of Glauber gluon exchange in the double Drell-Yan process*, JHEP **01** (2016) 076, [arXiv:1510.08696].

[98] M. G. Echevarria, T. Kasemets, C. Pisano, J.-P. Lansberg, and A. Signori, *Gluon TMDs and quarkonium production in hadronic collisions*, [in preparation].

[99] H. R. Quinn, *A word of caution*, in *XIVth International Symposium on Multiparticle Dynamics Lake Tahoe, California, June 22-27, 1983*, 1983.

[100] T. C. Rogers, *Extra spin asymmetries from the breakdown of transverse-momentum-dependent factorization in hadron-hadron collisions*, Phys. Rev. **D88** (2013), no. 1, 014002, [arXiv:1304.4251].

[101] M. G. Echevarria, I. Scimemi, and A. Vladimirov, *Universal transverse momentum dependent soft function at NNLO*, Phys. Rev. **D93** (2016), no. 5, 054004, [arXiv:1511.05590].

[102] M. G. Echevarria, I. Scimemi, and A. Vladimirov, *Unpolarized Transverse Momentum Dependent Parton Distribution and Fragmentation Functions at next-to-next-to-leading order*, [arXiv:1604.07869].

[103] Y. Li and H. X. Zhu, *Bootstrapping rapidity anomalous dimension for transverse-momentum resummation*, [arXiv:1604.01404].

[104] A. Bacchetta, F. Conti, and M. Radici, *Transverse-momentum distributions in a diquark spectator model*, Phys. Rev. **D78** (2008) 074010, [arXiv:0807.0323].

[105] J. C. Collins, D. E. Soper, and G. F. Sterman, *Transverse Momentum Distribution in Drell-Yan Pair and W and Z Boson Production*, Nucl.Phys. **B250** (1985) 199.

[106] G. Bozzi, S. Catani, G. Ferrera, D. de Florian, and M. Grazzini, *Production of Drell-Yan lepton pairs in hadron collisions: transverse-momentum resummation at next-to-next-to-leading logarithmic accuracy*, Phys. Lett. **B696** (2011) 207–213, [arXiv:1007.2351].

[107] S. Catani, D. de Florian, G. Ferrera, and M. Grazzini, *Vector boson production at hadron colliders: transverse-momentum resummation and leptonic decay*, JHEP **12** (2015) 047, [arXiv:1507.06937].

[108] T. Becher, M. Neubert, and D. Wilhelm, *Electroweak Gauge-Boson Production at Small q_T: Infrared Safety from the Collinear Anomaly*, JHEP **02** (2012) 124, [arXiv:1109.6027].

[109] T. Becher, M. Neubert, and D. Wilhelm, *Higgs-Boson Production at Small Transverse Momentum*, JHEP **05** (2013) 110, [arXiv:1212.2621].

[110] Y. L. Dokshitzer, D. Diakonov, and S. I. Troian, *Hard Processes in Quantum Chromodynamics*, Phys. Rept. **58** (1980) 269–395.

[111] P. B. Arnold and R. P. Kauffman, *W and Z production at next-to-leading order: From large q_T to small*, Nucl.Phys. **B349** (1991) 381–413.

[112] M. Boglione, J. O. G. Hernandez, S. Melis, and A. Prokudin, *A study on the interplay between perturbative QCD and CSS/TMD formalism in SIDIS processes*, JHEP **1502** (2015) 095, [arXiv:1412.1383].

[113] J. Collins, L. Gamberg, A. Prokudin, T. C. Rogers, N. Sato, and B. Wang, *Relating Transverse Momentum Dependent and Collinear Factorization Theorems in a Generalized Formalism*, [arXiv:1605.00671].

[114] U. D'Alesio, M. G. Echevarria, S. Melis, and I. Scimemi, *Non-perturbative QCD effects in q_T spectra of Drell-Yan and Z-boson production*, JHEP **1411** (2014) 098, [arXiv:1407.3311].

[115] J.-Y. Chiu, A. Jain, D. Neill, and I. Z. Rothstein, *The Rapidity Renormalization Group*, Phys. Rev. Lett. **108** (2012) 151601, [arXiv:1104.0881].

[116] D. Boer, *Average transverse momentum quantities approaching the lightfront*, Few Body Syst. **56** (2015), no. 6-9, 439–445, [arXiv:1409.8317].

[117] J. C. Collins, *What exactly is a parton density?*, Acta Phys. Polon. **B34** (2003) 3103, [hep-ph/0304122].

[118] E. Laenen, G. F. Sterman, and W. Vogelsang, *Higher order QCD corrections in prompt photon production*, Phys. Rev. Lett. **84** (2000) 4296–4299, [hep-ph/0002078].

[119] E. Laenen, G. F. Sterman, and W. Vogelsang, *Recoil and threshold corrections in short distance cross sections*, Phys. Rev. **D63** (2001) 114018, [hep-ph/0010080].

[120] A. Kulesza, G. F. Sterman, and W. Vogelsang, *Joint resummation in electroweak boson production*, Phys. Rev. **D66** (2002) 014011, [hep-ph/0202251].

[121] Y. Koike, J. Nagashima, and W. Vogelsang, *Resummation for polarized semi-inclusive deep-inelastic scattering at small transverse momentum*, Nucl.Phys. **B744** (2006) 59–79, [hep-ph/0602188].

[122] M. G. Echevarria, A. Idilbi, A. Schäfer, and I. Scimemi, *Model-Independent Evolution of Transverse Momentum Dependent Distribution Functions (TMDs) at NNLL*, Eur. Phys. J. **C73** (2013), no. 12, 2636, [arXiv:1208.1281].

[123] G. Parisi and R. Petronzio, *Small Transverse Momentum Distributions in Hard Processes*, Nucl.Phys. **B154** (1979) 427.

[124] G. Bozzi, S. Catani, D. de Florian, and M. Grazzini, *Transverse-momentum resummation and the spectrum of the Higgs boson at the LHC*, Nucl. Phys. **B737** (2006) 73–120, [hep-ph/0508068].

[125] D. Boer and W. J. den Dunnen, *TMD evolution and the Higgs transverse momentum distribution*, Nucl. Phys. **B886** (2014) 421–435, [arXiv:1404.6753].

[126] D. Boer, *Linearly polarized gluon effects in unpolarized collisions*, PoS **QCDEV2015** (2015) 023, [arXiv:1510.05915].

[127] A. Bacchetta, F. Delcarro, C. Pisano, M. Radici, and A. Signori, *Extraction of partonic transverse momentum distributions from semi-inclusive deep-inelastic scattering and Drell-Yan data*, [in preparation].

[128] J. Collins and T. Rogers, *Understanding the large-distance behavior of transverse-momentum-dependent parton densities and the Collins-Soper evolution kernel*, Phys. Rev. **D91** (2015), no. 7, 074020, [arXiv:1412.3820].

[129] D. Boer, L. Gamberg, B. Musch, and A. Prokudin, *Bessel-Weighted Asymmetries in Semi Inclusive Deep Inelastic Scattering*, JHEP **10** (2011) 021, [arXiv:1107.5294].

[130] J. C. Collins and R. K. Ellis, *Factorization at small x*, Nucl. Phys. Proc. Suppl. **18C** (1991) 80–85.

[131] J. C. Collins and R. K. Ellis, *Heavy quark production in very high-energy hadron collisions*, Nucl. Phys. **B360** (1991) 3–30.

[132] F. Dominguez, C. Marquet, B.-W. Xiao, and F. Yuan, *Universality of Unintegrated Gluon Distributions at small x*, Phys.Rev. **D83** (2011) 105005, [arXiv:1101.0715].

[133] F. Dominguez, *Unintegrated Gluon Distributions at Small-x*, PhD thesis, Columbia U., 2011.

[134] A. Mueller, B.-W. Xiao, and F. Yuan, *Sudakov Resummation in Small-x Saturation Formalism*, Phys.Rev.Lett. **110** (2013), no. 8, 082301, [arXiv:1210.5792].

[135] A. Mueller, B.-W. Xiao, and F. Yuan, *Sudakov double logarithms resummation in hard processes in the small-x saturation formalism*, Phys.Rev. **D88** (2013), no. 11, 114010, [arXiv:1308.2993].

[136] I. Balitsky and A. Tarasov, *Rapidity evolution of gluon TMD from low to moderate x*, JHEP **10** (2015) 017, [arXiv:1505.02151].

[137] F. Hautmann, H. Jung, M. Krämer, P. J. Mulders, E. R. Nocera, T. C. Rogers, and A. Signori, *TMDlib and TMDplotter: library and plotting tools for transverse-momentum-dependent parton distributions*, Eur. Phys. J. **C74** (2014) 3220, [arXiv:1408.3015].

[138] E. Avsar, *TMD factorization and the gluon distribution in high energy QCD*, [arXiv:1203.1916].

[139] A. Bacchetta, M. G. Echevarria, P. J. G. Mulders, M. Radici, and A. Signori, *Effects of TMD evolution and partonic flavor on e^+ e^- annihilation into hadrons*, JHEP **11** (2015) 076, [arXiv:1508.00402].

[140] W. Ehrenberg and R. E. Siday, *The refractive index in electron optics and the principles of dynamics*, Proceedings of the Physical Society. Section B **62** (1949), no. 1, 8.

[141] Y. Aharonov and D. Bohm, *Significance of electromagnetic potentials in the quantum theory*, Phys. Rev. **115** (1959) 485–491.

[142] J. J. Sakurai and J. Napolitano, *Modern quantum physics*. Boston, USA: Addison-Wesley (2011) 550 p, 2011.

[143] European Muon, J. Ashman et al., *A Measurement of the Spin Asymmetry and Determination of the Structure Function g(1) in Deep Inelastic Muon-Proton Scattering*, Phys. Lett. **B206** (1988) 364.

[144] A. Lesnik, D. M. Schwartz, I. Ambats, E. Hayes, W. T. Meyer, C. E. W. Ward, T. M. Knasel, E. C. Swallow, R. Winston, and T. A. Romanowski, *Observation of a Difference Between Polarization and Analyzing Power in Λ^0 Production with 6 GeV/c Polarized Protons*, Phys. Rev. Lett. **35** (1975) 770.

[145] G. Bunce et al., Λ^0 *Hyperon Polarization in Inclusive Production by 300 GeV Protons on Beryllium.*, Phys. Rev. Lett. **36** (1976) 1113–1116.

[146] E704, E581, D. L. Adams et al., *Comparison of spin asymmetries and cross sections in π^0 production by 200 GeV polarized anti-protons and protons*, Phys. Lett. **B261** (1991) 201–206.

[147] FNAL-E704, D. L. Adams et al., *Analyzing power in inclusive π^+ and π^- production at high x(F) with a 200 GeV polarized proton beam*, Phys. Lett. **B264** (1991) 462–466.

[148] E704, E581, D. L. Adams et al., *Large x(F) spin asymmetry in π^0 production by 200 GeV polarized protons*, Z. Phys. **C56** (1992) 181–184.

[149] K. Krueger et al., *Large analyzing power in inclusive $\pi^\pm$ production at high x(F) with a 22 GeV/c polarized proton beam*, Phys. Lett. **B459** (1999) 412–416.

[150] V. Barone and P. G. Ratcliffe, *Transverse spin physics*. River Edge, USA: World Scientific (2003) 294 p, 2003.

[151] E. Leader, *Spin in particle physics*, Camb. Monogr. Part. Phys. Nucl. Phys. Cosmol. **15** (2011) pp.1–500.

[152] C. J. Bomhof, *Azimuthal spin asymmetries in hadronic processes*, PhD thesis, Vrije U., Amsterdam, 2007.

[153] V. Barone, A. Drago, and P. G. Ratcliffe, *Transverse polarisation of quarks in hadrons*, Phys.Rept. **359** (2002) 1–168, [hep-ph/0104283].

[154] C. Bourrely, J. Soffer, and E. Leader, *Polarization Phenomena in Hadronic Reactions*, Phys. Rept. **59** (1980) 95–297.

[155] M. Anselmino, A. Efremov, and E. Leader, *The Theory and phenomenology of polarized deep inelastic scattering*, Phys. Rept. **261** (1995) 1–124, [Erratum: Phys. Rept.281,399(1997)], [hep-ph/9501369].

[156] Z.-T. Liang and C. Boros, *Single spin asymmetries in inclusive high-energy hadron hadron collision processes*, Int. J. Mod. Phys. **A15** (2000) 927–982, [hep-ph/0001330].

[157] M. Boglione and A. Prokudin, *Phenomenology of Transverse Spin: Past, Present and Future*, [arXiv:1511.06924].

[158] E. C. Aschenauer, U. D'Alesio, and F. Murgia, *TMDs and SSAs in hadronic interactions*, 2015. [arXiv:1512.05379].

[159] A. Prokudin, *A_N in inclusive lepton-proton collisions: TMD and twist-3 approaches*, EPJ Web Conf. **85** (2015) 02028, [arXiv:1410.3867].

[160] A. V. Efremov and O. V. Teryaev, *On Spin Effects in Quantum Chromodynamics*, Sov. J. Nucl. Phys. **36** (1982) 140, [Yad. Fiz.36,242(1982)].

[161] J.-W. Qiu and G. F. Sterman, *Single transverse spin asymmetries*, Phys.Rev.Lett. **67** (1991) 2264–2267.

[162] D. W. Sivers, *Single Spin Production Asymmetries from the Hard Scattering of Point-Like Constituents*, Phys. Rev. **D41** (1990) 83.

[163] D. W. Sivers, *Hard scattering scaling laws for single spin production asymmetries*, Phys. Rev. **D43** (1991) 261–263.

[164] J. C. Collins, *Fragmentation of transversely polarized quarks probed in transverse momentum distributions*, Nucl. Phys. **B396** (1993) 161–182, [hep-ph/9208213].

[165] J. C. Collins, *Leading twist single transverse-spin asymmetries: Drell-Yan and deep inelastic scattering*, Phys.Lett. **B536** (2002) 43–48, [hep-ph/0204004].

[166] A. Bacchetta, U. D'Alesio, M. Diehl, and C. A. Miller, *Single-spin asymmetries: the Trento conventions*, Phys. Rev. **D70** (2004) 117504, [hep-ph/0410050].

[167] P. Schweitzer, T. Teckentrup, and A. Metz, *Intrinsic transverse parton momenta in deeply inelastic reactions*, Phys.Rev. **D81** (2010) 094019, [arXiv:1003.2190].

[168] J. Collins, A. Efremov, K. Goeke, S. Menzel, A. Metz, et al., *Sivers effect in semi-inclusive deeply inelastic scattering*, Phys.Rev. **D73** (2006) 014021, [hep-ph/0509076].

[169] S. Forte and G. Watt, *Progress in the determination of the partonic structure of the proton*, [arXiv:1301.6754].

[170] J. Gao, M. Guzzi, J. Huston, H.-L. Lai, Z. Li, et al., *The CT10 NNLO global analysis of QCD*, [arXiv:1302.6246].

[171] J. Owens, A. Accardi, and W. Melnitchouk, *Global parton distributions with nuclear and finite-Q^2 corrections*, Phys.Rev. **D87** (2013), no. 9, 094012, [arXiv:1212.1702].

[172] R. D. Ball, V. Bertone, S. Carrazza, C. S. Deans, L. Del Debbio, et al., *Parton distributions with LHC data*, Nucl. Phys. **B867** (2013) 244–289, [arXiv:1207.1303].

[173] M. Anselmino, M. Boglione, J. O. Gonzalez Hernandez, S. Melis, and A. Prokudin, *Unpolarised Transverse Momentum Dependent Distribution and Fragmentation Functions from recent HERMES and COMPASS SIDIS Multiplicities*, PoS **DIS2014** (2014) 201.

[174] A. Signori, A. Bacchetta, M. Radici, and G. Schnell, *Investigations into the flavor dependence of partonic transverse momentum*, JHEP **1311** (2013) 194, [arXiv:1309.3507].

[175] A. Signori, A. Bacchetta, and M. Radici, *Flavor dependence of unpolarized TMDs from semi-inclusive pion production*, Int.J.Mod.Phys.Conf.Ser. **25** (2014) 1460020, [arXiv:1309.5929].

[176] A. Signori, A. Bacchetta, and M. Radici, *Phenomenology of unpolarized TMDs from Semi-Inclusive DIS data*, PoS **DIS2014** (2014) 202, [arXiv:1407.2445].

[177] M. Radici, A. Bacchetta, A. Signori, and G. Schnell, *Exploring the Flavor Dependence of Partonic Transverse Momentum*, Int. J. Mod. Phys. Conf. Ser. **37** (2015) 1560024.

[178] M. Anselmino, M. Boglione, U. D'Alesio, A. Kotzinian, F. Murgia, et al., *The role of Cahn and Sivers effects in deep inelastic scattering*, Phys.Rev. **D71** (2005) 074006, [hep-ph/0501196].

[179] C. A. Aidala, B. Field, L. P. Gamberg, and T. C. Rogers, *Limits on transverse momentum dependent evolution from semi-inclusive deep inelastic scattering at moderate Q*, Phys. Rev. **D89** (2014), no. 9, 094002, [arXiv:1401.2654].

[180] U. D'Alesio and F. Murgia, *Parton intrinsic motion in inclusive particle production: unpolarized cross sections, single spin asymmetries and the Sivers effect*, Phys. Rev. **D70** (2004) 074009, [hep-ph/0408092].

[181] F. Landry, R. Brock, P. M. Nadolsky, and C. Yuan, *Tevatron Run-1 Z boson data and Collins-Soper-Sterman resummation formalism*, Phys.Rev. **D67** (2003) 073016, [hep-ph/0212159].

[182] A. V. Konychev and P. M. Nadolsky, *Universality of the Collins-Soper-Sterman nonperturbative function in gauge boson production*, Phys.Lett. **B633** (2006) 710–714, [hep-ph/0506225].

[183] S. M. Aybat and T. C. Rogers, *TMD Parton Distribution and Fragmentation Functions with QCD Evolution*, Phys.Rev. **D83** (2011) 114042, [arXiv:1101.5057].

[184] F. A. Ceccopieri and L. Trentadue, *On the QCD Evolution of Transverse Momentum Dependent Distributions*, Phys.Lett. **B741** (2015) 97–102, [arXiv:1407.7972].

[185] J. Kodaira and L. Trentadue, *Summing Soft Emission in QCD*, Phys.Lett. **B112** (1982) 66.

[186] A. Bassetto, M. Ciafaloni, and G. Marchesini, *Inelastic Distributions and Color Structure in Perturbative QCD*, Nucl.Phys. **B163** (1980) 477.

[187] D. Amati, A. Bassetto, M. Ciafaloni, G. Marchesini, and G. Veneziano, *A Treatment of Hard Processes Sensitive to the Infrared Structure of QCD*, Nucl.Phys. **B173** (1980) 429.

[188] M. Hirai, H. Kawamura, and K. Tanaka, *New determination of the nonperturbative form factor in QCD transverse-momentum resummation for vector boson production*, in *Proceedings, 20th International Workshop on Deep-Inelastic Scattering and Related Subjects (DIS 2012)*, pp. 535–538, 2012.

[189] A. Kulesza and W. J. Stirling, *Nonperturbative effects and the resummed Higgs transverse momentum distribution at the LHC*, JHEP **0312** (2003) 056, [hep-ph/0307208].

[190] M. Guzzi, P. M. Nadolsky, and B. Wang, *Nonperturbative contributions to a resummed leptonic angular distribution in inclusive neutral vector boson production*, Phys.Rev. **D90** (2014), no. 1, 014030, [arXiv:1309.1393].

[191] P. Sun and F. Yuan, *Transverse momentum dependent evolution: Matching semi-inclusive deep inelastic scattering processes to Drell-Yan and W/Z boson production*, Phys. Rev. **D88** (2013), no. 11, 114012, [arXiv:1308.5003].

[192] P. Sun, J. Isaacson, C. P. Yuan, and F. Yuan, *Universal Non-perturbative Functions for SIDIS and Drell-Yan Processes*, [arXiv:1406.3073].

[193] M. G. Echevarria, A. Idilbi, Z.-B. Kang, and I. Vitev, *QCD Evolution of the Sivers Asymmetry*, Phys.Rev. **D89** (2014), no. 7, 074013, [arXiv:1401.5078].

[194] L. D. McLerran and R. Venugopalan, *Fock space distributions, structure functions, higher twists and small x*, Phys.Rev. **D59** (1999) 094002, [hep-ph/9809427].

[195] A. H. Mueller, *Parton saturation at small x and in large nuclei*, Nucl.Phys. **B558** (1999) 285–303, [hep-ph/9904404].

[196] C. Marquet, B.-W. Xiao, and F. Yuan, *Semi-inclusive Deep Inelastic Scattering at small x*, Phys.Lett. **B682** (2009) 207–211, [arXiv:0906.1454].

[197] A. Metz and A. Vossen, *Parton Fragmentation Functions*, [arXiv:1607.02521].

[198] D. de Florian, R. Sassot, M. Epele, R. J. Hernández-Pinto, and M. Stratmann, *Parton-to-Pion Fragmentation Reloaded*, Phys.Rev. **D91** (2015), no. 1, 014035, [arXiv:1410.6027].

[199] D. Boer, W. J. den Dunnen, C. Pisano, M. Schlegel, and W. Vogelsang, *Linearly Polarized Gluons and the Higgs Transverse Momentum Distribution*, Phys.Rev.Lett. **108** (2012) 032002, [arXiv:1109.1444].

[200] D. Boer and C. Pisano, *Impact of gluon polarization on Higgs boson plus jet production at the LHC*, Phys. Rev. **D91** (2015), no. 7, 074024, [arXiv:1412.5556].

[201] D. Boer and C. Pisano, *Polarized gluon studies with charmonium and bottomonium at LHCb and AFTER*, Phys.Rev. **D86** (2012) 094007, [arXiv:1208.3642].

[202] K. J. Golec-Biernat and M. Wusthoff, *Saturation in diffractive deep inelastic scattering*, Phys.Rev. **D60** (1999) 114023, [hep-ph/9903358].

[203] F. Hautmann and H. Jung, *Transverse momentum dependent gluon density from DIS precision data*, Nucl.Phys. **B883** (2014) 1–19, [arXiv:1312.7875].

[204] A. A. Grinyuk, H. Jung, G. I. Lykasov, A. V. Lipatov, and N. P. Zotov, *Unintegrated Gluon Distribution and Soft pp Collisions at LHC*, in *Proceedings, 3rd International Workshop on Multiple Partonic Interactions at the LHC (MPI@LHC 2011): Hamburg, Germany, 21-25 Nov 2011*, pp. 169–176, 2012. [arXiv:1203.0939].

[205] B. Ermolaev, M. Greco, and S. Troyan, *QCD Factorization for Forward Hadron Scattering at High Energies*, Eur.Phys.J. **C72** (2012) 1953, [arXiv:1112.1854].

[206] S. Catani, F. Fiorani, and G. Marchesini, *QCD Coherence in Initial State Radiation*, Phys. Lett. **B234** (1990) 339–345.

[207] S. Catani, F. Fiorani, and G. Marchesini, *Small x Behavior of Initial State Radiation in Perturbative QCD*, Nucl. Phys. **B336** (1990) 18–85.

[208] A.-V. Lipatov, G. Lykasov, and N. Zotov, *LHC soft physics and transverse momentum dependent gluon density at low x*, Phys.Rev. **D89** (2014), no. 1, 014001, [arXiv:1310.7893].

[209] H1, C. Alexa et al., *Measurement of Charged Particle Spectra in Deep-Inelastic ep Scattering at HERA*, Eur.Phys.J. **C73** (2013), no. 4, 2406, [arXiv:1302.1321].

[210] A. Bacchetta, H. Jung, A. Knutsson, K. Kutak, and F. Samson-Himmelstjerna, *A method for tuning parameters of Monte Carlo generators and its application to the determination of the unintegrated gluon density*, Eur. Phys. J. **C70** (2010) 503–511, [arXiv:1001.4675].

[211] G. Altarelli, R. K. Ellis, M. Greco, and G. Martinelli, *Vector Boson Production at Colliders: A Theoretical Reappraisal*, Nucl.Phys. **B246** (1984) 12.

[212] D. Boer, M. G. A. Buffing, and P. J. Mulders, *Operator analysis of p_T-widths of TMDs*, JHEP **08** (2015) 053, [arXiv:1503.03760].

[213] P. J. Mulders and T. C. Rogers, *Gauge Links, TMD-Factorization, and TMD-Factorization Breaking*, [arXiv:1102.4569].

[214] A. Bacchetta, M. G. Echevarria, M. Radici, and A. Signori, *Phenomenology from SIDIS and e^+e^- multiplicities*, EPJ Web Conf. **85** (2015) 02016, [arXiv:1409.7227].

[215] NNPDF, R. D. Ball et al., *Unbiased global determination of parton distributions and their uncertainties at NNLO and at LO*, Nucl.Phys. **B855** (2012) 153–221, [arXiv:1107.2652].

[216] S. Alekhin et al., *HERAFitter*, Eur. Phys. J. **C75** (2015), no. 7, 304, [arXiv:1410.4412].

[217] A. Buckley, J. Ferrando, S. Lloyd, K. Nordström, B. Page, M. Rüfenacht, M. Schönherr, and G. Watt, *LHAPDF6: parton density access in the LHC precision era*, Eur. Phys. J. **C75** (2015) 132, [arXiv:1412.7420].

[218] A. Martin, W. Stirling, R. Thorne, and G. Watt, *Parton distributions for the LHC*, Eur.Phys.J. **C63** (2009) 189–285, [arXiv:0901.0002].

[219] P. Jimenez-Delgado and E. Reya, *Dynamical NNLO parton distributions*, Phys. Rev. **D79** (2009) 074023, [arXiv:0810.4274].

[220] A. Bacchetta, M. Radici, F. Conti, and M. Guagnelli, *Weighted azimuthal asymmetries in a diquark spectator model*, Eur. Phys. J. **A45** (2010) 373–388, [arXiv:1003.1328].

[221] M. Wakamatsu, *Transverse momentum distributions of quarks in the nucleon from the chiral quark soliton model*, Phys. Rev. **D79** (2009) 094028, [arXiv:0903.1886].

[222] A. Efremov, P. Schweitzer, O. Teryaev, and P. Zavada, *The relation between TMDs and PDFs in the covariant parton model approach*, Phys. Rev. **D83** (2011) 054025, [arXiv:1012.5296].

[223] C. Bourrely, F. Buccella, and J. Soffer, *Semi-inclusive DIS cross sections and spin asymmetries in the quantum statistical parton distributions approach*, Phys. Rev. **D83** (2011) 074008, [arXiv:1008.5322].

[224] H. H. Matevosyan, W. Bentz, I. C. Cloet, and A. W. Thomas, *Transverse momentum dependent fragmentation and quark distribution functions from the NJL-jet model*, Phys. Rev. **D85** (2012) 014021, [arXiv:1111.1740].

[225] P. Schweitzer, M. Strikman, and C. Weiss, *Intrinsic transverse momentum and parton correlations from dynamical chiral symmetry breaking*, JHEP **1301** (2013) 163, [arXiv:1210.1267].

[226] B. Pasquini, S. Cazzaniga, and S. Boffi, *Transverse momentum dependent parton distributions in a light-cone quark model*, Phys. Rev. **D78** (2008) 034025, [arXiv:0806.2298].

[227] C. Lorce, B. Pasquini, and M. Vanderhaeghen, *Unified framework for generalized and transverse-momentum dependent parton distributions within a 3Q light-cone picture of the nucleon*, JHEP **1105** (2011) 041, [arXiv:1102.4704].

[228] H. Avakian, A. V. Efremov, P. Schweitzer, and F. Yuan, *The transverse momentum dependent distribution functions in the bag model*, Phys. Rev. **D81** (2010) 074035, [arXiv:1001.5467].

[229] B. U. Musch, P. Hägler, J. W. Negele, and A. Schäfer, *Exploring quark transverse momentum distributions with lattice QCD*, Phys. Rev. **D83** (2011) 094507, [arXiv:1011.1213].

[230] A. Bacchetta, L. P. Gamberg, G. R. Goldstein, and A. Mukherjee, *Collins fragmentation function for pions and kaons in a spectator model*, Phys. Lett. **B659** (2008) 234–243, [arXiv:0707.3372].

[231] A. Bacchetta, D. Boer, M. Diehl, and P. J. Mulders, *Matches and mismatches in the descriptions of semi-inclusive processes at low and high transverse momentum*, JHEP **08** (2008) 023, [arXiv:0803.0227].

[232] J. C. Collins and D. E. Soper, *Back-to-back jets in QCD*, Nucl. Phys. **B193** (1981) 381.

[233] J. C. Collins and T. C. Rogers, *Equality of Two Definitions for Transverse Momentum Dependent Parton Distribution Functions*, Phys. Rev. **D87** (2013), no. 3, 034018, [arXiv:1210.2100].

[234] P. J. Mulders and R. D. Tangerman, *The complete tree-level result up to order $1/Q$ for polarized deep-inelastic leptoproduction*, Nucl. Phys. **B461** (1996) 197–237, Erratum-ibid. **B484** (1996) 538, [http://arXiv.org/abs/hep-ph/9510301].

[235] J.-F. Rajotte, *Hadron muoproduction at the COMPASS experiment*, PhD thesis, München U., 2010.

[236] R. Jakob, P. J. Mulders, and J. Rodrigues, *Modelling quark distribution and fragmentation functions*, Nucl. Phys. **A626** (1997) 937–965, [http://arXiv.org/abs/hep-ph/9704335].

[237] S. J. Brodsky, D. S. Hwang, B.-Q. Ma, and I. Schmidt, *Light-cone representation of the spin and orbital angular momentum of relativistic composite systems*, Nucl. Phys. **B593** (2001) 311–335, [hep-th/0003082].

[238] D. Hwang and D. Müller, *Implication of the overlap representation for modelling generalized parton distributions*, Phys. Lett. **B660** (2008) 350–359, [arXiv:0710.1567].

[239] T. Gutsche, V. E. Lyubovitskij, I. Schmidt, and A. Vega, *Light-front quark model consistent with Drell-Yan-West duality and quark counting rules*, Phys. Rev. **D89** (2014), no. 5, 054033, [Erratum: Phys. Rev.D92,no.1,019902(2015)], [arXiv:1306.0366].

[240] M. Hirai, S. Kumano, T. H. Nagai, and K. Sudoh, *Determination of fragmentation functions and their uncertainties*, Phys. Rev. **D75** (2007) 094009, [hep-ph/0702250].

[241] D. de Florian, R. Sassot, and M. Stratmann, *Global analysis of fragmentation functions for pions and kaons and their uncertainties*, Phys. Rev. **D75** (2007) 114010, [hep-ph/0703242].

[242] M. Boglione and P. J. Mulders, *Time reversal odd fragmentation and distribution functions in pp and ep single spin asymmetries*, Phys. Rev. **D60** (1999) 054007, [hep-ph/9903354].

[243] P. Schweitzer and A. Bacchetta, *Azimuthal single spin asymmetries in SIDIS in the light of chiral symmetry breaking*, Nucl. Phys. **A732** (2004) 106–124, [hep-ph/0310318].

[244] A. Bacchetta, R. Kundu, A. Metz, and P. J. Mulders, *Estimate of the Collins fragmentation function in a chiral invariant approach*, Phys. Rev. **D65** (2002) 094021, [hep-ph/0201091].

[245] M. Epele, R. Llubaroff, R. Sassot, and M. Stratmann, *Uncertainties in pion and kaon fragmentation functions*, Phys. Rev. **D86** (2012) 074028, [arXiv:1209.3240].

[246] A. Bacchetta, A. Courtoy, and M. Radici, *First extraction of valence transversities in a collinear framework*, JHEP **1303** (2013) 119, [arXiv:1212.3568].

[247] S. Forte, L. Garrido, J. I. Latorre, and A. Piccione, *Neural network parametrization of deep-inelastic structure functions*, JHEP **0205** (2002) 062, [hep-ph/0204232].

[248] NNPDF, R. D. Ball et al., *A determination of parton distributions with faithful uncertainty estimation*, Nucl. Phys. **B809** (2009) 1–63, [arXiv:0808.1231].

[249] R. D. Ball et al., *A first unbiased global NLO determination of parton distributions and their uncertainties*, Nucl. Phys. **B838** (2010) 136–206, [arXiv:1002.4407].

[250] A. Accardi, J. Albacete, M. Anselmino, N. Armesto, E. Aschenauer, et al., *Electron Ion Collider: the next QCD frontier - Understanding the glue that binds us all*, [arXiv:1212.1701].

[251] R. N. Cahn, *Azimuthal dependence in leptoproduction: a simple parton model calculation*, Phys. Lett. **B78** (1978) 269.

[252] M. Anselmino, M. Boglione, J. O. Gonzalez Hernandez, S. Melis, and A. Prokudin, *Unpolarised Transverse Momentum Dependent Distribution and Fragmentation Functions from SIDIS Multiplicities*, JHEP **04** (2014) 005, [arXiv:1312.6261].

[253] P. M. Nadolsky, D. R. Stump, and C. P. Yuan, *Phenomenology of multiple parton radiation in semi-inclusive deep-inelastic scattering*, Phys. Rev. **D64** (2001) 114011, [hep-ph/0012261].

[254] A. Bacchetta, M. García-Echevarría, M. Radici, and A. Signori, *Predictions for Transverse-Momentum Dependence in Electron-Positron Annihilation*, Int.J.Mod.Phys.Conf.Ser. **37** (2015) 1560023.

[255] Z.-B. Kang, A. Prokudin, P. Sun, and F. Yuan, *Extraction of Quark Transversity Distribution and Collins Fragmentation Functions with QCD Evolution*, Phys. Rev. **D93** (2016), no. 1, 014009, [arXiv:1505.05589].

[256] D. Boer, R. Jakob, and P. J. Mulders, *Asymmetries in polarized hadron production in e^+e^- annihilation up to order 1/Q*, Nucl. Phys. **B504** (1997) 345–380, [hep-ph/9702281].

[257] A. Bacchetta, P. J. Mulders, M. Radici, M. Ritzmann, and A. Signori, *Nonperturbative effects in q_T spectra of electroweak bosons at the LHC*, [in preparation].

[258] O. Stal, G. Weiglein, and L. Zeune, *Improved prediction for the mass of the W boson in the NMSSM*, JHEP **09** (2015) 158, [arXiv:1506.07465].

[259] S. Quackenbush and Z. Sullivan, *Parton distributions and the W mass measurement*, [arXiv:1502.04671].

[260] CDF, T. A. Aaltonen et al., *Precise measurement of the W boson mass with the Collider Detector at Fermilab*, Phys. Rev. **D89** (2014), no. 7, 072003, [arXiv:1311.0894].

[261] D0, V. M. Abazov et al., *Measurement of the W boson mass with the D0 detector*, Phys. Rev. **D89** (2014), no. 1, 012005, [arXiv:1310.8628].

[262] M. P. Mulders, *Direct measurement of the W boson mass in e^+e^- collisions at LEP*, PhD thesis, FOM, Amsterdam, 2001.

[263] ATLAS Collaboration, G. Aad et al., *Measurement of the Transverse Momentum Distribution of W Bosons in pp Collisions at $\sqrt{s} = 7$ TeV with the ATLAS Detector*, Phys.Rev. **D85** (2012) 012005, [arXiv:1108.6308].

[264] ATLAS Collaboration, G. Aad et al., *Measurement of the Z/γ^* boson transverse momentum distribution in pp collisions at $\sqrt{s} = 7$ TeV with the ATLAS detector*, JHEP **1409** (2014) 145, [arXiv:1406.3660].

[265] CMS, V. Khachatryan et al., *Measurement of the Z boson differential cross section in transverse momentum and rapidity in proton–proton collisions at 8 TeV*, Phys. Lett. **B749** (2015) 187–209, [arXiv:1504.03511].

[266] CMS, V. Khachatryan et al., *Angular coefficients of Z bosons produced in pp collisions at $\sqrt{s}$ = 8 TeV and decaying to $\mu^+\mu^-$ as a function of transverse momentum and rapidity*, Phys. Lett. **B750** (2015) 154–175, [arXiv:1504.03512].

[267] P. M. Nadolsky, *Theory of W and Z boson production*, AIP Conf. Proc. **753** (2005) 158–170, [hep-ph/0412146].

[268] G. A. Ladinsky and C. P. Yuan, *The Nonperturbative regime in QCD resummation for gauge boson production at hadron colliders*, Phys. Rev. **D50** (1994) 4239, [hep-ph/9311341].

[269] ATLAS, *Studies of vector boson transverse momentum simulation in Monte Carlo event generators*, [inspirehep 1196914].

[270] A. Pich, *Review of α_s determinations*, [arXiv:1303.2262].

[271] A. Signori, *Gluon TMDs in quarkonium production*, Few Body Syst. **57** (2016), no. 8, 651–655, [arXiv:1602.03405].

[272] G. T. Bodwin, E. Braaten, and G. P. Lepage, *Rigorous QCD analysis of inclusive annihilation and production of heavy quarkonium*, Phys.Rev. **D51** (1995) 1125–1171, [hep-ph/9407339].

[273] J. P. Lansberg, S. J. Brodsky, F. Fleuret, and C. Hadjidakis, *Quarkonium Physics at a Fixed-Target Experiment using the LHC Beams*, Few Body Syst. **53** (2012) 11–25, [arXiv:1204.5793].

[274] F. Maltoni and A. D. Polosa, *Observation potential for η_b at the Tevatron*, Phys. Rev. **D70** (2004) 054014, [hep-ph/0405082].

[275] P. Mathews, P. Poulose, and K. Sridhar, *η_c production at the Tevatron: A Test of NRQCD*, Phys. Lett. **B438** (1998) 336–340, [Erratum: Phys. Lett.B450,479(1999)], [hep-ph/9803424].

[276] S. S. Biswal and K. Sridhar, *η_c production at the Large Hadron Collider*, J. Phys. **G39** (2012) 015008, [arXiv:1007.5163].

[277] M. Butenschoen, Z.-G. He, and B. A. Kniehl, *η_c production at the LHC challenges nonrelativistic-QCD factorization*, Phys. Rev. Lett. **114** (2015), no. 9, 092004, [arXiv:1411.5287].

[278] L. D. Landau, *On the angular momentum of a system of two photons*, Dokl. Akad. Nauk Ser. Fiz. **60** (1948), no. 2, 207–209.

[279] C.-N. Yang, *Selection Rules for the Dematerialization of a Particle Into Two Photons*, Phys. Rev. **77** (1950) 242–245.

[280] J. Ma, J. Wang, and S. Zhao, *Transverse momentum dependent factorization for quarkonium production at low transverse momentum*, Phys.Rev. **D88** (2013), no. 1, 014027, [arXiv:1211.7144].

[281] J. Ma, J. Wang, and S. Zhao, *Breakdown of QCD Factorization for P-Wave Quarkonium Production at Low Transverse Momentum*, Phys.Lett. **B737** (2014) 103–108, [arXiv:1405.3373].

[282] W. J. den Dunnen, J.-P. Lansberg, C. Pisano, and M. Schlegel, *Accessing the Transverse Dynamics and Polarization of Gluons inside the Proton at the LHC*, Phys.Rev.Lett. **112** (2014) 212001, [arXiv:1401.7611].

[283] S. Fleming, A. K. Leibovich, and T. Mehen, *Resumming the color octet contribution to $e^+e^- \to J/\psi + X$*, Phys. Rev. **D68** (2003) 094011, [hep-ph/0306139].

[284] S. Fleming, A. K. Leibovich, and T. Mehen, *J/ψ photo-production at large Z in soft collinear effective theory*, in *Proceedings, Ringberg Workshop on New Trends in HERA Physics 2005*, pp. 239–252, 2005. [hep-ph/0512194].

[285] S. Fleming, A. K. Leibovich, and T. Mehen, *Resummation of Large Endpoint Corrections to Color-Octet J/ψ Photoproduction*, Phys. Rev. **D74** (2006) 114004, [hep-ph/0607121].

[286] S. Fleming, A. K. Leibovich, T. Mehen, and I. Z. Rothstein, *The Systematics of Quarkonium Production at the LHC and Double Parton Fragmentation*, Phys. Rev. **D86** (2012) 094012, [arXiv:1207.2578].

[287] S. Fleming, A. K. Leibovich, T. Mehen, and I. Z. Rothstein, *Anomalous dimensions of the double parton fragmentation functions*, Phys. Rev. **D87** (2013) 074022, [arXiv:1301.3822].

[288] P. Sun, C.-P. Yuan, and F. Yuan, *Heavy Quarkonium Production at Low P_T in NRQCD with Soft Gluon Resummation*, Phys.Rev. **D88** (2013) 054008, [arXiv:1210.3432].

[289] R. Zhu, P. Sun, and F. Yuan, *Low Transverse Momentum Heavy Quark Pair Production to Probe Gluon Tomography*, Phys. Lett. **B727** (2013) 474–479, [arXiv:1309.0780].

[290] Y.-Q. Ma, J.-W. Qiu, G. Sterman, and H. Zhang, *Factorized power expansion for high-p_T heavy quarkonium production*, Phys. Rev. Lett. **113** (2014), no. 14, 142002, [arXiv:1407.0383].

[291] Z.-B. Kang, Y.-Q. Ma, J.-W. Qiu, and G. Sterman, *Heavy Quarkonium Production at Collider Energies: Factorization and Evolution*, Phys. Rev. **D90** (2014), no. 3, 034006, [arXiv:1401.0923].

[292] S. Catani, M. Grazzini, and A. Torre, *Transverse-momentum resummation for heavy-quark hadroproduction*, Nucl. Phys. **B890** (2014) 518–538, [arXiv:1408.4564].

[293] A. Pineda, *Review of Heavy Quarkonium at weak coupling*, Prog. Part. Nucl. Phys. **67** (2012) 735–785, [arXiv:1111.0165].

[294] D. Boer, S. J. Brodsky, P. J. Mulders, and C. Pisano, *Direct Probes of Linearly Polarized Gluons inside Unpolarized Hadrons*, Phys.Rev.Lett. **106** (2011) 132001, [arXiv:1011.4225].

[295] C. Pisano, D. Boer, S. J. Brodsky, M. G. A. Buffing, and P. J. Mulders, *Linear polarization of gluons and photons in unpolarized collider experiments*, JHEP **1310** (2013) 024, [arXiv:1307.3417].

[296] J.-W. Qiu, M. Schlegel, and W. Vogelsang, *Probing Gluonic Spin-Orbit Correlations in Photon Pair Production*, Phys.Rev.Lett. **107** (2011) 062001, [arXiv:1103.3861].

[297] A. Metz and J. Zhou, *Distribution of linearly polarized gluons inside a large nucleus*, Phys.Rev. **D84** (2011) 051503, [arXiv:1105.1991].

[298] F. Dominguez, J.-W. Qiu, B.-W. Xiao, and F. Yuan, *On the linearly polarized gluon distributions in the color dipole model*, Phys.Rev. **D85** (2012) 045003, [arXiv:1109.6293].

[299] S. Catani and M. Grazzini, *QCD transverse-momentum resummation in gluon fusion processes*, Nucl.Phys. **B845** (2011) 297–323, [arXiv:1011.3918].

[300] D. Boer, W. J. den Dunnen, C. Pisano, and M. Schlegel, *Determining the Higgs spin and parity in the diphoton decay channel*, Phys.Rev.Lett. **111** (2013), no. 3, 032002, [arXiv:1304.2654].

[301] P. M. Nadolsky, C. Balazs, E. L. Berger, and C.-P. Yuan, *Gluon-gluon contributions to the production of continuum diphoton pairs at hadron colliders*, Phys.Rev. **D76** (2007) 013008, [hep-ph/0702003].

[302] B. Gong, J.-P. Lansberg, C. Lorce, and J. Wang, *Next-to-leading-order QCD corrections to the yields and polarisations of J/Ψ and Upsilon directly produced in association with a Z boson at the LHC*, JHEP **1303** (2013) 115, [arXiv:1210.2430].

[303] J. H. Kuhn, J. Kaplan, and E. G. O. Safiani, *Electromagnetic Annihilation of e^+e^- Into Quarkonium States with Even Charge Conjugation*, Nucl. Phys. **B157** (1979) 125.

[304] B. Guberina, J. H. Kuhn, R. D. Peccei, and R. Ruckl, *Rare Decays of the Z^0*, Nucl. Phys. **B174** (1980) 317.

[305] R. Baier and R. Ruckl, *Hadronic Collisions: A Quarkonium Factory*, Z. Phys. **C19** (1983) 251.

[306] G. T. Bodwin, H. S. Chung, D. Kang, J. Lee, and C. Yu, *Improved determination of color-singlet nonrelativistic QCD matrix elements for S-wave charmonium*, Phys. Rev. **D77** (2008) 094017, [arXiv:0710.0994].

[307] G. T. Bodwin, E. Braaten, and J. Lee, *Comparison of the color-evaporation model and the NRQCD factorization approach in charmonium production*, Phys. Rev. **D72** (2005) 014004, [hep-ph/0504014].

[308] J. P. Ma and C. Wang, *QCD factorization for quarkonium production in hadron collisions at low transverse momentum*, Phys. Rev. **D93** (2016), no. 1, 014025, [arXiv:1509.04421].

[309] J. H. Kuhn and E. Mirkes, *QCD corrections to toponium production at hadron colliders*, Phys. Rev. **D48** (1993) 179–189, [hep-ph/9301204].

[310] A. Petrelli, M. Cacciari, M. Greco, F. Maltoni, and M. L. Mangano, *NLO production and decay of quarkonium*, Nucl. Phys. **B514** (1998) 245–309, [hep-ph/9707223].

[311] LHCb, R. Aaij et al., *Measurement of the $\eta_c(1S)$ production cross section in proton-proton collisions via the decay $\eta_c(1S) \to p\bar{p}$*, Eur. Phys. J. **C75** (2015), no. 7, 311, [arXiv:1409.3612].

[312] J. C. Collins, *Light cone variables, rapidity and all that*, [hep-ph/9705393].

[313] L. P. Gamberg, A. Mukherjee, and P. J. Mulders, *Spectral analysis of gluonic pole matrix elements for fragmentation*, Phys. Rev. **D77** (2008) 114026, [arXiv:0803.2632].

[314] S. Meissner and A. Metz, *Partonic pole matrix elements for fragmentation*, Phys. Rev. Lett. **102** (2009) 172003, [arXiv:0812.3783].

[315] L. P. Gamberg, A. Mukherjee, and P. J. Mulders, *A model independent analysis of gluonic pole matrix elements and universality of TMD fragmentation functions*, Phys. Rev. **D83** (2011) 071503, [arXiv:1010.4556].

[316] F. Yuan and J. Zhou, *Collins Fragmentation and the Single Transverse Spin Asymmetry*, Phys. Rev. Lett. **103** (2009) 052001, [arXiv:0903.4680].

[317] A. Aprahamian et al., *Reaching for the horizon: The 2015 long range plan for nuclear science*, [inspire 1398831].

[318] M. Radici, *Imaging the proton*, AIP Conf. Proc. **1735** (2016) 020003.